

ABSTRACT

LEE, DENNIS TAE-SUNG. Chemical Protective Metal-Organic Framework Thin Films on Fiber Systems Driven by Atomic Layer Deposition. (Under the direction of Dr. Gregory N. Parsons).

Various toxic chemical warfare agents (CWAs) are still being regarded as an increasing menace not only to military populations but also to civilians since World War I in 1917. Despite global efforts to ban the use of CWAs through the Chemical Weapons Convention (CWC) effective as of April 29, 1997, terrorist groups and some unscrupulous countries are still deemed to secure considerable stockpiles of such hazardous chemical weapons, such as sarin, soman, VX, chlorine, and sulfur mustard.

As shown in Chapter 1, this research is motivated by the international-level issue, and therefore is focused on novel porous materials called as metal-organic frameworks (MOFs) which possess high structural tunability and exceptional porosity. MOFs as unprecedented porous solids are constructed from inorganic metal clusters bridged by organic linkers, thus leading to highly tunable pore sizes and reactive sites for selective adsorption and/or catalytic detoxification of CWAs and their simulants.

This doctorate dissertation mainly describes four different synthetic approaches to integrating various MOF crystals or thin films into polymeric fibrous platforms for their practical deployment and use in realistic contaminated environments. Metal oxide thin films (e.g., Al_2O_3 , TiO_2 , or ZnO) deposited on polymeric fibrous scaffolds via atomic layer deposition (ALD) technique commonly play a critical role in each integration strategy, but in a different manner.

The first integration method introduced in Chapter 2 and Chapter 4 is conventional "direct solvothermal growth" of UiO-66-NH_2 MOF onto ALD surface with different compositions (i.e., Al_2O_3 , ZnO , or TiO_2) conformally coated on various polymeric fibers is implemented, and new

insight into how the different inorganic nucleation films and the type of polymer can affect the quality, overall surface area, and the fractional yield of UiO-66-NH₂ on the fiber substrates is depicted. Based on the results obtained and compared with other ALD layers, TiO₂ surface results in the most effective MOF crystal distribution on fibers, MOF/fiber adhesion, and catalytic activity for a CWA simulant, DMNP with half-life of 15 min.

In Chapter 3 "MOF-assembly" on non-woven textiles is described. In this study, we develop a novel route to physically and chemically assemble as-synthesized UiO-66-NH₂ crystals onto ALD metal oxide surface (i.e., Al₂O₃, TiO₂, or ZnO) using β -cyclodextrin (β -CD) and cetyltrimethylammonium bromide (CTAB) as surfactant assembly agents at room temperature. We find that ZnO surface drives the highest MOF mass loading (40 wt%), and the most rapid catalytic hydrolysis of dimethyl 4-nitrophenyl phosphate (DMNP), a CWA simulant, with half-life of less than 5 min in the presence of the MOF/fiber catalyst.

Chapter 5 demonstrates "direct replication method", where ALD Al₂O₃ film on fiber surface directly reacts with porphyrin linkers (H₂TCPP) in solvothermal condition and subsequently converts into Al-PMOF at relatively low temperature. It is substantiated that a proper ratio of cosolvent system (DMF and water) is significantly important to balance the Al₂O₃ dissolution rate and the Al-PMOF crystallization rate near the surface of fibers to render Al-PMOF/fiber textile composites. On a per unit mass of MOF basis, the surface-immobilized Al-PMOF thin films considerably improve CEES detoxification turn-over-frequency ($\text{mol}_{\text{CEES}} \cdot \text{mol}_{\text{chromophore}}^{-1} \cdot \text{min}^{-1}$) by a factor of 19 compared to their bulk powder counterparts prepared via a conventional solvothermal method.

The last method presented in Chapter 6 is the fabrication of water-stable 2D Cu-TCPP MOFs densely coated and radially oriented on polymeric fibrous scaffolds by exploiting a facile

"hydroxy double salt (HDS) replication" method. Herein, the mechanism of the successful 2D MOF formation on the curved surface of the fiber substrates, which is not readily facilitated by the conventional "direct solvothermal growth" approach, is elucidated. Furthermore, the intensified adsorptive capacity out of the MOF/fiber systems for NH_3 and 2-chloroethyl ethyl sulfide (CEES), a blistering agent simulant, is elaborated with systematic supporting results.

© Copyright 2019 by Dennis Tae-Sung Lee

All Rights Reserved

Chemical Protective Metal-Organic Framework Thin Films on Fiber Systems Driven by Atomic
Layer Deposition

by
Dennis Tae-Sung Lee

A dissertation submitted to the Graduate Faculty of
North Carolina State University
in partial fulfillment of the
requirements for the degree of
Doctor of Philosophy

Chemical Engineering

Raleigh, North Carolina

2019

APPROVED BY:

Dr. Gregory N. Parsons
Chair of Advisory Committee

Dr. Saad A. Khan

Dr. Orlin D. Velev

Dr. Joseph B. Tracy

DEDICATION

To my parents, Gyejin Lee and Youngok Song, and my younger sister Soojung Lee
for all their unfailing support and love

BIOGRAPHY

Dennis Tae-Sung Lee was born in Boulder, Colorado in 1987, and grew up in Seoul, South Korea. He received a Bachelor of Science degree with *summa cum laude* in Chemical and Biomolecular Engineering from Gachon University in Gyeonggi-do, South Korea in 2011. Then, Dennis went on to pursue graduate-level research and received a Master of Science degree in Chemical and Biomolecular Engineering from Korea Advanced Institute of Science and Technology (KAIST) in Daejeon, South Korea in 2013. In 2014, Dennis was enrolled in a doctorate program in the Department of Chemical and Biomolecular Engineering at North Carolina State University (NCSU), where he joined Dr. Gregory N. Parsons' research group in January 2015. Since then, Dennis has focused on several research projects relevant to functionalizing polymeric textiles with metal-organic frameworks (MOFs) by harnessing various synthetic techniques including atomic layer deposition (ALD) and other chemistry-related strategies to realize chemical protective textiles against toxic industrial chemicals, chemical warfare agents and their simulants. In June 2019, Dennis will be driving to Baltimore, Maryland to continue his research career as a postdoctoral fellow at Johns Hopkins University.

ACKNOWLEDGMENTS

I would like first to express my gratitude and appreciation to my research advisor, Prof. Gregory N. Parsons for his sincere support and insightful advice on my career development all throughout my PhD period. I am very grateful to my committee members, Prof. Saad A. Khan, Prof. Orlin D. Velev, and Prof. Joseph B. Tracy for their constructive discussion and inspiring comments on my research. I also thank the members of staff in the Department of Chemical and Biomolecular Engineering, especially, Alison Stieglitz, Sandra Bailey, Joan O'Sullivan, Mike Mantini, and Michelle Bunce for their prompt help on demand.

I also would like to thank former colleagues in the Parsons research group, including especially Dr. Phil Williams, Dr. Moataz Mousa, Dr. Berc Kalanyan, Dr. Alex, Bronzena, Dr. Junjie Zhao, Dr. Paul Lemaire, Dr. Eric Stevens, and Dr. Michael Fusco for their cordial help on adjusting myself to the research group. In addition, I have been also very fortunate to have considerate and brilliant members currently in the Parsons group, including Dr. Chris Oldham, Wenyi Xie, Heather Barton, Seung Keun Song, Siyao Wang, Amanda Volk, Holger Saare, Zijian Dai, Rachel Nye, Jungsik Kim, and Sarah Smith. I am also very pleased to have an opportunity to closely interact and work with smart undergraduate researchers, Grant Hill and Jovenal Jamir.

As for various collaborative work and discussion outside NC State, I greatly appreciate Gregory Peterson (Edgewood Chemical Biological Center), Dr. Natalie Pomerantz (US Army Natick Soldier Center), and Dr. Howard Walls (Research Triangle Institute) for their helpful and practical comments on my research in monthly teleconference meetings and thank Derek Dwyer (Binghamton University) and Prof. Wayne Jones (University of New Hampshire) for our past project well completed.

I would be remiss without signifying my appreciation to the Staff at Analytical Instrumentation Facility (AIF) at NC State, my friends, and family. I am also grateful to Hanna Lee for her emotional support especially while I had been desperately searching out my next position. Without all the aforementioned support, none of my PhD work would have been possible.

TABLE OF CONTENTS

LIST OF TABLES	x
LIST OF FIGURES	xi
Chapter 1: Introduction and Background	1
1.1. Introduction to Metal-Organic Frameworks and Their Use	2
1.2. MOF Integration Methods on Planar Substrates.....	6
1.2.1. Conventional Solvothermal Growth	6
1.3. MOF Integration Methods on Polymeric Fibers (With No ALD Processes).....	8
1.3.1. Direct Solvothermal Growth.....	8
1.3.2. Microwave Irradiation-Assisted Solvothermal Growth.....	10
1.3.3. Direct Solvothermal Growth Using a Seeding Strategy	11
1.3.4. Growth on Surface Coated with Reactive Polymers.....	14
1.4. MOF Integration Methods on Polymeric Fibers (ALD-Driven).....	16
1.4.1. Atomic Layer Deposition (ALD) to Polymer Textiles	16
1.4.2. MOF Integration into ALD-treated Textiles.....	19
1.4.2.1. Direct Solvothermal Growth (MOF on ALD)	19
1.4.2.2. Direct Replication Method (ALD to MOF).....	22
1.4.2.3. Hydroxy Double Salt Replication Method (ALD to HDS to MOF).....	25
1.5. References.....	29
Chapter 2: UiO-66-NH₂ MOF Nucleation on TiO₂, ZnO, and Al₂O₃ ALD-treated Polymer Fibers: Role of Metal Oxide on MOF Growth and Catalytic Hydrolysis of Chemical Warfare Agent Simulants	35
2.1. Abstract	36

2.2. Introduction	37
2.3. Experimental Section	39
2.4. Results and Discussion	44
2.5. Conclusions	50
2.6. Figures	52
2.7. References	60
2.8. Supporting Information	66
Chapter 3: Catalytic "MOF-Cloth" Formed via Directed Supramolecular Assembly of UiO-66-NH₂ Crystals on Atomic Layer Deposition-coated Textiles for Rapid Degradation of Chemical Warfare Agent Simulants.....	76
3.1. Abstract	77
3.2. Introduction	78
3.3. Experimental Section	80
3.4. Results and Discussion.....	84
3.5. Conclusions	92
3.6. Figures	94
3.7. References	104
3.8. Supporting Information	112
Chapter 4: Toxic Organophosphate Hydrolysis Using Nanofiber-Templated UiO-66-NH₂ Metal–Organic Framework Polycrystalline Cylinders.....	122
4.1. Abstract	123
4.2. Introduction	124
4.3. Experimental Section	127

4.4. Results and Discussion	130
4.5. Conclusions	136
4.6. Figures	138
4.7. References	151
Chapter 5: Rapid Photocatalytic Detoxification of Mustard-Gas Simulant Using Porphyrin-based Al-PMOF/fiber Textiles Prepared by Atomic Layer Deposition and Cosolvent System Approach	157
5.1. Abstract	158
5.2. Introduction	159
5.3. Experimental Section	161
5.4. Results and Discussion	167
5.5. Conclusions	176
5.6. Figures	178
5.7. References	183
5.8. Supporting Information	187
Chapter 6: Water-Stable Chemical-Protective Textiles via Euhedral Surface-Oriented 2D Cu-TCPP Metal-Organic Frameworks.....	206
6.1. Abstract	207
6.2. Introduction	208
6.3. Experimental Section	209
6.4. Results and Discussion	216
6.5. Conclusions	220
6.6. Figures	222

6.7. References	227
6.8. Supporting Information	231

LIST OF TABLES

Table 2.1	Fiber-Based Material Properties, Calculated “Active” MOF Fraction, and Catalytic Performance toward a CWA Simulant, DMNP.....	5
Table S2.1	Material properties and catalytic performance of UiO-66-NH ₂ MOF powder towards a CWA simulant, DMNP.....	71
Table S2.2	Material properties used for calculating overall MOF yield and extracting MOF yield on fabric.....	75
Table 3.1	Material properties and catalytic performance of degrading a CWA simulant, DMNP	102
Table 4.1	Raman Modes of UiO-66-NH ₂ , PMMA, PVDF, PA-6, and PP along with IR Modes of UiO-66-NH ₂	144
Table 4.2	BET SA Results of Fibers Samples and MOF Powders along with Calculated Weight Percent Based on SA Analysis	148
Table 4.3	Apparent Rate Constant of Each MOF Powder Sample and the Mass Fraction of Active MOF for Each MOF/Fiber Sample.....	150
Table S6.1	Material properties of PP fiber substrates, MOF-coated textiles, and Cu-TCPP powder	247

LIST OF FIGURES

Figure 1.1 Schematic illustration of representative building blocks for metal-organic framework (MOF) construction	3
Figure 1.2 Chemical depiction of representative MOFs	4
Figure 1.3 Growth of the Cambridge Structural Database (CSD) and MOF entries since 1972	4
Figure 1.4 (a) MOF-5 chemical structure illustrated for a single cube fragment of their respective cubic three-dimensional extended structure. (b) The concept, (c) optical microscope, and (d) an AFM image of anchoring a selective MOF-5 building unit to a carboxylic acid-terminated SAM. The figure (b) represents a simplified model, not excluding alternative possibilities of the linkage.	6
Figure 1.5 Scanning electron microscopy images of MOF-5 thin films on different pretreated alumina substrates. No crystal growth can be observed on CF ₃ -terminated surfaces whereas densely packed MOF-5 thin films occur for ALD-Al ₂ O ₃ or COOH-terminated surfaces	7
Figure 1.6 SEM images of HKUST-1 (Cu ₃ (BTC) ₂) MOF coatings on (a) bare SiO ₂ , (b) Al ₂ O ₃ (sapphire) and (c) ALD Al ₂ O ₃ . (d) Single pyramidal crystal of HKUST-1 grown on c-plane sapphire. (e) Octahedral single crystals of HKUST-1 on COOH-functionalized Si/SiO ₂ . (f) Chemical depiction of HKUST-1 MOF structures	8
Figure 1.7 SEM images of (a) HKUST-1 (Cu ₃ (BTC) ₂) paper hand sheets and (b) HKUST-1 crystals on CMTP fibers	9
Figure 1.8 SEM images of (a) electrospun polyacrylonitrile (PAN) fiber mats, coated with MIL-47 material as a function of time: (b) 5 s and (c) 6 min. SEM image of (d) MIL-47-coated grooved PAN. Inset in (c) is chemical structure of MIL-47 MOF	10
Figure 1.9 (a) Schematic illustration of electrospun nanofibrous mats used as skeletons to produce free-standing MOF membranes. SEM image of (b) the ZIF-8 nanocrystal embedded electrospun nanofibrous mat (c) with magnified TEM image; SEM images of the fibrous mat after ZIF-8 growth period of (d) 1 cycle, (e) 4 cycles, (f) 5 cycles, and (g) the cross-section of the ZIF-8 membrane after 5-cycle growth. The insets in (b) and (f) are optical images of the corresponding samples	12
Figure 1.10 Schematic of in situ growth of UiO-66-NH ₂ on plain polyacrylonitrile fibers and polyacrylonitrile (PAN) fibers seeded with the aminoterephthalic acid (ATA linker). Electrospun swatches are sandwiched between two cellulose filter papers before being placed in a Parr bomb with the UiO-66-NH ₂ precursors: equimolar	

concentrations of ATA linker and zirconium chloride (metal), in acetone. Increasing concentrations of precursors are used for synthesis, 1, 2, and 3 mmol, to observe effects of concentration of precursors on UiO-66-NH₂ synthesized on the fiber: (a) control PAN swatch; (b) PAN with ATA linker. (c) Control PAN postsynthesis (d) PAN with ATA linker postsynthesis. Scale bar 3 μm..... 13

Figure 1.11(a) Schematic illustration of the strategy of effective deposition MOF on the "inert" polymer fibrous membranes by using polydopamine layer as nucleation center to fabricate hierarchically structured porous films. SEM images of (b) original PP fibrous membrane and (c) PDA-coated PP membrane; SEM images of PDA-modified PP membrane followed by the deposition of (d) HKUST-1, and (e) MOF-5..... 15

Figure 1.12(a) Schematic illustration of the homemade hot-wall viscous-flow ALD reactor used for ALD metal oxide coatings on polymeric fibers. Optical images of (b) inserting fabric samples into the deposition chamber and (c) representative fabric swatches used. All reactor lines of the setup were resistively heated to around 100 °C to avoid precursor condensation during the gas carrying process..... 17

Figure 1.13(a) ALD on a hydroxyl rich polymer surface leads to conformal deposition as shown in the example of Al₂O₃ ALD growth on cotton (top TEM image). (b) ALD on a polymer surface that lacks reactive functional groups can result in subsurface diffusion and growth within the fiber core, resulting in a less uniform coating at some temperatures. ALD growth on polypropylene (PP) at high temperatures (90 °C) results in this kind of subsurface deposition (lower TEM image)..... 18

Figure 1.14(a-c) Schematic illustration of the synthesis route. (a) Polymer fiber substrate. (b) Al₂O₃-coated polymer fiber via atomic layer deposition (ALD). The cross section in the dashed square illustrates the conformal coating of ALD Al₂O₃ with hydroxyl surface termination. (c) MOFs integrated on Al₂O₃-coated polymer fiber using solvothermal MOF synthesis. (d) SEM image of HKUST-1 MOF crystals grown on an ALD-Al₂O₃-coated polypropylene fiber (MOF-PP/ALD)..... 20

Figure 1.15(a) Synthetic procedure for Zr-based MOF–nanofiber kebab structures on polyamide-6 nanofibers (PA-6). The MOF crystal structures are illustrated in the dashed box. (b) SEM and (c) TEM images of PA-6@TiO₂@UiO-66. (d) SEM image of UiO-66-NH₂ grown on untreated PA-6 nanofibers (PA-6@UiO-66-NH₂)..... 21

Figure 1.16(a) Schematic illustration of the synthesis of ZIF-8 films from ZnO precursor films deposited on solid substrates. TEM images of (b) a FIB-prepared cross-sectional specimen, (c) an enlargement of ZIF-8 film (~95 ± 10 nm) grown from ALD-ZnO with the observed layers indicated, and (d) magnification image of (c). Thick Pt layers are deposited on the top of the material prior to milling for protection..... 23

Figure 1.17	SEM images of PAN nanofibers coated by ALD with thin layers of (a) ZnO and (b) Al ₂ O ₃ . SEM images of (c) PAN/ZnO/ZIF-8 and (d) PAN/Al ₂ O ₃ /MIL-53-NH ₂ composite materials obtained under MW-assisted heating (1.5 h); (diffraction peaks of Al-foil are marked with (*)) and diffraction patterns of ZIF-8 and MIL-53-NH ₂ reference powders are reported for comparison)	24
Figure 1.18	(a) Schematic drawing of the rapid room-temperature synthesis of HKUST-1. ZnO reacts with Cu(NO ₃) ₂ to form (Zn,Cu) HDS, which converts to HKUST-1 via fast anion exchange. (b) Schematic of the rapid room-temperature synthesis of MOF coatings on various form factors. (c-e) SEM images of HKUST-1 deposited onto PS spheres, Si wafer, and PAN nanofibers, respectively.....	26
Figure 1.19	(a) Optical image of ZnO-loaded fiber sorbent bundles (left) and the postsynthesis MOF-loaded fiber sorbent bundles (right) in the Swagelok stainless tube. (b) (Top) Synthesis of MOF materials within ZnO-loaded fiber sorbent materials. (Bottom) SEM images of the green ZnO-loaded fiber sorbents (left) and the postsynthesis MOF-loaded fiber sorbent (right). (c) Image of the sealed Swagelok® module used to house, transport, and test the fibers. The gas-tight connections maintain an inert atmosphere and protect the fibers from humid degradation. All connections are ¼” 316 SS fittings	28
Figure 2.1	SEM images of (a) a bare polypropylene (PP) and ALD-treated PP: (b) PP@Al ₂ O ₃ , (c) PP@ZnO, and (d) PP@TiO ₂ . Cross-sectional TEM images of (e) PP@Al ₂ O ₃ , (f) PP@ZnO, and (g) PP@TiO ₂ microfibers	52
Figure 2.2	Synthetic procedure for integrating UiO-66-NH ₂ MOF onto ALD-treated polymeric fibrous scaffolds	53
Figure 2.3	SEM images of UiO-66-NH ₂ crystals solvothermally grown on (a, e) PP, (b, f) PP@ZnO, (c, g) PP@Al ₂ O ₃ , and (d, h) PP@TiO ₂ microfibers. Insets in (a-d) are optical photographs of corresponding actual samples.....	54
Figure 2.4	XRD patterns of untreated PP, PP@ALD, UiO-66-NH ₂ MOF coated PP or PP@ALD, and UiO-66-NH ₂ MOF powder.....	55
Figure 2.5	(a) FTIR spectra captured in differential mode, (b) XRD patterns of UiO-66-NH ₂ grown on ALD-coated silicon wafer pieces (Si@SiO ₂), and (c) optical photographs of samples after the solvothermal reaction for MOF integration. The dark coating corresponds to visible UiO-66-NH ₂ MOF film growth.....	57
Figure 2.6	(a) Catalytic destruction of DMNP using MOF powder or PP@ALD@MOF microfibers. (b) UV-vis trace of the hydrolysis of DMNP as a function of reaction time using PP@ZnO@UiO-66-NH ₂ as a catalyst. (c) Conversion profiles of DMNP to <i>p</i> -nitrophenoxide versus reaction time using PP, PP@ALD@MOF, or UiO-66-NH ₂ MOF powder.....	58

Figure 2.7 Equations for the hydrolysis of DMNP catalyzed by MOF into the nontoxic products	59
Figure S2.1 (a) N ₂ isotherms and (b) overall BET surface area for UiO-66-NH ₂ MOF, PP@ZnO@MOF, PP@TiO ₂ @MOF, and PP@Al ₂ O ₃ @MOF	66
Figure S2.2 SEM images of a stability test for ALD ZnO layer on PP immersed in various solutions at 85 °C for 24 h. (a and e) a control PP@ZnO, (b and f) PP@ZnO in DMF + DI water, (c and g) PP@ZnO in 2-ATA + DMF + DI water, and (d and h) PP@ZnO in ZrCl ₄ + DMF + DI water	66
Figure S2.3 (a) Mass changes and (b) XRD patterns of PP@ZnO microfibers after being immersed in the various solutions at 85 °C for 24 h	67
Figure S2.4 SEM and EDS mapping images of PP@ZnO microfibers after being immersed in the various solutions at 85 °C for 24 h. (a) PP@ZnO in DMF + DI water, (b) PP@ZnO in 2-ATA + DMF + DI water, and (c) PP@ZnO in ZrCl ₄ + DMF + DI water	67
Figure S2.5 Kinetic analysis of (a) untreated PP, (b) PP@Al ₂ O ₃ @MOF, (c) PP@TiO ₂ @MOF, (d) PP@ZnO@MOF, and (e) UiO-66-NH ₂ MOF powder.....	68
Figure S2.6 (a) Conversion profiles and (b) kinetic analysis of untreated PP, PP@Al ₂ O ₃ , PP@TiO ₂ , and PP@ZnO.....	69
Figure S2.7 (a) Conversion profiles and (b) kinetic analysis of DMNP to <i>p</i> -nitrophenoxide versus reaction time using UiO-66-NH ₂ MOF powders with different amounts as catalysts	69
Figure S2.8 Calculated reaction rate constant, k_{app} , versus the amount of MOF powder catalyst added for destructing DMNP to <i>p</i> -nitrophenoxide.....	70
Figure S2.9 (a) Actual UiO-66-NH ₂ MOF/fabric composites and MOF powder synthesized in 20 mL scintillation vial (ZrCl ₄ (0.080 g, 0.343 mmol) + 2-ATA (0.062 g, 0.343 mmol) + DMF (20 mL) + DI water (25 μL) mixture). (b) Histogram of the fractional yield of MOF crystals on the different fiber surfaces and MOF powder collected from the liquid phase relative to the starting solution molar precursor concentration	74
Figure 3.1 (a) The N ₂ adsorption (□) and desorption (○) isotherm for the UiO-66-NH ₂ powder prepared through solvothermal synthesis at 85 °C for 24 h. Inset indicates SEM image of UiO-66-NH ₂ crystals used for the assembly method. BET surface area of the powder is 956 ± 81 m ² /g with total pore volume of 16 mmol/g calculated at a relative pressure (P/P _o) of 0.95. (b) PXRD data for the UiO-66-NH ₂ powder used.....	94

- Figure 3.2** SEM images of samples: (a) PP + Assembly, (b) PP/Al₂O₃ + Assembly, (c) PP/TiO₂ + Assembly, (d) PP/ZnO + Assembly, and magnified images in dotted circular area of individual images: (e), (f), (g), and (h), respectively. Assembly solution contains as-synthesized UiO-66-NH₂ crystals + β -CD + CTAB 95
- Figure 3.3** The proposed mechanism of interactions (a) between MOF crystals and ALD ZnO surfaces and (b) MOF crystals themselves by means of β -CD + CTAB structures 96
- Figure 3.4** (a) XRD spectra of (from bottom to top) UiO-66-NH₂ powder, polypropylene as a substrate, and samples: PP/Al₂O₃ + Assembly, PP/TiO₂ + Assembly, and PP/ZnO + Assembly. (b) Photographs of a virgin PP swatch (bottom) and actual PP/ZnO swatch after “Assembly method” (top). Assembly solution contains as-synthesized UiO-66-NH₂ crystals + β -CD + CTAB 97
- Figure 3.5** (a) Mass fraction of MOFs on ALD-treated PP + Assembly (left y-axis and blank columns) and overall BET surface area for ALD-treated PP + Assembly (right y-axis and filled columns). (b) Overall BET surface area for PP, PP/ZnO, PP + Assembly, and PP/ZnO + Assembly. Overall BET surface area means BET surface area of (MOF + Fiber). Assembly solution contains UiO-66-NH₂ + β -CD + CTAB 98
- Figure 3.6** (a) A schematic of the adhesion test during which samples are immersed in ethanol with vigorous stirring at 500 rpm for 24 h and (b) a table revealing comparison of mass change of each sample after the adhesion test. m is mass after completion of adhesion test, and m_0 is initial mass before the adhesion test. [\perp] For comparison with the conventional solvothermal approach in the attachment of MOF crystals, rather than using “Assembly method”, UiO-66-NH₂ is nucleated and grown on PP/ZnO at 85 °C for 24 h 99
- Figure 3.7** (a) Schematic of expected interactions between MOFs and supramolecular complex (β -CD + CTAB). (b-c) FTIR spectra of CTAB, β -CD, supramolecular complex (β -CD + CTAB) on Si/SiO₂, UiO-66-NH₂ assembly on ALD-treated (Al₂O₃, TiO₂, or ZnO) Si/SiO₂, and UiO-66-NH₂ grown via solvothermal synthesis (85 °C for 24 h) on Si/SiO₂/TiO₂. Note that Si/SiO₂ is used as a background for all FTIR patterns 100
- Figure 3.8** (a) Catalytic hydrolysis reaction for DMNP (top) and UV-Vis trace of the hydrolysis of DMNP as a function of time (0 - 120 min) using PP/ZnO + Assembly fiber mats (bottom). (b) Conversion profiles for the hydrolysis of DMNP in the presence of PP, PP/ZnO, PP/ZnO + Assembly, and UiO-66-NH₂ powder at room temperature as a function of time. Inset shows transparent color of solution before hydrolysis reaction starts remarkably changed into yellowish one after the reaction completes. *UiO-66-NH₂ powder used is collected from remnants of assembly solution. The slight drop in the data at ~30 minutes is within the statistical uncertainty of the results 101

- Scheme 3.1** Comparison of “Assembly method” at ambient temperature between untreated polypropylene (PP) and ALD-treated PP 103
- Figure S3.1** SEM images of fiber substrates: (a) Polypropylene (PP) and (b) PP coated with ZnO (PP/ZnO). SEM images of (c) PP/ZnO after assembly (UiO-66-NH₂ + β -CD + CTAB) in DMF and (d) that after being immersed in only UiO-66-NH₂ crystals without β -CD and CTAB in DMF. The amount of UiO-66-NH₂ (0.24 g) in 80 mL of DMF used in (c) and (d) is same as each other 112
- Figure S3.2** (a) Mass fraction comparison of UiO-66-NH₂ MOF crystals assembled on PP/ZnO substrates by β -CD, CTAB, and β -CD + CTAB, respectively. (b) A photograph of actual fiber mats used for the assembly with different component 113
- Figure S3.3** SEM images of assembled feature of UiO-66-NH₂ MOF crystals on PP/ZnO by means of β -CD (a and d), CTAB (b and e), and β -CD + CTAB (c and f) 114
- Figure S3.4** (a) XRD spectra of (from bottom to top) UiO-66-NH₂ powder, polypropylene (PP) as a substrate, and PP + Assembly fabric sample. (b) Actual fabric samples before (left) and after (right) “Assembly method” to untreated PP. Assembly solution contains as-synthesized UiO-66-NH₂ crystals + β -CD + CTAB..... 115
- Figure S3.5** Photographs of fiber mats with assembled MOFs after adhesion test was performed. (a) Assembly with β -CD, (b) with CTAB, and (c) with β -CD + CTAB. Each fiber mat was swept 30 times using the brush in the image. All the assembly method was carried out on PP/ZnO..... 116
- Figure S3.6** (a) Conversion profiles of DMNP to 4-nitrophenoxide versus the hydrolysis reaction time and (b) kinetic analysis using untreated PP and PP/ZnO fibrous scaffolds..... 117
- Figure S3.7** Fabric size effect on DMNP hydrolysis reaction catalyzed in the presence of PP/ZnO + Assembly. (a) Conversion profiles for the hydrolysis of DMNP with one piece ($m_{\text{(MOF+Fabric)}} = 13.7$ mg) or smaller pieces ($m_{\text{(MOF+Fabric)}} = 13.6$ mg) of PP/ZnO + Assembly at room temperature as a function of time. (b) Actual samples used before and after the catalytic reaction 118
- Figure S3.8** (a) Conversion profiles for the hydrolysis of DMNP in the presence of UiO-66-NH₂ powder with varying loading: 5.6 mg (\square), 2.6 mg (\circ), and 1.5 mg (Δ). Kinetics plot of the reaction of DMNP in *N*-ethylmorpholine buffer solution with UiO-66-NH₂ powder at different catalyst loading: (b) 5.6 mg, (c) 2.6 mg, and (d) 1.5 mg to identify a reaction rate constant (*k*) and initial half-life ($t_{1/2}$) of each case. *UiO-66-NH₂ powder used is collected from remnants of assembly solution. 119
- Figure S3.9** (a) Conversion profiles for the hydrolysis of DMNP in the presence of PP/ZnO + Assembly with different mass loading of the MOF-assembled fiber mats*: 10.0

mg (□) and 17.6 mg (○). (b) Kinetics plot of the reaction of DMNP in *N*-ethylmorpholine buffer solution with the MOF-assembled fiber mats at different catalyst loading: b) 10 mg and c) 17.6 mg to identify a reaction rate constant (*k*) and initial half-life (*t*_{1/2}) of each case. *MOF-assembled fiber mats used are PP/ZnO + Assembly..... 120

Figure S3.10 (a) PXRD data for UiO-66-NH₂ postcatalysis (top), precatalysis* (mid), and a simulated pattern (bottom). (b) SEM image of UiO-66-NH₂ postcatalysis, which is collected after being used for the catalysis of DMNP. There is no substantial change in peak intensity or position for UiO-66-NH₂ before and after functioning as a catalyst to decompose DMNP. Intensity of the peaks has been normalized at 7.3° in 2-theta corresponding to (111) of UiO-66-NH₂. *UiO-66-NH₂ precatalysis is collected from remnants of assembly solution 121

Figure 4.1 Reaction of decontamination of DMNP using MOF/fiber or MOF powder catalyst 138

Figure 4.2 SEM images of untreated fibers, fibers after ALD treatment of TiO₂, and MOF/fiber samples after ALD and solvothermal synthesis of MOF 139

Figure 4.3 SEM images of PMMA/Ti(OH)₄@TiO₂ (A) and PMMA/ Ti(OH)₄@TiO₂@MOF (B)..... 140

Figure 4.4 SEM images of PMMA/Ti(OH)₄ fibers (A-C) and PMMA/Ti(OH)₄@TiO₂ fibers (D-F) after solvothermal treatment without organic linker (i.e., 2-ATA) at 85 °C for 24 h 141

Figure 4.5 Schematic illustration of MOF integration procedures on PVDF/Ti(OH)₄ (A) and PMMA/Ti(OH)₄ (B) composite fibers 142

Figure 4.6 TEM images of hollowed PMMA/Ti(OH)₄@TiO₂@MOF (A,B), PVDF/Ti(OH)₄@TiO₂@MOF (C,D), PA-6@TiO₂@MOF (E,F), and PP@TiO₂@MOF (G,H) 143

Figure 4.7 Raman spectra of PMMA/Ti(OH)₄@TiO₂@MOF (A) and PVDF/Ti(OH)₄@TiO₂@MOF (C) along with ATR-FTIR spectra of PMMA/Ti(OH)₄@TiO₂@MOF (B) and PVDF/Ti(OH)₄@TiO₂@MOF (D) 145

Figure 4.8 Raman spectra of PP@TiO₂@MOF (A) and PA-6@TiO₂@MOF (B)..... 146

Figure 4.9 N₂ isotherms of PP@TiO₂@MOF (A), PA-6@TiO₂@MOF (B), PVDF/Ti(OH)₄@TiO₂@MOF (C), and PMMA/Ti(OH)₄@TiO₂@MOF (D) with corresponding MOF powder 147

Figure 4.10 DMNP results for fibers samples (12 mg) (A) and corresponding MOF powders (3 mg) (B) with table of kinetic data 149

- Figure 5.1** (a) Schematic illustration of a synthetic procedure of MOF/fiber textiles using ALD Al₂O₃-treated PP fibers, followed by reacting with H₂TCPP organic linkers. (b) Crystal structure of Al₂(OH)₂TCPP MOF (i.e., Al-PMOF), consisting of octahedral Al(OH) clusters interconnected to H₂TCPP organic linkers. (c) XRD patterns, (d) N₂ sorption isotherms at 77 K, and (e) water vapor isotherms at 298 K of Al-PMOF powders prepared with AlCl₃·6H₂O and H₂TCPP under varied synthetic conditions 178
- Figure 5.2** SEM images of (a) Al-PMOF powder, (b) Si/SiO₂@Al-PMOF, and (c) PP@Al-PMOF obtained with different ratios of solvents (DMF:Water) at 120 °C for 20 h. MOF powder was synthesized by AlCl₃·6H₂O and H₂TCPP, and MOF on solid substrates was driven by reaction of ALD Al₂O₃ on the substrates with H₂TCPP.. 179
- Figure 5.3** (a) XRD patterns and (b) N₂ sorption isotherms at 77 K of PP@Al-PMOF, and (c) FTIR spectra of Si/SiO₂@Al-PMOF (Si/SiO₂@Al₂O₃ as a background for each sample). The samples are synthesized using ALD Al₂O₃-coated substrates with H₂TCPP linkers dissolved in varied ratios of solvent mixtures (DMF:Water) at 120 °C for 20 h. XPS data for (d) C 1s, (e) O 1s, and (f) Al 2p for Si/SiO₂@Al-PMOF made from ALD Al₂O₃-coated substrates and H₂TCPP linkers dissolved in a solvent mixture (DMF:Water=1:3)..... 180
- Figure 5.4** (a, b) Schematic illustration of Al-PMOF film formation mechanism in cross-sectional view and (c, d) HAADF-STEM images for a cross section of the Al-PMOF formed on ALD Al₂O₃-coated Si wafer (Si/SiO₂@Al-PMOF). The green box in (c) indicates the location of (d–h). (e–h) High-resolution EDX mapping images of the cross section. (i) A digital photograph of the actual sample measured, Si/SiO₂@Al-PMOF (DMF:Water=1:3). Arrows in (d) are indicative of voids in alumina film, which are generated during the film dissolution process by water 181
- Figure 5.5** Multifunctionality of Al-PMOF/fiber textiles. (a) Selective photo-oxidation of 2-chloroethyl ethyl sulfide (CEES) under blue LED irradiation and O₂ environment catalyzed by MOF-based catalysts. (b) Oxidation profiles of CEES to CEESO conversion over time using varied photo-catalysts. (c) Gas chromatography (GC) signals exhibiting the selective oxidation progress of CEES (5.2 min) to CEESO (7.8 min) in the presence of Al-PMOF powder. 1-bromo-3,5-difluorobenzene was used as an internal standard (IS) during the reaction. (d) A colorimetric MOF/fiber textile pH sensor. (e) Snapshots of selective removal of chloroform contaminants from water using MOF/fiber textiles (left to right). The rightmost picture in (d) shows a hydrophobic feature of the MOF/fiber textiles 182
- Figure S5.1** (a) UV-Vis absorption spectra and (b) XRD patterns of H₂TCPP linker and powder samples synthesized with AlCl₃·6H₂O and H₂TCPP in pure water at 120 °C for 20 h, in pure water at 180 °C for 20 h, and in cosolvent (DMF:Water=1:3) at 120 °C for 20 h, respectively (from bottom to top)..... 187

Figure S5.2 XRD patterns (left) of Al-PMOF simulated pattern, H₂TCPP linker, Al₂O₃ solid powder, and synthesized powders made with Al₂O₃ powder and H₂TCPP, and with AlCl₃·6H₂O and H₂TCPP in cosolvent (DMF:Water=1:3) at 120 °C for 20 h, respectively (from bottom to top). SEM images (right) of solid products after corresponding reactions. Well-defined Al-PMOF crystals (top), made with AlCl₃·6H₂O, were observed, whereas unreacted Al₂O₃ solids and nonporous assembled H₂TCPP salts were dominantly found when Al₂O₃ powder was used as a metal source..... 188

Figure S5.3 (a) N₂ sorption isotherms at 77 K, and (b) water vapor isotherms at 298 K of H₂TCPP linker, Al₂O₃ solid powder, and synthesized powders made with Al₂O₃ powder and H₂TCPP, and with AlCl₃·6H₂O and H₂TCPP in cosolvent (DMF:Water=1:3) at 120 °C for 20 h, respectively 189

Figure S5.4 (a) XRD patterns and (b) N₂ sorption isotherms at 77 K of powder samples synthesized with different ratios of solvents (DMF:Water) at 120 °C for 20 h. MOF powder was synthesized with AlCl₃·6H₂O and H₂TCPP precursors..... 190

Figure S5.5 (a) FTIR spectra of progressive Al-PMOF film formation on Si/SiO₂ substrate (Si/SiO₂@Al-PMOF) over time of reaction between Si/SiO₂ coated with ALD Al₂O₃ (Si/SiO₂@Al₂O₃) and H₂TCPP dissolved in cosolvent (DMF:Water=1:3) at 120 °C. Note that Si/SiO₂@Al₂O₃ was used as a background for all FTIR spectra. (b) Optical photographs of each sample collected at 3 h, 6 h, and 10 h of corresponding reaction 191

Figure S5.6 FTIR spectra captured in differential mode. For the spectra obtained here, the Si/SiO₂@TiO₂ and Si/SiO₂@Al₂O₃ were subtracted as a background for first two samples from the bottom (black and red) and for the sample on top (green), respectively. The reaction condition for the samples here were conducted with (DMF:Water=1:3) mixture at 120 °C for 20 h. The spectrum on Si/SiO₂@TiO₂+H₂TCPP (black) after a background subtraction shows that ALD TiO₂ was remained intact and no reaction occurred with H₂TCPP in the synthetic condition. AlCl₃·6H₂O and H₂TCPP can form Al-PMOF film on stable TiO₂ surface but poor film uniformity was obtained (Si/SiO₂@TiO₂+AlCl₃+H₂TCPP, red). The well-defined and densely coated Al-PMOF film was observed by the optimal synthetic route with Si/SiO₂@Al₂O₃ reacting with H₂TCPP (Si/SiO₂@Al₂O₃+H₂TCPP, green) in the synthetic condition. Optical photographs and SEM images of each sample are shown on the bottom and on the right side, respectively 192

Figure S5.7 (a) Difference FTIR spectra following sequential ALD Al₂O₃ (black), H₂O treatment (red), and reaction with H₂TCPP in pure DMF (blue) on Si/SiO₂ substrate. (b) Difference FTIR spectra following sequential ALD Al₂O₃ (black), H₂O treatment (red), and reaction with H₂TCPP in the optimized cosolvent (DMF:Water=1:3) (green). The IR spectra of Si/SiO₂@Al₂O₃ (black) was obtained by subtracting the spectrum of Si/SiO₂ as a background from the

spectrum collected after ALD Al₂O₃ to Si@SiO₂. H₂O treatment was conducted by submerging Si/SiO₂@Al₂O₃ in liquid water at 90 °C for 1 h. The reactions with H₂TCPP in pure DMF or in the optimized cosolvent was carried out at 120 °C for 20 h 194

Figure S5.8 FTIR spectra captured in differential mode. The spectra of each Si/SiO₂@Al₂O₃ was subtracted as a background for the entire sample after reacting with H₂TCPP solutions. The reactions for Si/SiO₂@Al₂O₃+H₂TCPP (10, 30, or 50 mg (from bottom)) and for Si/SiO₂@Al₂O₃+H₂O treatment+H₂TCPP (200 mg, topmost) were implemented with (DMF:Water=1:3) mixture and pure DMF at 120 °C for 20 h, respectively. H₂O treatment was conducted by submerging Si/SiO₂@Al₂O₃ in liquid water at 90 °C for 1 h..... 195

Figure S5.9 GC-MS spectra monitored at 10 min of CEES oxidation using Al-PMOF powder catalyst. Selective oxidation of CEES (t = 5.2 min) into 2-chloroethyl ethyl sulfoxide (CEESO, t = 7.8 min) was observed. 1-bromo-3,5-difluorobenzene was used as an internal standard (IS, t = 4.5 min) 196

Figure S5.10 Mass spectrometry of (a) 1-bromo-3,5-difluorobenzene as an internal standard (IS), (b) CEES as a blistering agent simulant, and (c) CEESO as the only product obtained from the photooxidation of CEES with Al-PMOF powder catalyst..... 197

Figure S5.11 GC-MS spectra monitored during CEES photooxidation with (a) H₂TCPP (0.8 mol%), (b) with PP@Al-PMOF (0.2 mol%), or (c) with PP@Al₂O₃ (0 mol%). The catalyst loading (mol%) is calculated based on moles of porphyrins in Al-PMOF. No CEESO was observed in the catalytic reaction with PP@Al₂O₃ due to the absence of porphyrin-contained components functioning as catalysts..... 200

Figure S5.12 Kinetic analysis of oxidative detoxification profiles of CEES using (a) Al-PMOF powder (0.7 mol%), (b) H₂TCPP powder (0.8 mol%), (c) PP@Al-PMOF (0.2 mol%), or (d) PP@Al₂O₃ (0 mol%). The profiles were fit to a first-order kinetic model. The catalyst loading (mol%) is calculated based on moles of porphyrins in Al-PMOF 201

Figure S5.13 Effect of LED light irradiation on the rate of CEES oxidation using textile catalysts. (a) CEES degradation profile, (c) GC-MS spectra, and (e) kinetic analysis obtained in the dark. (b) CEES degradation profile, (d) GC-MS spectra, and (f) kinetic analysis monitored with light irradiation (0 - 10 min) and subsequently in the dark (10 - 50 min)..... 202

Figure S5.14 SEM images of (a) PP@Al-PMOF and (b) PP@Al₂O₃. Fluorescence imaging of (c) PP@Al-PMOF and (d) PP@Al₂O₃. The fluorescence imaging results indicate that Al-PMOF integrated into PP fiber surface is uniform and functions well in visible light 204

Figure 6.1 Schematic illustration of metal-TCPP MOF growth on PP fibers via different synthetic routes. (a) ALD ZnO-treated PP (PP@ZnO), (b) 1 (PP@Zn-TCPP), (c) 2 (PP@Cu-TCPP), (d) 3 (PP@HDS), and (e) 4 (PP@Cu-TCPP) composites. Components of Cu-TCPP are illustrated in the dashed box	222
Figure 6.2 SEM images of (a) 1 , (b) 2 , (c) 3 , and (d) 4 composites. The insets in the SEM images are corresponding schematic illustrations and digital photographs of the actual samples.....	223
Figure 6.3 (a) XRD patterns for untreated PP, PP@ZnO, 3 , 2 , 4 , and Cu-TCPP powder. (b) FTIR spectra for untreated PP, 3 , 4 , and Cu-TCPP powder. (c) N ₂ isotherms at 77 K and (d) overall BET surface area (m ² /g _(MOF+fiber)) for PP@ZnO, 3 , 2 , 4 , and Cu-TCPP powder	224
Figure 6.4 Water stability tests of PP@MOF textiles. SEM images for PP@Cu-BTC (a) before and (b) after submerged in water at 25 °C for 17 h (water treatment), and for 4 (c) before and (d) after the water treatment. The insets in Figure 4a-d are corresponding schematic illustrations and digital photographs of the actual samples. (e) N ₂ isotherms at 77 K and (f) water vapor isotherms at 298 K before water treatment for PP@ZnO, PP@Cu-BTC, and 4 on a per gram of MOF basis.....	225
Figure 6.5 Dynamic loading (mol _(adsorbate) /kg _(MOF)) calculated from microbreakthrough tests. NH ₃ dynamic loading for 4 and Cu-TCPP powder under (a) dry condition and (b) wet condition. CEES dynamic loading for 4 and Cu-TCPP powder under (c) dry condition and (d) wet condition. The insets are chemical structures of NH ₃ and CEES	226
Figure S6.1 SEM images of (a) untreated polypropylene (PP) fibrous mats, (b) ALD ZnO-treated PP (PP@ZnO), (c) HDS(Zn,Cu) coated PP (PP@HDS), and (d) PP@Cu-TCPP composites made by reacting PP@HDS(Zn,Cu) and H ₂ TCPP linker solution (4: PP@Cu-TCPP) at 40°C for 12 h. The insets in the SEM images are digital photographs of corresponding actual samples	231
Figure S6.2 SEM images of vertically grown Cu-TCPP MOFs on PP micro-fibers (a) in a top-view and (b) a cross-sectional view. (c) MOF thickness distribution measured based on the SEM images	232
Figure S6.3 Measured XRD patterns of powder samples including ZnO, HDS(Zn,Cu), H ₂ TCPP, and Cu-TCPP, and PP@film composite materials including PP@ZnO, PP@HDS(Zn,Cu), and 4 : PP@Cu-TCPP	233
Figure S6.4 SEM images of Cu-TCPP MOFs grown on PP micro-fibers (a-b) (PP@HDS(Zn,Cu)+TCPP) in a vertical and (c-d) (PP@ZnO+Cu(NO ₃) ₂ +TCPP) in a horizontal manner. (e) XRD patterns for both PP@HDS(Zn,Cu)+TCPP and PP@ZnO+Cu(NO ₃) ₂ +TCPP composite materials. Synthetic condition for both	

samples was performed at 40°C for 12 h. PP@ZnO+Cu(NO₃)₂+TCPP is equal to **3**: PP@Cu-TCPP. PP@HDS(Zn,Cu)+TCPP is equal to **4**: PP@Cu-TCPP 234

Figure S6.5 (a) SEM images and (b) XRD pattern of Cu-TCPP MOFs drop-cast on a flat glass substrate obtained by a grazing-incidence XRD (GIXRD) technique (the inset shows the actual sample measured). (c) XPS data collected on Cu-TCPP MOFs drop-cast on a piece of silicon wafer. Cu-TCPP MOF powder used was prepared by a conventional solvothermal method conducted at 80°C for 24 h 235

Figure S6.6 (a) A graph of MOF mass fraction (%) ($= \frac{m_{MOF+Fiber} - m_{Fiber}}{m_{MOF+Fiber}} \times 100$ (%)) and overall BET surface area (m²/g_(MOF+fiber)) as a function of a varied reaction time (min), (b) N₂ isotherms for PP@ZnO, PP@HDS(Zn,Cu), PP@HDS(Zn,Cu) reacted with TCPP solution at 40°C for varied reaction time, and (c) schematic illustration of Cu-TCPP MOF growth mechanism onto PP@HDS(Zn,Cu). PP@HDS(Zn,Cu)+TCPP is equal to **4**: PP@Cu-TCPP 236

Figure S6.7 (a-d) SEM images and (e) XRD patterns captured at varied reaction time (i.e., 2h 20 min, 3h 30 min, 6h 30 min, and 12 h) for PP@HDS(Zn,Cu)+TCPP at 40°C. PP@HDS(Zn,Cu)+TCPP is equal to **4**: PP@Cu-TCPP 237

Figure S6.8 SEM images of (a-b) PP@HDS(Zn,Cu)+TCPP at 40°C for 12 h and (c-d) PP@HDS(Zn,Cu)+TCPP at 60°C for 12 h. (e) N₂ isotherms at 77 K for the samples imaged. This proves that a relatively low temperature, 40°C, is enough to grow good quality of 2D Cu-TCPP MOF crystals for PP@HDS(Zn,Cu)+TCPP. PP@HDS(Zn,Cu)+TCPP is equal to **4**: PP@Cu-TCPP..... 238

Figure S6.9 (a) XRD patterns and (b) N₂ isotherms at 77 K for PP fibrous mats, PP@ZnO, PP@HDS(Zn,Cu), PP@HDS(Zn,Cu)+TCPP synthesized at 25°C for 24 h, and PP@HDS(Zn,Cu)+TCPP synthesized at 40°C. (c) Actual PP@HDS(Zn,Cu)+TCPP samples collected at varied reaction time (1 h, 6 h, 12 h, and 24 h) conducted at room temperature. (d-e) SEM images of PP@HDS(Zn,Cu)+TCPP prepared at 25°C for 24 h. This result indicates that PP@HDS(Zn,Cu) swatch can absorb more amounts of H₂TCPP organic linkers for a longer dipping time, but not enough to grow crystalline Cu-TCPP MOFs ... 239

Figure S6.10 (a) SEM and (b-e) EDS mapping images of PP@HDS(Zn,Cu)+TCPP prepared at 40°C for 12 h. (f) A digital photograph of the actual sample (size: 2”×2” composite swatch) and (g) its EDS spectra. PP@HDS(Zn,Cu)+TCPP is equal to **4**: PP@Cu-TCPP 240

Figure 6.11 Digital photographs of the actual polypropylene (PP) substrates with 40 grams per square meter (gsm) or 75 gsm (a) before, (b) when, and (c) after twisted by binder clips. PP(75) swatch shows much higher mechanical strength compared to PP(40) polymeric fibrous mats..... 241

- Figure 6.12** XRD patterns of (a) PP@Cu-BTC and (b) **4**: PP@Cu-TCPP before and after the water stability test (17 h, ambient temperature) together with reference substrates including PP, PP@ZnO, PP@HDS(Zn,Cu) 242
- Figure S6.13** FTIR spectra for untreated PP fibers and PP@Cu-BTC before and after the water treatment, and for untreated PP fibers and **4**: PP@Cu-TCPP before and after the water treatment. The water treatment was done by dipping samples in liquid water for 28 h. PP@Cu-BTC was prepared by reacting PP@HDS(Zn,Cu) with H₃BTC solution at room temperature for 2 min. **4**: PP@Cu-TCPP was synthesized by reacting PP@HDS(Zn,Cu) with H₂TCPP solution at 40°C for 12 h 243
- Figure S6.14** N₂ isotherms at 77 K for (a) PP@Cu-BTC and (b) **4**: PP@Cu-TCPP before and after a water stability test. (c) BET surface area (m²/g_(MOF+fiber)) for PP, PP@ZnO, and PP@Cu-BTC and **4**: PP@Cu-TCPP before and after the water stability test. The water stability test was performed by dipping samples in liquid water for 17 h. PP@Cu-BTC was prepared by reacting PP@HDS(Zn,Cu) with H₃BTC solution at room temperature for 2 min. **4**: PP@Cu-TCPP was synthesized by reacting PP@HDS(Zn,Cu) with H₂TCPP solution at 40°C for 12 h..... 244
- Figure S6.15** (a) Water vapor adsorption (open symbol) and desorption (closed symbol) isotherms at 298 K and (b) N₂ adsorption (open symbol) and desorption (closed symbol) isotherms at 77 K for Cu-BTC (red, square) and Cu-TCPP MOF powder (blue, triangle). SEM images of (c) Cu-BTC and (d) Cu-TCPP MOF powder 245
- Figure S6.16** Ammonia microbreakthrough tested under (a) dry condition (0% RH) and (b) wet condition (80% RH) and 2-CEES microbreakthrough tested under (c) dry condition (0% RH) and (d) wet condition (80% RH) for PP(40), **4**: PP(40)@Cu-TCPP, PP(75), **4**: PP(75)@Cu-TCPP, and Cu-TCPP powder. Weighted time (min/g) is defined as time divided by adsorbent mass employed in the test. C/C₀ is a normalized concentration, with the feed concentration to the composite (C₀), and the concentration exiting the composite at time *t* (C). **4**: PP(75)@Cu-TCPP was synthesized by reacting PP@HDS(Zn,Cu) with H₂TCPP solution at 40°C for 12 h. Cu-TCPP MOF powder used was prepared by a conventional solvothermal method conducted at 80°C for 24 h..... 246
- Figure S6.17** (a) N₂ isotherms at 77 K and (b) H₂O isotherms at 298 K for PP@ZnO, **4**: PP@Cu-TCPP, and Cu-TCPP MOF powder. (c) BET surface area based on N₂ isotherms (m²/g_{MOF+fiber}) and total pore volume (cm³/g_{MOF+fiber}) based on H₂O isotherms for the samples measured..... 248
- Figure S6.18** XRD patterns of Cu-TCPP powder before and after the microbreakthrough tests under dry (0% RH) and wet condition (80% RH) with ammonia or with 2-CEES. Cu-TCPP MOF powder used was prepared by a conventional solvothermal method conducted at 80°C for 24 h..... 250

- Figure S6.19** ATR-FTIR spectra for Cu-TCPP powder before and after the microbreakthrough tests under dry (0% RH) and wet condition (80% RH) with ammonia or with 2-CEES. Cu-TCPP MOF powder used was prepared by a conventional solvothermal method conducted at 80°C for 24 h 251
- Figure S6.20** SEM images of (a) PP@ZnO, (b) PP@HDS(Zn,Cu), (c) PP@HDS(Zn,Zn), and (d) PP@(HDS) and (e) their XRD patterns 251
- Figure S6.21** (a-b) SEM images for PP@Zn-TCPP composites synthesized via PP@HDS(Zn,Zn) + TCPP at 60°C for 12 h and XRD patterns (c) for PP, PP@ZnO, PP@HDS(Zn,Zn), and PP@Zn-TCPP. (d-e) SEM images for PP@Co-TCPP composites synthesized via PP@HDS(Zn,Co) + TCPP at 80°C for 20 h. XRD patterns for (e) PP, PP@ZnO, PP@HDS(Zn,Co), and PP@Co-TCPP. The insets in (a-b) and (d-e) are digital photographs of corresponding actual samples 252
- Figure S6.22** SEM images of Zn-TCPP MOFs grown on PP micro-fibers (a-b) (PP@HDS(Zn,Zn)+TCPP) in a vertical and (c-d) (PP@ZnO+TCPP) in a horizontal manner. (e) XRD patterns for PP@ZnO, PP@HDS(Zn,Zn), PP@HDS(Zn,Cu)+TCPP, and PP@ZnO+Cu(NO₃)₂+TCPP composite materials. Synthetic condition for both samples was performed at 40°C for 12 h 253
- Figure S6.23** (a) SEM, (b-d) EDS mapping images, and (e) EDS spectra of PP@HDS(Zn,Zn)+TCPP prepared at 40°C for 12 h 253
- Figure S6.24** SEM images of (a) PP@ZnO, (b) PP@HDS(Zn,Co), (c) PP@HDS(Zn,Co) reacted with TCPP solution at 80°C for 6 h (PP@HDS(Zn,Co)+TCPP (80°C, 6 h)), and (d) PP@HDS(Zn,Co) reacted with TCPP solution at 80 °C for 24 h (PP@HDS(Zn,Co)+TCPP (80°C, 24 h)) (e) their XRD patterns 254
- Figure S6.25** (a) SEM, (b-e) EDS mapping images, and (g) EDS spectra of PP@HDS(Zn,Co)+TCPP prepared at 80°C for 24 h 255
- Figure S6.26** (a) N₂ isotherms at 77 K and (b) BET surface area (m²/g_(MOF+Fiber)) for PP, PP@ZnO, PP@HDS(Zn,Co) reacted with TCPP solution at 80 °C for 6 h (PP@HDS(Zn,Co)+TCPP (80°C, 6 h)), and (d) PP@HDS(Zn,Co) reacted with TCPP solution at 80°C for 24 h (PP@HDS(Zn,Co)+TCPP (80°C, 24 h)) 255
- Figure S6.27** (a-b) SEM images of double MOF/fabric composites where Cu-BTC MOFs are overgrown on the 2D Cu-TCPP MOFs of PP@Cu-TCPP fibers prepared by reacting PP@HDS(Zn,Cu) with H₂TCPP solution at 40°C for 12 h. The Cu-BTC overgrowth was done by conducting 100 cycles of ALD ZnO to PP@Cu-TCPP composites, followed with reacting with a mixture of Cu(NO₃)₂ and H₃BTC at room temperature for 2 min to make PP@Cu-TCPP@Cu-BTC composites 256

CHAPTER 1

Introduction and Background

Dennis T. Lee,[†] and Gregory N. Parsons,^{*,†}

Department of Chemical & Biomolecular Engineering, North Carolina State University, 911

Partners Way, Raleigh, NC 27695, United States

1.1. Introduction to Metal-Organic Frameworks and Their Use

Metal-organic frameworks (MOFs) are crystalline and highly porous materials which are constructed from inorganic metal clusters and organic linkers.¹ The metal nodes, consisting of metal ions connected to non-metals (e.g., oxygen or nitrogen), are bridged by coordination bonds to multidentate organic struts mostly containing carboxylate and imidazolate functional groups.² Well-defined molecular building blocks constituting MOFs are displayed in Figure 1.1, and representative MOF structures made with varied combinations of building units are exhibited in Figure 1.2.

Because of a tremendous variety in molecular building units, the number of MOFs has sharply surged in the past decade and reached a milestone of 70,000 materials in 2016 (Figure 1.3), which has been collected and organized by the Cambridge Crystallographic Data Center (CCDC).³ The fast-track evolution of MOF chemistry is realized by complementary research in cluster chemistry for inorganic metal nodes, organic synthesis for ligands, and X-ray crystallography⁴ for structural identification. As a class of porous materials, what differentiates MOFs from the conventional porous solids, such as activated carbon and zeolites, is structural and compositional variety, ease of functional tunability, and extraordinary surface area⁵ as high as 10,000 m²/g associated with large pore volume. Fueling interest in MOFs is extended to their promise in a wide range of applications from gas storage for methane⁶ or hydrogen to CO₂ capture,⁷ chemical sensing,⁸ catalysis,⁹ drug delivery,¹⁰ and hazardous gas detoxification.¹¹

Although MOF crystals with such fascinating characteristic features can be prepared via conventional solvo-/hydrothermal approaches, their bulk powder forms insoluble in many solvents limit their practical use in many applications.¹² In the past decade, therefore, numerous research has focused on growth of MOF thin films on various substrates and made efforts to control the

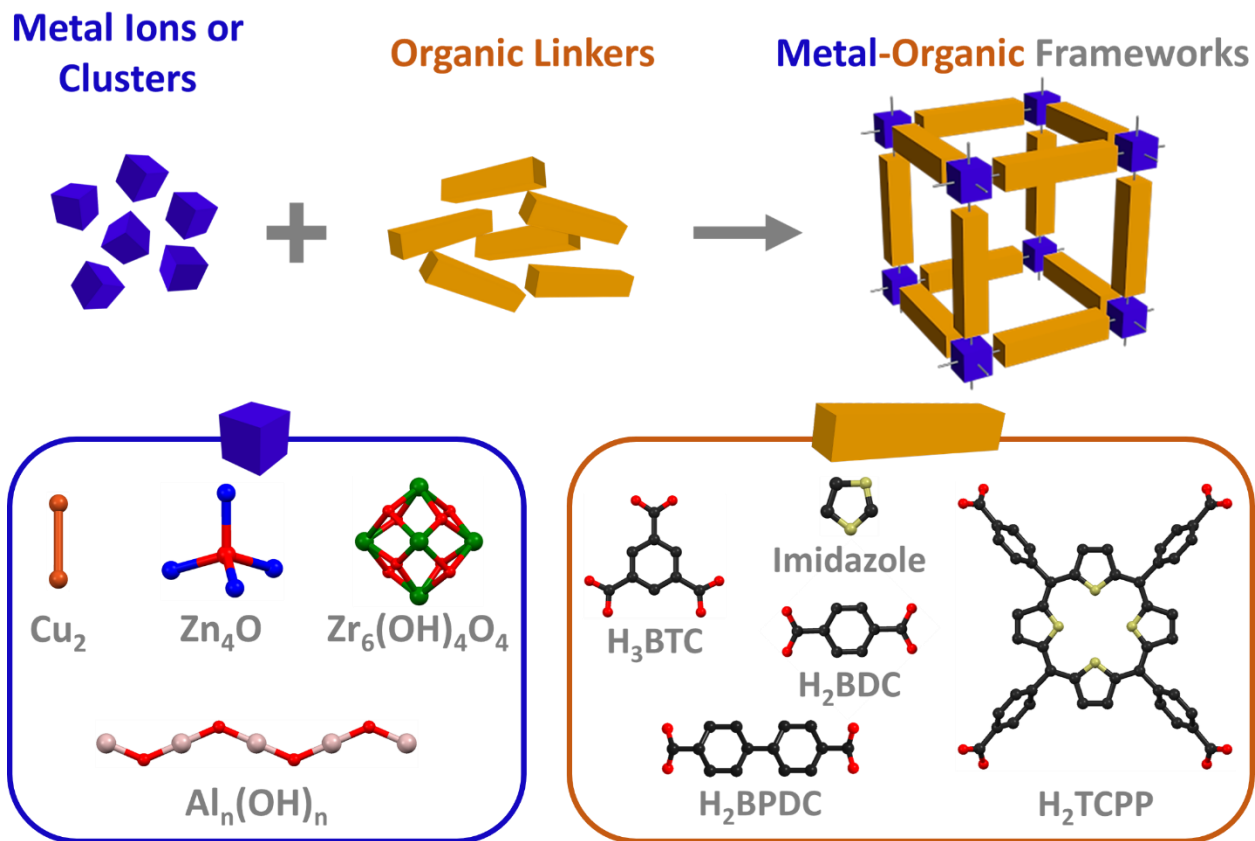


Figure 1.1. Schematic illustration of representative building blocks for metal-organic framework (MOF) construction.

orientation of the films to improve performance of surface-anchored MOF thin film devices in catalysis, gas separation, or sensor application.¹³ There has been representative concepts exploited so far to integrate MOF thin films on solid substrates: (1) the direct growth from solvothermal precursor solutions, (2) the assembly of pre-synthesized MOF crystals, (3) the stepwise layer-by-layer (LBL) deposition onto the substrates, (4) the electro-chemical growth of MOF thin films on metal substrates, and (5) the direct or indirect conversion of metal oxide thin films on the substrates into thin MOF films.¹³

These days, MOF thin film integration into flexible and permeable polymeric fibrous scaffolds using diverse synthetic strategies has garnered increasing attention. This is because

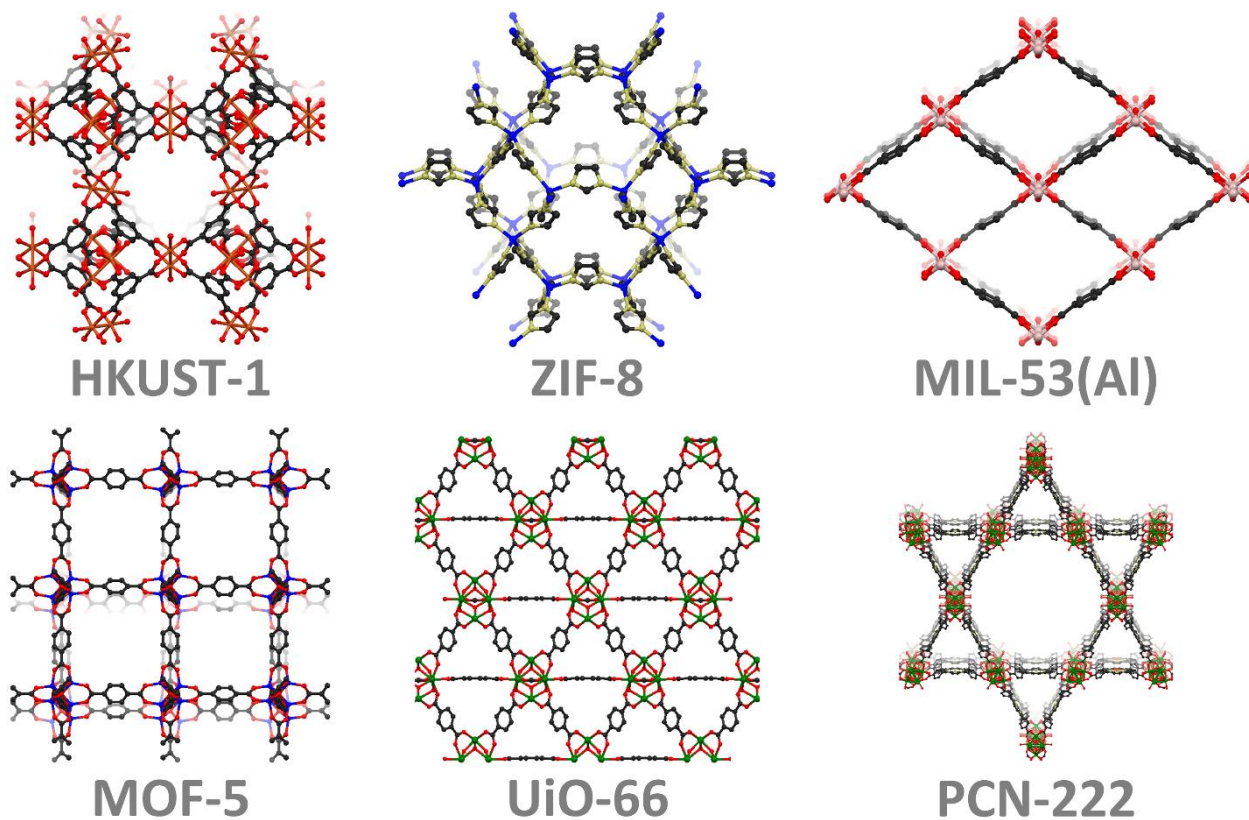


Figure 1.2. Chemical depiction of representative MOFs.

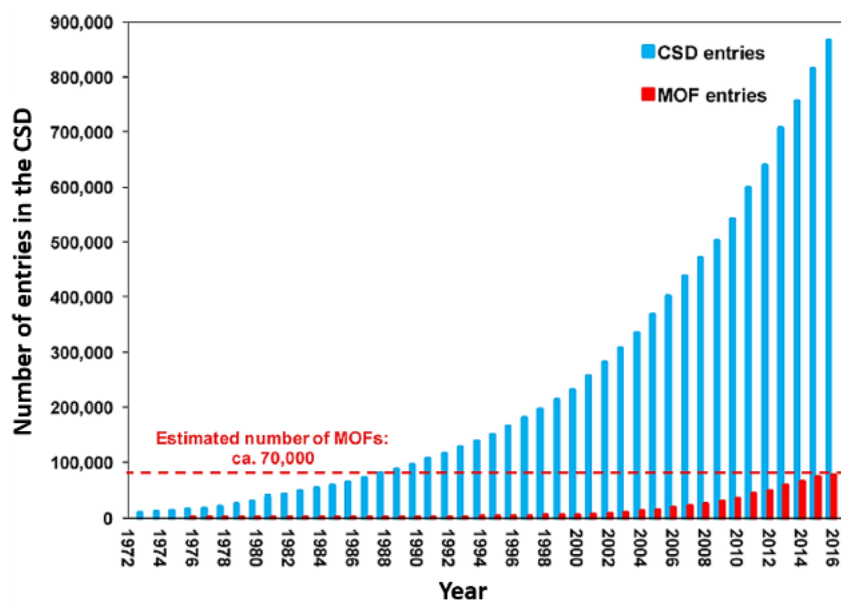


Figure 1.3. Growth of the Cambridge Structural Database (CSD) and MOF entries since 1972 (Figure adapted³).

handling and deploying the composite materials are significantly easier to effectively harness, for example, the desired separation and filtration properties of MOFs on fabrics compared to the native MOF powder materials.¹⁴ The textiles functionalized with MOF crystals have been recently sought-after and extended to sensing, chemical neutralization, and capture of a range of toxic industrial chemicals (TICs) (e.g., NH_3 and H_2S)¹⁵ and chemical warfare agents (CWAs) (e.g., chlorine; nerve agents: sarin, soman, and VX; and blistering agent: sulfur mustard (HD)) and their simulants (e.g., nerve agent simulants: dimethyl *p*-nitrophenyl phosphate (DMNP), diisopropyl fluorophosphate (DFP); and blistering agent simulant: 2-chloroethyl ethyl sulfide (CEES)).¹⁶⁻¹⁸

1.2. MOF Integration Methods on Planar Substrates

1.2.1. Conventional Solvothermal Growth

Hermes et al. were in the first few groups who actively explored the integration of metal-organic frameworks (MOFs) as functional units into thin film devices that bulk counterparts cannot drive. The researchers found that control in heterogeneous MOF nucleation on substrates pretreated with self-assembled organic monolayers (SAMs) is feasible. SAM of 16-mercaptohexadecanoic acid on Au(111) surface showed the improved deposition of MOF-5 crystals (100-500 nm) in an aged mother solution ($\text{Zn}(\text{NO}_3)_2 \cdot 4\text{H}_2\text{O}$ (3.14 g) and terephthalic acid (0.67 g) dissolved in pure diethylformamide (DEF)) at 25 °C for 24 h (Figure 1.4).¹⁹

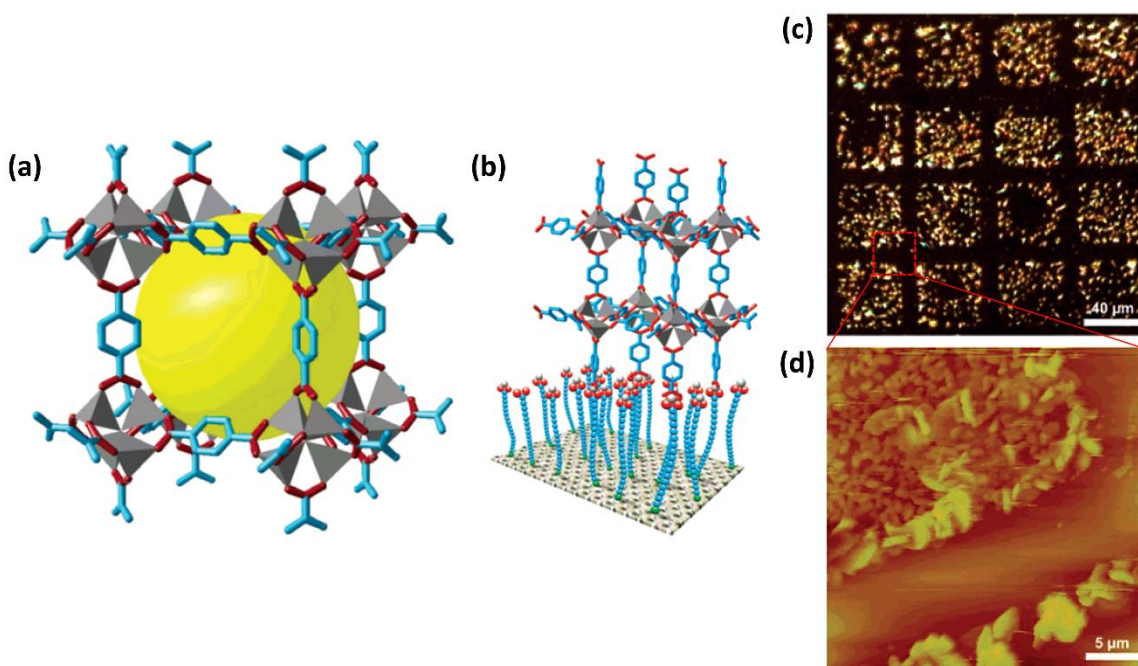


Figure 1.4. (a) MOF-5 chemical structure illustrated for a single cube fragment of their respective cubic three-dimensional extended structure.²⁰ (b) The concept, (c) optical microscope, and (d) an AFM image of anchoring a selective MOF-5 building unit to a carboxylic acid-terminated SAM. The figure (b) represents a simplified model, not excluding alternative possibilities of the linkage.¹⁹

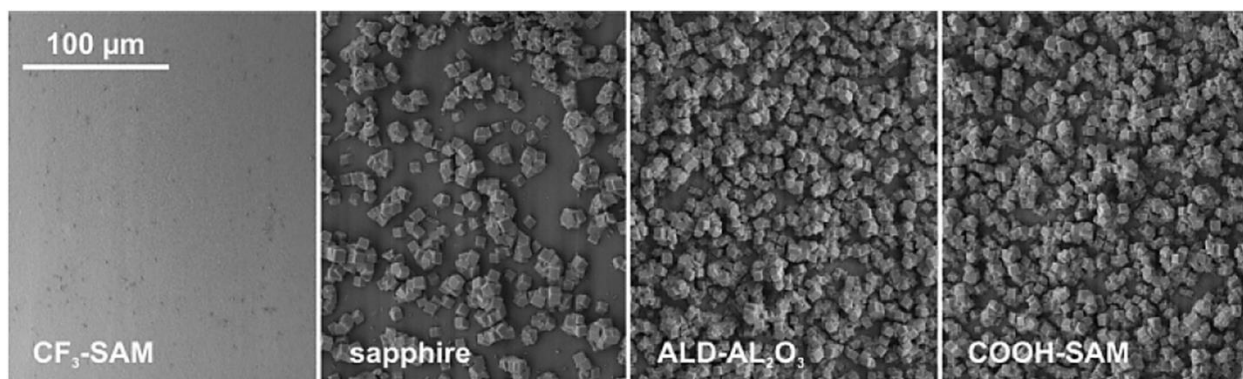


Figure 1.5. Scanning electron microscopy images of MOF-5 thin films on different pretreated alumina substrates. No crystal growth can be observed on CF_3 -terminated surfaces whereas densely packed MOF-5 thin films occur for ALD- Al_2O_3 or COOH-terminated surfaces.²⁰

In addition, Hermes et al. demonstrated that the density of anchoring sites for MOF seeds was relatively low on almost defect free surfaces (i.e., single crystalline Al_2O_3 (c-plane sapphire)), whereas amorphous atomic layer deposition (ALD) Al_2O_3 -treated and COOH-functionalized silicon substrates exhibited a dense MOF-5 film growth (Figure 1.5).²⁰ No growth of MOF crystals was observed on the fluorinated surface (CF_3 -SAM) attributed to its low surface energy with which heterogeneous nucleation was remarkably prohibited (Figure 1.5).

Zacher et al. also reported similar results with HKUST-1, displaying the impact of the nature of the substrate surface on the degree of MOF nucleation and subsequent growth behavior. What the authors further found was that acid/base properties of the substrates dictated whether the MOF film can grow on the substrates used. As shown in Figure 1.6, HKUST-1 densely grew on the more basic substrates (Al_2O_3 , c-plane sapphire), whereas no crystals were found on the more acidic substrates (SiO_2). This was because carboxylic acid linkers for HKUST-1 mediated the binding between MOF film and the substrates, therefore the MOF cannot be readily immobilized onto the more acidic SiO_2 surface. As demonstrated with MOF-5 in Figure 1.5, the structural

imperfection of ALD Al_2O_3 film can also better promote HKUST-1 nucleation in comparison with the single crystalline Al_2O_3 surface (c-plane sapphire) (Figure 1.6b-c). Interestingly, preferred orientation of MOF single crystals depending upon the nature of the substrate surface were also observed (Figure 1.6d-e).

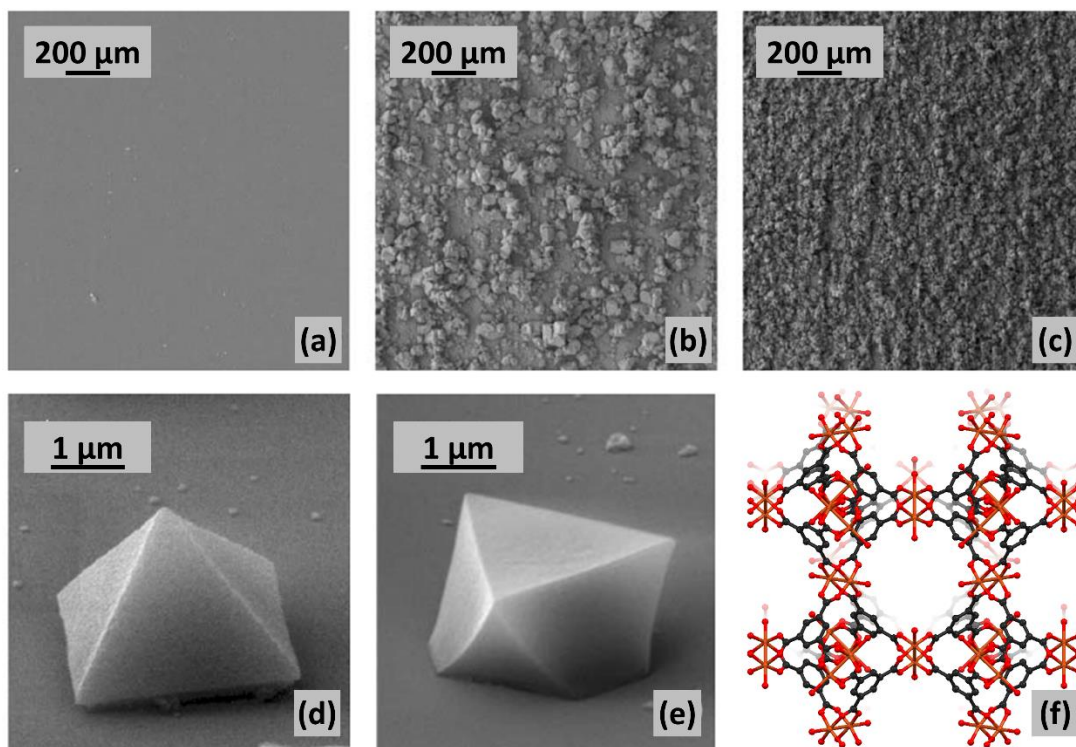


Figure 1.6. SEM images of HKUST-1 ($\text{Cu}_3(\text{BTC})_2$) MOF coatings on (a) bare SiO_2 , (b) Al_2O_3 (sapphire) and (c) ALD Al_2O_3 . (d) Single pyramidal crystal of HKUST-1 grown on c-plane sapphire. (e) Octahedral single crystals of HKUST-1 on COOH-functionalized Si/ SiO_2 . (f) Chemical depiction of HKUST-1 MOF structures. (scale bars and figure arrangement adapted from Ref.²¹)

1.3. MOF Integration Methods on Polymeric Fibers (With No ALD Processes)

1.3.1. Direct Solvothermal Growth

Küsgens et al., who early recognized the importance of porous thin film deposition on suitable substrates for filter technology applications, investigated HKUST-1 ($\text{Cu}_3(\text{btc})_2$) integration into pulp fibers.²² As a control experiment, as-prepared HKUST-1 powder was directly mixed with the pulp slurry in a Rapid-Köthen mold to render composite sheets. As shown in scanning electron micrograph (SEM) image (Figure 1.7a), an inhomogeneous distribution of MOF crystals and their aggregates was observed, and the crystal bundles were physically entrapped within the interstitial spaces of the fibrous network. To enhance MOF crystal mass loading with improved homogeneous distribution on the fibrous scaffolds, the authors conducted the in-situ synthesis of HKUST-1 in the presence of chemi-thermo mechanical pulp (CTMP) fibers with high lignin content (Figure 1.7b). Due to dense carboxylic functional groups contained in the lignin on the CTMP fibers, well-distributed and chemically-bound HKUST-1 crystals on the flexible substrates were obtained. The result was agreed well with the promoted MOF growth on the COOH-functionalized silicon substrates denoted in Figure 1.5.

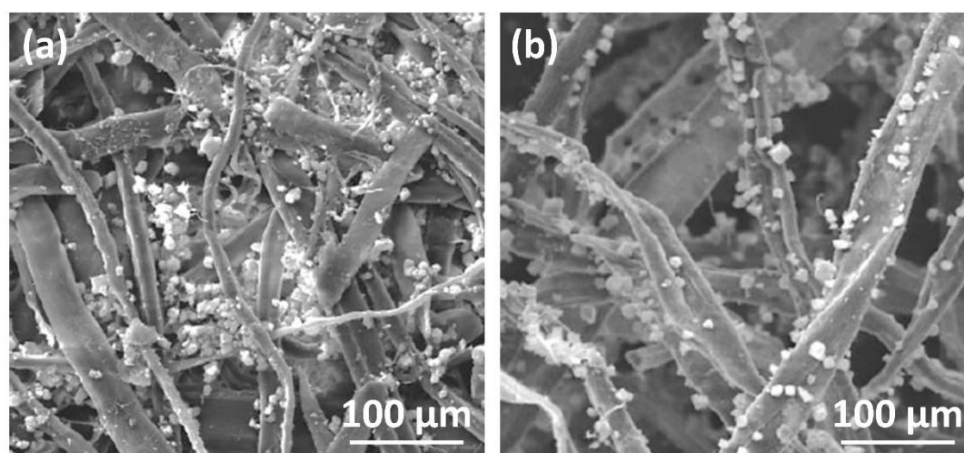


Figure 1.7. SEM images of (a) HKUST-1 ($\text{Cu}_3(\text{BTC})_2$) paper hand sheets and (b) HKUST-1 crystals on CMTP fibers. (figure arrangement adapted from Ref.²²)

1.3.2. Microwave Irradiation-Assisted Solvothermal Growth

Centrone et al. also functionalized polymeric substrates composed of polyacrylonitrile (PAN) with a representative MOF, MIL-47 consisting of corner-sharing vanadium(III) oxide octahedra bridged by terephthalate linkers (Figure 1.8).²³ In this work, MIL-47 was rapidly synthesized using microwave irradiation method due to substantially enhanced local heating processes, and the effect of microwave irradiation time on the MOF growth behavior on the PAN surface was investigated.

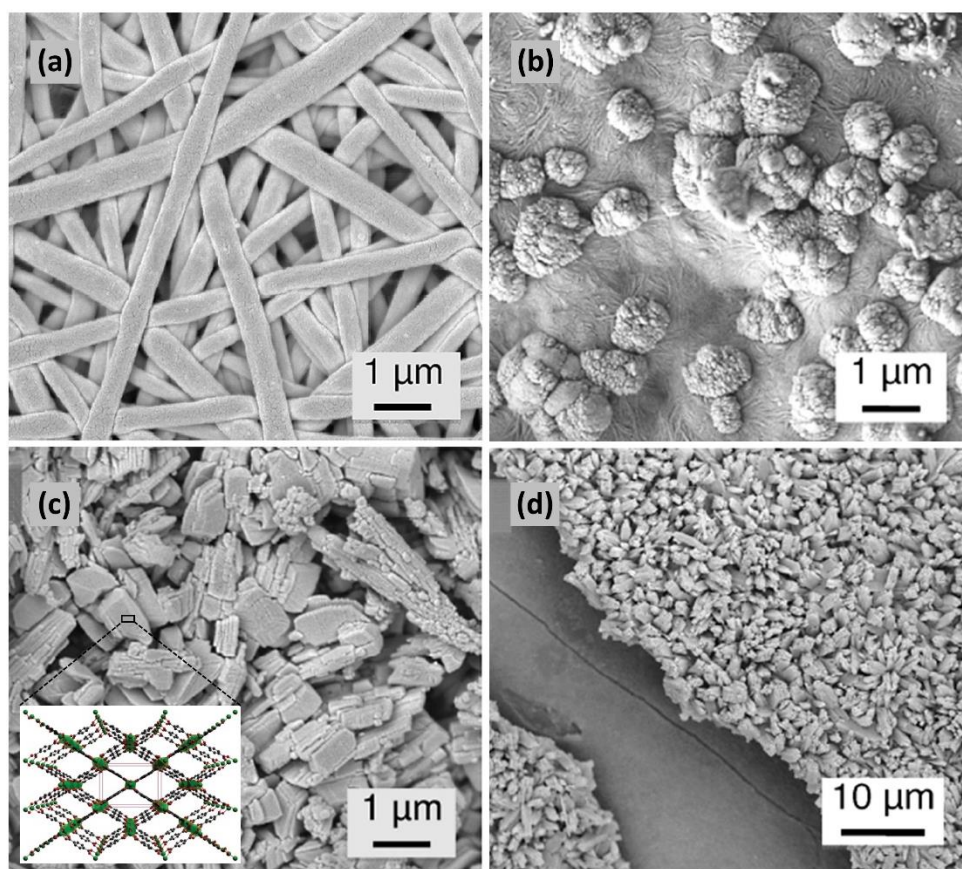


Figure 1.8. SEM images of (a) electrospun polyacrylonitrile (PAN) fiber mats, coated with MIL-47 material as a function of time: (b) 5 s and (c) 6 min. SEM image of (d) MIL-47-coated grooved PAN. Inset in (c) is chemical structure of MIL-47 MOF. (figure arrangement adapted from Ref.²³)

Through this study, the authors identified that PAN surface first hydrolyzed under the reaction conditions (MOF precursors in water, 200 °C, pH=1), thus generating poly(acrylic acid) groups which were subsequently cross-linked in the bulk. Therefore, the PAN substrates functionalized with carboxylic acid facilitated the compact growth of MOF crystals on the polymer surface. However, the electrospun PAN fibers lost their structural identity within the first 5 s of the microwave-assisted reaction so the MOF-polymer hybrid materials produced were not ideal to be used for membrane separations, filtration, and protective functional textiles.

1.3.3. Direct Solvothermal Growth Using a Seeding Strategy

Wu et al. reported a new strategy combining an electrospinning technique and a seeding solvothermal growth approach to produce free-standing MOF membranes.²⁴ The electrospinning has been well known as a simple and versatile strategy to fabricate continuous fibrous membranes with highly tunable fiber diameters from nanometers to micrometers.²⁵ The facile control in material compositions (e.g., inorganic, organic or hybrid) and in surface properties of the electrospun fibers made the electrospinning a fascinating technique to produce functional textiles.

However, intrinsic property of functional particles entrapped within polymeric fibers could be considerably reduced when the particles dissolved in polymer solutions are directly electrospun. In order to overcome such a critical drawback, Wu et al. simply conducted a solvothermal growth (secondary step) in the presence of the electrospun fibers doped with MOF crystals as nucleation sites to improve MOF growth on the external surface area of the fiber mats (Figure 1.9a). As shown in Figure 1.9b-c, ZIF-8 MOF crystals strongly embedded in the polystyrene (PS) fibers were remained intact after the electrospinning process. Subsequently, the cyclic in-situ solvothermal synthesis with a growth solution containing $Zn(NO_3)_2 \cdot 6H_2O$ and 2-methylimidazole dissolved in

methanol at 65 °C for 12 h in the presence of the MOF-doped fibers gave rise to a well-intergrown ZIF-8 MOF film (Figure 1.9f-g).

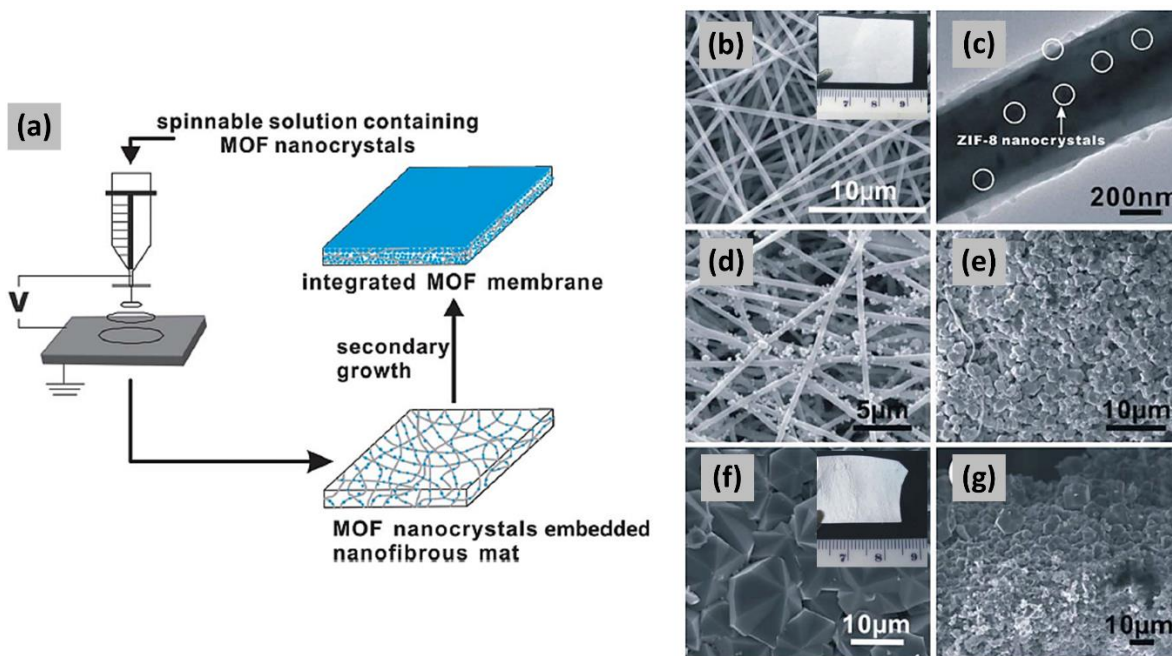


Figure 1.9. (a) Schematic illustration of electrospun nanofibrous mats used as skeletons to produce free-standing MOF membranes. SEM image of (b) the ZIF-8 nanocrystal embedded electrospun nanofibrous mat (c) with magnified TEM image; SEM images of the fibrous mat after ZIF-8 growth period of (d) 1 cycle, (e) 4 cycles, (f) 5 cycles, and (g) the cross-section of the ZIF-8 membrane after 5-cycle growth. The insets in (b) and (f) are optical images of the corresponding samples. (figure arrangement adapted from Ref.²⁴)

Lu et al. similarly adopted a seeding strategy to integrate UiO-66-NH₂, composed of Zr₆(OH)₄O₄ clusters linked by aminoterephthalic acid (ATA) linkers, into PAN nanofibers.²⁶ In this study, instead of as-synthesized MOF particles the authors first dissolved pure ATA linkers in PAN polymer solution, followed with electrospinning the solution into fibrous membranes. The ATA linkers densely embedded within the PAN fiber mats acted as anchoring or nucleation sites for heterogeneous MOF nucleation. Throughout the research, Lu et al. found that the ATA-

embedded seeding PAN fiber scaffolds resulted in the highest MOF mass loading compared to MOF particle-embedded fibrous mats after the direct solvothermal growth of UiO-66-NH₂ (Figure 1.10). Here acetone was employed in place of DMF as a typical solvent to initiate a solvothermal reaction between ZrCl₄ and ATA precursors and importantly to prevent PAN fiber substrates from being solubilized during the reaction. Therefore, the MOF-polymer composites could maintain integrity of both microporous UiO-66-NH₂ and macroporous PAN fibrous network, showing decent chlorine gas uptake compared to other control samples prepared.²⁷

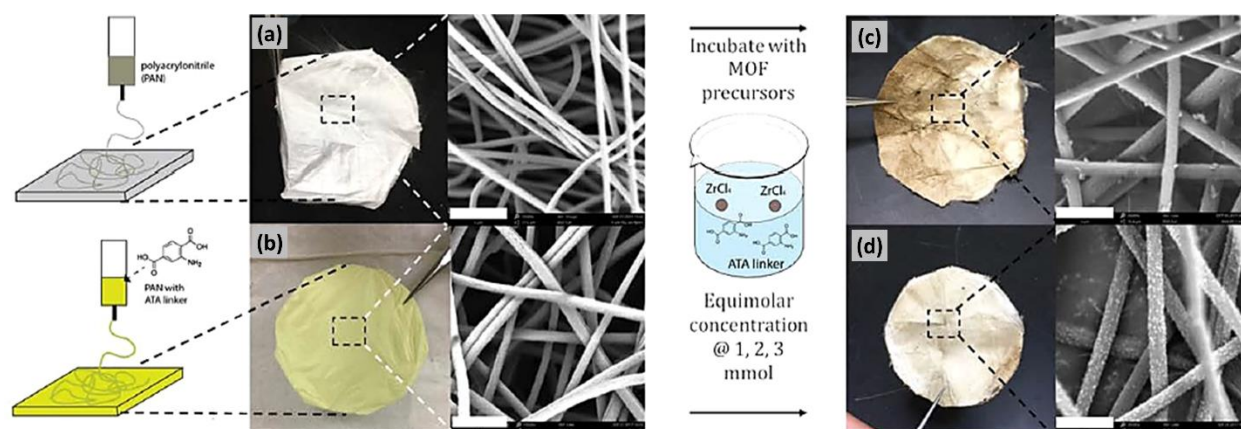


Figure 1.10. Schematic of in situ growth of UiO-66-NH₂ on plain polyacrylonitrile fibers and polyacrylonitrile (PAN) fibers seeded with the aminoterephthalic acid (ATA linker). Electrospun swatches are sandwiched between two cellulose filter papers before being placed in a parr bomb with the UiO-66-NH₂ precursors: equimolar concentrations of ATA linker and zirconium chloride (metal), in acetone. Increasing concentrations of precursors are used for synthesis, 1, 2, and 3 mmol, to observe effects of concentration of precursors on UiO-66-NH₂ synthesized on the fiber: (a) control PAN swatch; (b) PAN with ATA linker. (c) Control PAN postsynthesis (d) PAN with ATA linker postsynthesis. Scale bar 3 μm.²⁶

1.3.4. Growth on Surface Coated with Reactive Polymers

As introduced in previous sections about immobilization of MOF films on any substrates, functionalizing the substrates with reactive groups was necessary to significantly increase nucleation sites for MOFs and to enhance binding strength between MOF films and the substrates. However, reactive sites anchored on the substrates were not always amenable to MOF nucleation so developing a new and universal technique for effective integration of MOF materials on polymer surface was highly desirable. Considering the importance of the issue, Zhou et al. paid attention to polydopamine (PDA) as a glue layer on substrates as well as a nucleation layer for MOFs. As described in Figure 1.11a, without the use of any other additives, dopamine can self-polymerize and morph into a strongly adhesive PDA coating on any surface by simply immersing substrates into polymerization media.

With this facile approach, the researchers realized successful PDA coatings on commercially available and even on chemically inert nanofibrous polymer membranes (e.g., polypropylene (PP), polyethylene (PE), polystyrene (PS), and polyvinylidene fluoride (PVDF)). PDA was uniformly coated on PP membranes, for instance, with a distinct color change from white to dark brown (Figure 1.11b-c), and HKUST-1 and MOF-5 materials were continuously integrated into PDA-modified membranes via layer-by-layer (LBL) deposition method at room temperature (Figure 1.11d-e). In contrast to the conventional solvothermal methods, LBL strategy is driven by sequential immersion of substrate in an alternating bath of organic linker solution and metal ion solution to precisely control thickness of MOF thin film on substrates.

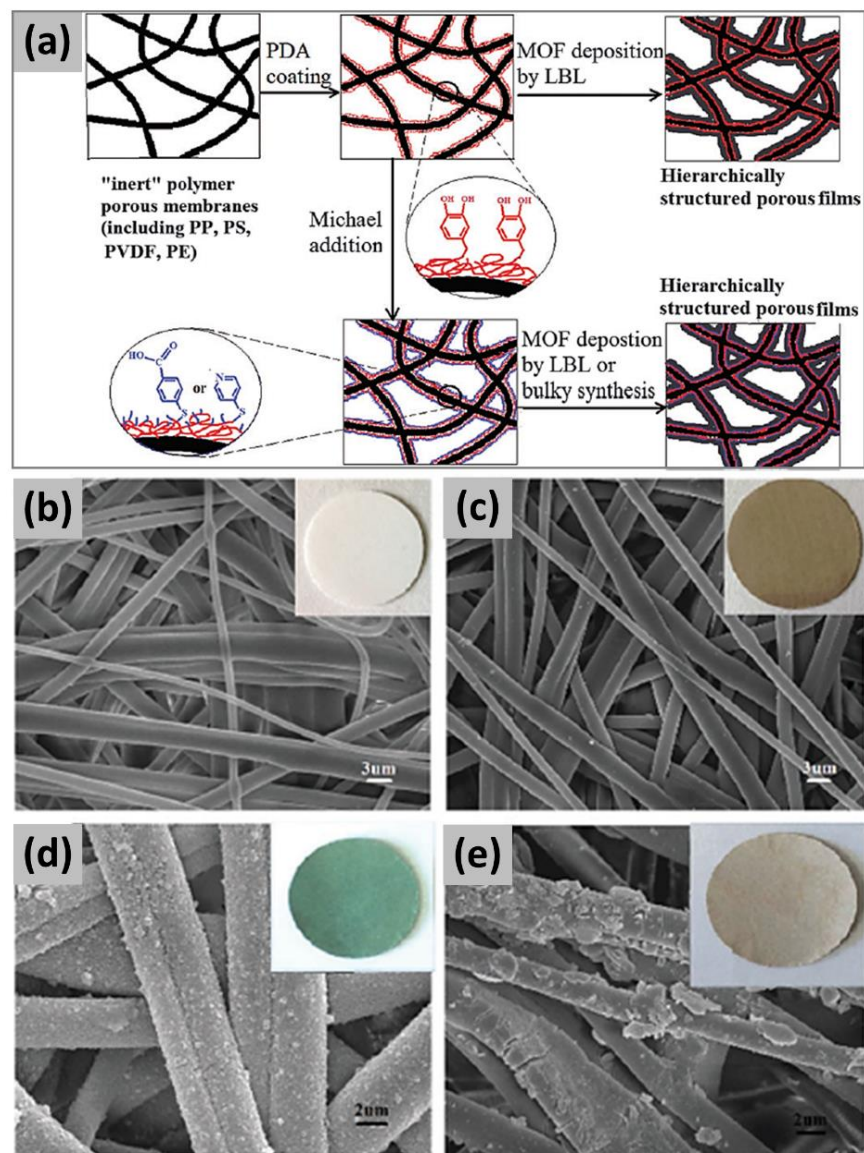


Figure 1.11. (a) Schematic illustration of the strategy of effective deposition MOF on the "inert" polymer fibrous membranes by using polydopamine layer as nucleation center to fabricate hierarchically structured porous films. SEM images of (b) original PP fibrous membrane and (c) PDA-coated PP membrane; SEM images of PDA-modified PP membrane followed by the deposition of (d) HKUST-1, and (e) MOF-5. (figure arrangement adapted from Ref.²⁸)

1.4. MOF Integration Methods on Polymeric Fibers (ALD-Driven)

1.4.1. Atomic Layer Deposition (ALD) to Polymer Textiles

Atomic layer deposition (ALD)²⁹ is a well-known vapor-phase thin-film deposition technique together with physical vapor deposition (PVD)³⁰ and chemical vapor deposition (CVD)³¹ methods. Among the techniques, ALD uniquely possesses a capability to produce highly uniform and exceptionally conformal thin film of metal oxides or elemental metals on nonuniform high aspect ratio surfaces.³² The matchless attribute of ALD has made it become commercially significant process in large-scale semiconductor manufacturing and the fabrication of semiconductor devices since the early 2000s when the semiconductor industry started adopting the method.³³

Due to its relatively low temperature processability, conventional thermal ALD technique has been also widely used to add new functionality to various polymer substrates to realize multi-functional textiles.³⁴ In practice, many attempts to coat different synthetic and natural polymer textiles with various inorganic films have been made through thermal ALD reactors (Figure 1.12). In one ALD cycle for Al₂O₃ deposition, for instance, trimethylaluminum (TMA) and water are sequentially dosed into the deposition chamber, with a N₂ purge step in between to get rid of any unreacted species and by-products. The dosing step with diethylzinc (DEZ) instead of TMA can form ZnO thin film on substrates. Repeating the ALD cycle with selected precursors can result in a fine control in film thickness at atomic level on any substrates with complex geometries.

ALD process on soft substrates (e.g., polymers), as opposed to hard ones (e.g., silicon wafers), can cause a very different outcome in the extent of precursor diffusion into the polymers and in film roughness depending upon different ALD precursors, polymer types, and deposition conditions.

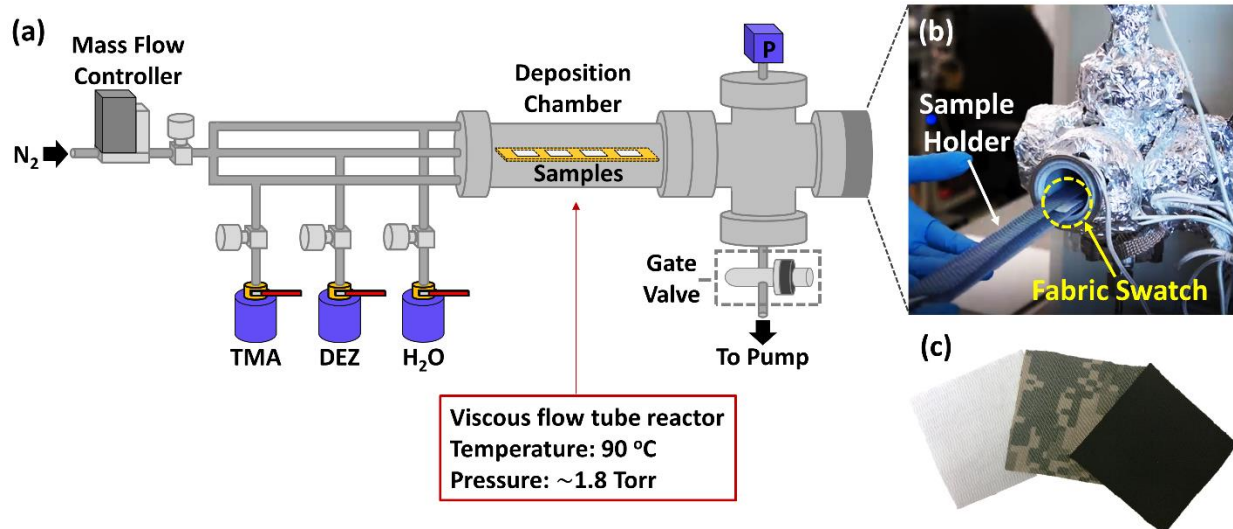


Figure 1.12. (a) Schematic illustration of the homemade hot-wall viscous-flow ALD reactor used for ALD metal oxide coatings on polymeric fibers. Optical images of (b) inserting fabric samples into the deposition chamber and (c) representative fabric swatches used. All reactor lines of the setup were resistively heated to around $100\text{ }^\circ\text{C}$ to avoid precursor condensation during the gas carrying process.

As represented in Figure 1.13a, cotton fibers with reactive Lewis basic sites (e.g., hydroxyl groups) are favorable to immediate chemical reactions with Lewis acidic reactants (TMA, $TiCl_4$, or DEZ), thus giving rise to a relatively abrupt interface between polymer surface and inorganic film. On the other hand, the reactants are prone to diffuse into the chemically inert PP fibers and subsequently brings about metal oxide nuclei formation within the subsurface region, which ultimately produces a roughened inorganic film texture on the fibers (Figure 1.13b).

The mechanism studies on the interaction between reactants and polymer substrates during the ALD processes manifest that ALD has a great potential to tune or modify surface properties of any type of polymer membranes to become functional platforms for even further processing.

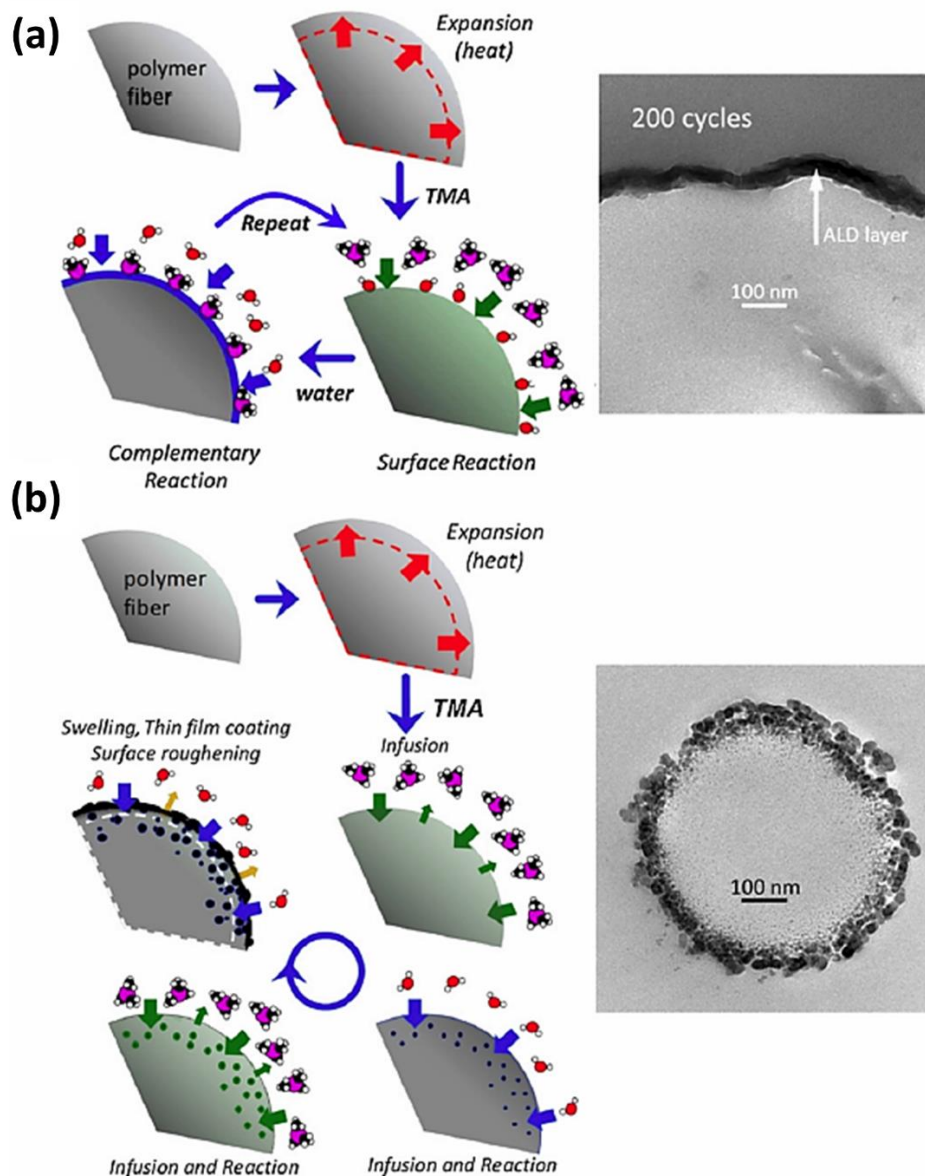


Figure 1.13. (a) ALD on a hydroxyl rich polymer surface leads to conformal deposition as shown in the example of Al_2O_3 ALD growth on cotton (top TEM image). (b) ALD on a polymer surface that lacks reactive functional groups can result in subsurface diffusion and growth within the fiber core, resulting in a less uniform coating at some temperatures. ALD growth on polypropylene (PP) at high temperatures (90°C) results in this kind of subsurface deposition (lower TEM image).³²

1.4.2. MOF Integration into ALD-treated Textiles

1.4.2.1. Direct Solvothermal Growth (MOF on ALD)

Zhao et al. reported that highly packed hydroxyl terminal groups on ALD metal oxide coatings onto polymeric fibrous mats can provide decent nucleation sites where MOF crystals can heterogeneously nucleate and be chemically bound (Figure 1.14a-c).

The authors found that, the solvothermal synthesis of HKUST-1 MOF at 120 °C for 24 h in the presence of ALD Al₂O₃-coated PP nonwoven textiles gave rise to MOF mass uptake around 50% larger than that on bare fiber substrates (Figure 1.14d). The resulting MOF-coated textiles exhibited 700 m²/g_(MOF+fiber) of high surface area and showed >5 mol_{NH₃}/kg_(MOF+fiber) of NH₃ adsorptive capacity which was larger than the capacity from other MOF films on fibers reported.

In a separate study, the researchers successfully fabricated chemical protective textiles functionalized with Zr-based MOFs (e.g., UiO-66, UiO-66-NH₂, and UiO-67) for efficiently detoxifying chemical warfare agents (CWAs) and their simulants. To help promote nucleation of catalytic MOF crystals onto polyamide-6 nanofibers (PA-6) as a chosen substrate in the study, the authors treated the PA-6 nanofibers with ALD TiO₂ (~7 nm), followed by solvothermal growth for the Zr-based MOFs (Figure 1.15a). As shown in Figure 1.15b-c, irregular round-shaped UiO-66 MOF crystals were completely immobilized around the TiO₂ thin film deposited on a free-standing PA-6 nanofiber mat. As expected, on the other hand, very sparse and patchy distribution of UiO-66-NH₂ crystals were observed on untreated PA-6 nanofiber substrates under the same synthetic conditions.

The best hydrolysis performance with the resulting textile catalysts displayed that the half-lives of soman (GD) and its simulant dimethyl *p*-nitrophenyl phosphate (DMNP) were as short as 2.3 min and 7.3 min, respectively.

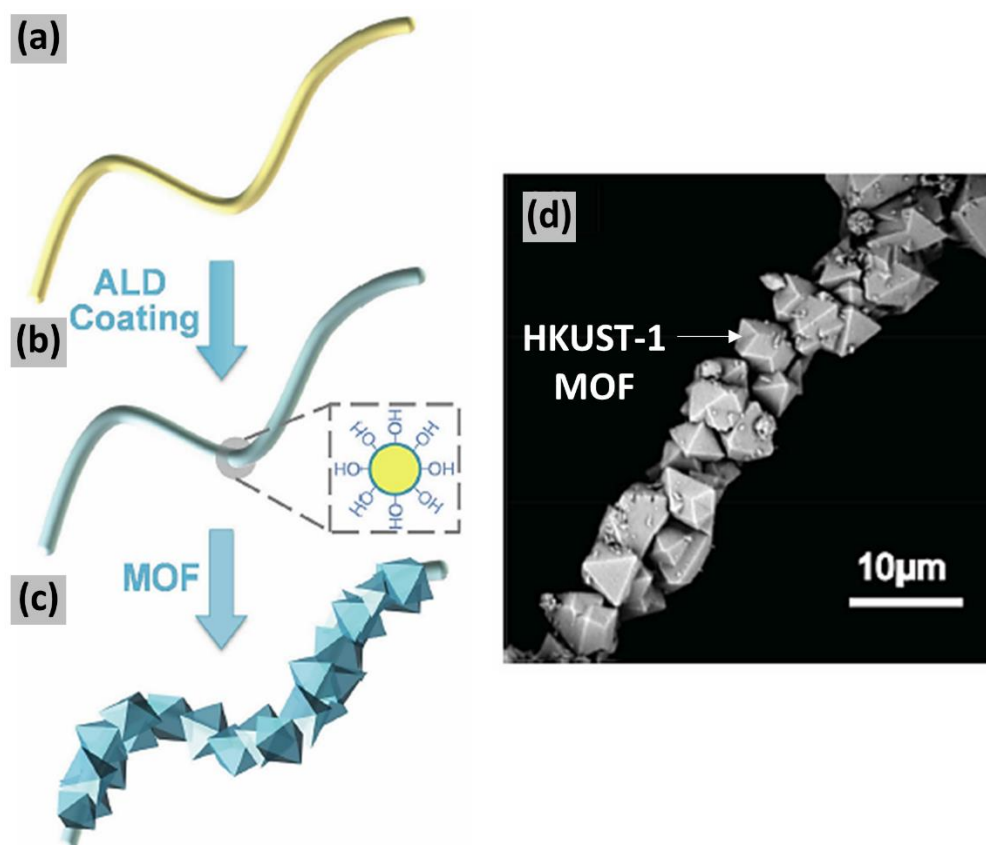


Figure 1.14. (a-c) Schematic illustration of the synthesis route. (a) Polymer fiber substrate. (b) Al_2O_3 -coated polymer fiber via atomic layer deposition (ALD). The cross section in the dashed square illustrates the conformal coating of ALD Al_2O_3 with hydroxyl surface termination. (c) MOFs integrated on Al_2O_3 -coated polymer fiber using solvothermal MOF synthesis. (d) SEM image of HKUST-1 MOF crystals grown on an ALD- Al_2O_3 -coated polypropylene fiber (MOF-PP/ALD). (figure arrangement adapted from Ref.³⁵)

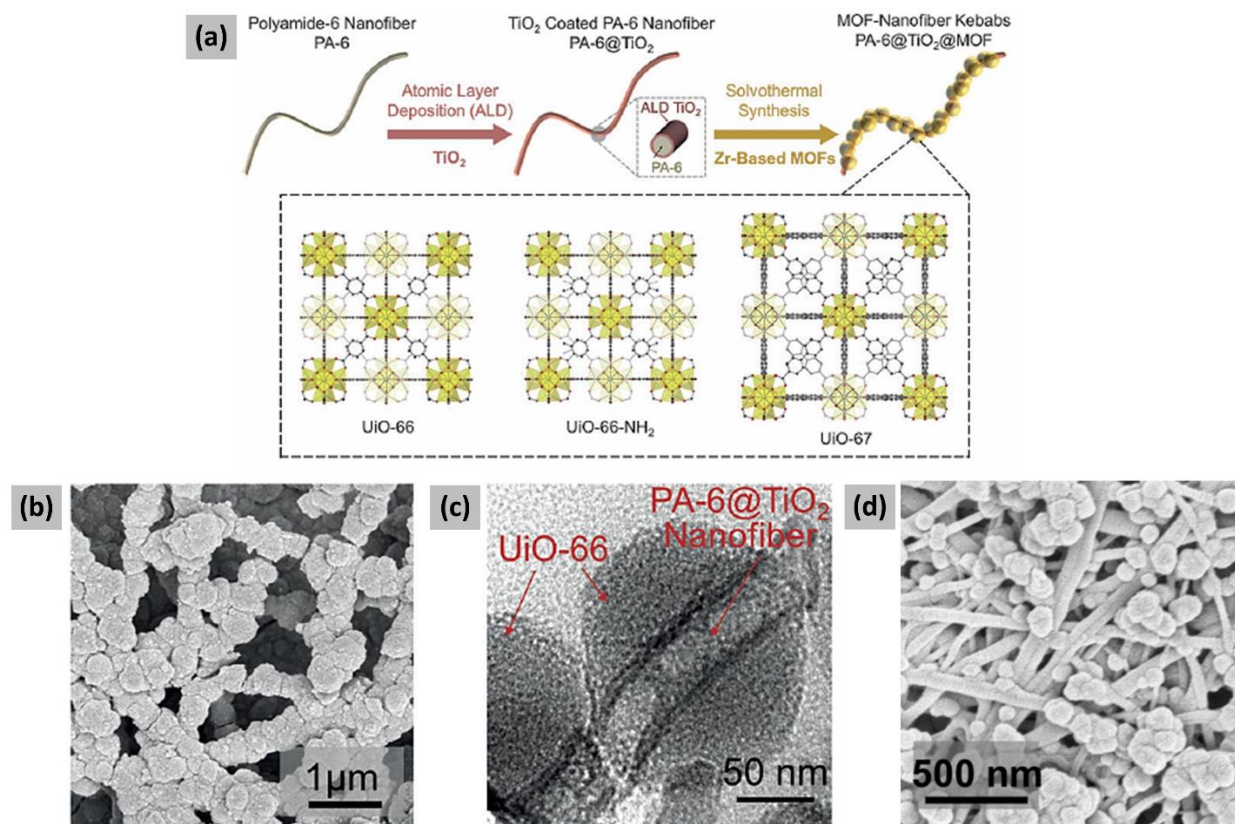


Figure 1.15. (a) Synthetic procedure for Zr-based MOF–nanofiber kebab structures on polyamide-6 nanofibers (PA-6). The MOF crystal structures are illustrated in the dashed box. (b) SEM and (c) TEM images of PA-6@TiO₂@UiO-66. (d) SEM image of UiO-66-NH₂ grown on untreated PA-6 nanofibers (PA-6@UiO-66-NH₂). (figure arrangement adapted from Ref.³⁶)

1.4.2.2. Direct Replication Method (ALD to MOF)

Khaletskaya et al., for the first time, investigated and demonstrated the self-directed localization of ZIF-8 thin film on solid substrates by conversion of ALD and sputter deposited ZnO thin film (Figure 1.16a).³⁷ The vapor phase deposition techniques (ALD and magnetron sputtering) used in the study are reliable methodology for spatial positioning of ZnO film onto solid substrates. The well-controlled ZnO nanolayers can be used as a localized Zn^{2+} source for ZIF-8 formation on the substrates by reacting with 2-methylimidazole (Hmim) ligands.

The specimen of ZIF-8 thin film directly converted from ALD ZnO on silicon (Si/SiO₂) was prepared by a focused ion beam (FIB) milling technique (Figure 1.16b), and its cross-sectional views were imaged by TEM to identify each layer of the film. As shown in Figure 1.16c-d, intergrown polycrystalline ZIF-8 film ($\sim 95 \pm 10$ nm) was integrated into the silicon substrate with the remaining ZnO interlayer (~ 50 nm) relatively uneven compared to the initial seamless ALD ZnO film.

The authors emphasized that Hmim organic linkers dissolved in mixed solvent medium (DMF and water) acts both as an etching agent to partially dissolve ZnO films to offer Zn^{2+} ions and as a ligand for the coordination with the ions to crystallize ZIF-8, respectively. In addition, the residual ZnO interlayer between the ZIF-8 film and the silicon substrate provides a robust adhesion for the ZIF-8 film on the substrate.

A similar synthetic approach was employed by Bechelany et al. who created a composite material where highly crystalline MOF crystals were densely coated on a flexible scaffold of electrospun polymeric fibers.³⁸ As shown in Figure 1.17a and c, a conformal ZnO thin film deposited via ALD on electrospun polyacrylonitrile (PAN) nanofibers was transformed into ZIF-8 crystals by reacting with Hmim linkers under microwave (MW)-assisted or conventional

solvothermal conditions. Furthermore, conversion of ALD Al_2O_3 film into MIL-53- NH_2 MOF crystals on nanofibers was demonstrated by the same approach with aminoterephthalic acid (ATA) linkers in place of Hmim ligands (Figure 1.17b and d). Both MOF crystals (ZIF-8 and MIL-53- NH_2) converted under optimized conditions from each corresponding metal oxide film on fiber substrates exhibited highly porous and crystalline solids with conversion yield of around 90%.

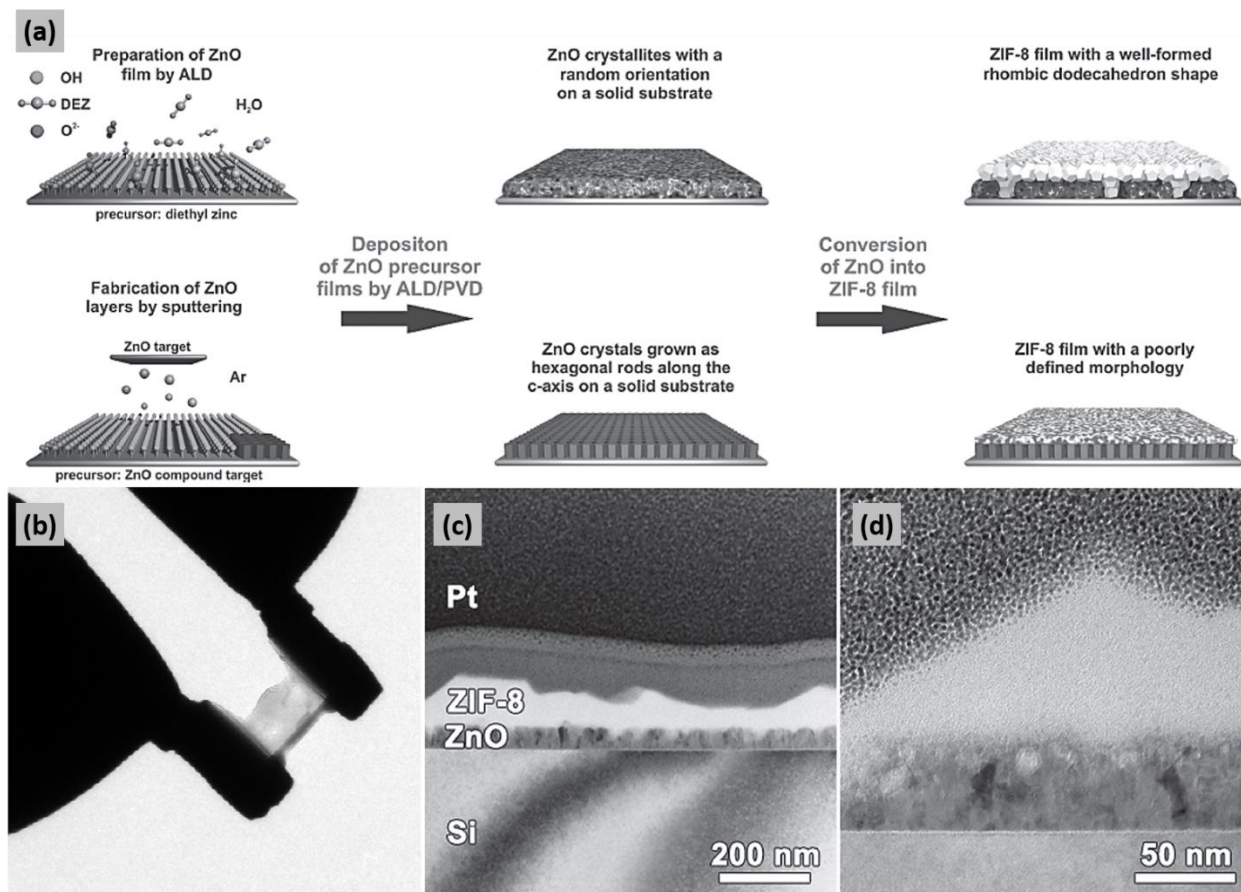


Figure 1.16. (a) Schematic illustration of the synthesis of ZIF-8 films from ZnO precursor films deposited on solid substrates. TEM images of (b) a FIB-prepared cross-sectional specimen, (c) an enlargement of ZIF-8 film ($\sim 95 \pm 10$ nm) grown from ALD-ZnO with the observed layers indicated, and (d) magnification image of (c). Thick Pt layers are deposited on the top of the material prior to milling for protection. (figure arrangement adapted from Ref.³⁷)

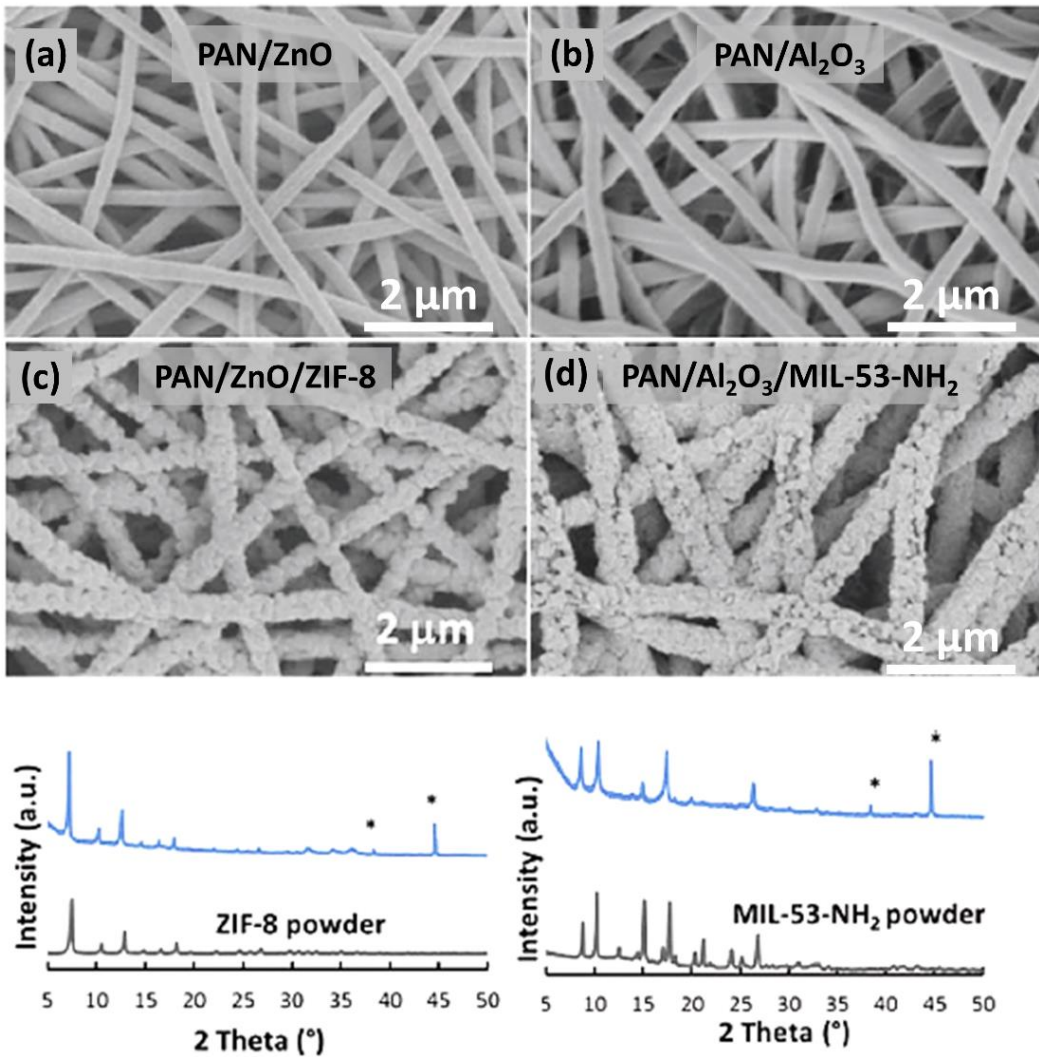


Figure 1.17. SEM images of PAN nanofibers coated by ALD with thin layers of (a) ZnO and (b) Al₂O₃. SEM images of (c) PAN/ZnO/ZIF-8 and (d) PAN/Al₂O₃/MIL-53-NH₂ composite materials obtained under MW-assisted heating (1.5 h); (diffraction peaks of Al-foil are marked with (*) and diffraction patterns of ZIF-8 and MIL-53-NH₂ reference powders are reported for comparison). (figure arrangement adapted from Ref.³⁸)

1.4.2.3. Hydroxy Double Salt Replication Method (ALD to HDS to MOF)

Zhao et al. discovered a novel strategy for the rapid synthesis of MOF crystals at room temperature using hydroxy double salts (HDSs) as intermediates.³⁹ In general, HDSs can form by reaction between one divalent metal oxide and another discrepant divalent cation. The layered structure of HDSs is comprised of cationic sheets linked by inorganic/organic interlamellar anions.⁴⁰ Due to their structural feature, HDSs with excellent anion exchangeability can be intentionally harnessed to transform into new other functional materials.

Figure 1.18a describes a representative two-step method for the rapid synthesis of HKUST-1 MOF crystals. First, crystalline ZnO reacts with $\text{Cu}(\text{NO}_3)_2$ dissolved in solvent mixture (DMF and water) to produce (Zn,Cu)HDS compounds, and the intermediate HDS is directly converted into HKUST-1 within 1 min via rapid anion exchange with 1,3,5-benzenetricarboxylic acid (H_3BTC) as a linker. The calculated space-time-yield (STY) for HKUST-1 synthesized by the HDS conversion method showed $3.6 \times 10^4 \text{ kg}\cdot\text{m}^{-3}\cdot\text{d}^{-1}$, at least 1 order of magnitude greater than any previous reports.³⁹

To apply the facile HDS conversion approach to surface-bound HKUST-1 film on various form factors, ALD technique was adopted to provide conformal ZnO thin film with well-controlled thickness at atomic regime (Figure 1.18b). Polystyrene (PS) spheres, Si wafers, and polyacrylonitrile (PAN) fibers were exemplified as substrates to be coated with ZnO (~36 nm). After being exposed to the mother solution ($\text{Cu}(\text{NO}_3)_2$ and H_3BTC dissolved in DMF/water/ethanol solvent mixture) for HKUST-1 at room temperature, ZnO thin film deposited on each substrate was immediately converted to dense films of HKUST-1 within 1 min (Figure 1.18c). All the substrates tested maintained their structural integrity intact after the procedure,

indicating its high practicality not only for powder synthesis but also for surface-functionalized thin film formation.

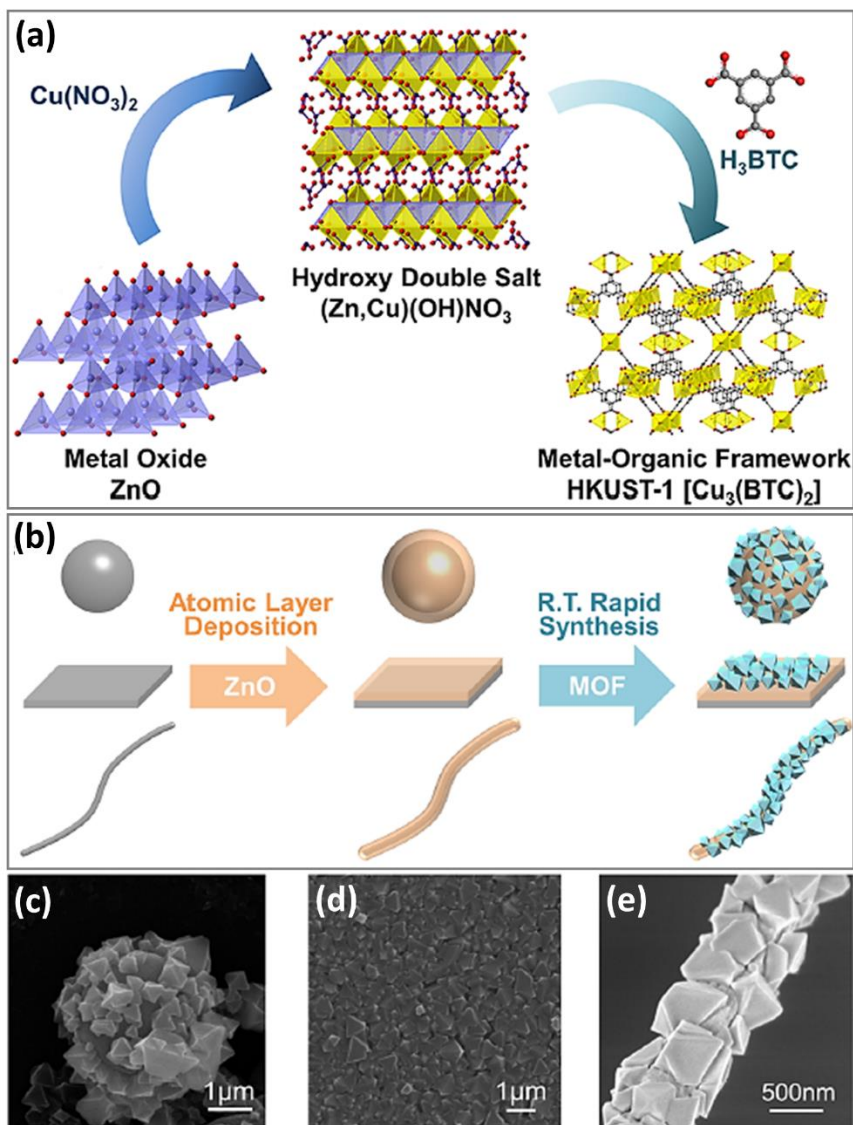


Figure 1.18. (a) Schematic drawing of the rapid room-temperature synthesis of HKUST-1. ZnO reacts with $\text{Cu}(\text{NO}_3)_2$ to form (Zn,Cu) HDS, which converts to HKUST-1 via fast anion exchange. (b) Schematic of the rapid room-temperature synthesis of MOF coatings on various form factors. (c-e) SEM images of HKUST-1 deposited onto PS spheres, Si wafer, and PAN nanofibers, respectively. (figure arrangement adapted from Ref.³⁹)

Pimentel et al. took advantage of the facile synthetic method of converting HDS intermediates into MOFs,³⁹ and ultimately facilitated high volume loadings of HKUST-1 (85 wt%) or ZIF-8 (66 wt%) crystals within porous polymer fiber sorbents for application in gas separation.

The researchers first prepared ZnO-loaded cellulose acetate (CA) fiber sorbents utilizing a dry-jet, wet-quench spinning technique using water as a quench bath coagulant.⁴¹ After the fiber spinning process, the relatively flexible CA/ZnO fibers obtained were assembled into close-packed modules (left in Figure 1.19a). Liquid reservoirs of $\text{Cu}(\text{NO}_3)_2 \cdot 3\text{H}_2\text{O}$ (12 g) in DI water (120 mL) and of H_3TBC (0.583 g) in ethanol (90 mL) and DI water (27 mL) were then alternately flowed through the module with fibers to generate (Zn,Cu)HDS intermediates and subsequently form sorbent fibers with high HKUST-1 loading (right in Figure 1.19a and Figure 1.19b).

The MOF-loaded porous polymer sorbents inside the sealed Swagelok module (Figure 1.19 c) was all prepared in dry conditions with minimal handling processes, so that even water-sensitive MOFs can preserve their adsorptive performance during the gas separation processes.

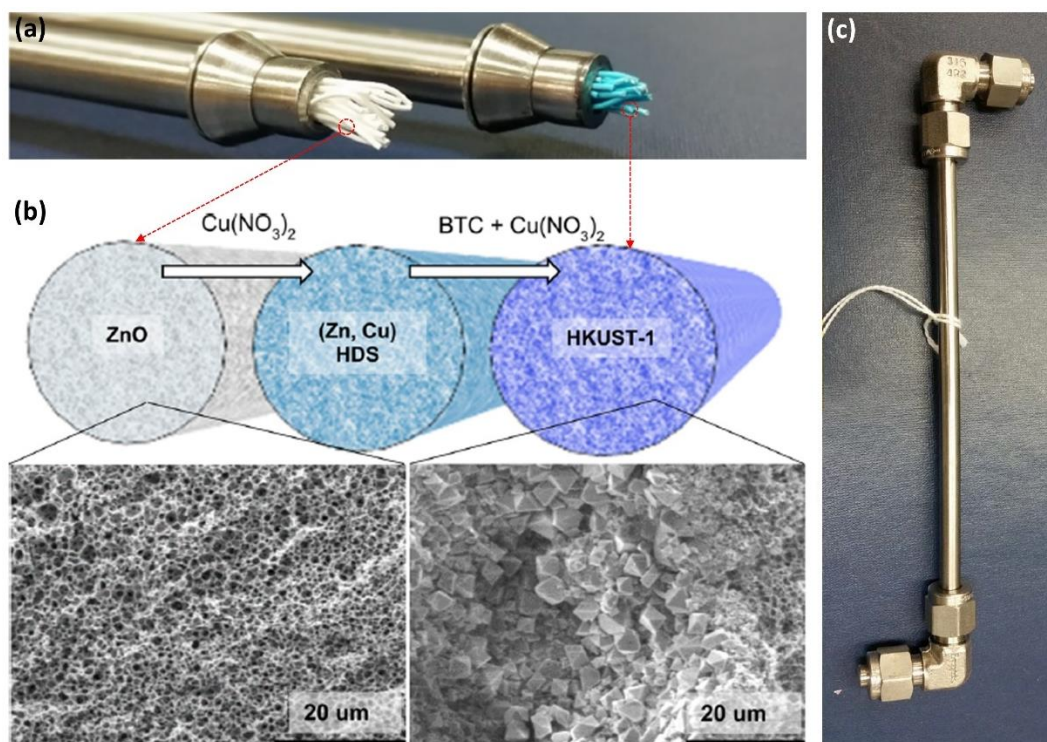


Figure 1.19. (a) Optical image of ZnO-loaded fiber sorbent bundles (left) and the postsynthesis MOF-loaded fiber sorbent bundles (right) in the Swagelok stainless tube. (b) (Top) Synthesis of MOF materials within ZnO-loaded fiber sorbent materials. (Bottom) SEM images of the green ZnO-loaded fiber sorbents (left) and the postsynthesis MOF-loaded fiber sorbent (right). (c) Image of the sealed Swagelok® module used to house, transport, and test the fibers. The gas-tight connections maintain an inert atmosphere and protect the fibers from humid degradation. All connections are 1/4" 316 SS fittings. (figure arrangement adapted from Ref.⁴¹)

1.5. References

- (1) Li, H.; Eddaoudi, M.; O’Keeffe, M.; Yaghi, O. M. Design and Synthesis of an Exceptionally Stable and Highly Porous Metal–Organic Framework. *Nature* **1999**, *402*, 276.
- (2) Patterson, J. P.; Abellan, P.; Denny, M. S.; Park, C.; Browning, N. D.; Cohen, S. M.; Evans, J. E.; Gianneschi, N. C. Observing the Growth of Metal–Organic Frameworks by in Situ Liquid Cell Transmission Electron Microscopy. *J. Am. Chem. Soc.* **2015**, *137*, 7322–7328.
- (3) Moghadam, P. Z.; Li, A.; Wiggin, S. B.; Tao, A.; Maloney, A. G. P.; Wood, P. A.; Ward, S. C.; Fairen-Jimenez, D. Development of a Cambridge Structural Database Subset: A Collection of Metal–Organic Frameworks for Past, Present, and Future. *Chem. Mater.* **2017**, *29*, 2618–2625.
- (4) Halder, G. J.; Kepert, C. J. In Situ Single-Crystal X-Ray Diffraction Studies of Desorption and Sorption in a Flexible Nanoporous Molecular Framework Material. *J. Am. Chem. Soc.* **2005**, *127*, 7891–7900.
- (5) Farha, O. K.; Eryazici, I.; Jeong, N. C.; Hauser, B. G.; Wilmer, C. E.; Sarjeant, A. A.; Snurr, R. Q.; Nguyen, S. T.; Yazaydin, A. Ö.; Hupp, J. T. Metal–Organic Framework Materials with Ultrahigh Surface Areas: Is the Sky the Limit? *J. Am. Chem. Soc.* **2012**, *134*, 15016–15021.
- (6) Eddaoudi, M.; Kim, J.; Rosi, N.; Vodak, D.; Wachter, J.; O’Keeffe, M.; Yaghi, O. M. Systematic Design of Pore Size and Functionality in Isoreticular MOFs and Their Application in Methane Storage. *Science* (80-.). **2002**, *295*, 469 LP-472.
- (7) Luz, I.; Soukri, M.; Lail, M. Flying MOFs: Polyamine-Containing Fluidized MOF/SiO₂

- Hybrid Materials for CO₂ Capture from Post-Combustion Flue Gas. *Chem. Sci.* **2018**, *9*, 4589–4599.
- (8) Allendorf, M. D.; Bauer, C. A.; Bhakta, R. K.; Houk, R. J. T. Luminescent Metal–organic Frameworks. *Chem. Soc. Rev.* **2009**, *38*, 1330–1352.
- (9) Lee, J.; Farha, O. K.; Roberts, J.; Scheidt, K. A.; Nguyen, S. T.; Hupp, J. T. Metal–Organic Framework Materials as Catalysts. *Chem. Soc. Rev.* **2009**, *38*, 1450–1459.
- (10) Faust, T. MOFs Deliver. *Nat. Chem.* **2015**, *7*, 270.
- (11) Mondloch, J. E.; Katz, M. J.; Isley III, W. C.; Ghosh, P.; Liao, P.; Bury, W.; Wagner, G. W.; Hall, M. G.; DeCoste, J. B.; Peterson, G. W.; et al. Destruction of Chemical Warfare Agents Using Metal–organic Frameworks. *Nat. Mater.* **2015**, *14*, 512.
- (12) Zacher, D.; Shekhah, O.; Wöll, C.; Fischer, R. A. Thin Films of Metal–organic Frameworks. *Chem. Soc. Rev.* **2009**, *38*, 1418–1429.
- (13) Shekhah, O.; Liu, J.; Fischer, R. A.; Wöll, C. MOF Thin Films: Existing and Future Applications. *Chem. Soc. Rev.* **2011**, *40*, 1081–1106.
- (14) Zhang, Y.; Yuan, S.; Feng, X.; Li, H.; Zhou, J.; Wang, B. Preparation of Nanofibrous Metal–Organic Framework Filters for Efficient Air Pollution Control. *J. Am. Chem. Soc.* **2016**, *138*, 5785–5788.
- (15) Zhao, J.; Gong, B.; Nunn, W. T.; Lemaire, P. C.; Stevens, E. C.; Sidi, F. I.; Williams, P. S.; Oldham, C. J.; Walls, H. J.; Shepherd, S. D.; et al. Conformal and Highly Adsorptive Metal–organic Framework Thin Films via Layer-by-Layer Growth on ALD-Coated Fiber Mats. *J. Mater. Chem. A* **2015**, *3*, 1458–1464.
- (16) Decoste, J. B.; Peterson, G. W. Metal–Organic Frameworks for Air Purification of Toxic Chemicals. *Chem. Rev.* **2014**, *114*, 5695–5727.

- (17) Bobbitt, N. S.; Mendonca, M. L.; Howarth, A. J.; Islamoglu, T.; Hupp, J. T.; Farha, O. K.; Snurr, R. Q. Metal–organic Frameworks for the Removal of Toxic Industrial Chemicals and Chemical Warfare Agents. *Chem. Soc. Rev.* **2017**, *46*, 3357–3385.
- (18) Soares, C. V.; Leitão, A. A.; Maurin, G. Computational Evaluation of the Chemical Warfare Agents Capture Performances of Robust MOFs. *Microporous Mesoporous Mater.* **2019**, *280*, 97–104.
- (19) Hermes, S.; Schröder, F.; Chelmoski, R.; Wöll, C.; Fischer, R. A. Selective Nucleation and Growth of Metal–Organic Open Framework Thin Films on Patterned COOH/CF₃-Terminated Self-Assembled Monolayers on Au(111). *J. Am. Chem. Soc.* **2005**, *127*, 13744–13745.
- (20) Hermes, S.; Zacher, D.; Baunemann, A.; Wöll, C.; Fischer, R. A. Selective Growth and MOCVD Loading of Small Single Crystals of MOF-5 at Alumina and Silica Surfaces Modified with Organic Self-Assembled Monolayers. *Chem. Mater.* **2007**, *19*, 2168–2173.
- (21) Zacher, D.; Baunemann, A.; Hermes, S.; Fischer, R. A. Deposition of Microcrystalline [Cu₃(Btc)₂] and [Zn₂(Bdc)₂(Dabco)] at Alumina and Silica Surfaces Modified with Patterned Self Assembled Organic Monolayers: Evidence of Surface Selective and Oriented Growth. *J. Mater. Chem.* **2007**, *17*, 2785–2792.
- (22) Küsgens, P.; Siegle, S.; Kaskel, S. Crystal Growth of the Metal—Organic Framework Cu₃(BTC)₂ on the Surface of Pulp Fibers. *Adv. Eng. Mater.* **2009**, *11*, 93–95.
- (23) Centrone, A.; Yang, Y.; Speakman, S.; Bromberg, L.; Rutledge, G. C.; Hatton, T. A. Growth of Metal–Organic Frameworks on Polymer Surfaces. *J. Am. Chem. Soc.* **2010**, *132*, 15687–15691.
- (24) Wu, Y.; Li, F.; Liu, H.; Zhu, W.; Teng, M.; Jiang, Y.; Li, W.; Xu, D.; He, D.; Hannam, P.;

- et al. Electrospun Fibrous Mats as Skeletons to Produce Free-Standing MOF Membranes. *J. Mater. Chem.* **2012**, *22*, 16971–16978.
- (25) Jin, Y.; Yang, D.; Kang, D.; Jiang, X. Fabrication of Necklace-like Structures via Electrospinning. *Langmuir* **2010**, *26*, 1186–1190.
- (26) Lu, A. X.; Ploskonka, A. M.; Tovar, T. M.; Peterson, G. W.; DeCoste, J. B. Direct Surface Growth Of UIO-66-NH₂ on Polyacrylonitrile Nanofibers for Efficient Toxic Chemical Removal. *Ind. Eng. Chem. Res.* **2017**, *56*, 14502–14506.
- (27) Ploskonka, A. M.; Marzen, S. E.; DeCoste, J. B. Facile Synthesis and Direct Activation of Zirconium Based Metal–Organic Frameworks from Acetone. *Ind. Eng. Chem. Res.* **2017**, *56*, 1478–1484.
- (28) Zhou, M.; Li, J.; Zhang, M.; Wang, H.; Lan, Y.; Wu, Y.; Li, F.; Li, G. A Polydopamine Layer as the Nucleation Center of MOF Deposition on “Inert” Polymer Surfaces to Fabricate Hierarchically Structured Porous Films. *Chem. Commun.* **2015**, *51*, 2706–2709.
- (29) George, S. M. Atomic Layer Deposition: An Overview. *Chem. Rev.* **2010**, *110*, 111–131.
- (30) Min, J.-H.; Chen, Y.-A.; Chen, I.-T.; Sun, T.; Lee, D. T.; Li, C.; Zhu, Y.; O’Connor, B. T.; Parsons, G. N.; Chang, C.-H. Conformal Physical Vapor Deposition Assisted by Atomic Layer Deposition and Its Application for Stretchable Conductors. *Adv. Mater. Interfaces* **2018**, *5*, 1801379.
- (31) Coclite, A. M.; Howden, R. M.; Borrelli, D. C.; Petruczuk, C. D.; Yang, R.; Yagüe, J. L.; Ugur, A.; Chen, N.; Lee, S.; Jo, W. J.; et al. 25th Anniversary Article: CVD Polymers: A New Paradigm for Surface Modification and Device Fabrication. *Adv. Mater.* **2013**, *25*, 5392–5423.
- (32) Brozena, A. H.; Oldham, C. J.; Parsons, G. N. Atomic Layer Deposition on Polymer

- Fibers and Fabrics for Multifunctional and Electronic Textiles. *J. Vac. Sci. Technol. A* **2015**, *34*, 10801.
- (33) Parsons, G. N.; Elam, J. W.; George, S. M.; Haukka, S.; Jeon, H.; (Erwin) Kessels, W. M. M.; Leskelä, M.; Poodt, P.; Ritala, M.; Rossnagel, S. M. History of Atomic Layer Deposition and Its Relationship with the American Vacuum Society. *J. Vac. Sci. Technol. A* **2013**, *31*, 50818.
- (34) Parsons, G. N.; Atanasov, S. E.; Dandley, E. C.; Devine, C. K.; Gong, B.; Jur, J. S.; Lee, K.; Oldham, C. J.; Peng, Q.; Spagnola, J. C.; et al. Mechanisms and Reactions during Atomic Layer Deposition on Polymers. *Coord. Chem. Rev.* **2013**, *257*, 3323–3331.
- (35) Zhao, J.; Losego, M. D.; Lemaire, P. C.; Williams, P. S.; Gong, B.; Atanasov, S. E.; Blevins, T. M.; Oldham, C. J.; Walls, H. J.; Shepherd, S. D.; et al. Highly Adsorptive, MOF-Functionalized Nonwoven Fiber Mats for Hazardous Gas Capture Enabled by Atomic Layer Deposition. *Adv. Mater. Interfaces* **2014**, *1*, 1400040.
- (36) Zhao, J.; Lee, D. T.; Yaga, R. W.; Hall, M. G.; Barton, H. F.; Woodward, I. R.; Oldham, C. J.; Walls, H. J.; Peterson, G. W.; Parsons, G. N. Ultra-Fast Degradation of Chemical Warfare Agents Using MOF – Nanofiber Kebabs *Angewandte. Angew. Chem. Int. Ed.* **2016**, *55*, 13224–13228.
- (37) Khaletskaya, K.; Turner, S.; Tu, M.; Wannapaiboon, S.; Schneemann, A.; Meyer, R.; Ludwig, A.; Van Tendeloo, G.; Fischer, R. A. Self-Directed Localization of ZIF-8 Thin Film Formation by Conversion of ZnO Nanolayers. *Adv. Funct. Mater.* **2014**, *24*, 4804–4811.
- (38) Bechelany, M.; Drobek, M.; Vallicari, C.; Abou Chaaya, A.; Julbe, A.; Miele, P. Highly Crystalline MOF-Based Materials Grown on Electrospun Nanofibers. *Nanoscale* **2015**, *7*,

5794–5802.

- (39) Zhao, J.; Nunn, W. T.; Lemaire, P. C.; Lin, Y.; Dickey, M. D.; Oldham, C. J.; Walls, H. J.; Peterson, G. W.; Losego, M. D.; Parsons, G. N. Facile Conversion of Hydroxy Double Salts to Metal–Organic Frameworks Using Metal Oxide Particles and Atomic Layer Deposition Thin-Film Templates. *J. Am. Chem. Soc.* **2015**, *137*, 13756–13759.
- (40) Meyn, M.; Beneke, K.; Lagaly, G. Anion-Exchange Reactions of Hydroxy Double Salts. *Inorg. Chem.* **1993**, *32*, 1209–1215.
- (41) Pimentel, B. R.; Fultz, A. W.; Presnell, K. V.; Lively, R. P. Synthesis of Water-Sensitive Metal-Organic Frameworks within Fiber Sorbent Modules. *Ind. Eng. Chem. Res.* **2017**, *56*, 5070–5077.

CHAPTER 2

UiO-66-NH₂ MOF Nucleation on TiO₂, ZnO, and Al₂O₃ ALD-treated Polymer Fibers: Role of Metal Oxide on MOF Growth and Catalytic Hydrolysis of Chemical Warfare Agent Simulants

CHAPTER 2 is a reprint of a manuscript published in *ACS Applied Materials & Interfaces*

Dennis T. Lee,[†] Junjie Zhao,[†] Christopher J. Oldham,[†] Gregory W. Peterson,[‡] and Gregory N. Parsons^{†,*}

[†]Department of Chemical & Biomolecular Engineering, North Carolina State University, 911 Partners Way, Raleigh, NC 27695, United States

[‡]Edgewood Chemical Biological Center, 5183 Blackhawk Road, Aberdeen Proving Ground, MD 21010, United States

2.1. Abstract

Metal-organic frameworks (MOFs) chemically bound to polymeric microfibrous textiles show promising performance for many future applications. In particular, Zr-based UiO-66-family MOF-textiles have been shown to catalytically degrade highly toxic chemical warfare agents (CWAs), where favorable MOF/polymer bonding and adhesion are attained by placing a nanoscale metal-oxide layer on the polymer fiber preceding MOF growth. To date, however, the nucleation mechanism of Zr-based MOFs on different metal oxides and how product performance is affected are not well understood. Herein, we provide new insight into how different inorganic nucleation films (i.e., Al_2O_3 , ZnO , or TiO_2) conformally coated on polypropylene (PP) nonwoven textiles via atomic layer deposition (ALD) influence the quality, overall surface area, and the fractional yield of UiO-66- NH_2 MOF crystals solvothermally grown on fiber substrates. Of the materials explored, we find that TiO_2 ALD layers lead to the most effective overall MOF/fiber adhesion, uniformity, and a rapid catalytic degradation rate for a CWA simulant, dimethyl p-nitrophenyl phosphate (DMNP) with $t_{1/2} = 15$ min, 580-fold faster than the catalytic performance of untreated PP textiles. Interestingly, compared to ALD TiO_2 and Al_2O_3 , ALD ZnO induces a larger MOF yield in solution and mass loading on PP fibrous mats. However, this larger MOF yield is ascribed to chemical instability of the ZnO layer under MOF formation condition, leading to Zn^{2+} ions that promote further homogeneous MOF growth. Insights presented here improve understanding of compatibility between active MOF materials and substrate surfaces which we believe will help advanced MOF composite materials for a variety of useful functions.

2.2. Introduction

Highly toxic compounds such as chemical warfare agents (CWAs) (e.g., sarin (GB), soman (GD), VX),¹⁻² chlorine gas,³⁻⁴ or common toxic pollutants like NO_x-based chemicals⁵ pose a significant health threat in tactical or emergency response, or in industrial environments. Current approaches to circumvent such threats include filters or respirators containing metal oxides⁶⁻⁷ or impregnated activated carbon-based materials.⁸ However, these display limited degradation of the toxic chemicals after prolonged environmental exposure. As a more general problem, oxide or carbon-based materials have limited ability to be chemically adjusted or “tuned” to improve reaction rates with toxic compounds.

In recent work, various solid materials with catalytic performance for destroying CWAs have been synthesized and demonstrated.⁹⁻¹⁴ In particular, highly crystalline and porous Zr-based metal-organic frameworks (MOFs) functionalized with amine groups show high catalytic performance in decontaminating CWAs and their simulants. Specifically, soman (GD), a nerve agent, was catalytically hydrolyzed with a half-life of less than 3.5 min, and under similar conditions, the simulant dimethyl p-nitrophenyl phosphate (DMNP) showed a half-life of ~1 min.^{9, 15-16} This outstanding performance is ascribed to the presence of Lewis acidic sites within the metal-containing Zr⁴⁺ centers¹⁷ acting synergistically with Brønsted base amino moieties¹⁵ in the organic linkers to adsorb and catalyze agent hydrolysis.

While MOF powders show very good performance, a key problem is that isolated powders are not ideal for hazard abatement in practical applications such as on the battlefield. More specifically, when physically adhered MOF particles to scarves or clothes are used in the real applications, the particles on the substrates tend to be not only aggregated, but also easily fall off from the substrates. This can diminish the MOF catalytic activity, and procedures to effectively

contain, transport and rapidly distribute powder materials under emergency conditions are not well defined. A desirable approach, therefore, is to covalently integrate and evenly distribute diverse types of MOFs onto polymeric textiles or fibrous mats that can be worn as protective clothing or readily deployed under imminent threat.¹⁸⁻²⁴

Previously, our group demonstrated that pretreating various polymer fiber substrates with thin conformal metal oxide coatings formed by atomic layer deposition (ALD) enables dense, uniform and conformal MOF crystal layers to form via hydrothermal synthesis on the fiber surfaces.²⁵ Several reports analyzed a range of ALD material coatings (i.e., Al₂O₃, ZnO, or TiO₂) as viable nucleation sites for growth of HKUST-1 (Cu-BTC) MOF crystals, and demonstrated that the metal oxide composition played a critical role in defining the initial MOF nucleation reaction.²⁶⁻²⁸ In other related work, UiO-type MOFs were also studied on fibrous nylon (PA-6) scaffolds pre-treated with ALD TiO₂, and these materials showed high rates for catalytic decomposition of CWAs and their related simulants.¹⁹ Specifically, the agent, soman (GD) and a CWA simulant, DMNP reacted with half-lives as short as 2.3 min and 7.3 min, respectively.¹⁹ Furthermore, we recently proved that ALD ZnO coating (vs Al₂O₃ and TiO₂) on PP polymeric fibrous mats can act as effective adhesion layers where presynthesized UiO-66-NH₂ crystals can self-assemble at ambient temperature.²⁴ These MOF-cloths also exhibited a fast catalytic degradation rate of DMNP with a half-life of less than 5 min.²⁴ However, MOF nucleation and growth mechanisms and how differently they are induced by ALD metal oxide composition have remained as an open question.

Therefore, in this work, we address the question of the role of ALD metal oxide composition as heterogeneous MOF nucleation sites for UiO-66-NH₂ MOF crystals on polypropylene fibers. We demonstrate that the starting metal oxide and substrate control both MOF

growth rates, the extent of MOF loading during growth, and the fractional yield of MOF film formation on fibers vs homogeneous MOF crystal formation. Furthermore, for the first time, we quantitatively analyze the quality of MOF on ALD surfaces as well as the extent of MOF loading in relation to the subsequent rate of DMNP simulant degradation kinetics.

2.3. Experimental Section

All reagents were purchased from commercial sources and used without further treatment. Tri-methyl aluminum (TMA, 98% STREM Chemicals, Inc.), titanium (IV) chloride (TiCl_4 , 99%, STREM Chemicals), diethylzinc (DEZ, 95% STREM Chemicals, Inc.), Zirconium(IV) chloride (ZrCl_4 , Alfa Aesar, $\geq 99.5\%$), 2-aminoterephthalic acid (2-ATA, Acros Organics, 99%), N,N-dimethylformamide (DMF, Fisher), deionized water, anhydrous ethanol (200 proof, VWR), N-ethylmorpholine (Sigma-Aldrich, $\geq 97\%$), and dimethyl p-nitrophenyl phosphate (DMNP, Sigma-Aldrich).

Polymeric fibrous scaffolds. Non-woven polypropylene (PP) micro-fibrous mats were used as received from Nonwovens Cooperative Research Center (NCRC), North Carolina State University.²⁹ The polymeric fibrous mats are 0.30 mm thick, with fiber diameter ranging from 0.6 μm to 9.0 μm .

Atomic layer deposition (ALD) on PP microfibers and on Si wafers. Non-woven polypropylene (PP) fibrous mats were conformally coated with inorganic Al_2O_3 , TiO_2 , and ZnO using a home built hot-wall viscous-flow atomic layer deposition reactor. The reactor design for the processes was described in previous work.²⁷ ALD deposition with the inorganic materials was conducted at 90 °C under ~1.8 Torr. The sequence times (in second) of x exposure/ N_2 purge/ H_2O exposure/ N_2 purge were 1/30/1/30 for Al_2O_3 , 1/40/1/40 for TiO_2 , and 2/60/2/60 for ZnO

deposition, where x is TMA, TiCl₄, and DEZ, respectively. These samples are referred to as PP@Al₂O₃, PP@TiO₂, and PP@ZnO, respectively.

Silicon wafers with thin native oxide (~2 nm) (Si@SiO₂) were also placed together with PP fibrous mats inside the reactor under the same ALD condition. PP mats were prepared with 200-, 300-, and 200 cycles of ALD Al₂O₃, TiO₂, and ZnO, respectively, on PP fibrous mats. Si wafer monitors were also used to measure thickness of the ALD coatings along with PP substrates. Around 20 nm of inorganic film on the Si@SiO₂ was confirmed from a J.A. Woollam alpha-spectroscopic ellipsometry (SE) ellipsometer at an incidence angle of 70°. These samples are referred to as Si@SiO₂@Al₂O₃, Si@SiO₂@TiO₂, and Si@SiO₂@ZnO, respectively.

Synthesis of UiO-66-NH₂ MOFs. 0.080 g (0.343 mmol) of ZrCl₄ was first loaded in 20 mL glass scintillation vial and dissolved in 20 mL of DMF via 1 min of sonication, followed by stirring the solution for 5 min. 0.062 g (0.343 mmol) of 2-ATA and 20 µL of deionized water were subsequently added to the prepared solution under stirring (~500 rpm). This as-prepared mixture was heated at 85 °C for 24 h in a box furnace (Thermo Scientific). The UiO-66-NH₂ MOF product was then collected by filtering out unreacted precursors, byproducts, and residual DMF through polypropylene membrane (0.45 µm pore size, Whatman). After that, the filtered solid was rinsed with 80 mL of DMF and 80 mL of anhydrous ethanol in a sequential manner in the filtration system. Eventually, the final solid was obtained via filtration and dried at room temperature at reduced pressure for 12 h. The fully dried MOF powder was stored in a desiccator until being used for further characterizations.

Synthesis of UiO-66-NH₂ MOF coatings on PP@ALD fibrous mats and Si@SiO₂@ALD substrates. Precursor solutions (20 mL) for each UiO-66-NH₂ MOF coating on PP@ALD fibrous mats and Si@SiO₂@ALD substrates were prepared using the same recipe depicted above for the

synthesis of UiO-66-NH₂ MOF powder. A free-standing PP fabric swatch (1" × 2") coated with ALD Al₂O₃, TiO₂, or ZnO was soaked in the as-prepared precursor solution in 20 mL scintillation vial. ALD coated Si@SiO₂ planar substrates (1" × 1") were also immersed in the as-prepared precursor solution in 20 mL scintillation vial. These vials with samples were placed in a box furnace (Thermo Scientific) and heated at 85 °C for 24 h. After the solvothermal synthesis procedure is finished, the MOF coated PP fibrous mats were transferred into a fine aluminum mesh and rinsed with 80 mL of DMF twice under magnetic stirring (~500 rpm) for 12 h. Subsequently, the MOF coated fibrous mats were further washed with 80 mL of anhydrous ethanol, and the solvent was replaced every 12 h for at least a total of three times. As for the MOF coated Si@SiO₂@ALD planar substrates, they were vigorously rinsed with anhydrous ethanol for 10 min. The finally obtained products were dried at room temperature at a reduced pressure for 12 h and stored in a desiccator until being used for further characterizations.

Stability tests of ALD ZnO layer on PP micro fibers in UiO-66-NH₂ precursor solutions.

PP polymeric fibrous mats (1" × 2") coated with ALD ZnO (PP@ZnO) were submerged in a DMF (20 mL) + DI water (25 µL) mixture, and then heated at 85 °C for 24 h. This experiment was carried out to identify stability of the ZnO layer in DMF solvent under the synthetic condition of MOF growth.

PP polymeric fibrous mats (1" × 2") coated with ALD ZnO (PP@ZnO) were submerged in a 2-ATA (0.062 g (0.343 mmol)) + DMF (20 mL) + DI water (25 µL) mixture, and then heated at 85 °C for 24 h. This experiment was conducted to figure out the effect of the organic linkers (i.e., 2-ATA) on stability of the ZnO layer under the synthetic environment of MOF growth.

PP polymeric fibrous mats (1" × 2") coated with ALD ZnO (PP@ZnO) were submerged in a ZrCl₄ (0.080 g (0.343 mmol)) + DMF (20 mL) + DI water (25 µL) mixture, and then heated at

85 °C for 24 h. This experiment was performed to examine the influence of the metal-containing precursors (i.e., $ZrCl_4$) on stability of the ZnO layer under the synthetic environment of MOF growth.

Catalytic hydrolysis reaction of dimethyl p-nitrophenyl phosphate (DMNP) using UiO-66-NH₂ powder. The catalytic hydrolysis reaction with as-synthesized UiO-66-NH₂ powder was carried out at room temperature.¹⁹ Three respective runs were conducted with varied amounts of UiO-66-NH₂ powder as catalysts (1) 2.6 mg (0.0015 mmol), 2) 4.0 mg (0.0023 mmol), and 3) 5.6 mg (0.0033 mmol)) added to an aqueous solution of *N*-ethylmorpholine (1 mL, 0.45 M) in a 1.5 mL Eppendorf micro-centrifuge tube at room temperature. The mixture was vigorously stirred (1100 rpm) for 30 min until well enough to disperse the UiO-66-NH₂ powder in the solution. DMNP (~6.2 mg (0.025 mmol)) was then added to the suspension. The final reaction solution was kept stirred at 1100 rpm. 20 μ L of aliquot was taken out of the reaction mixture and diluted with 10 mL aqueous solution of *N*-ethylmorpholine (0.45 M) to investigate the extent of reaction as a function of time. The progressive changes in absorbance intensity between 250 and 500 nm wavelength range during the hydrolysis reaction were monitored by a Thermo Scientific Evolution 300 UV/Vis spectrophotometer. We especially focused on tracing an alteration in an absorbance peak intensity at 407 nm corresponding to *p*-nitrophenoxide produced during the reaction.

Catalytic hydrolysis reaction of dimethyl p-nitrophenyl phosphate (DMNP) using UiO-66-NH₂ coated fabric or control samples. The catalytic hydrolysis reaction with UiO-66-NH₂ MOF coated fibrous mats or with control samples was similarly implemented as described in section 2.7 for the reaction with MOF powder. We tested the catalytic reaction with untreated PP, PP@ALD, and PP@ALD@MOF, where ALD is Al₂O₃, TiO₂, or ZnO. We kept consistency in the amount of all fabric samples (14 mg) added to the reaction solution. The fabric samples were cut

into several pieces to be well immersed in the reaction solution.²⁴ The way of monitoring the reaction progresses was carried out as explained above for the experiments with MOF powder.

Material Characterization. Scanning electron microscopic (SEM) and energy dispersive X-ray analysis (EDX) were carried out using an FEI Verios 460 L field emission SEM. A thin layer of Au-Pd (5~10 nm) was sputter-coated onto the prepared samples before SEM imaging. We microtomed the ALD coated PP microfibrinous mats to image cross section through a JEOL 2010F transmission electron microscope (TEM). X-ray diffraction (XRD) was conducted with a Rigaku SmartLab X-ray diffraction tool (Cu K α X-ray source) for crystalline phase analysis. UiO-66-NH₂ MOF powder diffraction pattern was simulated using Mercury 3.0 software and the crystallographic information file from Cambridge Crystallographic Data Centre (CCDC 837796 for UiO-66). A Quantachrome Autosorb-1C surface area and pore size analyzer was utilized for measuring N₂ adsorption-desorption isotherms at 77 K. The fabric-based samples were dried in vacuum ($\sim 1 \times 10^{-5}$ Torr) in BET instrument at room temperature for 1 h and at 110 °C for 24 h in a subsequent way before N₂ adsorption-desorption measurement. BET surface area was calculated on the basis of the N₂ adsorption data within a relative pressure range of $P/P_0 = 0.02 \sim 0.08$.³⁰⁻³¹ A Thermo Scientific Nicolet 6700 Fourier transform infrared spectrometer was used for analyzing MOF growth on IR silicon wafers coated with ALD metal oxides (i.e., Al₂O₃, TiO₂, or ZnO). A progressive change in absorbance intensity during the DMNP hydrolysis reaction was traced by a Thermo Scientific Evolution 300 UV/Vis spectrophotometer.

2.4. Results and Discussion

Scanning electron microscope and cross-sectional TEM images of PP fibers as-received, and after coating with ALD Al₂O₃, ZnO, or TiO₂ are shown in Figure 2.1. As-received PP fibers

were found to have a smooth surface, whereas after coating with the ALD metal oxides, the PP fibers showed a slightly roughened surface. From the cross-sectional TEM images, the ALD Al₂O₃ coating on PP fibers²⁷ revealed an abrupt interface between the polymer and the metal oxide with minimal subsurface growth, whereas the ALD ZnO and TiO₂ coating process both led to a graded polymer/inorganic layer. These results are consistent with previously quantified growth temperature- and precursor-dependent diffusion and sub-surface reaction during ALD on polypropylene and other polymers.²⁵ The surface roughness generated by ALD on polymers is also previously described and understood in terms of the propensity for ALD reactants to adsorb on the fiber surface vs diffuse into the polymer near-surface region.³²⁻³⁷ For all ALD-treated fiber materials studied here, the ALD conditions and coating thickness were defined such that the outer surface of the substrate was fully coated with the targeted metal oxide.

Figure 2.2 illustrates the procedure for creating UiO-66-NH₂ MOF thin films onto non-woven PP textiles. The ALD technique was used to conformally coat the inert PP microfibers with Al₂O₃, ZnO, or TiO₂ under conditions described in the experimental section. We expect the MOF crystal size and nucleation rate to depend upon the composition of the ALD metal oxide, thus providing flexibility and control to modulate the ultimate reactivity and performance for efficiently detoxifying CWA agents or simulants.

As demonstrated in SEM images shown in Figure 2.3, PP fibers that are pre-treated with ALD Al₂O₃, ZnO or TiO₂ lead to well-distributed and relatively dense UiO-66-NH₂ crystals, whereas fewer MOF crystals grow on PP without the ALD pre-treatment. In practice, the MOF crystals on the native untreated PP fibers are loosely entrapped within the fiber mat so that the powders easily fall off during common sample handling. SEM images at relatively low magnification (Figure 2.3a-d) further confirm that the extent of UiO-66-NH₂ growth on ALD

surface exceeds that on a bare PP, particularly for the ALD ZnO and TiO₂. The XRD patterns in Figure 2.4 show main characteristic peaks (7.45° and 8.6° 2θ) of UiO-66-NH₂ on all ALD surfaces, matching the spectra collected from powder UiO-66-NH₂. Interestingly, for the PP coated with ZnO, three distinct XRD peaks associated with wurtzite hexagonal ZnO phase (31.7°, 34.4°, and 36.2° 2θ) are present after ALD, but disappear after solvothermal growth of UiO-66-NH₂. Furthermore, a new finding from this work found the MOF/fiber assemblage created using ZnO-coated PP microfibers was markedly different from those with ALD Al₂O₃ or TiO₂. Specifically, the ZnO-coated substrate generated MOF crystals within the spaces and voids of the fiber mesh, whereas the TiO₂ coating formed dense MOF crystals uniformly dispersed and attached to the fibers. Thus, we speculate that the ALD ZnO layer may dissolve into the UiO-66-NH₂ solvothermal synthesis solution, leading to Zn²⁺ ions in solution that promote homogeneous MOF crystallization near and within the fiber mesh, facilitating entrapment and physisorption of MOF crystals within the fabric and on the fiber surface.

The N₂ adsorption-desorption isotherms (Figure S2.1a) were measured to confirm the quality of MOF crystals grown on PP@ALD surfaces. Both PP@ALD@UiO-66-NH₂ and UiO-66-NH₂ powders plateau out in N₂ uptake at a low relative pressure range (i.e., P/P₀ = 0.02-0.80) without detectable hysteresis, indicative of the expected physical structure provided by microporous MOF. The rapid increase in N₂ uptake at high relative pressures (i.e., P/P₀ > 0.90) is probably due to the presence of nonporous or macroporous gaps between fibers or MOF crystals within the structure. Without the MOF coating, the ALD-treated PP fibers show a Brunauer-Emmett-Teller (BET) surface area of only 1-2 m²/g consistent with N₂ adsorption only on the external fiber surface. The BET surface area after UiO-66-NH₂ coating on PP@ALD (Figure S2.1b) shows that the ALD ZnO treatment produces the largest N₂ gas physisorption capacity,

consistent with corresponding SEM images (Figure 2.3) and XRD analysis (Figure 2.4). For the ZnO case, some of the MOF crystals between fibers may be poorly adhered, but significant MOF shedding was not observed during routine laboratory handling.

To determine the total MOF mass on the fibers, we found that solvent and water absorption in the fibers during handling and MOF growth led to significant uncertainties in physical mass measurements. Therefore, following previous methodology,³⁸ the total MOF mass was determined from the BET surface area of the MOF/fiber samples normalized to that of the free MOF powder (Table 2.1). As expected from the SEM and XRD results, the PP@ZnO@MOF showed the largest MOF mass fraction (~15 wt%), compared to ~3.5 and ~7 wt% for the PP@Al₂O₃@MOF and PP@TiO₂@MOF samples, respectively. The nonwoven polypropylene fiber mats have a starting mass of approximately 40 grams per square meter (gsm).³⁶ Therefore, MOF mass fraction values of ~15, 3.5 and 7 wt% correspond to a MOF mass of ~7, 1.5 and 3 g_{MOF}/m²_{swatch} for the MOF/fiber composites created here.

To explore the role of the ALD metal oxide more fully, we used Fourier transform infrared (FTIR) spectroscopy to analyze the reaction during MOF growth on ALD Al₂O₃, ZnO and TiO₂ on silicon wafers, and results are shown in Figure 2.5a. For this experiment, first we collected IR transmission spectra for blanket ALD films on silicon. The samples were then subjected to MOF solvothermal growth under the same conditions used for the fiber samples. The samples were then analyzed again by IR. Results in Figure 2.5a show the spectra associated with each starting ALD metal oxide, as well as spectra collected after MOF growth. For the MOF spectra, the Si@SiO₂+ALD data are subtracted as background. The ALD coatings display absorbance peaks near 600 cm⁻¹ for Al₂O₃ and ~400 cm⁻¹ for ZnO and TiO₂, respectively. After UiO-66-NH₂ growth, we observe characteristic vibrational modes from the amine-functionalized MOF linkers

including: $\nu_{\text{asym}}[\text{COO}^-]$ (1570 cm^{-1}), $\nu_{\text{sym}}[\text{COO}^-]$ (1390 cm^{-1} and 1430 cm^{-1}), $\nu_{\text{asym}}[\text{NH}_2]$ (3515 cm^{-1}), $\nu_{\text{sym}}[\text{NH}_2]$ (3390 cm^{-1}), and $\nu[\text{C-N}]$ (1260 cm^{-1}). A range of Zr-OH stretching modes (from the MOF $\text{Zr}_6\text{O}_4(\text{OH})_4$ nodes) are seen centered near 3650 cm^{-1} .³⁹ These MOF modes are readily observed on the samples which started with ALD Al_2O_3 or TiO_2 , but are notably absent for the ZnO samples. Also, remarkably, the ZnO sample shows a negative-going feature near 400 cm^{-1} after MOF synthesis, demonstrating dissolution of the ZnO thin film. The disappearance of the ZnO during MOF growth is also consistent with the XRD data shown in Figure 2.4. Also, consistent with ZnO dissolution, the ZnO-coated samples tend to produce more extensive homogeneous MOF crystal growth compared to Al_2O_3 and TiO_2 . As for the samples we tested, no strong vibration modes of C=O of DMF (1660 cm^{-1}) were not observed, indicating that the activation processes we conducted were enough to exchange and remove DMF out of the MOF structures.⁴⁰

XRD patterns and digital photographs of silicon wafer samples after ALD and MOF solvothermal synthesis are shown in Figure 2.5b and c, respectively, revealing that UiO-66-NH₂ crystals are adhered to the surface of Al_2O_3 - or TiO_2 -coated silicon wafer, whereas the original ALD ZnO-treated silicon appears to have no MOF crystals. These findings suggest the more basic ZnO tends to dissolve during UiO-66-NH₂ solvothermal synthesis.

To further understand the mechanisms of the ALD ZnO layer on PP during MOF synthesis, we performed a series of stability experiments. Control substrates of PP@ZnO fibrous mats were prepared and immersed in various MOF synthesis solutions at $85 \text{ }^\circ\text{C}$ for 24 h, as described in detail in the experimental section. SEM images (Figure S2.2), and mass changes and XRD data (Figure S2.3) were analyzed to study the mechanism. From the mass and images collected, we find that ALD ZnO layer on PP microfibers is vulnerable under acidic conditions present during exposure

to either 2-ATA or $ZrCl_4$. The 2-ATA organic linkers react with ZnO to form surface-bound non-crystalline salts. On the other hand, $ZrCl_4$ reagents completely dissolve the ZnO layer, leaving only uncoated PP microfibers. We conclude that acidic HCl produced by $ZrCl_4$ in DMF + DI water at 85 °C readily etches the ZnO layer on the PP microfibers.⁴¹ These results are further supported by energy-dispersive X-ray spectroscopy (EDS) mapping of the material (Figure S2.4).

To probe the catalytic efficacy of MOF-microfiber composite materials, we investigated the rate of DMNP hydrolysis in contact with the coated fibers (Figure 2.6a). Starting with an aqueous solution of DMNP with N-ethylmorpholine buffer (0.45 M, pH 10), we added 2.6 mg of MOF powders and 14 mg of either untreated PP or PP@ALD@MOF composite materials, and determined the rate of DMNP hydrolysis by periodically measuring the absorbance at 407 nm corresponding to the p-nitrophenoxide reaction product. The absorbance data and corresponding fractional conversion are plotted in Figure 2.6b and c, respectively. For the MOF powder, we observed 100% conversion after approximately 60 min, with a half-life ($t_{1/2}$) of ~4.8 min. This value is similar, but slightly slower than reported previously.¹⁹ The previous report used MOFs with a higher surface area (1334 m²/g vs 956 ± 81 m²/g used here) consistent with a higher density of active missing linker sites.¹⁹ After reacting for 60 minutes, DMNP conversion was 21%, 83%, and 94% for PP@Al₂O₃@MOF, PP@TiO₂@MOF, and PP@ZnO@MOF, respectively, and the corresponding $t_{1/2}$ values (Table 2.1) were PP@Al₂O₃@MOF: 78 min; PP@TiO₂@MOF: 15 min; and PP@ZnO@MOF: 10 min. The fastest degradation kinetics was observed for PP@ZnO@MOF, consistent with these materials exhibiting the highest MOF loading (Figure S2.1b). The comprehensive analyses of the above reaction kinetics are presented in Figure S2.5. As a control, the untreated PP shows DMNP hydrolysis with $t_{1/2}$ exceeding 6 days. Previous results from our lab (Figure S2.6) show that the ALD layers (without MOF present) can also promote

DMNP hydrolysis, but with very slow kinetics ($t_{1/2} = 77, 40, \text{ and } 20$ hours for $\text{Al}_2\text{O}_3, \text{TiO}_2, \text{ and } \text{ZnO}$, respectively).^{19, 24} Generally, we find that the rate of degradation correlates with the extent of MOF mass loading, which is influenced by the composition of the ALD metal oxide nucleation layer. In addition to characterizing the effect of metal oxide nucleation layer on subsequent MOF growth, we are interested in understanding any quantitative differences in the catalytic performance of the surface-bound MOFs relative to similarly prepared powders. To determine the fraction of “catalytically active” MOF on the fibers relative to the total mass of surface-bound MOF, we first analyzed the rate of DMNP hydrolysis using various amounts of UiO-66-NH₂ powder. Following the reaction scheme in Figure 2.7, the rate data (Figure S2.7) was fit to a pseudo-first-order rate expression (Figure S2.8 and Table S2.1) yielding an apparent rate constant for the hydrolysis reaction, $k_{\text{app,powder}} = 93 \pm 1.7 \text{ M}^{-1}\text{min}^{-1}$. Using this value, the mass of the “catalytically active” MOF on the fibers can be estimated by fitting the observed degradation rate data for the MOF/fiber composites. Comparing the “active” MOF mass to the total MOF mass, we find the PP@ZnO@MOF samples, both show ~15 wt%. The Al_2O_3 and TiO_2 coated fibers also show reasonable agreement, with “active” vs total of 2.1 vs 3.5 wt% and 9.3 vs 7 wt%. for the PP@ Al_2O_3 @MOF and PP@ TiO_2 @MOF samples, respectively. These results suggest that the PP@ TiO_2 provides a surface that is more favorable for growth of high-quality UiO-66-NH₂ MOFs that readily adhere to the oxide surface compared to PP@ZnO and PP@ Al_2O_3 .

As a final analysis (Figure S2.9), we also examined the fractional yield of MOF crystals on the fiber surfaces relative to the starting solution molar precursor concentration. We find that PP@ZnO fiber presents the highest MOF growth yield on the surface (9.6%) compared to 1.6% for PP@ Al_2O_3 and 3.8% for PP@ TiO_2 surface (Table S2). This result coincides well with the trend

of other analyses observed from SEM, XRD, FTIR, and BET and calculated from DMNP degradation.

In addition, we find that the presence of the ZnO appears to produce a catalytic enhancement to the overall MOF yield. Specifically, in the presence of PP@ZnO fabric, the overall MOF yield (MOF on fabric + MOF powder) is measured to be ~47%. However, without the ZnO the yield is slightly smaller, ~43% (Table S2). This yield calculation further supports our reasoning that Zn^{2+} ions dissolved from ZnO layer can function as additional nucleation sites, promoting extensive homogeneous MOF growth near and within the fiber networks.

2.5. Conclusions

We quantitatively compared ALD metal oxide surfaces including Al_2O_3 , ZnO, and TiO_2 on polypropylene textiles as starting surfaces for heterogeneous nucleation of UiO-66- NH_2 MOF as catalysts for hydrolysis of DMNP, as chemical warfare agent simulant. Compared to ALD ZnO and Al_2O_3 , the TiO_2 layers led to more uniform MOF coating with highest overall MOF loading and net surface area ($\text{m}^2/\text{g}_{(\text{MOF}+\text{Fiber})}$). We confirmed the MOFs on TiO_2 treated polypropylene catalyzed the DMNP hydrolysis with $t_{1/2} = 15$ min, comparable to previous results and appreciably faster than PP fibrous mats with only the ALD coating. The Al_2O_3 coated PP performed nearly the same as TiO_2 in MOF nucleation and growth, but the ALD ZnO was unstable under MOF solvothermal synthesis conditions, resulting in ZnO dissolution and more favorable homogeneous MOF nucleation, likely promoted by the presence of Zn^{2+} ions in solution. Faster homogeneous nucleation led to more MOF crystals entrapped within the fiber mat, and an overall net larger mass loading. While the larger MOF loading increased the net rate of DMNP degradation ($t_{1/2} = 10$ min), we find the entrapped crystals are less robust under mechanical handling, and therefore likely less

desirable than covalently-bound crystals obtained on the TiO₂ surface. Further work is needed to specifically identify the likely nucleation sites and reactive species that enable favorable MOF nucleation on metal oxide or other growth surfaces.

2.6. Figures

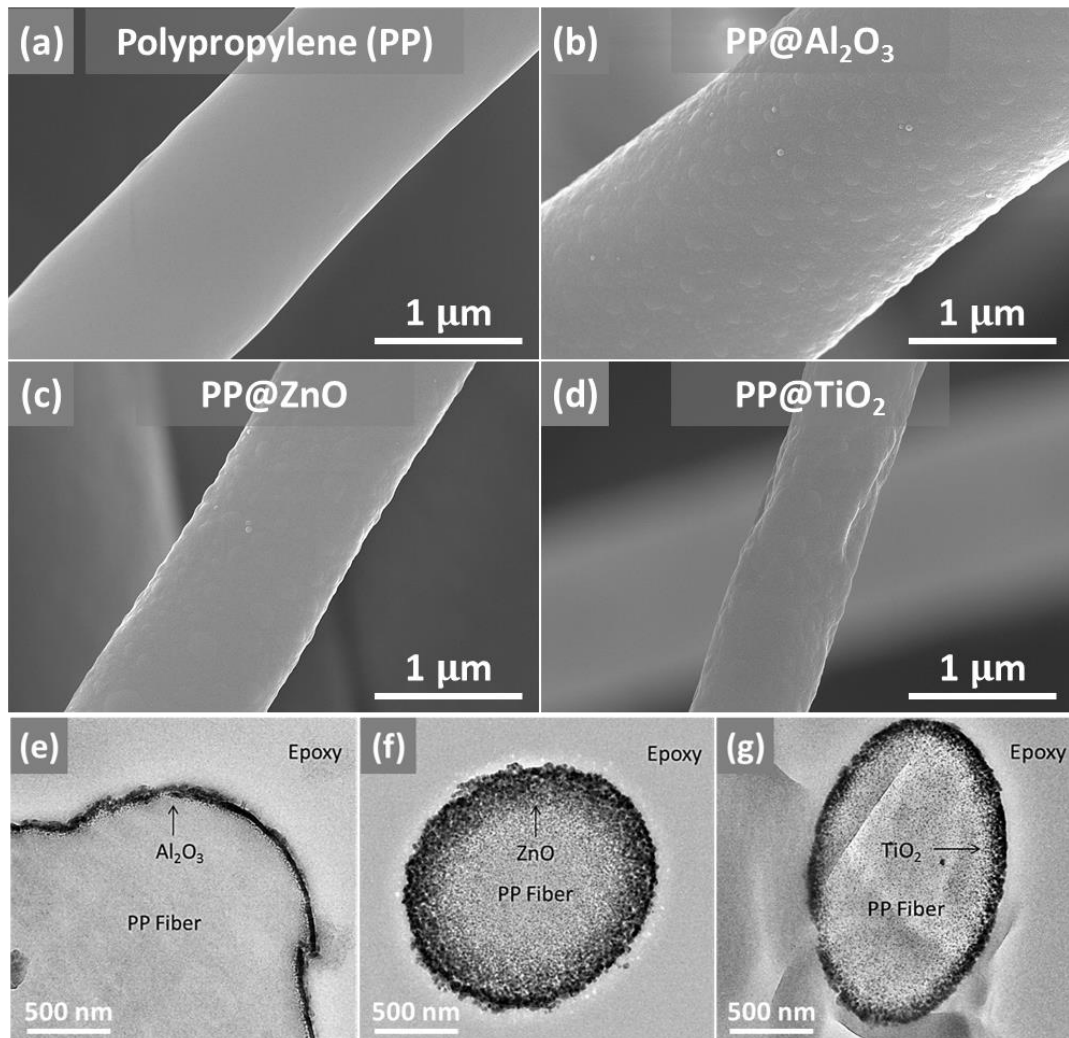


Figure 2.1. SEM images of (a) a bare polypropylene (PP) and ALD-treated PP: (b) PP@Al₂O₃, (c) PP@ZnO, and (d) PP@TiO₂. Cross-sectional TEM images of (e) PP@Al₂O₃, (f) PP@ZnO, and (g) PP@TiO₂ microfibers.

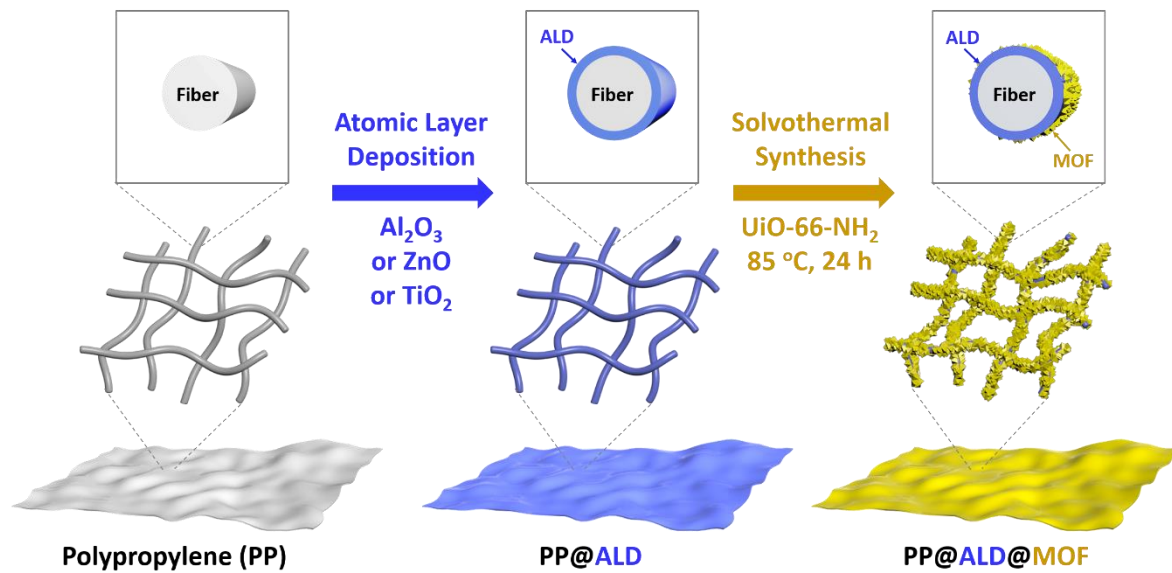


Figure 2.2. Synthetic procedure for integrating UiO-66-NH₂ MOF onto ALD-treated polymeric fibrous scaffolds.

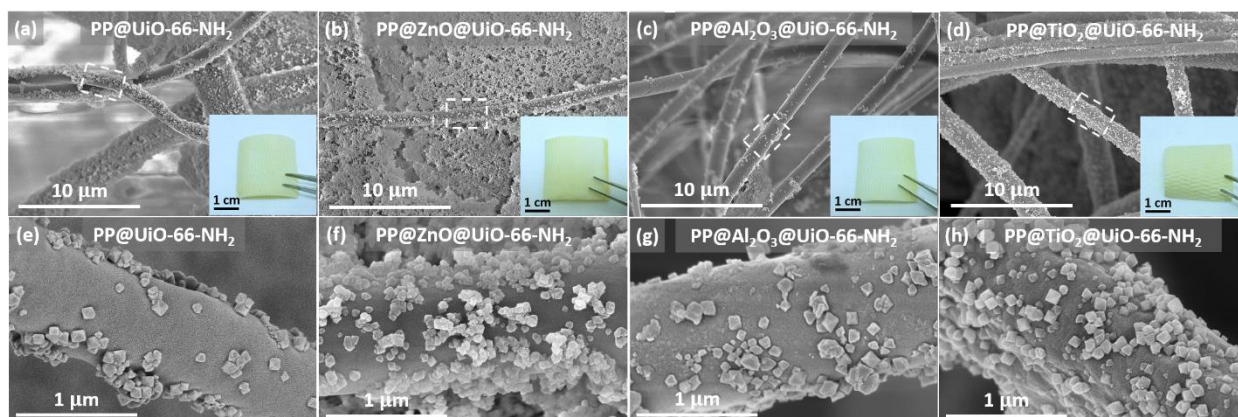


Figure 2.3. SEM images of UiO-66-NH₂ crystals solvothermally grown on (a, e) PP, (b, f) PP@ZnO, (c, g) PP@Al₂O₃, and (d, h) PP@TiO₂ microfibers. Insets in (a-d) are optical photographs of corresponding actual samples.

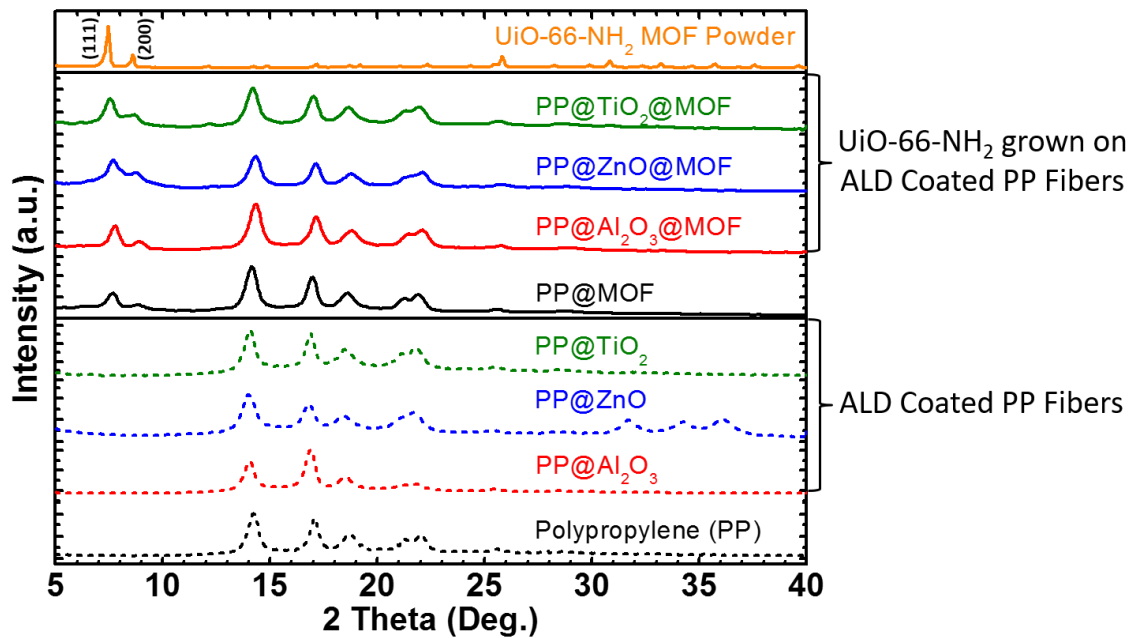


Figure 2.4. XRD patterns of untreated PP, PP@ALD, UiO-66-NH₂ MOF coated PP or PP@ALD, and UiO-66-NH₂ MOF powder.

Table 2.1. Fiber-Based Material Properties, Calculated “Active” MOF Fraction, and Catalytic Performance toward a CWA Simulant, DMNP

	BET surface area (m ² /g)	slope (min ⁻¹)	$k_{\text{app,powder}}^a$ (M ⁻¹ min ⁻¹)	calculated active m _{MOF} (mg)	calculated active MOF wt %	measured ^b MOF wt %	DMNP $t_{1/2}$ (min)	TOF (s ⁻¹)
PP@ZnO@UiO-66-NH ₂	145	0.0696	93 ± 1.7 ^a	1.9	13.6	15.1 ± 1.3	10	0.019
PP@TiO ₂ @UiO-66-NH ₂	65	0.0465	93 ± 1.7 ^a	1.3	9.3	6.8 ± 0.6	15	0.018
PP@Al ₂ O ₃ @UiO-66-NH ₂	34	0.0089	93 ± 1.7 ^a	0.3	2.1	3.5 ± 0.3	78	0.015
PP@ZnO	1–2	5.87 × 10 ⁻⁴		0	0	0	1181	
PP@TiO ₂	1–2	2.88 × 10 ⁻⁴		0	0	0	2407	
PP@Al ₂ O ₃	1–2	1.50 × 10 ⁻⁴		0	0	0	4621	
PP (polypropylene)	1–2	7.98 × 10 ⁻⁵		0	0	0	8687	

^a93 ± 1.7 M⁻¹·min⁻¹ of a reaction constant ($k_{\text{app, powder}}$) is an average value from k_{app} values in Table S1. This value was used to estimate “calculated active” MOF wt % on PP@ALD@UiO-66-NH₂ fabric samples. ^b“Measured” MOF wt % was estimated based on BET surface area of MOF powder (956 ± 81 m²/g) collected from liquid phase after a solvothermal synthesis at 85 °C for 24 h. Turn over frequency (TOF) was calculated per Zr₆ cluster at $t_{1/2}$.

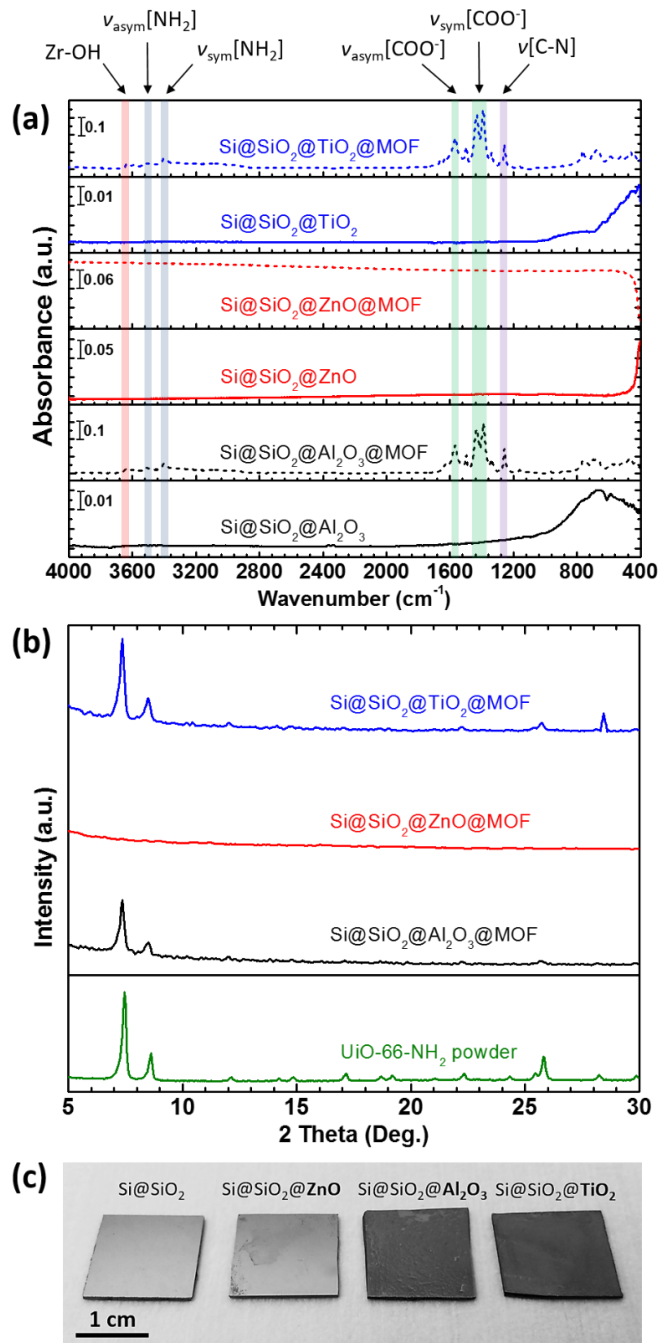


Figure 2.5. (a) FTIR spectra captured in differential mode, (b) XRD patterns of UiO-66-NH₂ grown on ALD-coated silicon wafer pieces (Si@SiO₂), and (c) optical photographs of samples after the solvothermal reaction for MOF integration. The dark coating corresponds to visible UiO-66-NH₂ MOF film growth.

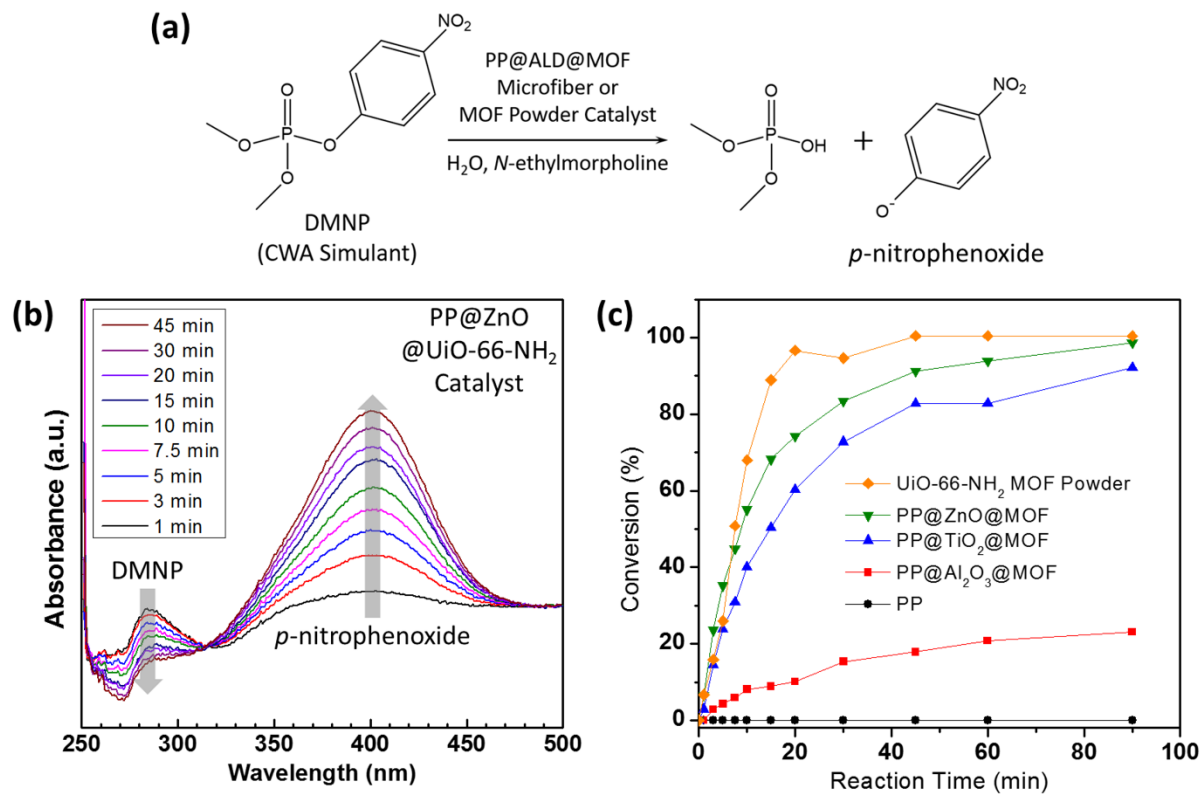


Figure 2.6. (a) Catalytic destruction of DMNP using MOF powder or PP@ALD@MOF microfibers. (b) UV-vis trace of the hydrolysis of DMNP as a function of reaction time using PP@ZnO@UiO-66-NH₂ as a catalyst. (c) Conversion profiles of DMNP to *p*-nitrophenoxide versus reaction time using PP, PP@ALD@MOF, or UiO-66-NH₂ MOF powder.

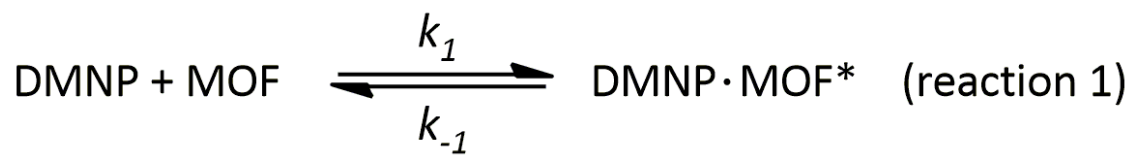


Figure 2.7. Equations for the hydrolysis of DMNP catalyzed by MOF into the nontoxic products.

2.7. References

- (1) Mondloch, J. E.; Katz, M. J.; Isley Iii, W. C.; Ghosh, P.; Liao, P.; Bury, W.; Wagner, G. W.; Hall, M. G.; DeCoste, J. B.; Peterson, G. W.; Snurr, R. Q.; Cramer, C. J.; Hupp, J. T.; Farha, O. K., Destruction of chemical warfare agents using metal–organic frameworks. *Nat. Mater.* **2015**, *14*, 512-516.
- (2) Gil-San-Millan, R.; López-Maya, E.; Hall, M.; Padial, N. M.; Peterson, G. W.; DeCoste, J. B.; Rodríguez-Albelo, L. M.; Oltra, J. E.; Barea, E.; Navarro, J. A. R., Chemical Warfare Agents Detoxification Properties of Zirconium Metal–Organic Frameworks by Synergistic Incorporation of Nucleophilic and Basic Sites. *ACS Applied Materials & Interfaces* **2017**, *9*, 23967-23973.
- (3) DeCoste, J. B.; Browe, M. A.; Wagner, G. W.; Rossin, J. A.; Peterson, G. W., Removal of chlorine gas by an amine functionalized metal-organic framework via electrophilic aromatic substitution. *Chem. Commun.* **2015**, *51*, 12474-12477.
- (4) Peterson, G. W.; DeCoste, J. B.; Fatollahi-Fard, F.; Britt, D. K., Engineering UiO-66-NH₂ for Toxic Gas Removal. *Ind. Eng. Chem. Res.* **2014**, *53*, 701-707.
- (5) Peterson, G. W.; Mahle, J. J.; DeCoste, J. B.; Gordon, W. O.; Rossin, J. A., Extraordinary NO₂ Removal by the Metal–Organic Framework UiO-66-NH₂. *Angew. Chem. Int. Ed.* **2016**, *55*, 6235-6238.
- (6) Smith, J. W. H.; Westreich, P.; Smith, A. J.; Fortier, H.; Croll, L. M.; Reynolds, J. H.; Dahn, J. R., Investigation of copper oxide impregnants prepared from various precursors for respirator carbons. *J. Colloid Interface Sci.* **2010**, *341*, 162-170.

- (7) Monge, M. E.; D'Anna, B.; George, C., Nitrogen dioxide removal and nitrous acid formation on titanium oxide surfaces-an air quality remediation process? *Phys. Chem. Chem. Phys.* **2010**, *12*, 8991-8998.
- (8) Rossin, J.; Petersen, E.; Tevault, D.; Lamontagne, R.; Isaacson, L., Effects of environmental weathering on the properties of ASC-whetlerite. *Carbon* **1991**, *29*, 197-205.
- (9) Peterson, G. W.; Moon, S.-Y.; Wagner, G. W.; Hall, M. G.; DeCoste, J. B.; Hupp, J. T.; Farha, O. K., Tailoring the Pore Size and Functionality of UiO-Type Metal–Organic Frameworks for Optimal Nerve Agent Destruction. *Inorg. Chem.* **2015**, *54*, 9684-9686.
- (10) Katz, M. J.; Mondloch, J. E.; Totten, R. K.; Park, J. K.; Nguyen, S. T.; Farha, O. K.; Hupp, J. T., Simple and Compelling Biomimetic Metal–Organic Framework Catalyst for the Degradation of Nerve Agent Simulants. *Angew. Chem. Int. Ed.* **2014**, *126*, 507-511.
- (11) Moon, S.-Y.; Liu, Y.; Hupp, J. T.; Farha, O. K., Instantaneous Hydrolysis of Nerve-Agent Simulants with a Six-Connected Zirconium-Based Metal–Organic Framework. *Angew. Chem. Int. Ed.* **2015**, *54*, 6795-6799.
- (12) Uzarevic, K.; Wang, T. C.; Moon, S.-Y.; Fidelli, A. M.; Hupp, J. T.; Farha, O. K.; Friscic, T., Mechanochemical and solvent-free assembly of zirconium-based metal-organic frameworks. *Chem. Commun.* **2016**, *52*, 2133-2136.
- (13) de Koning, M. C.; van Grol, M.; Breijaert, T., Degradation of Paraoxon and the Chemical Warfare Agents VX, Tabun, and Soman by the Metal–Organic Frameworks UiO-66-NH₂, MOF-808, NU-1000, and PCN-777. *Inorg. Chem.* **2017**, *56*, 11804-11809.
- (14) Bobbitt, N. S.; Mendonca, M. L.; Howarth, A. J.; Islamoglu, T.; Hupp, J. T.; Farha, O. K.; Snurr, R. Q., Metal-organic frameworks for the removal of toxic industrial chemicals and chemical warfare agents. *Chem. Soc. Rev.* **2017**, *46*, 3357-3385.

- (15) Katz, M. J.; Moon, S.-Y.; Mondloch, J. E.; Beyzavi, M. H.; Stephenson, C. J.; Hupp, J. T.; Farha, O. K., Exploiting parameter space in MOFs: a 20-fold enhancement of phosphate-ester hydrolysis with UiO-66-NH₂. *Chemical Science* **2015**, *6*, 2286-2291.
- (16) Moon, S.-Y.; Wagner, G. W.; Mondloch, J. E.; Peterson, G. W.; DeCoste, J. B.; Hupp, J. T.; Farha, O. K., Effective, Facile, and Selective Hydrolysis of the Chemical Warfare Agent VX Using Zr₆-Based Metal–Organic Frameworks. *Inorg. Chem.* **2015**, *54*, 10829-10833.
- (17) Valenzano, L.; Civalieri, B.; Chavan, S.; Bordiga, S.; Nilsen, M. H.; Jakobsen, S.; Lillerud, K. P.; Lamberti, C., Disclosing the Complex Structure of UiO-66 Metal Organic Framework: A Synergic Combination of Experiment and Theory. *Chem. Mater.* **2011**, *23*, 1700-1718.
- (18) López-Maya, E.; Montoro, C.; Rodríguez-Albelo, L. M.; Aznar Cervantes, S. D.; Lozano-Pérez, A. A.; Cenís, J. L.; Barea, E.; Navarro, J. A. R., Textile/Metal–Organic-Framework Composites as Self-Detoxifying Filters for Chemical-Warfare Agents. *Angew. Chem. Int. Ed.* **2015**, *54*, 6790-6794.
- (19) Zhao, J.; Lee, D. T.; Yaga, R. W.; Hall, M. G.; Barton, H. F.; Woodward, I. R.; Oldham, C. J.; Walls, H. J.; Peterson, G. W.; Parsons, G. N., Ultra-Fast Degradation of Chemical Warfare Agents Using MOF-Nanofiber Kebabs. *Angew. Chem. Int. Ed.* **2016**, *55*, 13224-13228.
- (20) Ostermann, R.; Cravillon, J.; Weidmann, C.; Wiebcke, M.; Smarsly, B. M., Metal-organic framework nanofibers viaelectrospinning. *Chem. Commun.* **2011**, *47*, 442-444.
- (21) Wang, C.; Liu, C.; Li, J.; Sun, X.; Shen, J.; Han, W.; Wang, L., Electrospun metal-organic framework derived hierarchical carbon nanofibers with high performance for supercapacitors. *Chem. Commun.* **2017**, *53*, 1751-1754.
- (22) Li, S.; Huo, F., Metal-organic framework composites: from fundamentals to applications. *Nanoscale* **2015**, *7*, 7482-7501.

- (23) Bechelany, M.; Drobek, M.; Vallicari, C.; Abou Chaaya, A.; Julbe, A.; Miele, P., Highly crystalline MOF-based materials grown on electrospun nanofibers. *Nanoscale* **2015**, *7*, 5794-5802.
- (24) Lee, D. T.; Zhao, J.; Peterson, G. W.; Parsons, G. N., Catalytic “MOF-Cloth” Formed via Directed Supramolecular Assembly of UiO-66-NH₂ Crystals on Atomic Layer Deposition-Coated Textiles for Rapid Degradation of Chemical Warfare Agent Simulants. *Chem. Mater.* **2017**, *29*, 4894-4903.
- (25) Brozena, A. H.; Oldham, C. J.; Parsons, G. N., Atomic layer deposition on polymer fibers and fabrics for multifunctional and electronic textiles. *J. Vac. Sci. Technol. A* **2016**, *34*, 010801.
- (26) Lemaire, P. C.; Zhao, J.; Williams, P. S.; Walls, H. J.; Shepherd, S. D.; Losego, M. D.; Peterson, G. W.; Parsons, G. N., Copper Benzenetricarboxylate Metal–Organic Framework Nucleation Mechanisms on Metal Oxide Powders and Thin Films formed by Atomic Layer Deposition. *ACS Appl. Mater. Interfaces* **2016**, *8*, 9514-9522.
- (27) Zhao, J.; Gong, B.; Nunn, W. T.; Lemaire, P. C.; Stevens, E. C.; Sidi, F. I.; Williams, P. S.; Oldham, C. J.; Walls, H. J.; Shepherd, S. D.; Browe, M. A.; Peterson, G. W.; Losego, M. D.; Parsons, G. N., Conformal and highly adsorptive metal-organic framework thin films via layer-by-layer growth on ALD-coated fiber mats. *J. Mater. Chem. A* **2015**, *3*, 1458-1464.
- (28) Zhao, J.; Losego, M. D.; Lemaire, P. C.; Williams, P. S.; Gong, B.; Atanasov, S. E.; Blevins, T. M.; Oldham, C. J.; Walls, H. J.; Shepherd, S. D.; Browe, M. A.; Peterson, G. W.; Parsons, G. N., Highly Adsorptive, MOF-Functionalized Nonwoven Fiber Mats for Hazardous Gas Capture Enabled by Atomic Layer Deposition. *Adv. Mater. Interfaces* **2014**, *1*, 1400040.

- (29) Hyde, G. K.; Park, K. J.; Stewart, S. M.; Hinestroza, J. P.; Parsons, G. N., Atomic Layer Deposition of Conformal Inorganic Nanoscale Coatings on Three-Dimensional Natural Fiber Systems: Effect of Surface Topology on Film Growth Characteristics. *Langmuir* **2007**, *23*, 9844-9849.
- (30) Wong-Foy, A. G.; Matzger, A. J.; Yaghi, O. M., Exceptional H₂ Saturation Uptake in Microporous Metal–Organic Frameworks. *J. Am. Chem. Soc.* **2006**, *128*, 3494-3495.
- (31) Walton, K. S.; Snurr, R. Q., Applicability of the BET Method for Determining Surface Areas of Microporous Metal–Organic Frameworks. *J. Am. Chem. Soc.* **2007**, *129*, 8552-8556.
- (32) Jur, J. S.; Spagnola, J. C.; Lee, K.; Gong, B.; Peng, Q.; Parsons, G. N., Temperature-Dependent Subsurface Growth during Atomic Layer Deposition on Polypropylene and Cellulose Fibers. *Langmuir* **2010**, *26*, 8239-8244.
- (33) Spagnola, J. C.; Gong, B.; Arvidson, S. A.; Jur, J. S.; Khan, S. A.; Parsons, G. N., Surface and sub-surface reactions during low temperature aluminium oxide atomic layer deposition on fiber-forming polymers. *J. Mater. Chem.* **2010**, *20*, 4213-4222.
- (34) Oldham, C. J.; Gong, B.; Spagnola, J. C.; Jur, J. S.; Senecal, K. J.; Godfrey, T. A.; Parsons, G. N., Encapsulation and Chemical Resistance of Electrospun Nylon Nanofibers Coated Using Integrated Atomic and Molecular Layer Deposition. *J. Electrochem. Soc.* **2011**, *158*, D549-D556.
- (35) Parsons, G. N.; Atanasov, S. E.; Dandley, E. C.; Devine, C. K.; Gong, B.; Jur, J. S.; Lee, K.; Oldham, C. J.; Peng, Q.; Spagnola, J. C.; Williams, P. S., Mechanisms and reactions during atomic layer deposition on polymers. *Coord. Chem. Rev.* **2013**, *257*, 3323-3331.

- (36) Sweet, W. J., III; Jur, J. S.; Parsons, G. N., Bi-layer Al₂O₃/ZnO atomic layer deposition for controllable conductive coatings on polypropylene nonwoven fiber mats. *J. Appl. Phys.* **2013**, *113*, 194303.
- (37) Sweet, W. J.; Parsons, G. N., In Situ Conductance Analysis of Zinc Oxide Nucleation and Coalescence during Atomic Layer Deposition on Metal Oxides and Polymers. *Langmuir* **2015**, *31*, 7274-7282.
- (38) Lu, A. X.; McEntee, M.; Browe, M. A.; Hall, M. G.; DeCoste, J. B.; Peterson, G. W., MOFabric: Electrospun Nanofiber Mats from PVDF/UiO-66-NH₂ for Chemical Protection and Decontamination. *ACS Applied Materials & Interfaces* **2017**, *9*, 13632-13636.
- (39) Lemaire, P. C.; Lee, D. T.; Zhao, J.; Parsons, G. N., Reversible Low-Temperature Metal Node Distortion during Atomic Layer Deposition of Al₂O₃ and TiO₂ on UiO-66-NH₂ Metal–Organic Framework Crystal Surfaces. *ACS Appl. Mater. Interfaces* **2017**, *9*, 22042-22054.
- (40) Kandiah, M.; Usseglio, S.; Svelle, S.; Olsbye, U.; Lillerud, K. P.; Tilset, M., Post-synthetic modification of the metal-organic framework compound UiO-66. *J. Mater. Chem.* **2010**, *20*, 9848-9851.
- (41) Tulig, K.; Walton, K. S., An alternative UiO-66 synthesis for HCl-sensitive nanoparticle encapsulation. *RSC Advances* **2014**, *4*, 51080-51083.

2.8. Supporting Information

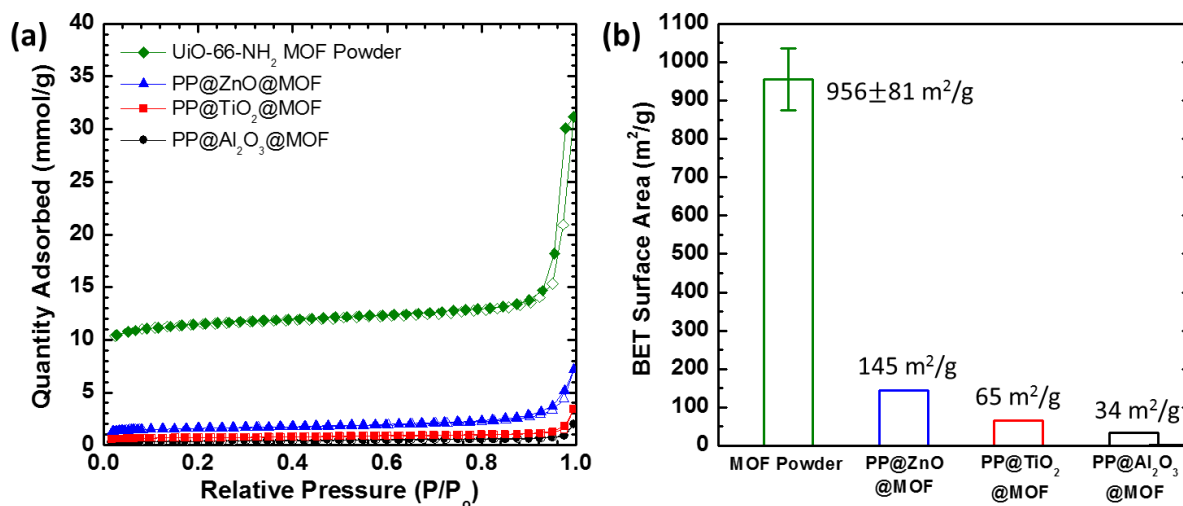


Figure S2.1. (a) N_2 isotherms and (b) overall BET surface area for UiO-66-NH₂ MOF, PP@ZnO@MOF, PP@TiO₂@MOF, and PP@Al₂O₃@MOF.

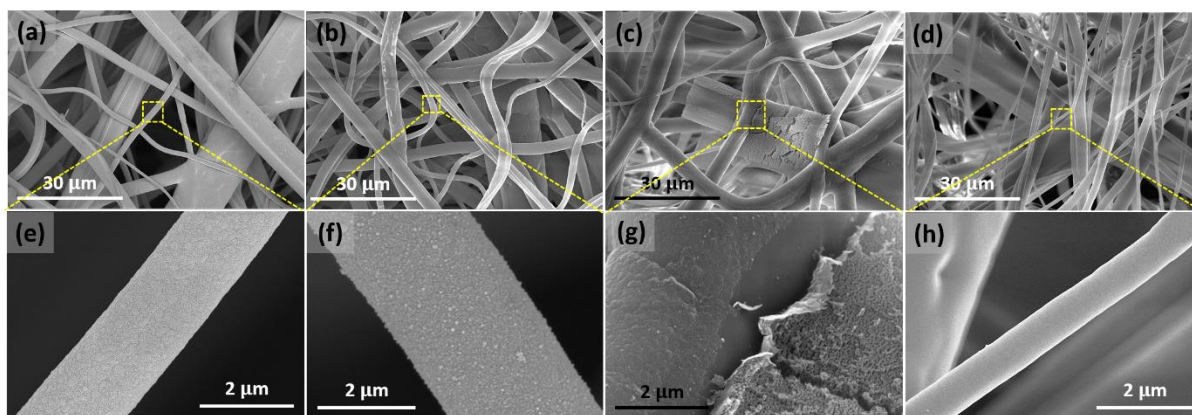


Figure S2.2. SEM images of a stability test for ALD ZnO layer on PP immersed in various solutions at 85 °C for 24 h. (a and e) a control PP@ZnO, (b and f) PP@ZnO in DMF + DI water, (c and g) PP@ZnO in 2-ATA + DMF + DI water, and (d and h) PP@ZnO in ZrCl₄ + DMF + DI water.

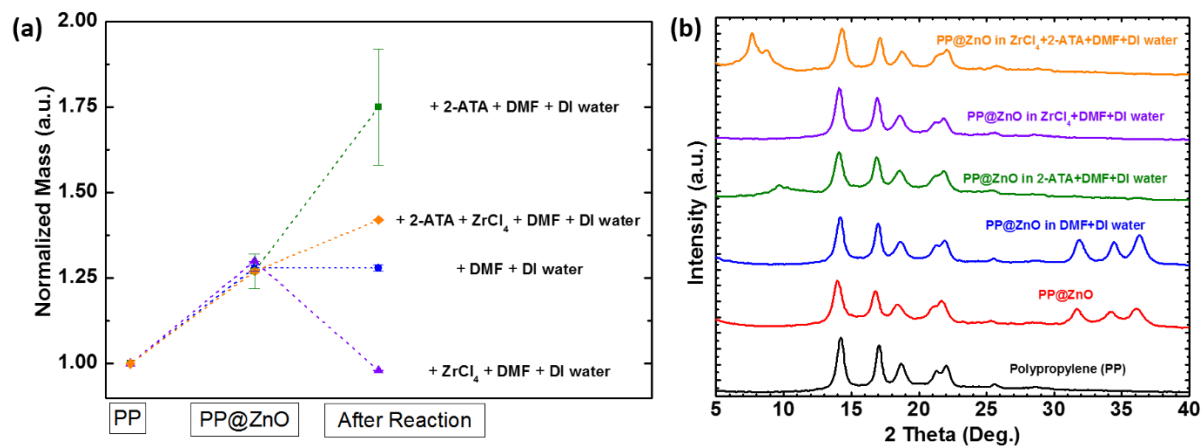


Figure S2.3. (a) Mass changes and (b) XRD patterns of PP@ZnO microfibrers after being immersed in the various solutions at 85 °C for 24 h

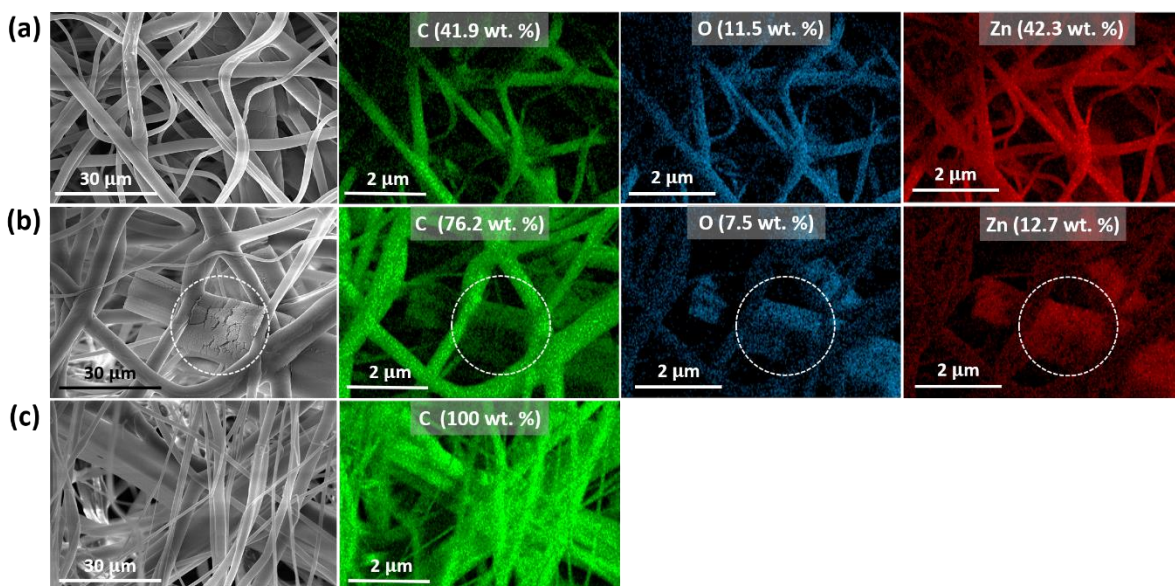


Figure S2.4. SEM and EDS mapping images of PP@ZnO microfibrers after being immersed in the various solutions at 85 °C for 24 h. (a) PP@ZnO in DMF + DI water, (b) PP@ZnO in 2-ATA + DMF + DI water, and (c) PP@ZnO in ZrCl₄ + DMF + DI water.

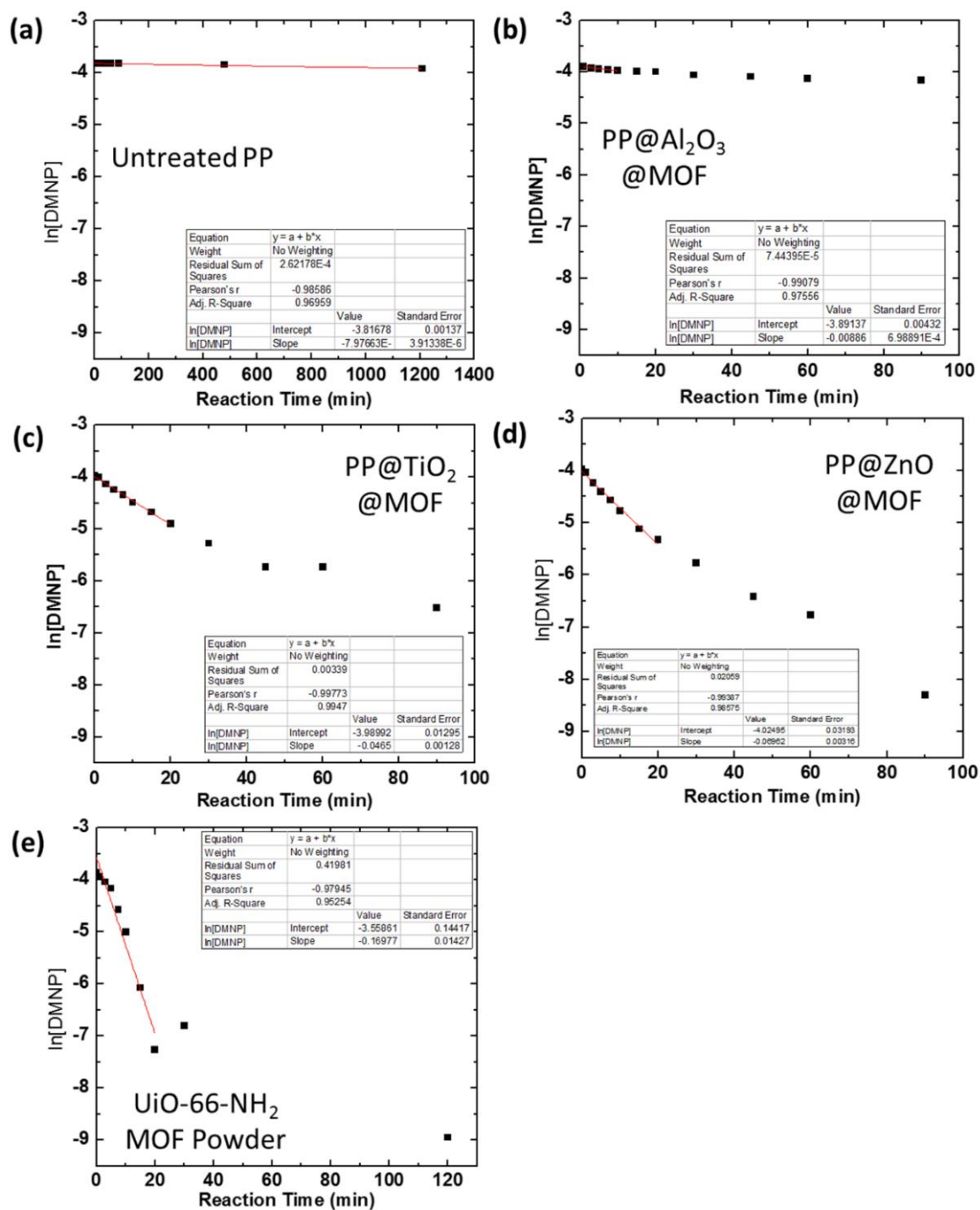


Figure S2.5. Kinetic analysis of (a) untreated PP, (b) PP@Al₂O₃@MOF, (c) PP@TiO₂@MOF, (d) PP@ZnO@MOF, and (e) UiO-66-NH₂ MOF powder.

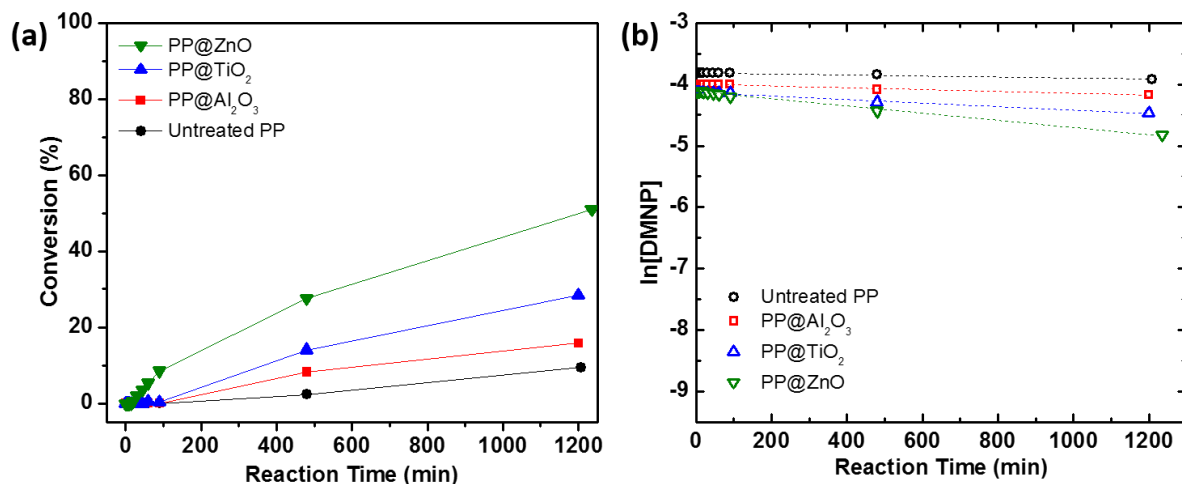


Figure S2.6. (a) Conversion profiles and (b) kinetic analysis of untreated PP, PP@Al₂O₃, PP@TiO₂, and PP@ZnO.

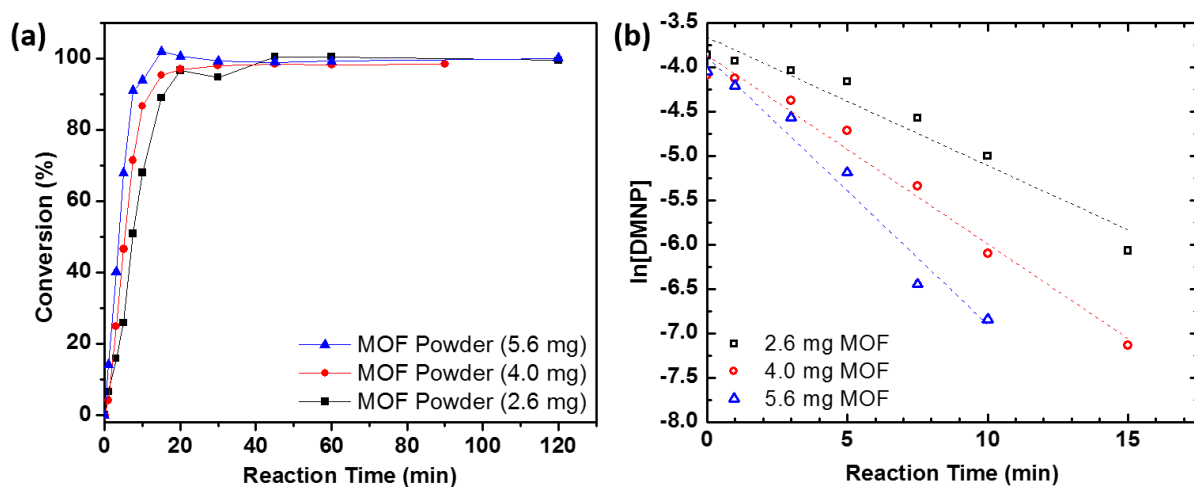


Figure S2.7. (a) Conversion profiles and (b) kinetic analysis of DMNP to *p*-nitrophenoxide versus reaction time using UiO-66-NH₂ MOF powders with different amounts as catalysts.

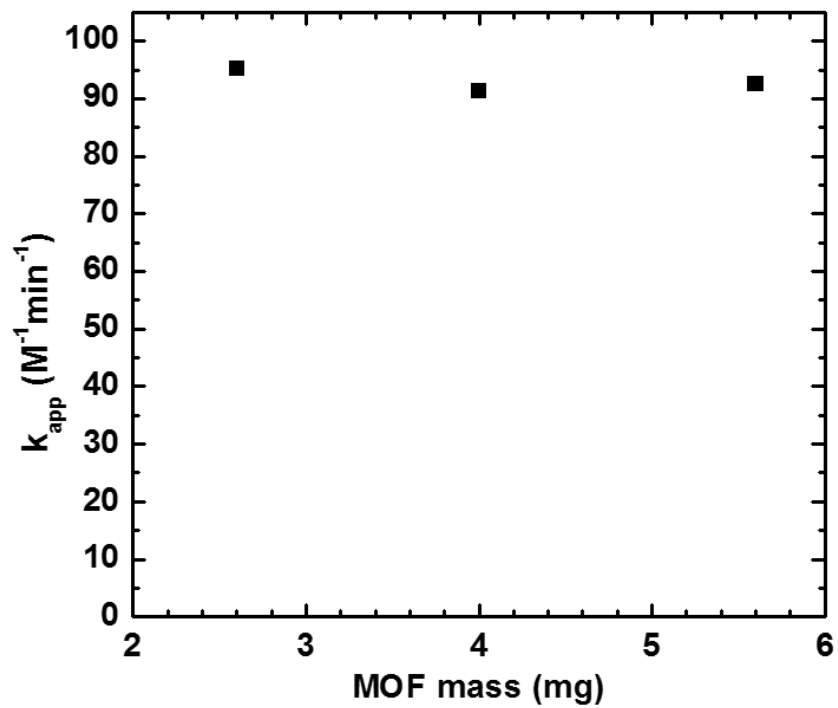


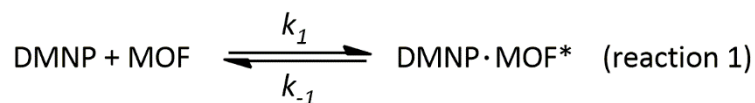
Figure S2.8. Calculated reaction rate constant, k_{app} , versus the amount of MOF powder catalyst added for destructing DMNP to *p*-nitrophenoxide.

Table S2.1. Material properties and catalytic performance of UiO-66-NH₂ MOF powder towards a CWA simulant, DMNP.

	BET Surface Area (m ² /g)	MOF wt.%	m _{MOF} (mg)	-Slope (min ⁻¹)	k _{app} (M ⁻¹ ·min ⁻¹)	DMNP t _{1/2} (min)	TOF (s ⁻¹)
UiO-66-NH ₂ Powder	956 ± 81	100	5.6	0.3012	92.45	2.3	0.028
			4.0	0.2125	91.31	3.3	0.027
			2.6	0.1445	95.23	4.8	0.028

*The half-lives are obtained on the basis of first-order kinetics. Turn over frequency (TOF) was calculated per Zr₆ cluster at t_{1/2}.

Derivations for DMNP hydrolysis reaction



$$\text{Rate (DMNP hydrolysis)} = -k_2[\text{DMNP} \cdot \text{MOF}^*] [M \cdot \text{min}^{-1}] \quad (1)$$

$$k_1[\text{DMNP}][\text{MOF}] = k_{-1}[\text{DMNP} \cdot \text{MOF}^*] [M \cdot \text{min}^{-1}] \text{ at equilibrium} \quad (2)$$

$$\text{An equilibrium reaction rate constant, } K_{eq} = \frac{k_1 [M^{-1} \cdot \text{min}^{-1}]}{k_{-1} [\text{min}^{-1}]}$$

$$= \frac{[\text{DMNP} \cdot \text{MOF}^*]}{[\text{DMNP}][\text{MOF}]} [M^{-1}] \quad (3)$$

$$[\text{DMNP} \cdot \text{MOF}^*] = K_{eq}[\text{DMNP}][\text{MOF}] \quad (4)$$

$$\text{Rate} = -k_2 K_{eq}[\text{DMNP}][\text{MOF}] = -k_{app}[\text{DMNP}][\text{MOF}] [M \cdot \text{min}^{-1}] \quad (5)$$

Let an apparent reaction rate constant, $k_{app} = k_2K_{eq} [M^{-1} \cdot \text{min}^{-1}]$ (6)

MOF Powder Samples

$$\text{Rate} = -\frac{d[DMNP]}{dt} = k_{app}[DMNP][MOF] [M \cdot \text{min}^{-1}] \quad (7)$$

$$\int_{[DMNP]_0}^{[DMNP]_t} \frac{1}{[DMNP]} d[DMNP] = -k_{app}[MOF] \int_0^t dt \quad (8)$$

$$\ln [DMNP]_t = -k_{app}[MOF] \cdot t + \ln[DMNP]_0 \quad (9)$$

$$[MOF] = \frac{m_{MOF}/M.W_{MOF}}{V_{total}} [M] \quad (10)$$

$$\text{slope} = -k_{app} \cdot \frac{m_{MOF}/M.W_{MOF}}{V_{total}} [\text{min}^{-1}] \quad (11)$$

$$k_{app} = -\text{slope} \cdot \frac{V_{total}}{m_{MOF}/M.W_{MOF}} [M^{-1} \cdot \text{min}^{-1}] \quad (12)$$

$$t_{1/2,MOF} = \frac{\ln 2}{k_{app}[MOF]} [\text{min}] \quad (13)$$

PP@ALD@MOF Samples

$$\text{"Calculated Active" } m_{MOF} = -\text{slope} \cdot \frac{V_{total} \times M.W_{MOF}}{k_{app,powder}} [g] \quad (14)$$

* $k_{app,powder}$, $93 \pm 1.7 \text{ M}^{-1}\text{min}^{-1}$, is an average value of the apparent reaction constant obtained from DMNP degradation kinetics catalyzed with varied amounts of MOF powder.

$$\text{"Calculated Active" MOF mass fraction } [\%] = \frac{\text{"Active" } m_{MOF}}{m_{PP@ALD@MOF}} \times 100 [\%] \quad (15)$$

$$\text{"Measured" MOF mass fraction [\%]} = \frac{\text{BET SA of PP@ALD@MOF}}{\text{BET SA of MOF powder}} \times 100 \text{ [\%]} \quad (16)$$

*We assume that only MOF can contribute to BET surface area in PP@ALD@MOF fabric samples.

$$t_{1/2,PP@ALD@MOF} = \frac{\ln 2}{k_{app,avg}} \text{ [min]} \quad (17)$$

PP or PP@ALD

$$\text{Rate} = -\frac{d[DMNP]}{dt} = k_{app}[DMNP] \text{ [M} \cdot \text{min}^{-1}] \quad (18)$$

$$\int_{[DMNP]_0}^{[DMNP]_t} \frac{1}{[DMNP]} d[DMNP] = -k_{app} \int_0^t dt \quad (19)$$

$$\ln [DMNP]_t = -k_{app} \cdot t + \ln [DMNP]_0 \quad (20)$$

$$t_{1/2,PP \text{ or } PP@ALD} = \frac{\ln 2}{k_{app}} \text{ [min]} \quad (21)$$

Here, k_{app} [min^{-1}] is equal to slope [min^{-1}] in PP or PP@ALD without MOF coating.

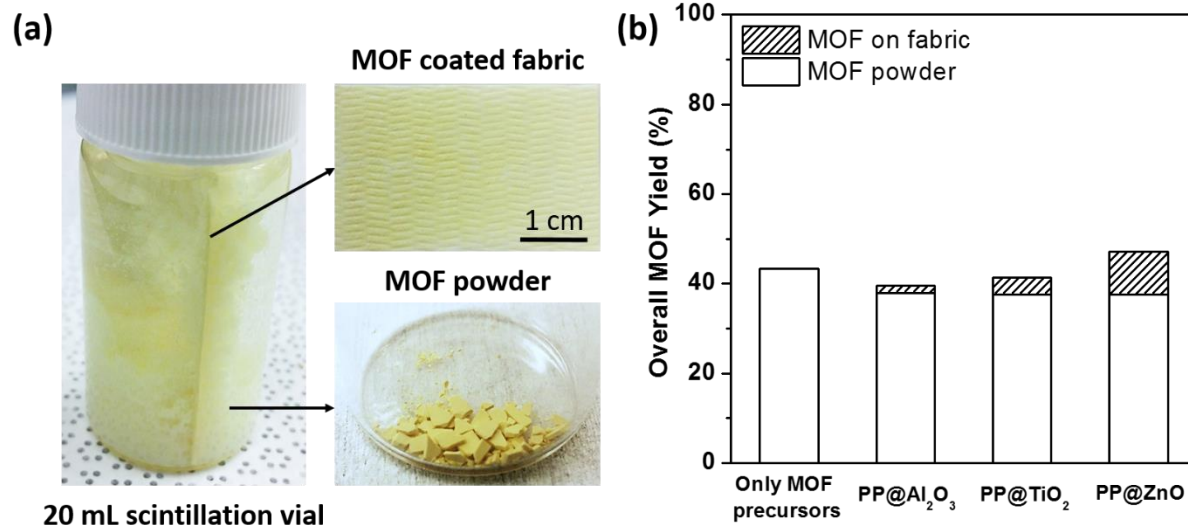


Figure S2.9. (a) Actual UiO-66-NH₂ MOF/fabric composites and MOF powder synthesized in 20 mL scintillation vial (ZrCl₄ (0.080 g, 0.343 mmol) + 2-ATA (0.062 g, 0.343 mmol) + DMF (20 mL) + DI water (25 μL) mixture). (b) Histogram of the fractional yield of MOF crystals on the different fiber surfaces and MOF powder collected from the liquid phase relative to the starting solution molar precursor concentration.

Table S2.2. Material properties used for calculating overall MOF yield and extracting MOF yield on fabric.

Substrates	After MOF growth				
	PP@ALD (g)	MOF powder (g)	MOF on fabric (g)	Overall MOF yield (%)	MOF yield on fabric (%)
-	0	0.0424	0	43.3	0
PP@Al ₂ O ₃	0.0447	0.0372	0.0016	39.6	1.6
PP@TiO ₂	0.0504	0.0368	0.0037	41.4	3.8
PP@ZnO	0.0529	0.0454	0.0094	47.2	9.6

* Theoretical mass of UiO-66-NH₂ MOF powder synthesized from our standard precursor concentration (ZrCl₄ (0.343 mmol) + 2-ATA (0.343 mmol) + DI water (25 μL) in 20 mL DMF) is 0.0979 g (0.014 mmol). PP@ALD indicates substrates before growing MOF on them. MOF powder is collected from liquid phase left behind the MOF growth reaction. Mass of the powder is measured after being activated at 110 °C for 24 h. Mass of MOF on fabric is obtained considering BET surface area of the MOF/fiber samples (Table S1) normalized to 956 ± 81 m²/g of MOF powder.

CHAPTER 3

Catalytic "MOF-Cloth" Formed via Directed Supramolecular Assembly of UiO-66-NH₂ Crystals on Atomic Layer Deposition-coated Textiles for Rapid Degradation of Chemical Warfare Agent Simulants

CHAPTER 3 is a reprint of a manuscript published in *Chemistry of Materials*

Dennis T. Lee,[†] Junjie Zhao,[†] Gregory W. Peterson,[‡] and Gregory N. Parsons,^{*,†}

[†]Department of Chemical & Biomolecular Engineering, North Carolina State University, 911 Partners Way, Raleigh, NC 27695, United States

[‡]Edgewood Chemical Biological Center, 5183 Blackhawk Road, Aberdeen Proving Ground, MD 21010, United States

3.1. Abstract

Highly tunable metal–organic framework (MOF) materials, including, for example, UiO-66-NH₂, are known to be effective catalysts to degrade chemical warfare agents (CWAs) with half-lives near 1 min. Therefore, many researchers have been actively working on producing supported MOF materials to improve application effectiveness by using relatively slow solvothermal synthesis or repetitious stepwise layer-by-layer methods. Herein, we demonstrate a facile route to rapidly assemble presynthesized UiO-66-NH₂ crystals onto nonwoven polypropylene (PP) fibrous mats at ambient temperature. Crystal assembly is chemically directed using β -cyclodextrin (β -CD) and cetyltrimethylammonium bromide (CTAB) as surfactant assembly agents, where the agents quickly (within 5 min) self-assemble on the crystal surface and promote physically robust chemical surface attachment while simultaneously impeding solution-phase crystal agglomeration. Furthermore, we find that when the PP is preconditioned using conformal metal oxide thin films, including Al₂O₃, TiO₂, or ZnO formed via atomic layer deposition (ALD), the hydrophilic metal oxide surface further helps improve assembly uniformity and MOF mass loading, producing MOF crystal loading as high as 40 wt % and an overall BET surface area exceeding 200 m²/g_(MOF+Fiber). Using these surface-assembled MOFs, we observe catalytic degradation of dimethyl 4-nitrophenyl phosphate (DMNP), a CWA simulant, with a half-life of less than 5 min.

3.2. Introduction

Metal–organic frameworks (MOFs) are porous and highly crystalline materials assembled by bridging nanoscale metal ions or clusters with multifunctional organic linkers.¹ Since MOFs can exhibit tunable porous structures, exceptionally high surface area, and good chemical, hydrolytic, and thermal stability,² they have been explored for a range of applications, such as gas storage and separation,³ catalysis,⁴ light harvesting and energy conversion,⁵ selective adsorption of anions from aqueous solutions,⁶ and recently degrading chemical warfare agents (CWAs).^{7,8} However, MOF batch synthesis methods often require both high reaction temperatures and long reaction time and result in powders that require further handling and processing for further applications.⁹

To overcome the problem of MOF processing, many approaches have been reported to integrate MOFs into polymeric,¹⁰ organic–inorganic fibrous mats,¹¹ and polymer matrices.^{12–14} To date, however, these approaches are limited to demonstrations using MOF precursor solutions to form crystals via methods including in situ solvothermal synthesis,^{15,16} layer-by-layer growth,¹⁷ counter-diffusion,¹⁸ or microwave irradiation,¹⁹ many of which require high temperatures or relatively long processing times. Unless care is taken to prepare the surface to promote MOF crystal nucleation,^{20,21} these methods commonly lead to poor coverage of MOFs and low MOF mass fraction on the substrate. Poor surface coverage results from relatively rapid nucleation in the solution phase, thereby depleting reactants available for slower surface nucleation and growth.

Herein, we report a facile and rapid strategy for integration of MOFs onto polymeric fibrous mats at ambient temperature using solvent-suspended presynthesized MOF crystals. To demonstrate this strategy, we use UiO-66-NH₂ and provide new insight to allow direct assembly and achieve high MOF mass fraction on polypropylene (PP) nonwoven mats. We examine UiO-

66-NH₂ because it is a highly stable Zr-based MOF known to be effective for catalytic destruction of organophosphorus nerve agents and related simulants, such as dimethyl 4-nitrophenyl phosphate (DMNP).^{22, 23} A challenge for MOF assembly on polypropylene is that the polymer surface displays only methyl groups, which cannot form covalent bonds with UiO-66-NH₂ crystals due to polar amine functional groups.²⁴ To promote the interaction between the MOF and the substrate, we introduced atomic layer deposition (ALD) of metal oxides to impart surface hydroxyl groups onto the inert PP.²⁵ A supramolecular complex comprised of β -cyclodextrin (β -CD) and cetyltrimethylammonium bromide (CTAB) was used as a self-assembly agent. The hydroxyl units on the cylindrical β -CD and cationic head groups on the linear CTAB molecules lead to a host-guest self-assembly interaction and bind to polar surfaces (including both the MOF and the modified PP) via van der Waals, electrostatic interactions, and hydrogen bonding.^{26–28} The modified surfaces then readily bind to each other at room temperature, leading to dense MOF assembly on the PP. Furthermore, the β -CD and CTAB surface assembly agents work to minimize MOF crystal agglomeration in solution, thereby enabling high mass-loading, conformal coverage, and physically robust surface-attachment of UiO-66-NH₂ crystals. To the best of our knowledge, this is the first demonstration of chemical assembly of presynthesized MOF crystals with high mass loading on textiles utilizing surface assembly agents. We also substantiate that the assembled MOFs retain their functional surface area and catalytic activity and show that the PP/ALD/MOF composites promote rapid catalytic degradation of DMNP CWA simulant with a half-life of less than 5 min.

3.3. Experimental Section

All reagents were purchased from commercial sources and used without further purification. Zirconium(IV) chloride ($ZrCl_4$, Alfa Aesar, $\geq 99.5\%$), 2-aminoterephthalic acid (Acros Organics, 99%), N,N-dimethylformamide (DMF), deionized water, ethanol, β -cyclodextrin (β -CD, Sigma-Aldrich, $\geq 97\%$), cetyltrimethylammonium bromide (CTAB, Sigma-Aldrich, $\geq 98\%$), N-ethylmorpholine (Sigma-Aldrich, $\geq 97\%$), and dimethyl 4-nitrophenyl phosphate (DMNP, Sigma-Aldrich).

Polymeric Fibrous Materials. Nonwoven polypropylene (PP) was received from Nonwovens Cooperative Research Center (NCRC), North Carolina State University. Nonwoven PP fiber mats are 0.30 mm thick, with fiber diameter ranging from 0.6 to 9.0 μm .

Atomic Layer Deposition (ALD). ALD was used to create thin conformal inorganic Al_2O_3 , TiO_2 , and ZnO coatings on the PP fiber mats. These samples are referred to as PP/ Al_2O_3 , PP/ TiO_2 , and PP/ ZnO, respectively. The PP/ Al_2O_3 , TiO_2 , and ZnO were deposited directly on the PP. The fiber coating and analysis procedures follow methods developed previously for ALD modification of polymers and textile media.²⁹

The ALD Al_2O_3 was deposited onto PP using a lab-made hot-wall viscous-flow vacuum reactor.²¹ Deposition pressure was kept at ~ 1 Torr, and the temperature was 90 °C. In a general ALD Al_2O_3 cycle, trimethyl aluminum (TMA) was first dosed to the reaction chamber for 1 s, followed with 30 s of N_2 purge between doses. After TMA dose and N_2 purge, deionized water was dosed with another 30 s of N_2 purge. We chose 200 cycles of ALD Al_2O_3 as a standard coating thickness.^{21,25,30}

ALD ZnO and TiO_2 were performed in the same lab-made hot-wall viscous-flow vacuum reactor as that used for ALD Al_2O_3 . The deposition pressures were both ~ 1 Torr, and the

temperatures were kept at 90 °C. In an ALD TiO₂ cycle, precursors of both TiCl₄ and H₂O were dosed alternately to the reaction chamber for 1 s, with 40 s of N₂ purge between dose steps. We deposited 300 cycles of ALD TiO₂ onto the fiber mats resulting in 20 nm of coating thickness, as determined by ellipsometry on monitor wafers coated simultaneously in the ALD reactor. In an ALD ZnO cycle, the substrate (i.e., PP) was exposed to 2 s of diethyl zinc (DEZ) and 2 s of deionized water alternately, with 60 s of N₂ purge between dose steps. We used 110 cycles of ALD ZnO as a standard coating thickness.^{20,31,32}

Synthesis of UiO-66-NH₂ in the Form of Powder. A 20 mL glass scintillation vial was loaded with 0.080 g (0.343 mmol) of ZrCl₄ followed by being dissolved in 20 mL of N,N-dimethylformamide (DMF) and then sonicated for at least 1 min until fully dissolved. After that, 20 μL of deionized water and 0.062 g (0.343 mmol) of 2-aminoterephthalic acid were added to the prepared solution. This as-prepared mixture was heated at 85 °C for 24 h. The resulting solid was then collected by filtering out unreacted precursors and residual DMF using a filtration system. Then the collected solid was rinsed with 80 mL of DMF and ethanol in a sequential manner in the filtration system. Eventually, the final solid was stored under vacuum in a desiccator until being used for the assembly experiment.

Assembly of UiO-66-NH₂ Crystals on Fibers. A total of 0.24 g of as-prepared UiO-66-NH₂ solid was dispersed in 40 mL of DMF and then sonicated for 5 min until fully dispersed (Solution A), and 0.254 g of β-cyclodextrin (β-CD) and 0.04 g of cetyltrimethylammonium bromide (CTAB) were simultaneously dissolved in 40 mL of DMF for an hour to form supramolecular complex (Solution B). Solution for assembly was prepared by slowly pouring solution B to solution A and then keeping the mixture stirred for 30 min.

Assembly of UiO-66-NH₂ crystals onto fiber substrates was performed by immersing PP fiber mats (4 × 2.5 cm) into as-prepared solution with a mild stirring for 20 h at room temperature.

The resulting PP fiber mats with assembled UiO-66-NH₂ crystals were rinsed first with DMF (3 × 80 mL) and then with ethanol (4 × 80 mL). After that, the ultimate products were dried in air for 1 h and stored under vacuum in a desiccator before being used for further characterization.

Hydrolysis of Dimethyl 4-Nitrophenyl Phosphate (DMNP). Hydrolysis for UiO-66-NH₂ powder was implemented at room temperature. UiO-66-NH₂ powder (three respective runs: (1) 1.5 mg, 0.0009 mmol, (2) 2.6 mg, 0.0015 mmol, and (3) 5.6 mg, 0.0032 mmol) was added to an aqueous solution of N-ethylmorpholine (1 mL, 0.45 M) in a 1.5 mL Eppendorf vial (room temperature). The resulting mixture was stirred for 30 min until finely dispersing the UiO-66-NH₂. DMNP (~6.2 mg, 0.025 mmol) was then added to the suspension. Stirring for each reaction was fixed at 1100 rpm.

For periodic monitoring prior to UV/vis measurement, we disposed of a 20 μL aliquot from the reaction mixture and diluting it with an aqueous solution of N-ethylmorpholine (10 mL, 0.45 M). Reaction progress was measured by observing the 4-nitrophenoxide absorbance at 407 nm. The solution for background was identical to the reaction solution except for the absence of catalyst.

Hydrolysis for fabric with assembled UiO-66-NH₂ was carried out the same as that for UiO-66-NH₂ powder. Instead of adding the powder sample, we chopped up PP/ZnO + Assembly (two respective runs: (1) 10 mg, 1.8 mg of UiO-66-NH₂ on the fabric, (2) 17.6 mg, 3.2 mg of UiO-66-NH₂ on the fabric; mass fraction of UiO-66-NH₂ on the fabric was about 30.7%) into six pieces and added them into solution for proper hydrolysis reaction with DMNP while being stirred at 1100 rpm.

For monitoring the reaction progress, prior to UV/vis measurement, we disposed of a 20 μL aliquot from the reaction mixture and diluted it with an aqueous solution of N-ethylmorpholine (10 mL, 0.45 M). Reaction progress was measured the same way of UiO-66-NH₂ powder. The solution for background was identical to the reaction solution except for the absence of catalyst.

Physical Adhesion Test for UiO-66-NH₂ onto Fabric. The physical adhesion test was conducted by immersing fabric with assembled UiO-66-NH₂ (PP/ZnO + Assembly) in ethanol with vigorous stirring at 500 rpm for 24 h. After the stirring step, the sample was dried in air for 1 h and dried under vacuum at 110 °C overnight. Then, the weight of the sample after vacuum drying was measured and compared with that before the physical adhesion test.

Regeneration of UiO-66-NH₂ (postcatalysis). The slurry of UiO-66-NH₂ after being used for the DMNP hydrolysis experiment was collected and poured onto an Anodisc filter membrane in a glass microanalysis vacuum filter apparatus equipped with a graduated cylinder. Once the sample was dried, 80 mL of deionized water was filtered through the membrane two times. After that, 80 mL of ethanol was passed through the membrane two times. Finally, the UiO-66-NH₂ solid was collected out of the membrane after being fully dried in air and then stored under vacuum in a desiccator for further characterization.

Material Characterization. Scanning electron microscopic (SEM) images were taken using a FEI Verios 460 L field emission SEM. A thin layer of Au-Pd (5–10 nm) was sputter-coated onto all samples before SEM imaging. X-ray diffraction (XRD) was carried out with a Rigaku SmartLab X-ray diffraction tool (Cu K α X-ray source) for crystalline phase analysis. Both MOF powder (UiO-66-NH₂) and fabric with assembled MOF crystals (PP/ZnO + Assembly) diffraction patterns were also simulated using Mercury 3.0 software and the crystallographic information file from Cambridge Crystallographic Data Centre (CCDC 837796 for UiO-66). A

Quantachrome Autosorb-1C surface area and pore size analyzer was used for measuring N₂ isotherm at 77 K. Samples were dried in vacuum ($\sim 1 \times 10^{-5}$ Torr) at room temperature for 1 h, at 80 °C for 6 h, 90 °C for 1 h, 100 °C for 1 h, and 110 °C for 12 h in a sequential fashion, before N₂ adsorption measurement. BET surface area was calculated based on the N₂ adsorption data within a relative pressure range of $P/P_0 = 0.02-0.08$.^{33,34} A Thermo Scientific Nicolet 6700 Fourier transform infrared spectrometer was used for analyzing MOF growth on IR silicon wafers. A progressive change in absorbance intensity during hydrolysis reaction was monitored by a Thermo Scientific Evolution 300 UV/vis spectrophotometer.

3.4. Results and Discussion

We prepared UiO-66-NH₂ crystals through solvothermal synthesis as described previously.^{35,36} The quality of the as-prepared UiO-66-NH₂ crystals was confirmed via N₂ adsorption isotherms and powder X-ray diffraction (PXRD). In Figure 3.1, The N₂ adsorption/desorption isotherms show a Brunauer–Emmett–Teller surface area (BET SA) of $956 \pm 81 \text{ m}^2/\text{g}$ and total pore volume of $0.57 \text{ cm}^3/\text{g}$, equivalent to 16 mmol/g, and the PXRD results directly matched the simulated UiO-66 pattern, indicating good quality starting MOF powder. To implement the assembly method, we prepared a solution containing UiO-66-NH₂ crystals, β -CD, and CTAB in DMF, along with a similar solution with only the MOF and DMF solvent. For initial experiments, PP substrates with and without ALD coating were immersed in each solution for prolonged periods (up to 20 h) with 500 rpm stirring at ambient temperature. Figure 3.2 shows SEM images of the uncoated and ALD coated PP after 20 h of assembly in the solution containing β -CD and CTAB. For the uncoated PP, the β -CD/CTAB assembly process leads to homogeneous MOF crystal only in the void regions between the fibers (Figure 3.2a,e), which we ascribe to crystal

entrapment and aggregation during stirring. For the ALD coated PP, we see well-dispersed MOF assembly on Al_2O_3 (Figure 3.2b,f) and TiO_2 (Figure 3.2c,d), with somewhat higher surface density on the TiO_2 . For the fibers coated with ALD ZnO (Figure 3.2d,h and Figure S3.1c), the UiO-66- NH_2 crystals surround and uniformly encase the PP microfibers in a highly packed layer. In some regions, the assembled crystal layer extends between fibers, which was not observed in previous reports for MOFs formed by direct solvothermal synthesis onto fibers.³⁷ Using ALD-coated PP without the supramolecular complex present, SEM images (Figure S3.1d) show that, after 20 h in solution, the MOF crystals become trapped and agglomerate within the fabric voids, similar to that in Figure 3.2a,e for the uncoated PP.³⁸

Using the ZnO-coated PP, we also examined assembly using only the individual β -CD or CTAB assembly promoters in the MOF solution. While some MOF loading was observed, the mass uptake with the β -CD or CTAB alone was less than that observed for the combined β -CD + CTAB (Figures S3.2 and S3.3). Possible interactions between MOF crystals by means of β -CD + CTAB assembly agents are illustrated in Figure 3.3. For these tests, the molar ratio of β -CD to CTAB was maintained at the stoichiometric ratio of 2 to 1 to maximize the assembly.²⁶ We speculate that the ALD ZnO surface deposited on PP fibrous scaffolds can hold hydroxyl groups of β -CD via hydrogen bonding with Zn-OH (Figure 3.3a). In addition, hydroxyl groups in the outer region of β -CD or cationic heads of CTAB can adhere to electron-rich amine functional groups of the outer MOF surface by means of hydrogen or electrostatic bonding, respectively.^{26,28} Therefore, MOF crystals surrounded by the assembly agents (β -CD + CTAB) can be bridged or connected through hydrogen bonding between β -CDs or through van der Waals attractive forces between CTAB tail groups (Figure 3.3b).

These results show that combining ALD surface preparation with β -CD/CTAB molecular assembly promoters enables well controlled assembly of UiO-66-NH₂ crystals on the surface of flexible fiber webs. Furthermore, we see that the molecular assembly agents or surfactants tend to prevent agglomeration UiO-66-NH₂ crystals in the solution phase, while facilitating assembly on the fiber surface.

Considering these results, we performed more detailed experiments to confirm that the assembled MOFs retained the good crystallinity, surface area, and catalytic activity of the original MOF powders. We also sought to better understand the mechanistic reasons for the observed differences in MOF adhesion on the various ALD metal oxides studied and to characterize the adhesion and stability of the MOFs on the fibers after assembly.

Figure 3.4a presents the simulated X-ray diffraction patterns of UiO-66-NH₂ powder, the PP substrate, and the MOF-coated PP/ALD fiber mats. The intensity of the primary UiO-66-NH₂ peaks at 7.2° and 8.3° in 2-theta are strongest for PP/ZnO, consistent with larger mass loading.¹⁰ This sample also shows peaks at 28° to 40° also assigned to UiO-66-NH₂ which are not readily seen in the other experimental patterns. Photographic images of uncoated PP and PP/ZnO fiber mats after MOF assembly are shown in Figure 3.4b. The yellowish color in the upper image demonstrates the uniform coverage of UiO-66-NH₂ crystals.

Next, we studied mass fraction and overall BET SA of UiO-66-NH₂ crystals assembled onto different ALD layers (Figure 3.5). In Figure 3.5a, PP/ZnO + β -CD + CTAB + MOF (referred to as “PP/ZnO + Assembly”) shows higher BET SA of 211 m²/g compared to that of PP/Al₂O₃ + Assembly (79 m²/g) and PP/TiO₂ + Assembly (90 m²/g). This is consistent with the result that the highest MOF mass fraction of 30.7% was obtained by PP/ZnO + Assembly. In comparison with overall BET SA of the control samples (i.e., untreated PP fiber mat, 1 m²/g; PP coated with ALD

ZnO, PP/ZnO, 1 m²/g; and PP + Assembly, 15 m²/g) the results in Figure 3.5b depict a large overall BET surface area of 211 m²/g for the PP/ZnO + Assembly. This value for the BET surface area is slightly less than 287 ± 24 m²/g expected from the value measured for the pure powder (956 ± 81 m²/g) and the estimated fraction of MOF mass loading on the fibers. This reduced value may reflect uncertainty in the mass loading analysis and/or some partial pore blocking of the surface-anchored MOF crystals by the β-CD + CTAB assembly agents.³⁹

The trend in mass loading and surface area with ALD coating composition demonstrates discrepant interactions between the ALD layer and the supramolecular complex (β-CD + CTAB) surrounding the UiO-66-NH₂ crystals. Previous measurements reported the different isoelectric points (IEP) for ALD coatings (i.e., Al₂O₃, TiO₂, or ZnO) and of untreated PP.³¹ The surface sites on ZnO and Al₂O₃ (e.g., hydroxyls and bridging oxygens) have predominantly Brønsted basic character, whereas the surfaces of untreated PP and TiO₂ are more acidic. The basic surface sites promote stronger interaction with the assembly agents (β-CD + CTAB), thus promoting MOF attachment. In addition, surface roughness of fiber after the ALD coating may also increase the surface area available for MOF attachment.²⁰

As shown in Figure 3.2a,e and Figure S3.1, the MOF assembly on the uncoated PP (PP + Assembly) leads to agglomeration of UiO-66-NH₂ crystals within the void regions on the fiber mat substrates. In addition, XRD analysis of MOFs formed within the PP fiber matrix without ALD coating (Figure S3.4) shows appreciably smaller MOF loading with poor dispersion. We anticipate that these agglomerated crystals do not chemically interact with untreated PP surface, and therefore a smaller amount of MOF crystals is randomly loaded on the fabric. This ultimately leads to relatively small surface area per unit mass (MOF + Fiber). We conclude, therefore, that for the

self-assembled MOF on fiber system high overall BET SA requires a procedure that produces both uniform MOF surface distribution and high surface loading.

To test how well the assembled UiO-66-NH₂ crystals are adhered to ALD ZnO-coated PP, we immersed the substrates into ethanol and then vigorously stirred at 500 rpm for 24 h (Figure 3.6a). From the measured mass change, we found this procedure produced less than 0.1% mass loss (Figure 3.6b), indicating very strong MOF/surface bonding. As a further test of MOF adhesion, we repeatedly sheared a nylon brush across the UiO-66-NH₂ coated PP substrates. After 30 manual brush strokes, no MOF powder could be visibly detected on the brush or on surrounding surfaces, and as shown in Figure S3.5, the fabric pieces retained their typical yellow color, indicating good MOF adhesion in the brushed regions.

This strong adhesion of the assembled MOFs on fibers is in distinct contrast to samples prepared without ALD coating or without the β -CD + CTAB complex, where MOFs present on the surface readily fell off under gentle shaking or handling. To examine the MOF assembly mechanism in more detail, we used Fourier transform infrared spectroscopy (FTIR) to investigate changes in the vibrational modes present in each type of prepared sample (Figure 3.7). Sample substrates were IR transparent silicon with thin native oxide solution coated with CTAB, β -CD, or β -CD + CTAB. Direct IR analysis of the PP fabric was not feasible because of absorbance by the relatively thick polymer fiber. Other silicon samples were coated with thin layers (20 nm) of ALD metal oxides (Al₂O₃, TiO₂, or ZnO) followed by assembly (UiO-66-NH₂ crystals + β -CD + CTAB in DMF) with mild stirring for 20 h. As a further control, we also analyzed silicon wafers coated with ALD TiO₂ followed by solvothermal MOF growth (85 °C for 24 h). All the samples were completely dried in air for 3 h before characterization. This allowed us to carefully trace changes

in intrinsic chemical functionalities of the MOF upon assembly and observe differences between assembled and directly grown crystals.

The IR spectra from these samples are shown in Figure 3.7b,c. The samples with β -CD or β -CD + CTAB show broad $\nu_{\text{sym}}(\text{OH})$ signals at 3600–3200 cm^{-1} associated with the expected β -CD hydroxyl moieties.⁴⁰

The topmost spectra in Figure 3.7b and c were collected from the solvothermal MOF films grown on ALD TiO_2 on silicon. The spectrum shows OH-related peaks at 3666–3635 cm^{-1} assigned to intrinsic μ_3 -OH groups in the $\text{Zr}_6\text{O}_4(\text{OH})_4$ MOF secondary building unit (SBU) clusters. Peaks associated with the organic aromatic linker (i.e., 2-aminoterephthalic acid) include $\nu_{\text{asym}}(\text{NH}_2)$ at 3523–3500 cm^{-1} , $\nu_{\text{sym}}(\text{NH}_2)$ near 3400 cm^{-1} , and aromatic C-H stretches, $\nu(\text{C}_{\text{ar}}\text{-H})$ at 3100–2850 cm^{-1} .⁴¹ Other MOF-related features in this sample in Figure 3.7c include $\delta(\text{NH}_2)$ at 1629 cm^{-1} , $\nu_{\text{asym}}(\text{COO}^-)$ at 1566 cm^{-1} , aromatic C=C stretch, $\text{C}_{\text{ar}}=\text{C}_{\text{ar}}$ near 1496 cm^{-1} , $\nu_{\text{sym}}(\text{COO}^-)$ at 1431 and 1390 cm^{-1} , and $\nu(\text{C}_{\text{ar}}\text{-N})$ at 1338 and 1259 cm^{-1} .^{42, 43}

Figure 3.7b,c also shows three additional spectra from MOF films formed by the β -CD/CTAB assembly on ALD TiO_2 , ZnO, and Al_2O_3 on silicon. As expected, these spectra show features consistent with the combined MOF and β -CD + CTAB assembly agents. Careful inspection, however, reveals noticeable differences. For example, the intensity of the NH_2 bending mode at 1629 cm^{-1} is reduced for the assembled MOF relative to the grown MOF, particularly for the MOF assembly on ZnO. This change, along with the observable differences in the OH and NH stretching features for the assembled versus grown MOF films, is indicative of the hydrogen bonding and electrostatic interactions that influence the μ_3 -OH (on the SBUs), electron-rich amines (on the organic linkers), and terminal OH groups (on β -CD) upon MOF/ β -CD/CTAB assembly. The expected structure of the fully assembled MOF on ALD surface is shown

schematically in Figure 3.7a.^{44,45} The larger change in the IR for assembly on ZnO is consistent with SEM (Figure 3.2), XRD (Figure 3.4), and BET surface area (Figure 3.5) showing more extensive assembly on ZnO relative to the other metal oxides. One possible difference for assembly on ZnO vs TiO₂ and Al₂O₃ on polypropylene may relate to the role of the ALD precursors in the surface modification of the polymer. On polypropylene, some ALD precursors can readily diffuse into the polymer surface, leading to subsurface metal oxide nucleation and surface roughening. The extent of roughening depends on the polymer, nature of the precursor, ALD reactant dose times, and ALD process temperature.^{46,47}

Generally, compared to TiO₂ and Al₂O₃, ZnO ALD tends to produce a roughened surface on PP, whereas on planar silicon, these ALD films will all show smooth surface texture.⁴⁸ Therefore, the increased MOF attachment on the ZnO-coated PP may be also associated with preferred attachment on roughened polymer substrates.

To evaluate the functional performance of the fiber-surface assembled UiO-66-NH₂ MOF crystals, we performed experiments using assembled UiO-66-NH₂ crystals as catalytic agents for hydrolysis of chemical warfare agent simulants.^{37,49,50} Here, we used DMNP and examined the rate of the phosphate ester bond hydrolysis to simulate hydrolysis of GB (Sarin) or GD (Soman) nerve agents that each contain a labile P–F bond.⁵¹ Katz et al. have recently found that the DMNP hydrolysis rate using UiO-66-NH₂ is approximately 20 times that of UiO-66.⁵² This noticeable enhancement was probably by the amino moiety functioning as a Brønsted-base in UiO-66-NH₂, improving proton transfer during the hydrolysis. Figure 3.8a shows a schematic of the hydrolysis of DMNP by MOF-based catalyst (left) and periodic monitoring (right) of the hydrolysis reaction using UV–vis measurements. As the reaction progresses, the intensity at 407 nm becomes enhanced due to emergence of the 4-nitrophenoxide hydrolysis product. Conversion profiles for

DMNP hydrolysis in the presence of untreated PP, PP/ZnO, PP/ZnO + Assembly, and UiO-66-NH₂ MOF powder are plotted, respectively. As shown in Figure 3.8b and Table 3.1, for untreated PP microfibers, the DMNP destruction rate is negligible with the estimated half-life of around 6 days. With ALD ZnO layers on PP microfibers (PP/ZnO), it lowers the half-life to less than 20 h (Figure S3.6). This shows consistency that metal oxides like TiO₂ or ZnO can function as catalysts for degrading CWAs or their simu-lants.^{53,54} The DMNP hydrolysis reaction rates are much faster with PP/ZnO + Assembly ($m_{\text{MOF+Fabric}} = 10 \text{ mg}$) fabric and ($m_{\text{MOF}} = 2.6 \text{ mg}$) UiO-66-NH₂ powder with the half-life of 6.5 min for both. The kinetic traces and half-lives of hydrolysis of DMNP using the fabric and powder samples are close to each other. We believe this observation is reasonable considering that mass fraction of UiO-66-NH₂ on the fabric (PP/ZnO + Assembly) was around 30.7%. Therefore, it is sensible to regard the amount of MOFs on the fabric as about 3.1 mg, which is a similar amount of MOFs in the powder sample ($m_{\text{MOF}} = 2.6 \text{ mg}$). Furthermore, the rates for DMNP degradation are similar to those recently reported for UiO-66-NH₂ formed on ALD-coated polymer fibers via direct solvothermal synthesis.³⁶ As for the hydrolysis reactions catalyzed with the fabric samples, we cut one piece of fabric into several pieces to well disperse in the reacting solution. As a control experiment, we kept the total amount of sample (MOF + fiber) fixed and varied the extent of fabric cutting used to prepare the samples for kinetic analysis. Results in Figure S3.7 show we obtained the same DMNP degradation rate using either a single fabric piece or a sample cut into small pieces, confirming that sample cutting did not influence measured reaction kinetics.

In another set of experiments, we varied the catalyst loading and found that the initial $t_{1/2}$ values are diminished as the amounts of the catalyst loading are increased (Figure S3.8 and Table 3.1). These results are analogous to those with UiO-67 derivatives previously reported.⁵² We also

identified that such kinetic traces with fabric (PP/ZnO + Assembly) samples showed similar propensity (Figure S3.9 and Table 3.1).

Concerning verified high mechanical and hydrostability of UiO-66-NH₂, XRD and SEM confirmed that UiO-66-NH₂ is fairly intact under our hydrolysis condition (Figure S3.10). Moreover, we confirmed that the microstructure of the UiO-66-NH₂ is retained after assembly, as determined by overall BET SA of the MOFs. The surface area of 817 m²/g after assembly is very close to 956 ± 81 m²/g measured for similarly prepared UiO-66-NH₂ crystals. This difference probably reflects the extra mass of the supramolecular complex or perhaps partial blocking of the accessibly MOF pores.³⁹ Even so, the BET surface area remains similar to values of ca. 830 m²/g reported for some pristine UiO-66-NH₂ powders.²² Considering all results collectively, chemical assembly of UiO-66-NH₂ on polymer fabric is a viable means to create MOF-cloths for chemical hydrolysis agents simulated by DMNP with half-life less than 5 min.

3.5. Conclusions

The results described here clearly demonstrate that combining ALD surface modification with solution-based β -CD + CTAB supramolecular complex adhesion promotor allows assembly of high density, robust, and functionally active MOF crystal coatings on fiber-based substrates. The assembly approach is summarized in Scheme 1. The ALD layer provides a chemically functional attachment layer for the supramolecular β -CD + CTAB complex, and the complex acts as an assembly agent to well disperse UiO-66-NH₂ crystals and allow them to assemble into dense coatings onto the ALD layers via electrostatic and hydrogen bonding interactions. We find that the extent of MOF loading depends on the composition of the metal oxide ALD coating, with a larger extent of loading on ZnO vs Al₂O₃ or TiO₂. Infrared analysis confirms that assembled layers

contain β -CD, CTAB, and MOF crystals, and analysis of the IR results suggests that surface composition as well as fiber surface roughness may be factors in the extent of MOF loading.

We also verified that the crystals assembled on PP fibrous mats retain their effectiveness for rapid catalytic degradation of hazardous chemical simulants, with rates in line with those observed for the same reactions on UiO-66-NH₂ MOFs in free-powder form. The results clearly show that chemically assembling a relatively small amount of MOF crystals on a fiber surface can be beneficial to overcome difficulties in deployment of MOF powders. Moreover, the assembly process proceeds readily at room temperature and therefore can be considered for extending to a wide range of substrate materials at large scale.

3.6. Figures

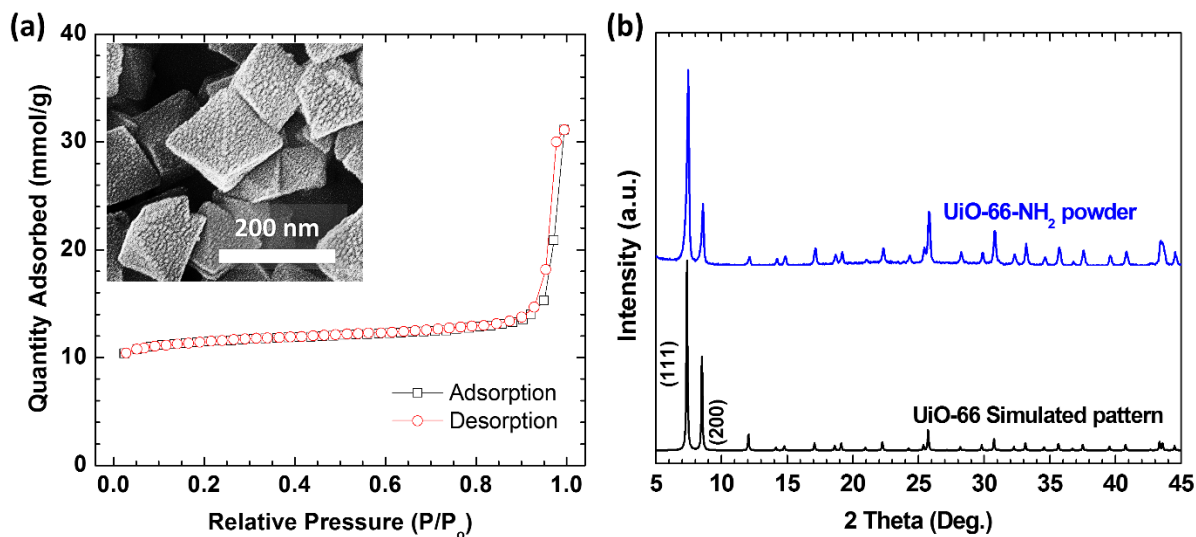


Figure 3.1. (a) The N_2 adsorption (\square) and desorption (\circ) isotherm for the UiO-66-NH₂ powder prepared through solvothermal synthesis at 85 °C for 24 h. Inset indicates SEM image of UiO-66-NH₂ crystals used for the assembly method. BET surface area of the powder is $956 \pm 81 \text{ m}^2/\text{g}$ with total pore volume of 16 mmol/g calculated at a relative pressure (P/P_0) of 0.95. (b) PXRD data for the UiO-66-NH₂ powder used.

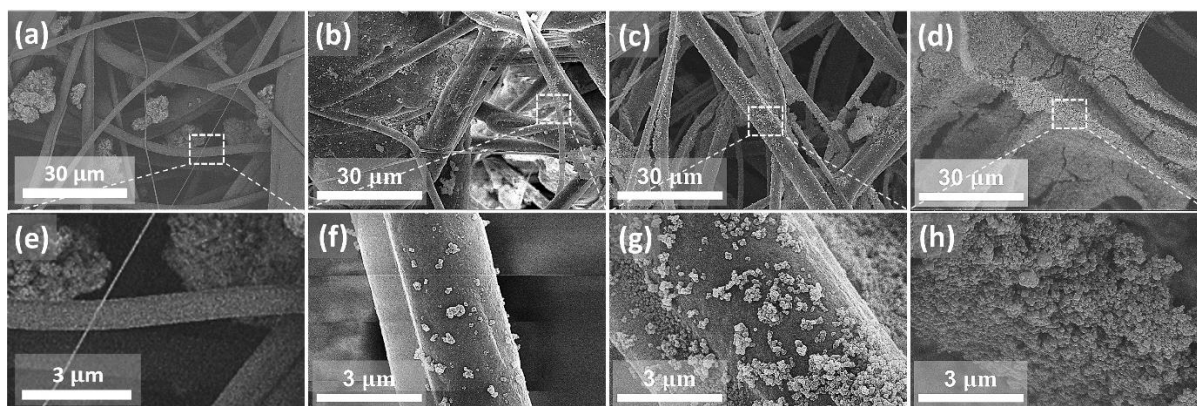


Figure 3.2. SEM images of samples: (a) PP + Assembly, (b) PP/Al₂O₃ + Assembly, (c) PP/TiO₂ + Assembly, (d) PP/ZnO + Assembly, and magnified images in dotted circular area of individual images: (e), (f), (g), and (h), respectively. Assembly solution contains as-synthesized UiO-66-NH₂ crystals + β -CD + CTAB.

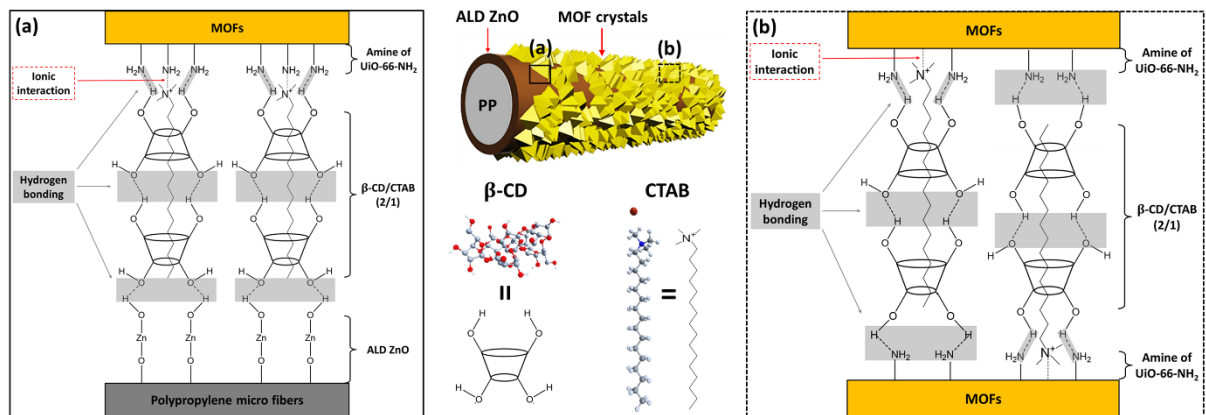


Figure 3.3. The proposed mechanism of interactions (a) between MOF crystals and ALD ZnO surfaces and (b) MOF crystals themselves by means of β -CD + CTAB structures.

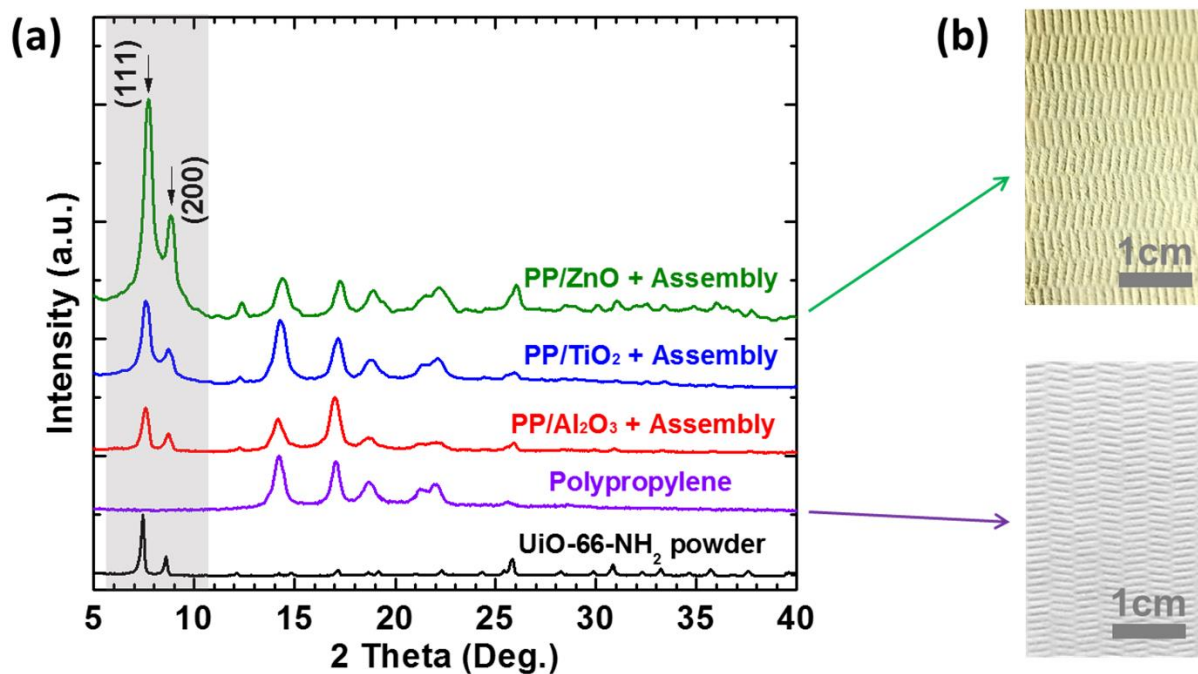


Figure 3.4. (a) XRD spectra of (from bottom to top) UiO-66-NH₂ powder, polypropylene as a substrate, and samples: PP/Al₂O₃ + Assembly, PP/TiO₂ + Assembly, and PP/ZnO + Assembly. (b) Photographs of a virgin PP swatch (bottom) and actual PP/ZnO swatch after “Assembly method” (top). Assembly solution contains as-synthesized UiO-66-NH₂ crystals + β -CD + CTAB.

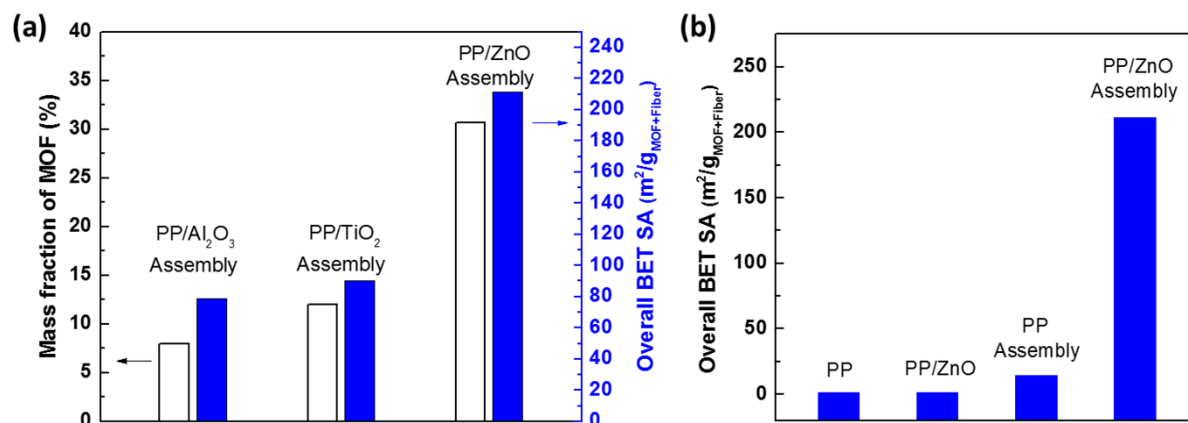
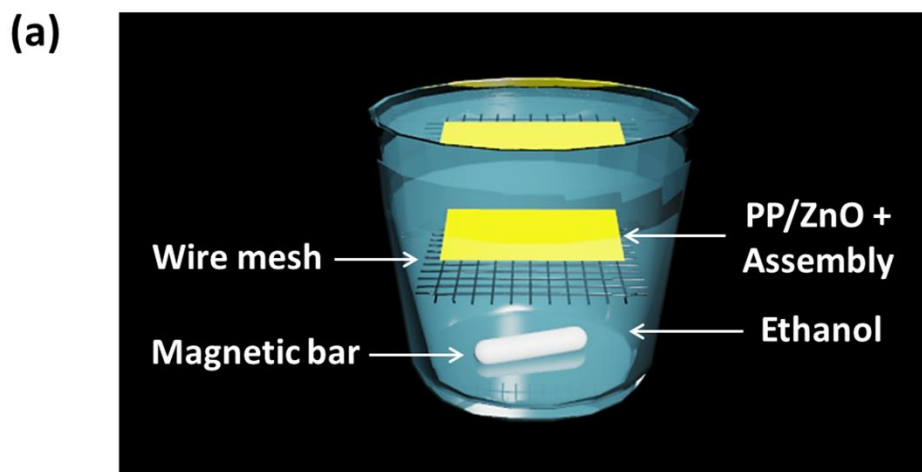


Figure 3.5. (a) Mass fraction of MOFs on ALD-treated PP + Assembly (left y-axis and blank columns) and overall BET surface area for ALD-treated PP + Assembly (right y-axis and filled columns). (b) Overall BET surface area for PP, PP/ZnO, PP + Assembly, and PP/ZnO + Assembly. Overall BET surface area means BET surface area of (MOF + Fiber). Assembly solution contains UiO-66-NH₂ + β -CD + CTAB.



(b)

Sample I.D.	$m/m_0 (t=0)$	$m/m_0 (t=24 h)$
PP/ZnO + Assembly	1.0	1.0
PP + Assembly	1.0	0.97
UiO-PP/ZnO ^[4]	1.0	0.93

Figure 3.6. (a) A schematic of the adhesion test during which samples are immersed in ethanol with vigorous stirring at 500 rpm for 24 h and (b) a table revealing comparison of mass change of each sample after the adhesion test. m is mass after completion of adhesion test, and m_0 is initial mass before the adhesion test. [4] For comparison with the conventional solvothermal approach in the attachment of MOF crystals, rather than using “Assembly method”, UiO-66-NH₂ is nucleated and grown on PP/ZnO at 85 °C for 24 h.

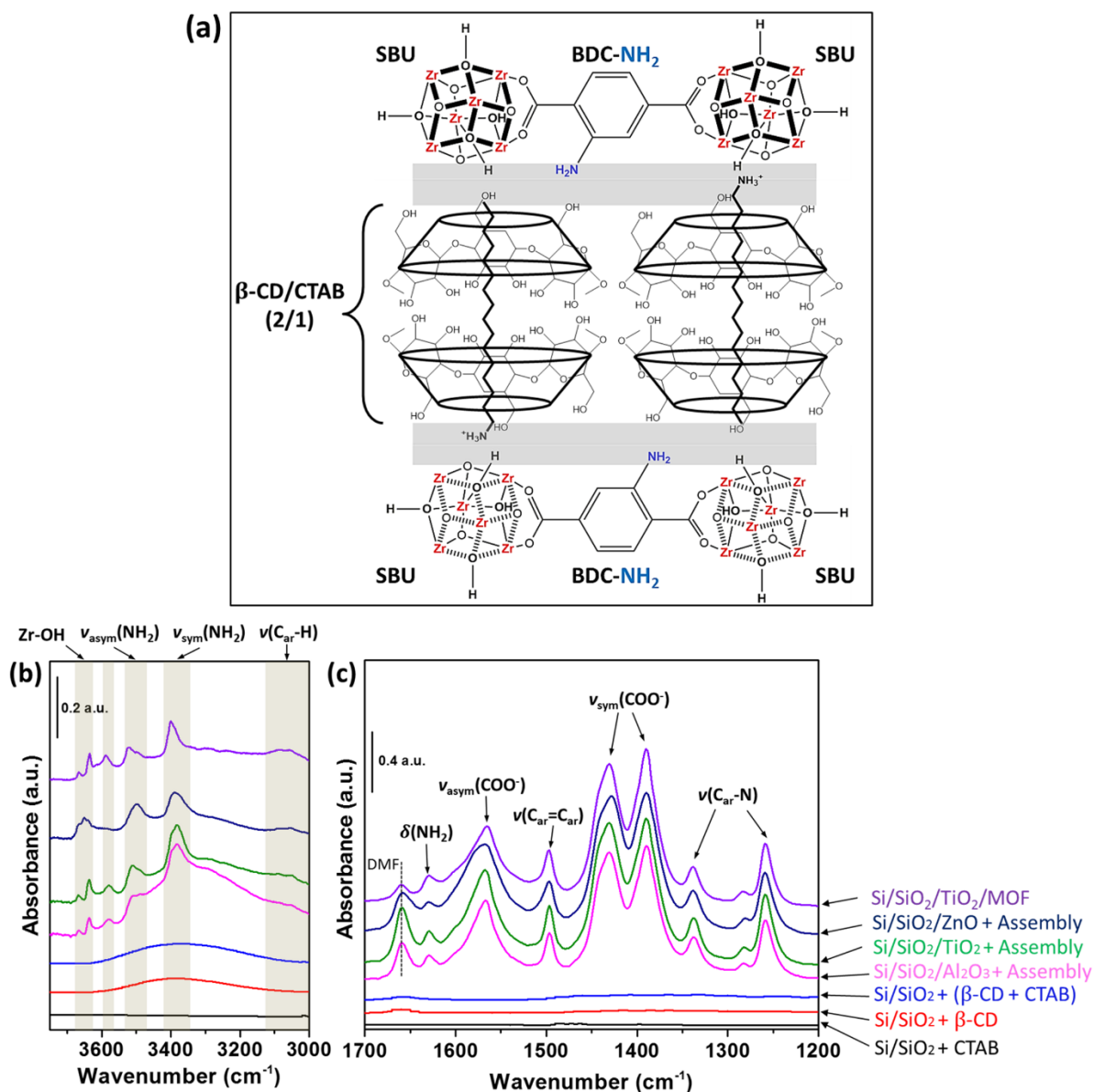


Figure 3.7. (a) Schematic of expected interactions between MOFs and supramolecular complex (β -CD + CTAB). (b-c) FTIR spectra of CTAB, β -CD, supramolecular complex (β -CD + CTAB) on Si/SiO₂, UiO-66-NH₂ assembly on ALD-treated (Al₂O₃, TiO₂, or ZnO) Si/SiO₂, and UiO-66-NH₂ grown via solvothermal synthesis (85 °C for 24 h) on Si/SiO₂/TiO₂. Note that Si/SiO₂ is used as a background for all FTIR patterns.

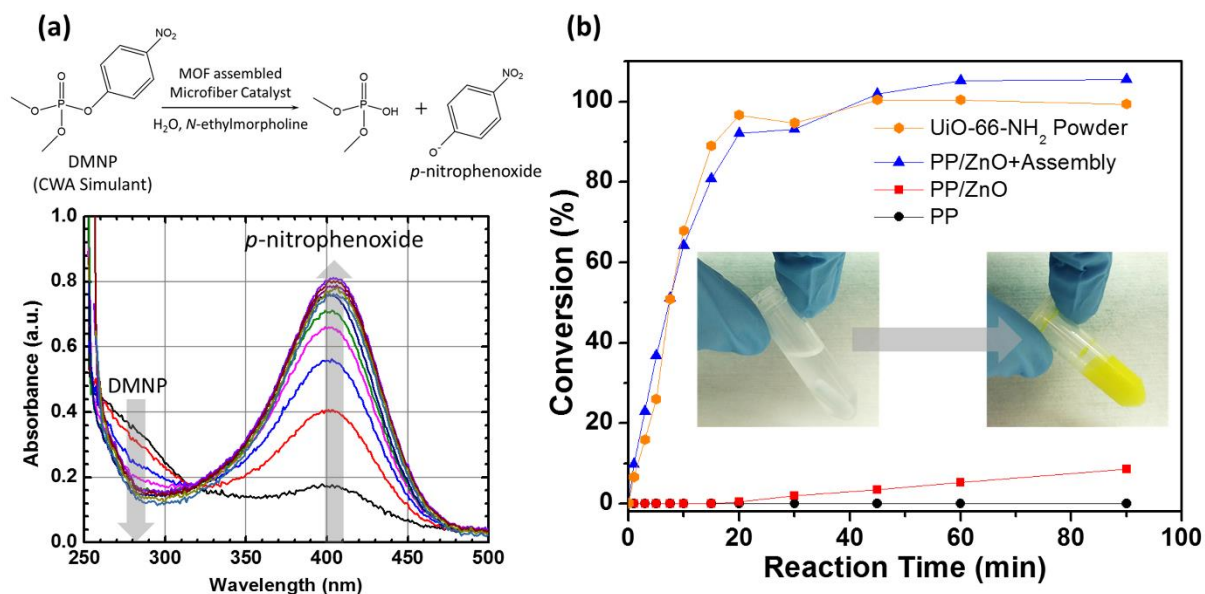


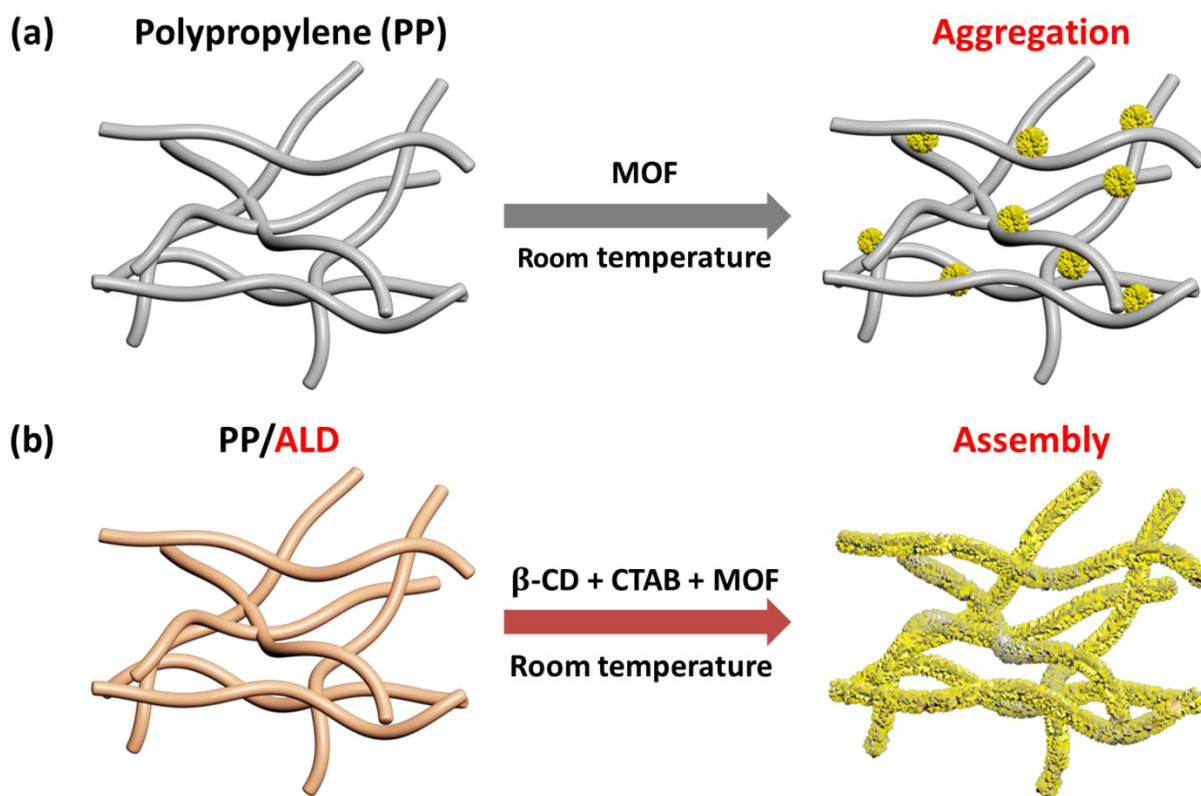
Figure 3.8. (a) Catalytic hydrolysis reaction for DMNP (top) and UV-Vis trace of the hydrolysis of DMNP as a function of time (0 - 120 min) using PP/ZnO + Assembly fiber mats (bottom). (b) Conversion profiles for the hydrolysis of DMNP in the presence of PP, PP/ZnO, PP/ZnO + Assembly, and UiO-66-NH₂ powder at room temperature as a function of time. Inset shows transparent color of solution before hydrolysis reaction starts remarkably changed into yellowish one after the reaction completes. *UiO-66-NH₂ powder used is collected from remnants of assembly solution. The slight drop in the data at ~30 minutes is within the statistical uncertainty of the results.

Table 3.1. Material properties and catalytic performance of degrading a CWA simulant, DMNP^a.

material	amount of catalyst [μmol]	MOF wt %	k [min^{-1}]	$t_{1/2}$ [min]	TOF (s^{-1})
Powder					
UiO-66-NH ₂ (1.5 mg)	0.9	100	0.019	36.5	0.0063
UiO-66-NH ₂ (2.6 mg)	1.5	100	0.111	6.5	0.021
UiO-66-NH ₂ (5.6 mg)	3.3	100	0.301	2.5	0.025
Fabric					
untreated PP (14.0 mg)	0	0	7.98×10^{-5}	8690	-
PP/ZnO (14.0 mg)	0	0	5.87×10^{-4}	1182	-
PP/ZnO + Assembly (10.0 mg]	1.8 ^b	30.7	0.105	6.5	0.018
PP/ZnO + Assembly (17.6 mg)	3.2 ^b	30.7	0.245	2.8	0.023

^aUiO-66-NH₂ powder used was collected from remnants of assembly solution. Turn over frequency (TOF) was calculated per Zr₆ cluster at $t_{1/2}$. ^bAmount of catalyst for fabric samples is corrected based on the actual mass fraction of UiO-66-NH₂ assembled on PP/ZnO, which is about 30.7% as calculated in Figure 3.5a.

Scheme 3.1. Comparison of “Assembly method” at ambient temperature between untreated polypropylene (PP) and ALD-treated PP^a.



^aSolution for assembly contains pre-synthesized UiO-66-NH₂ crystals and the supramolecular complex (β -cyclodextrin (β -CD) + cetyltrimethylammonium bromide (CTAB)).

3.7. References

- (1) Horike, S.; Shimomura, S.; Kitagawa, S. Soft porous crystals. *Nat. Chem.* **2009**, *1*, 695–704.
- (2) Howarth, A. J.; Liu, Y. Y.; Li, P.; Li, Z. Y.; Wang, T. C.; Hupp, J.; Farha, O. K. Chemical, thermal and mechanical stabilities of metal-organic frameworks. *Nat. Mater. Rev.* **2016**, *1*, 15018.
- (3) Mason, J. A.; Veenstra, M.; Long, J. R. Evaluating metal-organic frameworks for natural gas storage. *Chem. Sci.* **2014**, *5*, 32–51.
- (4) Lee, J.; Farha, O. K.; Roberts, J.; Scheidt, K. A.; Nguyen, S. T.; Hupp, J. T. Metal-organic framework materials as catalysts. *Chem. Soc. Rev.* **2009**, *38*, 1450–1459.
- (5) So, M. C.; Wiederrecht, G. P.; Mondloch, J. E.; Hupp, J. T.; Farha, O. K. Metal-organic framework materials for light-harvesting and energy transfer. *Chem. Commun.* **2015**, *51*, 3501–3510.
- (6) Howarth, A. J.; Wang, T. C.; Al-Juaid, S. S.; Aziz, S. G.; Hupp, J. T.; Farha, O. K. Efficient extraction of sulfate from water using a Zr-metal-organic framework. *Dalton Trans.* **2016**, *45*, 93–97.
- (7) DeCoste, J. B.; Peterson, G. W. Metal-Organic Frameworks for Air Purification of Toxic Chemicals. *Chem. Rev.* **2014**, *114*, 5695– 5727.
- (8) Peterson, G. W.; Moon, S. Y.; Wagner, G. W.; Hall, M. G.; DeCoste, J. B.; Hupp, J. T.; Farha, O. K. Tailoring the Pore Size and Functionality of UiO-Type Metal-Organic Frameworks for Optimal Nerve Agent Destruction. *Inorg. Chem.* **2015**, *54*, 9684–9686.
- (9) Li, J. R.; Kuppler, R. J.; Zhou, H. C. Selective gas adsorption and separation in metal-organic frameworks. *Chem. Soc. Rev.* **2009**, *38*, 1477–1504.

- (10) Pinto, M. L.; Dias, S.; Pires, J. Composite MOF Foams: The Example of UiO-66/Polyurethane. *ACS Appl. Mater. Interfaces* **2013**, *5*, 2360–2363.
- (11) Liu, C.; Wu, Y. N.; Morlay, C.; Gu, Y. F.; Gebremariam, B.; Yuan, X.; Li, F. T. General Deposition of Metal-Organic Frameworks on Highly Adaptive Organic-Inorganic Hybrid Electrospun Fibrous Substrates. *ACS Appl. Mater. Interfaces* **2016**, *8*, 2552–2561.
- (12) Fan, L. L.; Xue, M.; Kang, Z. X.; Li, H.; Qiu, S. L. Electrospinning technology applied in zeolitic imidazolate framework membrane synthesis. *J. Mater. Chem.* **2012**, *22*, 25272–25276.
- (13) Li, Y. B.; Wee, L. H.; Volodin, A.; Martens, J. A.; Vankelecom, I. F. J. Polymer supported ZIF-8 membranes prepared via an interfacial synthesis method. *Chem. Commun.* **2015**, *51*, 918–920.
- (14) Li, S.; Huo, F. Metal-organic framework composites: from fundamentals to applications. *Nanoscale* **2015**, *7*, 7482–7501.
- (15) Armstrong, M. R.; Arredondo, K. Y. Y.; Liu, C. Y.; Stevens, J. E.; Mayhob, A.; Shan, B. H.; Senthilnathan, S.; Balzer, C. J.; Mu, B. UiO-66 MOF and Poly(vinyl cinnamate) Nanofiber Composite Mem-branes Synthesized by a Facile Three-Stage Process. *Ind. Eng. Chem. Res.* **2015**, *54*, 12386–12392.
- (16) Guo, H.; Zhu, G.; Hewitt, I. J.; Qiu, S. Twin Copper Source” Growth of Metal–Organic Framework Membrane: Cu₃(BTC)₂ with High Permeability and Selectivity for Recycling H₂. *J. Am. Chem. Soc.* **2009**, *131*, 1646–1647.
- (17) So, M. C.; Jin, S.; Son, H. J.; Wiederrecht, G. P.; Farha, O. K.; Hupp, J. T. Layer-by-Layer Fabrication of Oriented Porous Thin Films Based on Porphyrin-Containing Metal-Organic Frameworks. *J. Am. Chem. Soc.* **2013**, *135*, 15698–15701.

- (18) Yao, J. F.; Dong, D. H.; Li, D.; He, L.; Xu, G. S.; Wang, H. T. Contra-diffusion synthesis of ZIF-8 films on a polymer substrate. *Chem. Commun.* **2011**, *47*, 2559–2561.
- (19) Yoo, Y.; Jeong, H. K. Rapid fabrication of metal organic framework thin films using microwave-induced thermal deposition. *Chem. Commun.* **2008**, *0*, 2441–2443.
- (20) Zhao, J.; Losego, M. D.; Lemaire, P. C.; Williams, P. S.; Gong, B.; Atanasov, S. E.; Blevins, T. M.; Oldham, C. J.; Walls, H. J.; Shepherd, S. D.; Browe, M. A.; Peterson, G. W.; Parsons, G. N. Highly Adsorptive, MOF-Functionalized Nonwoven Fiber Mats for Hazardous Gas Capture Enabled by Atomic Layer Deposition. *Adv. Mater. Interfaces* **2014**, *1*, 1400040.
- (21) Zhao, J.; Gong, B.; Nunn, W. T.; Lemaire, P. C.; Stevens, E. C.; Sidi, F. I.; Williams, P. S.; Oldham, C. J.; Walls, H. J.; Shepherd, S. D.; Browe, M. A.; Peterson, G. W.; Losego, M. D.; Parsons, G. N. Conformal and highly adsorptive metal-organic framework thin films via layer-by-layer growth on ALD-coated fiber mats. *J. Mater. Chem. A* **2015**, *3*, 1458–1464.
- (22) Katz, M. J.; Brown, Z. J.; Colon, Y. J.; Siu, P. W.; Scheidt, K. A.; Snurr, R. Q.; Hupp, J. T.; Farha, O. K. A facile synthesis of UiO-66, UiO-67 and their derivatives. *Chem. Commun.* **2013**, *49*, 9449–9451.
- (23) Mondloch, J. E.; Katz, M. J.; Isley, W. C., III; Ghosh, P.; Liao, P. L.; Bury, W.; Wagner, G.; Hall, M. G.; DeCoste, J. B.; Peterson, G. W.; Snurr, R. Q.; Cramer, C. J.; Hupp, J. T.; Farha, O. K. Destruction of chemical warfare agents using metal-organic frameworks. *Nat. Mater.* **2015**, *14*, 512–516.
- (24) Chen, Q.; He, Q. Q.; Lv, M. M.; Xu, Y. L.; Yang, H. B.; Liu, X. T.; Wei, F. Y. Selective adsorption of cationic dyes by UiO-66-NH₂. *Appl. Surf. Sci.* **2015**, *327*, 77–85.
- (25) Hyde, G. K.; Scarel, G.; Spagnola, J. C.; Peng, Q.; Lee, K.; Gong, B.; Roberts, K. G.; Roth, K. M.; Hanson, C. A.; Devine, C. K.; Stewart, S. M.; Hojo, D.; Na, J. S.; Jur, J. S.; Parsons,

- G. N. Atomic Layer Deposition and Abrupt Wetting Transitions on Nonwoven Polypropylene and Woven Cotton Fabrics. *Langmuir* **2010**, *26*, 2550– 2558.
- (26) Kumar, P.; Kim, W. D.; Lee, S.; Lee, D. T.; Lee, K.; Lee, D. C. Surface energy-driven growth of crystalline PbS octahedra and dendrites in the presence of cyclodextrin-surfactant supramolecular complexes. *J. Nanopart. Res.* **2015**, *17*, 108.
- (27) Depalo, N.; Comparelli, R.; Striccoli, M.; Curri, M. L.; Fini, P.; Giotta, L.; Agostiano, A. alpha-cyclodextrin functionalized CdS nanocrystals for fabrication of 2/3 D assemblies. *J. Phys. Chem. B* **2006**, *110*, 17388–17399.
- (28) Huang, T.; Meng, F.; Qi, L. M. Controlled Synthesis of Dendritic Gold Nanostructures Assisted by Supramolecular Complexes of Surfactant with Cyclodextrin. *Langmuir* **2010**, *26*, 7582– 7589.
- (29) Brozena, A. H.; Oldham, C. J.; Parsons, G. N. Atomic layer deposition on polymer fibers and fabrics for multifunctional and electronic textiles. *J. Vac. Sci. Technol., A* **2016**, *34*, 010801.
- (30) Jur, J. S.; Spagnola, J. C.; Lee, K.; Gong, B.; Peng, Q.; Parsons, G. N. Temperature-Dependent Subsurface Growth during Atomic Layer Deposition on Polypropylene and Cellulose Fibers. *Langmuir* **2010**, *26*, 8239–8244.
- (31) Lemaire, P. C.; Zhao, J. J.; Williams, P. S.; Walls, H. J.; Shepherd, S. D.; Losego, M. D.; Peterson, G. W.; Parsons, G. N. Copper Benzenetricarboxylate Metal-Organic Framework Nucleation Mechanisms on Metal Oxide Powders and Thin Films formed by Atomic Layer Deposition. *ACS Appl. Mater. Interfaces* **2016**, *8*, 9514– 9522.
- (32) Zhao, J.; Nunn, W. T.; Lemaire, P. C.; Lin, Y.; Dickey, M. D.; Oldham, C. J.; Walls, H. J.; Peterson, G. W.; Losego, M. D.; Parsons, G. N. Facile Conversion of Hydroxy Double Salts

- to Metal–Organic Frameworks Using Metal Oxide Particles and Atomic Layer Deposition Thin-Film Templates. *J. Am. Chem. Soc.* **2015**, *137*, 13756–13759.
- (33) Wong-Foy, A. G.; Matzger, A. J.; Yaghi, O. M. Exceptional H₂ saturation uptake in microporous metal-organic frameworks. *J. Am. Chem. Soc.* **2006**, *128*, 3494–3495.
- (34) Walton, K. S.; Snurr, R. Q. Applicability of the BET Method for Determining Surface Areas of Microporous Metal–Organic Frameworks. *J. Am. Chem. Soc.* **2007**, *129*, 8552–8556.
- (35) Schaate, A.; Roy, P.; Godt, A.; Lippke, J.; Waltz, F.; Wiebcke, M.; Behrens, P. Modulated Synthesis of Zr-Based Metal-Organic Frameworks: From Nano to Single Crystals. *Chem. - Eur. J.* **2011**, *17*, 6643–6651.
- (36) Zhao, J.; Lee, D. T.; Yaga, R. W.; Hall, M. G.; Barton, H. F.; Woodward, I. R.; Oldham, C. J.; Walls, H. J.; Peterson, G. W.; Parsons, G. N. Ultra-Fast Degradation of Chemical Warfare Agents Using MOF-Nanofiber Kebabs. *Angew. Chem., Int. Ed.* **2016**, *55*, 13224–13228.
- (37) Lopez-Maya, E.; Montoro, C.; Rodriguez-Albelo, L. M.; Cervantes, S. D. A.; Lozano-Perez, A. A.; Cenis, J. L.; Barea, E.; Navarro, J. A. R. Textile/Metal-Organic-Framework Composites as Self-Detoxifying Filters for Chemical-Warfare Agents. *Angew. Chem., Int. Ed.* **2015**, *54*, 6790–6794.
- (38) Wang, H.; Wu, Y. M.; Bai, Y. S.; Zhou, W.; An, Y. R.; Li, J. H.; Guo, L. The self-assembly of porous microspheres of tin dioxide octahedral nanoparticles for high performance lithium ion battery anode materials. *J. Mater. Chem.* **2011**, *21*, 10189–10194.
- (39) Qiu, L. G.; Xu, T.; Li, Z. Q.; Wang, W.; Wu, Y.; Jiang, X.; Tian, X. Y.; Zhang, L. D. Hierarchically Micro- and Mesoporous Metal-Organic Frameworks with Tunable Porosity. *Angew. Chem., Int. Ed.* **2008**, *47*, 9487–9491.

- (40) Shokuhfar, A.; Afghahi, S. S. S. The heating effect of iron-cobalt magnetic nanofluids in an alternating magnetic field: application in magnetic hyperthermia treatment. *Nanoscale Res. Lett.* **2013**, *8*, 540.
- (41) Peterson, G. W.; McEntee, M.; Harris, C. R.; Klevitch, A. D.; Fountain, A. W.; Soliz, J. R.; Balboa, A.; Hauser, A. J. Detection of an explosive simulant via electrical impedance spectroscopy utilizing the UiO-66-NH₂ metal-organic framework. *Dalton Trans.* **2016**, *45*, 17113–17116.
- (42) Kandiah, M.; Usseglio, S.; Svelle, S.; Olsbye, U.; Lillerud, K. P.; Tilset, M. Post-synthetic modification of the metal-organic framework compound UiO-66. *J. Mater. Chem.* **2010**, *20*, 9848–9851.
- (43) Cavka, J. H.; Jakobsen, S.; Olsbye, U.; Guillou, N.; Lamberti, C.; Bordiga, S.; Lillerud, K. P. A new zirconium inorganic building brick forming metal organic frameworks with exceptional stability. *J. Am. Chem. Soc.* **2008**, *130*, 13850–13851.
- (44) Lv, G. R.; Liu, J. M.; Xiong, Z. H.; Zhang, Z. H.; Guan, Z. Y. Selectivity Adsorptive Mechanism of Different Nitrophenols on UIO-66 and UIO-66-NH₂ in Aqueous Solution. *J. Chem. Eng. Data* **2016**, *61*, 3868–3876.
- (45) Howarth, A. J.; Liu, Y. Y.; Hupp, J. T.; Farha, O. K. Metal-organic frameworks for applications in remediation of oxyanion/ cation-contaminated water. *CrystEngComm* **2015**, *17*, 7245–7253.
- (46) Spagnola, J. C.; Gong, B.; Arvidson, S. A.; Jur, J. S.; Khan, S. A.; Parsons, G. N. Surface and sub-surface reactions during low temperature aluminium oxide atomic layer deposition on fiber-forming polymers. *J. Mater. Chem.* **2010**, *20*, 4213–4222.

- (47) Sweet, W. J.; Parsons, G. N. In Situ Conductance Analysis of Zinc Oxide Nucleation and Coalescence during Atomic Layer Deposition on Metal Oxides and Polymers. *Langmuir* **2015**, *31*, 7274–7282.
- (48) Sweet, W. J.; Jur, J. S.; Parsons, G. N. Bi-layer Al₂O₃/ZnO atomic layer deposition for controllable conductive coatings on polypropylene nonwoven fiber mats. *J. Appl. Phys.* **2013**, *113*, 194303.
- (49) Moon, S. Y.; Liu, Y. Y.; Hupp, J. T.; Farha, O. K. Instantaneous Hydrolysis of Nerve-Agent Simulants with a Six-Connected Zirconium-Based Metal-Organic Framework. *Angew. Chem., Int. Ed.* **2015**, *54*, 6795–6799.
- (50) Wang, S.; Bromberg, L.; Schreuder-Gibson, H.; Hatton, T. A. Organophosphorous Ester Degradation by Chromium(III) Terephthalate Metal-Organic Framework (MIL-101) Chelated to N,N-Dimethylaminopyridine and Related Aminopyridines. *ACS Appl. Mater. Interfaces* **2013**, *5*, 1269–1278.
- (51) Katz, M. J.; Mondloch, J. E.; Totten, R. K.; Park, J. K.; Nguyen, S. T.; Farha, O. K.; Hupp, J. T. Simple and Compelling Biomimetic Metal-Organic Framework Catalyst for the Degradation of Nerve Agent Simulants. *Angew. Chem., Int. Ed.* **2014**, *53*, 497–501.
- (52) Katz, M. J.; Moon, S. Y.; Mondloch, J. E.; Beyzavi, M. H.; Stephenson, C. J.; Hupp, J. T.; Farha, O. K. Exploiting parameter space in MOFs: a 20-fold enhancement of phosphate-ester hydrolysis with UiO-66-NH₂. *Chem. Sci.* **2015**, *6*, 2286–2291.
- (53) Wagner, G. W.; Chen, Q.; Wu, Y. Reactions of VX, GD, and HD with nanotubular titania. *J. Phys. Chem. C* **2008**, *112*, 11901–11906.

- (54) Bisio, C.; Carniato, F.; Palumbo, C.; Safronyuk, S. L.; Starodub, M. F.; Katsev, A. M.; Marchese, L.; Guidotti, M. Nanosized inorganic metal oxides as heterogeneous catalysts for the degradation of chemical warfare agents. *Catal. Today* **2016**, *277*, 192–199.

3.8. Supporting Information

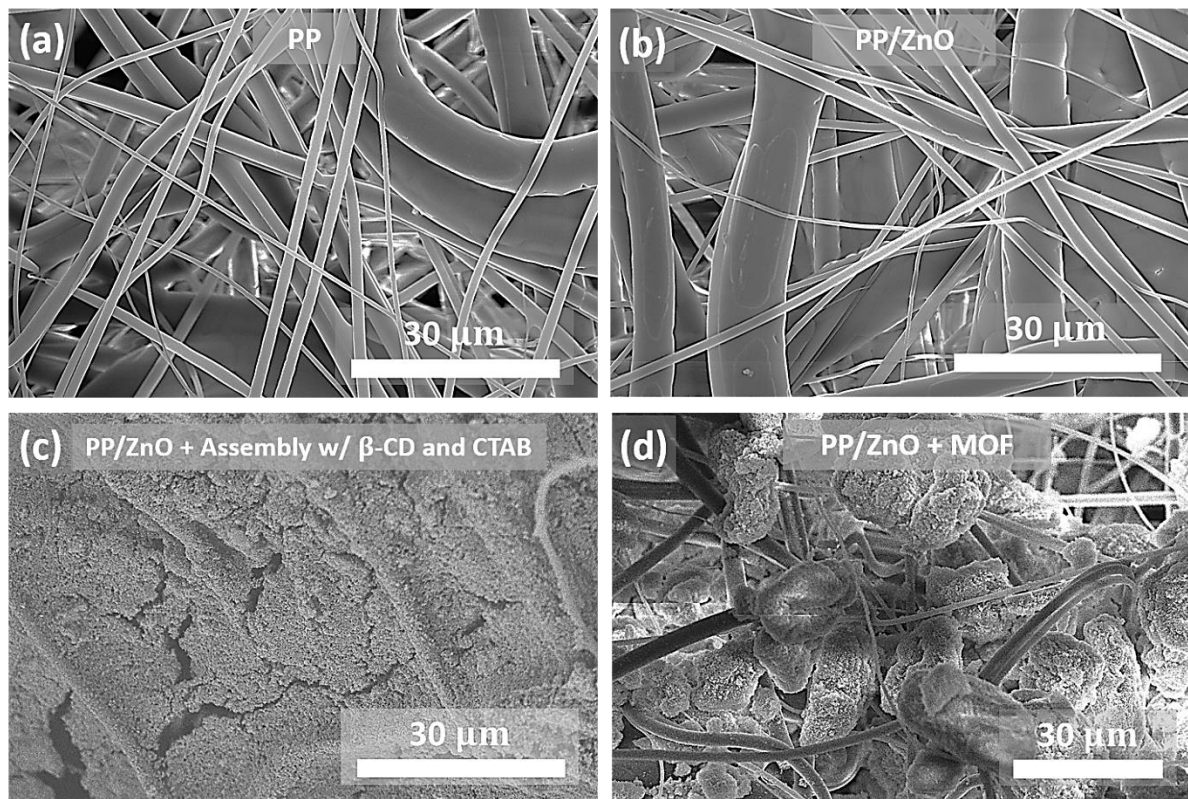


Figure S3.1. SEM images of fiber substrates: (a) Polypropylene (PP) and (b) PP coated with ZnO (PP/ZnO). SEM images of (c) PP/ZnO after assembly (UiO-66-NH₂ + β-CD + CTAB) in DMF and (d) that after being immersed in only UiO-66-NH₂ crystals without β-CD and CTAB in DMF. The amount of UiO-66-NH₂ (0.24 g) in 80 mL of DMF used in (c) and (d) is same as each other.

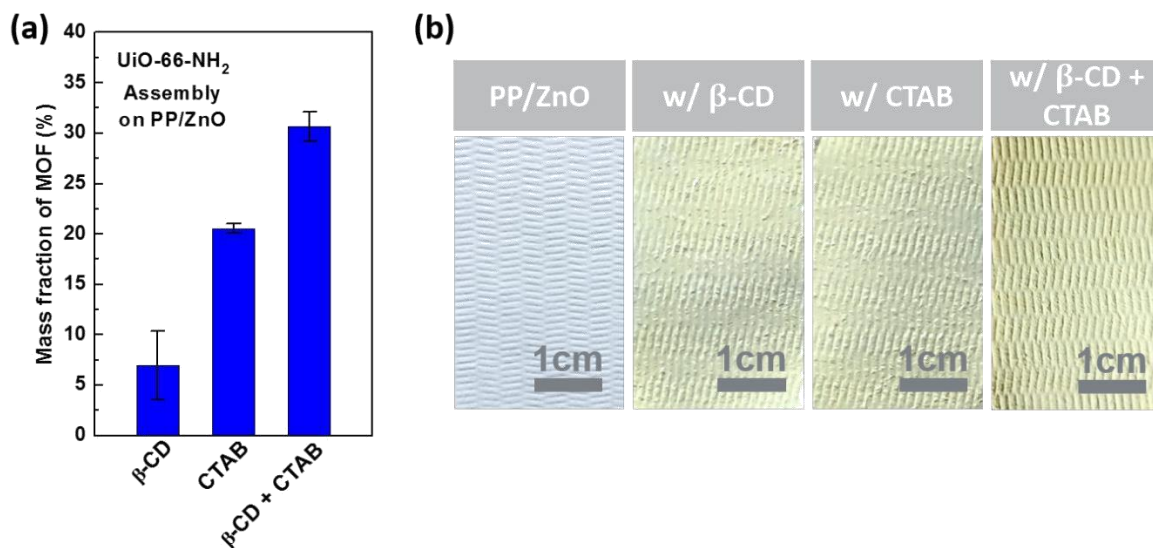


Figure S3.2. (a) Mass fraction comparison of UiO-66-NH₂ MOF crystals assembled on PP/ZnO substrates by β -CD, CTAB, and β -CD + CTAB, respectively. (b) A photograph of actual fiber mats used for the assembly with different component.

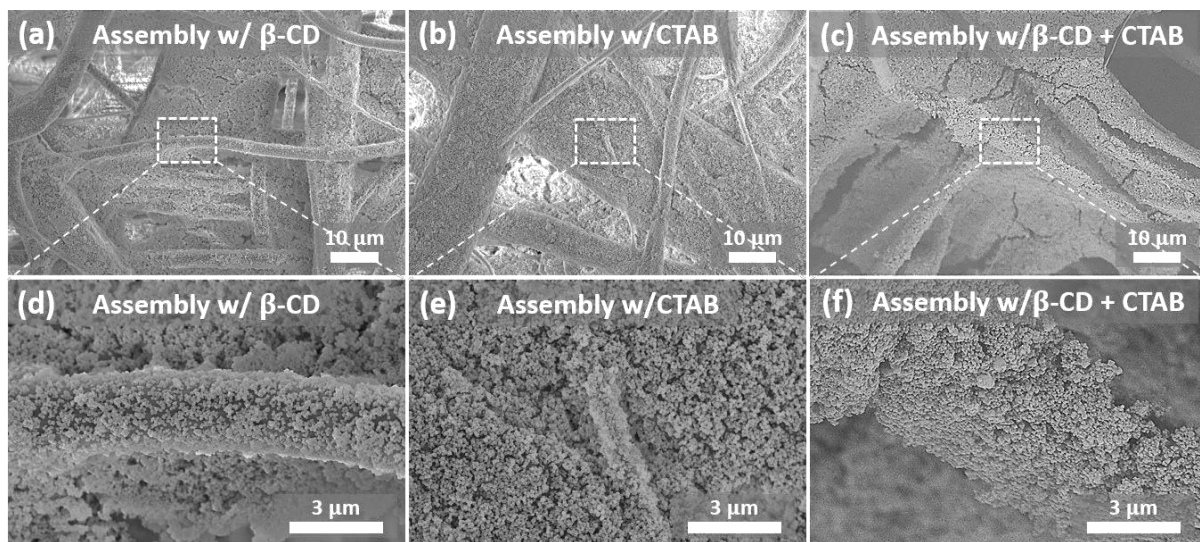


Figure S3.3. SEM images of assembled feature of UiO-66-NH₂ MOF crystals on PP/ZnO by means of β-CD (a and d), CTAB (b and e), and β-CD + CTAB (c and f).

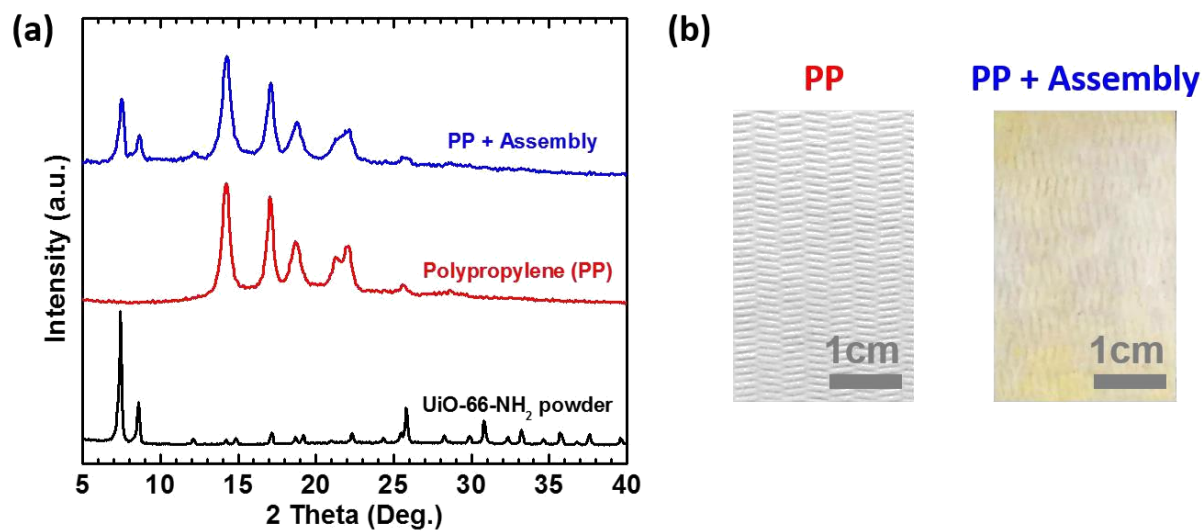


Figure S3.4. (a) XRD spectra of (from bottom to top) UiO-66-NH₂ powder, polypropylene (PP) as a substrate, and PP + Assembly fabric sample. (b) Actual fabric samples before (left) and after (right) “Assembly method” to untreated PP. Assembly solution contains as-synthesized UiO-66-NH₂ crystals + β -CD + CTAB.



Figure S3.5. Photographs of fiber mats with assembled MOFs after adhesion test was performed.

(a) Assembly with β -CD, (b) with CTAB, and (c) with β -CD + CTAB. Each fiber mat was swept 30 times using the brush in the image. All the assembly method was carried out on PP/ZnO.

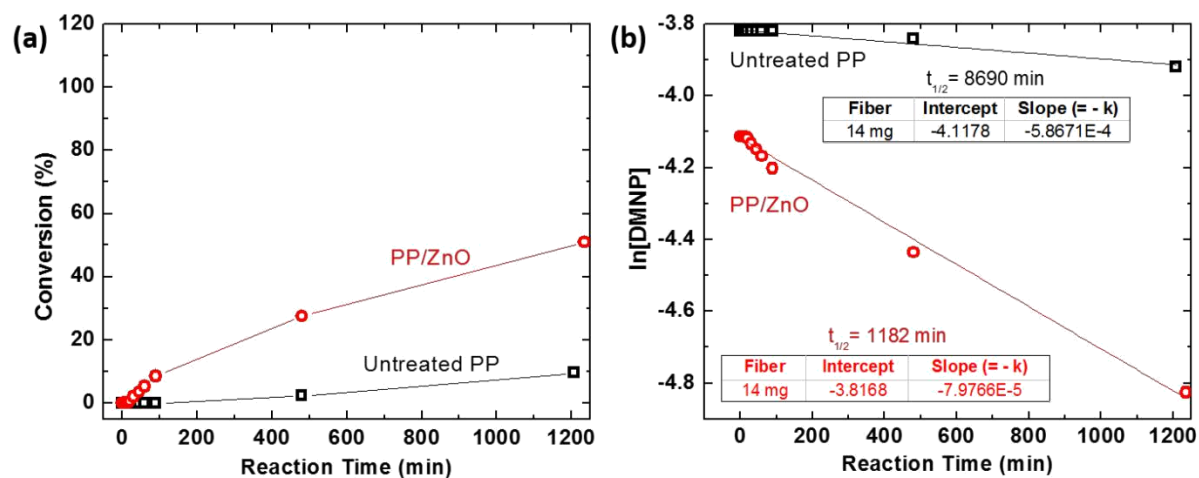


Figure S3.6. (a) Conversion profiles of DMNP to 4-nitrophenoxide versus the hydrolysis reaction time and (b) kinetic analysis using untreated PP and PP/ZnO fibrous scaffolds.

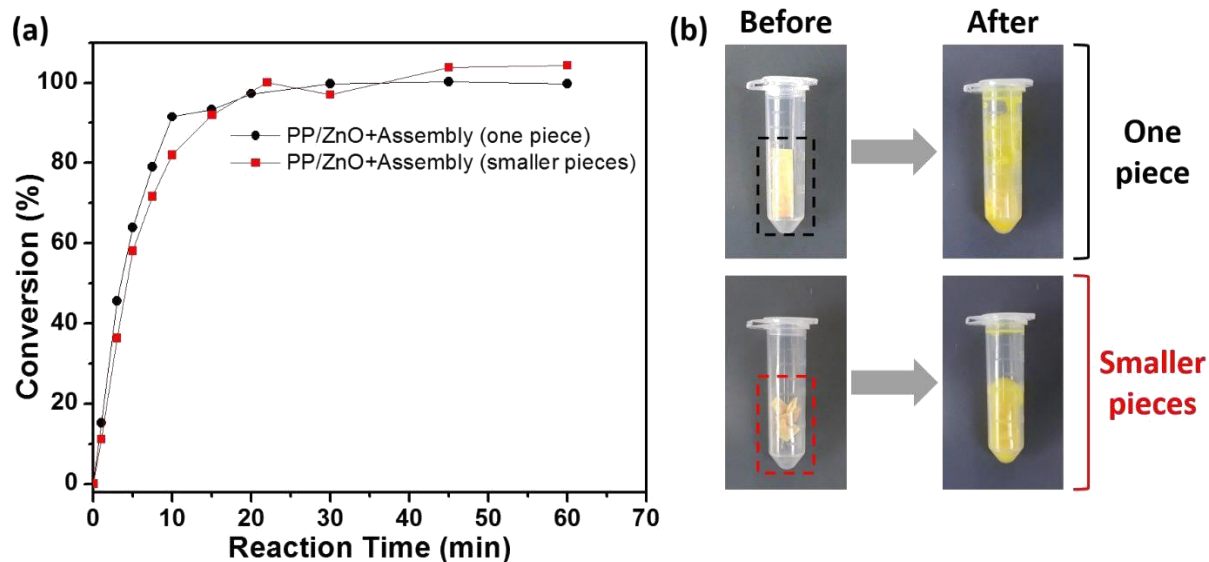


Figure S3.7. Fabric size effect on DMNP hydrolysis reaction catalyzed in the presence of PP/ZnO + Assembly. (a) Conversion profiles for the hydrolysis of DMNP with one piece ($m_{(\text{MOF}+\text{Fabric})} = 13.7 \text{ mg}$) or smaller pieces ($m_{(\text{MOF}+\text{Fabric})} = 13.6 \text{ mg}$) of PP/ZnO + Assembly at room temperature as a function of time. (b) Actual samples used before and after the catalytic reaction.

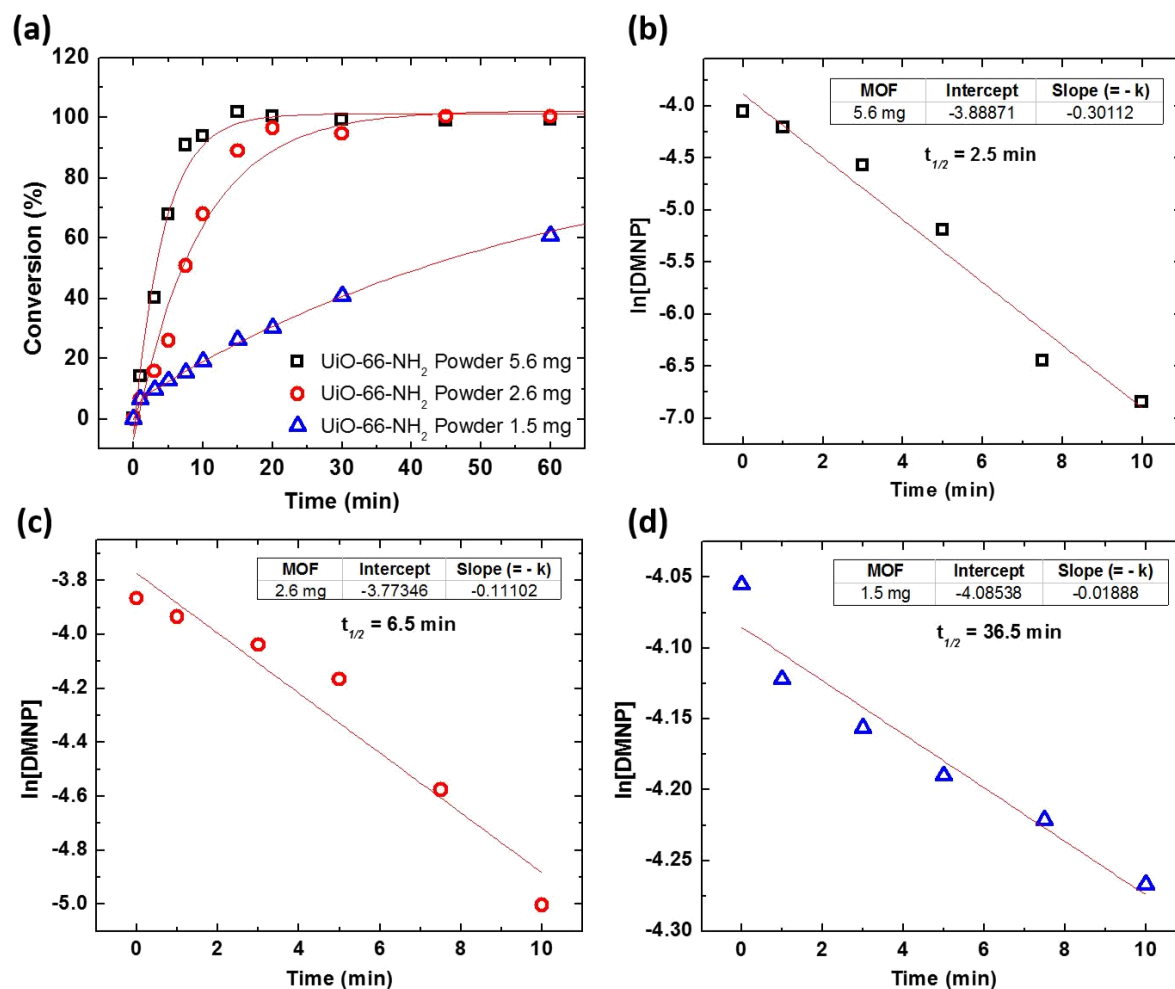


Figure S3.8. (a) Conversion profiles for the hydrolysis of DMNP in the presence of UiO-66-NH₂ powder with varying loading: 5.6 mg (□), 2.6 mg (○), and 1.5 mg (△). Kinetics plot of the reaction of DMNP in *N*-ethylmorpholine buffer solution with UiO-66-NH₂ powder at different catalyst loading: (b) 5.6 mg, (c) 2.6 mg, and (d) 1.5 mg to identify a reaction rate constant (k) and initial half-life ($t_{1/2}$) of each case. *UiO-66-NH₂ powder used is collected from remnants of assembly solution.

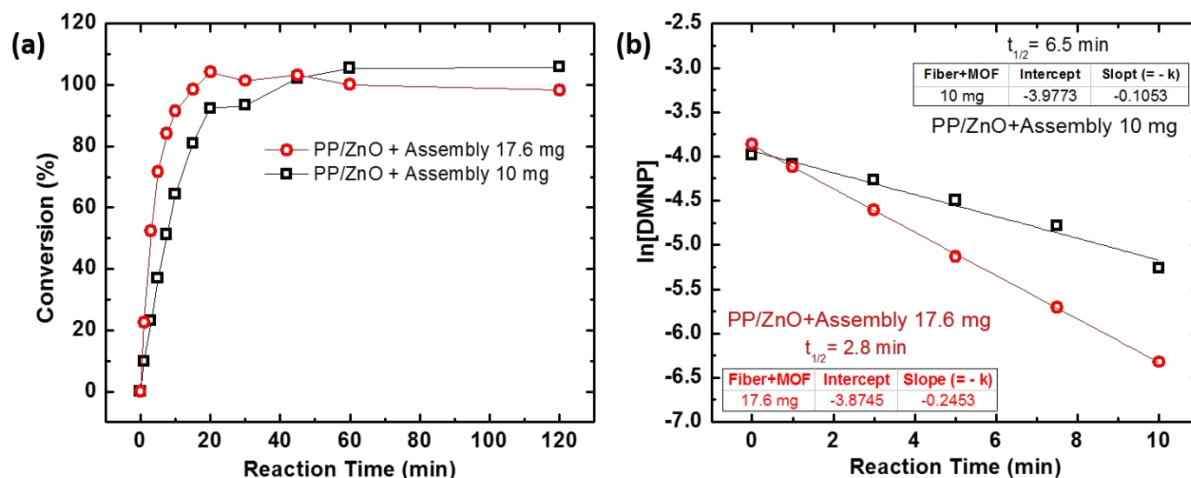


Figure S3.9. (a) Conversion profiles for the hydrolysis of DMNP in the presence of PP/ZnO + Assembly with different mass loading of the MOF-assembled fiber mats*: 10.0 mg (□) and 17.6 mg (○). (b) Kinetics plot of the reaction of DMNP in *N*-ethylmorpholine buffer solution with the MOF-assembled fiber mats at different catalyst loading: b) 10 mg and c) 17.6 mg to identify a reaction rate constant (k) and initial half-life ($t_{1/2}$) of each case. *MOF-assembled fiber mats used are PP/ZnO + Assembly.

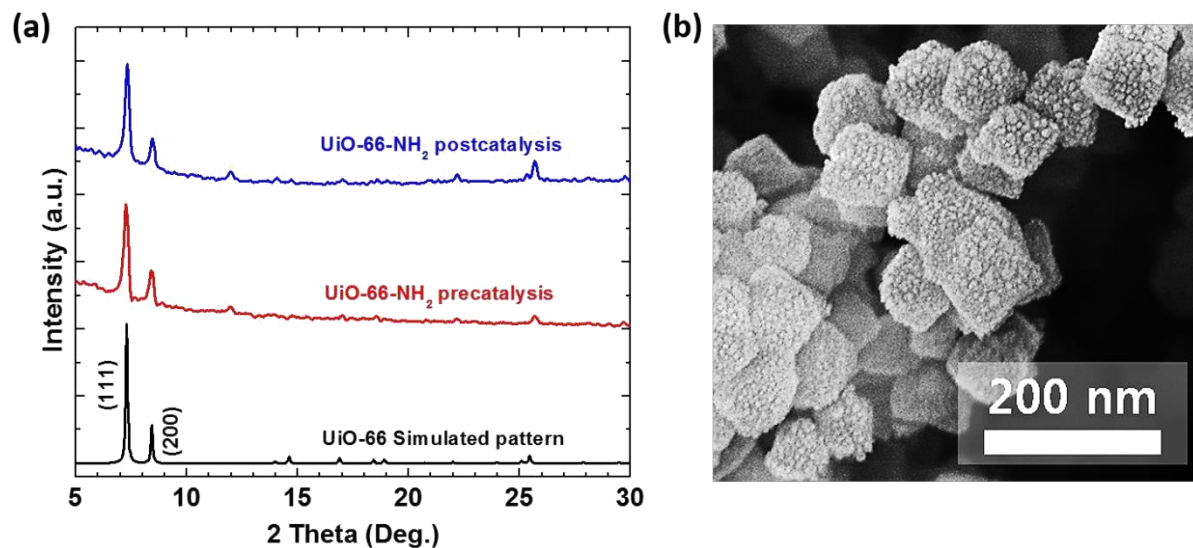


Figure S3.10. (a) PXRD data for UiO-66-NH₂ postcatalysis (top), precatalysis* (mid), and a simulated pattern (bottom). (b) SEM image of UiO-66-NH₂ postcatalysis, which is collected after being used for the catalysis of DMNP. There is no substantial change in peak intensity or position for UiO-66-NH₂ before and after functioning as a catalyst to decompose DMNP. Intensity of the peaks has been normalized at 7.3° in 2-theta corresponding to (111) of UiO-66-NH₂. *UiO-66-NH₂ precatalysis is collected from remnants of assembly solution.

CHAPTER 4

Toxic Organophosphate Hydrolysis Using Nanofiber-Templated UiO-66-NH₂ Metal–Organic Framework Polycrystalline Cylinders

CHAPTER 4 is a reprint of a manuscript published in *ACS Applied Materials & Interfaces*

Derek B. Dwyer,^{†,||} Dennis T. Lee,^{‡,||} Steven Boyer,[†] William E. Bernier,[†] Gregory N. Parsons,^{*,‡}
and Wayne E. Jones, Jr.^{*,†,§}

[†]Binghamton University State University of New York, 4400 Vestal Parkway East, Binghamton,
New York 13902, United States

[‡]Department of Chemical and Biomolecular Engineering, North Carolina State University, 911
Partners Way, Raleigh, North Carolina 27695, United States

[§]University of New Hampshire, 105 Main Street, Durham, New Hampshire 03824, United States

^{||}D.B.D. and D.T.L. contributed equally to this work.

4.1. Abstract

Metal organic frameworks (MOFs), the UiO series in particular, have attracted much attention because of the high surface area and ability to capture and decontaminate chemical warfare agents. Much work has been done on incorporating these MOFs into or onto textile materials while retaining the desirable properties of the MOF. Many different techniques have been explored to achieve this. Atomic layer deposition (ALD) of TiO_2 followed by solvothermal synthesis of MOF has become one of the most adaptable techniques for growing MOFs on the surface of many different polymer fabric materials. However, little work has been done with using this technique on polymer composite materials. In this work, UiO-66- NH_2 was grown onto the surface of poly(methyl methacrylate) (PMMA)/ $\text{Ti}(\text{OH})_4$ and poly(vinylidene fluoride) (PVDF)/ $\text{Ti}(\text{OH})_4$ composite fibers by first modifying the surface with ALD of TiO_2 (@ TiO_2) followed by solvothermal synthesis of MOF (@MOF). The catalytic activity of these materials was then evaluated using the simulant paraoxon-methyl (DMNP). These new MOF-functionalized composite fabrics were compared to polyamide-6 (PA-6)@ TiO_2 @MOF- and polypropylene (PP)@ TiO_2 @MOF-functionalized fabrics. PMMA/ $\text{Ti}(\text{OH})_4$ @ TiO_2 @MOF fibers resulted in unique hollowed fibers with high surface area of $264 \text{ m}^2/\text{g}$ and fast catalytic activity. The catalytic activity of these samples was found to be related to the active MOF mass fraction on the MOF-functionalized composite fabric, with the hollowed PMMA/ $\text{Ti}(\text{OH})_4$ @ TiO_2 @MOF having the highest weight percent of active MOF and a DMNP $t_{1/2}$ of 26 min followed by PA-6@ TiO_2 @MOF with 45 min, PVDF/ $\text{Ti}(\text{OH})_4$ @ TiO_2 @MOF with 61 min, and PP@ TiO_2 @MOF with 83 min.

4.2. Introduction

Chemical warfare agents (CWAs) are a continuing threat to military combatants and civilian personnel because of rogue use of these chemical weapons. The most dangerous of these chemical weapons are those containing phosphonate ester bonds.¹ Because of this, new materials that can capture and decontaminate CWAs, such as soman and sarin, are being developed. The most common materials used for capture and removal of CWAs are porous activated carbon materials.^{2,3} Zeolites have also shown potential in removal of CWA.^{4,5} Although these materials can capture the CWAs, they have limited capability in decontaminating the agent. New materials are being designed that are capable of both capturing these CWAs and decontaminating them to allow for safer handling of the contaminated materials.⁶ One of the most promising materials that can both capture and decontaminate chemical agents are zirconium-based metal-organic frameworks (MOFs).^{7,8} MOFs are highly porous materials made of inorganic metal-oxo nodes connected by organic linkers.⁹⁻¹¹

Zirconium-based MOFs have shown excellent thermal and hydrolytic stability and an ability to decontaminate simulants of CWAs along with the true agents.^{12,13} The UiO-66-NH₂ MOF specifically has attracted much interest because of the addition of the amine group on the organic linker which may act as a Brønsted base during the catalytic cycle, accelerating the rate of reaction for the phosphorus containing agents.¹⁴ Unfortunately, UiO-66-NH₂ is a powder when it is synthesized by a conventional solvothermal method which is not favorable for practical use in protective garments or fabric-like materials because of the difficulties with integrating powders into fabrics. Several groups have shown that incorporation of MOF into fabric material can make a functionalized fabric with similar or improved catalytic properties of the pure MOF powder, and that these functionalized fabrics are more useful in real application than the MOF in a powder

form.¹⁵⁻¹⁷ Recently published work has shown successful incorporation of UiO-66-NH₂ into a poly(vinylidene fluoride) (PVDF) fabric using electrospinning while retaining its catalytic ability toward CWAs.¹⁵ Work done by McCarthy et al. has shown when incorporating UiO-66 into a polymer nanofiber (NF) composite of poly(methyl methacrylate) (PMMA) along with hydrolyzed titania, in the form Ti(OH)₄, the catalytic activity of the material toward the CWA simulant paraoxon-methyl (DMNP) is increased because of the acid–base activity of the incorporated Ti(OH)₄.¹⁷ However, this method of incorporating MOF into fabric materials is limited to materials that can be prepared through a sol–gel synthesis and electrospinning. This method also has the disadvantage of potential loss of surface area (SA) and catalytic sites from the MOF due to aggregation of MOF in the polymer during preparation.¹⁸

Other methods have explored the incorporation of MOF onto the surface of fabrics instead of inside the fabric material. These methods include hot-pressing and surface growth using a fabric with a functional surface.^{19,20} However, both of these methods have limitations to what fabrics can be used; the hot-pressing method requires temperatures of 200 °C, whereas the surface growth method requires fabrics that have a surface with functional groups. Another method has shown successful growth of several Zr-based UiO series MOFs such as UiO-66, UiO-66-NH₂, and UiO-67 onto a polyamide-6 (PA-6) NF substrate through a combination of atomic layer deposition (ALD) of TiO₂ followed by solvothermal growth of the MOF.¹⁶ The underlying mechanism of interactions of ALD precursors (e.g., metal-organic species and water molecules) with a diverse types of polymers such as polypropylene (PP), polyvinyl alcohol, cotton, PA-6, poly(ethylene terephthalate), and PMMA had been well proved.²¹⁻²³ With that development, the ALD technique has been actively utilized to impart highly dense nucleation sites even to chemically inert polymers like PP for further processes.^{24,25}

The in situ hydrothermal MOF growth onto inorganic surfaces deposited via ALD processes has the advantage of allowing integration of MOF onto an array of different materials which are not limited to electrospinning preparation or polymer NFs. Lee et al. has recently demonstrated that ALD TiO₂ layer, compared with Al₂O₃ and ZnO, on PP microfibers led to the most effective MOF/cloth composites in terms of MOF adhesion to the fibers and DMNP degradation rate.²⁷ Therefore, in this work, we particularly utilized ALD TiO₂ to generate uniform MOF nucleation sites on the surface of both electrospun PMMA/Ti(OH)₄ and PVDF/Ti(OH)₄ composite fibers. The effects of using ALD followed by solvothermal synthesis of UiO-66-NH₂ MOF on the structure and the catalytic activity of the final MOF/fiber polymer composites were studied. The catalytic activity and morphology of PMMA/Ti(OH)₄@TiO₂@UiO-66-NH₂ and PVDF/Ti(OH)₄@TiO₂@UiO-66-NH₂ were compared with those of PP@TiO₂@UiO-66-NH₂ and previously published PA-6@TiO₂@UiO-66-NH₂.¹⁶ These four materials are characterized, and the catalytic activity of the materials was evaluated for hydrolysis of DMNP.

4.3. Experimental Section

PVDF ($M_w \approx 275\ 000$), PMMA ($M_w \approx 996\ 000$) titanium (IV)isopropoxide (TTiP), N,N-dimethylformamide (DMF), chloro-form, dimethyl 4-nitrophenyl phosphate (methyl paraoxon, DMNP), and acetone were purchased from Sigma-Aldrich and used without any further purification.

Fabrication of PVDF/Ti(OH)₄ and PMMA/Ti(OH)₄ Fibers. PVDF/Ti(OH)₄ and PMMA/Ti(OH)₄ polymer NFs were fabricated through a sol-gel synthesis and electrospinning. PVDF/Ti(OH)₄ was prepared by first dissolving 360 mg of PVDF pellets in 2 mL of DMF using sonication and heat at 50 °C. 0.67 mL (640 mg) of TTiP was then added along with 1 mL of acetone and stirred for half an hour. PMMA/Ti(OH)₄ NFs were prepared by dissolving 320 mg of

PMMA powder in 2 mL of chloroform, 0.67 mL of TTiP was added, and the sol–gel was stirred for 30 min. DMF (2 mL) was added, and the sol–gel was stirred for 2 h before electrospinning. A Spellman SL 30 generator was used to apply 25 kV across the sol–gel solution and deposited the fibers onto an aluminum foil collector at 11 cm for the PMMA/Ti(OH)₄ and 15 1/2 cm for PVDF/Ti(OH)₄. The as-spun fibers were then set out overnight to allow hydrolysis of TTiP to Ti(OH)₄.^{17,32,33}

ALD of TiO₂ on Polymeric Fibers. ALD TiO₂ was performed to different polymeric fibers [i.e., PP, PA-6, PVDF/Ti(OH)₄, and PMMA/Ti(OH)₄] before growing UiO-66-NH₂ MOF. A laboratory-made hot-wall viscous-flow vacuum reactor was used to carry out conformal TiO₂ coating on each fiber substrate.^{16,26,27} The ALD deposition condition was maintained at 90 °C under approximately 1.8 Torr. To obtain a well-controlled TiO₂ layer on each substrate, the chamber was first dosed titanium (IV)chloride (TiCl₄, 99%, STREM Chemicals) for 1 s, followed by 40 s of N₂ (99.999%, Airgas, further purified with an Entegris GateKeeper) to purge unreacted precursors and byproducts. After that, deionized H₂O was used to dose the chamber for 1 s with subsequent purge with N₂ for 40 s. All fibers were coated with 200 cycles of ALD TiO₂ before being used as substrates for MOF growth.

MOF Growth onto Polymeric Fibers. The MOF was prepared using previously published methods.^{28,29} First, 0.080 g, 0.343 mmol of ZrCl₄ was dissolved in 20 mL of DMF in 20 mL glass scintillation vial through 1 min of sonication. 2-Aminoterephthalic acid (0.062 g, 0.343 mmol, 2-ATA), 25 μL of deionized water, and 1.33 mL of concentrated hydrochloric acid (NF/FCC grade, Fisher) was added to the prepared ZrCl₄ solution under stirring (500 rpm). After 5 min of stirring, 10–15 mg of free-standing PP, PA-6, PVDF/Ti(OH)₄, or PMMA/Ti(OH)₄ fiber scaffolds were immersed into the MOF precursor solution prepared, respectively. The vial with fiber samples was

then heated in a box furnace (Thermo Scientific) to 85 °C for 24 h. After the solvothermal MOF growth procedure, composite products (MOF + fiber) were separately collected from MOF crystals grown in a liquid phase. The collected products were washed with 80 mL of DMF twice under magnetic stirring (500 rpm) for 12 h. After that, the MOF-coated fiber samples were further rinsed with 80 mL of anhydrous ethanol (200 proof, VWR), and the solvent was replaced every 12 h for 36 h in total. Finally, the products were dried at room temperature at reduced pressure for at least 12 h and stored in a desiccator before use. The UiO-66-NH₂ MOF powders in liquid phase of each batch were also collected by filtering out unreacted precursors, byproducts, and residual DMF through PP membrane (0.45 μm pore size, Whatman). After that, the filtered solid was rinsed with 80 mL of DMF and 80 mL of anhydrous ethanol in a sequential manner in the filtration system. Eventually, the final solid was obtained via filtration and dried at room temperature at reduced pressure for 12 h. The fully dried MOF powders were stored in a desiccator until being used for further characterizations.

Hydrolysis of Methyl Paraoxon. Degradation experiments were performed following a previously published procedure by Katz et al.³⁰ First, a buffer solution (pH 10) of N-ethyl morpholine (0.45 M) in distilled water was prepared. In a 4 mL glass vial, 12 mg of the MOF/fiber catalyst was added to 1 mL of prepared buffer solution. The fiber was dispersed in the solution for 30 min at a stir speed of 750 rpm. Next, 4 μL of DMNP simulant was added to solution, 10 μL aliquots were taken from the solution at specified times and diluted in 5 mL of prepared buffer solution for analysis with UV-vis spectroscopy using an hp Hewlett Packard diode array spectrophotometer. Product formation was observed by tracking the 4-nitrophoxide product peak at 407 nm. The reaction of DMNP with fibers catalyst is shown in Figure 4.1. The apparent rate constant of the corresponding MOF powder for each of the samples was determined by performing

hydrolysis experiments with varying amounts of MOF powder 5.6, 4.0, and 3.0 mg. The calculations used to determine the apparent rate constant and the weight fraction of active MOF are shown in the work published by Lee et al.²⁹

Stability Test of PMMA/Ti(OH)₄ Fibers. The stability of the PMMA/Ti(OH)₄ fibers with and without ALD TiO₂ layer under acidic environment at 85 °C was studied. A test solution in a glass scintillation vial containing ZrCl₄ (0.080 g), deionized water (25 μL), and HCl (1.33 mL) dispersed in 20 mL of DMF was prepared. The linker 2-ATA was intentionally left out in the test solution because the other chemicals have been known to form strong acidic environment.³¹ Untreated PMMA/Ti(OH)₄ and PMMA/Ti(OH)₄@TiO₂ fibers were transferred into each prepared vial with solution and heated them to 85 °C for 24 h in a box furnace. The product was then characterized using SEM.

4.4. Results and Discussion

All fibers were characterized by electron microscopy. SEM images were taken at each stage of synthesis for the different polymer substrates as shown in Figure 4.2. The images show very little change in the appearance of the fibers after ALD treatment with TiO₂. As seen in Figure 4.2, UiO-66-NH₂ MOF is clearly visible on the surface of the ALD treated fibers after solvothermal synthesis. The samples PMMA/Ti(OH)₄@TiO₂@MOF, PP@TiO₂@MOF, and PA-6@TiO₂@MOF show significant growth of MOF on the surface, whereas PVDF/Ti(OH)₄@TiO₂@MOF shows very little growth. The poor growth observed on the PVDF composite is potentially due to the fluorine titanium interaction that occurs between the PVDF and the ALD TiO₂. Fluorine–titanium interactions have been reported in the past,⁴⁰ and this interaction is likely changing the surface chemistry of the ALD TiO₂, creating a less favorable binding

environment for the MOF resulting in the poor growth observed. Both PMMA/Ti(OH)₄@TiO₂@MOF and PP@TiO₂@MOF samples have large fiber diameters with diameters over 500 nm while PVDF/Ti(OH)₄@TiO₂@MOF and PA-6@TiO₂@MOF have relatively small diameters less than 500 nm. The PMMA/Ti(OH)₄@TiO₂@MOF samples exhibit a very unique hollowed morphology compared with the other three samples prepared under the same synthetic and solvothermal conditions shown in Figure 4.3. Essentially all of the PMMA/Ti(OH)₄@TiO₂@MOF fibers have been completely hollowed from the preparation procedure.

A series of stability tests were performed on the PMMA/ Ti(OH)₄ polymer to better understand the hollowing process of the PMMA/Ti(OH)₄@TiO₂@MOF fibers. PMMA/Ti(OH)₄ NFs with and without an ALD TiO₂ layer were exposed to the acidic environment created when synthesizing the UiO-66-NH₂ MOF.³¹ The linker 2-ATA was left out to prevent the formation of MOF. The results of the PMMA/ Ti(OH)₄ are shown in Figure 4A-C. The PMMA/Ti(OH)₄ fiber structures were noticeably collapsed after the solvothermal treatment. On the other hand, PMMA/Ti(OH)₄@TiO₂ fibers retained their fiber morphology after solvothermal treatment, Figure 4D. Furthermore, hollow fiber structures are clearly observed in the corresponding magnified images, Figure 4E,F. The collapse of the PMMA/Ti(OH)₄ fibers, along with the formation of hollowed fiber structures for the ALD treated PMMA/Ti(OH)₄@TiO₂ show that ALD TiO₂ is essential for the formation of hollowed NF structures, and the ALD TiO₂ acts as a stable metal oxide shell, whereas the PMMA/Ti(OH)₄ composite fibers are etched away under the acidic environment of the solvothermal synthesis. This etching of the polymer composite is due to the instability of the PMMA polymer itself and does not result from reaction between the Ti(OH)₄ and the solution because this hollowing is not observed with the more chemically stable PVDF polymer

composite. A schematic illustration of MOF integration procedures on both unstable PMMA/Ti(OH)₄ and stable PVDF/Ti(OH)₄ composite fiber structures is presented in Figure 4.5.

TEM was performed on the four different samples to look at the morphology of the MOF on the surface of the different polymer substrates. Figure 4.6 shows that for the PA-6@TiO₂@MOF and PVDF/Ti(OH)₄@TiO₂@MOF the MOF is grown as large spherical nodes, while the MOF on PP@TiO₂@MOF is more globular. The hollowed PMMA/Ti(OH)₄@TiO₂@MOF fibers do not form these spherical or globular nodes but rather a relatively uniform MOF layer over the surface of the hollow fiber. We speculate that the microroughness observed by SEM (Figure 4.2) on the PMMA/Ti(OH)₄ fiber surface, which is retained after the conformal ALD TiO₂ step, may result in denser nucleation sites compared with the smoother PP and nylon fibers, giving rise to a larger number of smaller crystals on the PMMA/Ti(OH)₄ samples, as observed by TEM in Figure 4.6.

Raman spectrometry was used to characterize the different polymer substrates. ATR-FTIR was also performed on the PMMA/Ti(OH)₄@TiO₂@MOF and PVDF/Ti(OH)₄@TiO₂@MOF samples for further characterization. The Raman and IR modes of the respective samples are shown in Table 4.1. The Raman spectra of the PMMA/Ti(OH)₄@TiO₂@MOF sample, Figure 4.7A, show a significant loss of the primary C–H stretches from the PMMA after the growth of the MOF. This further supports that the PMMA/Ti(OH)₄ is completely etched away during the solvothermal synthesis of MOF because of poor stability of the PMMA/Ti(OH)₄ in the acidic MOF precursor solution. The UiO-66-NH₂ Raman signature is presented in the Raman spectrum of the PMMA/Ti(OH)₄@TiO₂@MOF, Figure 4.7A but is more prominent in the ATR-FTIR of the PMMA/Ti(OH)₄@TiO₂@MOF. Again, essentially all FTIR signals from the PMMA are lost after the solvothermal growth of MOF and are replaced by the C-NH₂, C=C and COO⁻ vibrational

modes from the MOF linker along with vibrational signals from the Zr-O of the MOF metal nodes, supporting the presence of the UiO-66-NH₂ MOF in the sample, Figure 4.7B. The PVDF/Ti(OH)₄@TiO₂ sample shows significant browning in color after ALD of TiO₂. The sample also becomes much more brittle after the treatment. After the solvothermal growth of UiO-66-NH₂ MOF, the PVDF/Ti(OH)₄@TiO₂@MOF sample appears to become even more brittle compared with the prior versions of the sample. The Raman spectra of PVDF/Ti(OH)₄@TiO₂@MOF sample show a decrease in intensity and broadening of the C-H stretches in the PVDF backbone over the course of the sample preparation, supporting the physical observation of the color change and brittleness of the material. This suggests that although the PVDF is more chemically stable than PMMA, the structure of the material is still compromised during the sample preparation, Figure 4.7C. As in the ATR-FTIR of PMMA/Ti(OH)₄@TiO₂@MOF, the ATR-FTIR of PVDF/Ti(OH)₄@TiO₂@MOF shows prominent MOF signals in the spectrum, supporting the presence of MOF on the fiber sample. The Raman spectra of the PP@TiO₂@MOF and PA-6@TiO₂@MOF samples show no change in the C-H stretches of either PP or PA-6, signifying that the polymers are stable over the course of the ALD and solvothermal treatments, Figure 4.8A,B. This is supported by work done in the past with these two polymers where no evidence of degradation of the polymer was reported from this treatment.^{16,27} The Raman spectra of both PP@TiO₂@MOF and PA-6@TiO₂@MOF show evidence of MOF present on the material, Figure 4.8A,B.

N₂ adsorption-desorption isotherms were performed on the MOF/fiber composites along with the residual UiO-66-NH₂ powder that was collected from each sample after synthesis, Figure 4.9. The SA analysis revealed that the hollowed PMMA/Ti(OH)₄@TiO₂@MOF sample featured the highest SA with 264 (m²/g_(MOF+fiber)) followed by PA-6@TiO₂@MOF with 158 (m²/g_(MOF+fiber))

and then PVDF/Ti(OH)₄@TiO₂@MOF and PP@TiO₂@MOF with 84 (m²/g_(MOF+fiber)) and 8 (m²/g_(MOF+fiber)), respectively, Table 4.2. The SA analysis of the MOF powder showed the opposite trend with the powder from the PP@TiO₂@MOF having the highest SA with 1411 (m²/g) followed by PA-6@TiO₂@MOF 900 (m²/g), PVDF/Ti(OH)₄@TiO₂@MOF 861 (m²/g) and PMMA/Ti(OH)₄@TiO₂@MOF 641 (m²/g). The weight percent of MOF on each of the four polymer samples can be estimated using the SA analysis of the fibers samples and the pure MOF is shown in the work done by Zhao et al.¹⁶ The sample PP@TiO₂@MOF was found to have the lowest weight percent of MOF with less than 1 wt %, PVDF/Ti(OH)₄@TiO₂@MOF has a weight percent of ~10 wt %, PA-6@TiO₂@MOF had the second highest weight percent of MOF with a weight percent of ~18 wt %, Table 4.2. Finally, the hollowed PMMA/Ti(OH)₄@TiO₂@MOF was found to have the highest weight percent of MOF with 41 wt %, Table 4.2. The large difference in weight percent of MOF between the PMMA/Ti(OH)₄@TiO₂@MOF and the other three samples is a result of the hollowed morphology of the fibers. There is no mass contribution from the PMMA polymer because of the hollowing process which leaves the bulk of the mass of the material from a combination of MOF that has been formed on the surface and the TiO₂ shell.

The catalytic activity of the samples was tested using a procedure developed by Katz et al. with the nerve agent simulant DMNP.³⁰ The results are shown in Figure 4.10. The PP@TiO₂@MOF showed the slowest reaction with a half-life of 83 min, PVDF/Ti(OH)₄@TiO₂@MOF exhibited the next fastest rate of reaction with a half-life of 61 min, PA-6@TiO₂@MOF had the second fastest rate of reaction with a half-life of 45 min. Finally, the PMMA/Ti(OH)₄@TiO₂@MOF showed the fastest rate of reaction with a half-life of 26 min, Figure 4.10. The rates achieved by the four fiber samples showed a correlation between the rate of hydrolysis and the mass of MOF on surface of the sample. As a comparison, we also measured the

rate of DMNP degradation using UiO-66-NH₂ MOF powder synthesized simultaneously with each batch of the UiO-66-NH₂ MOF on fiber samples, and the results are given in Figure 4.10. The MOF powders showed very similar rates with half-lives between 5 and 8 min.

To understand the difference in the catalytic activity of the surface bound MOF on each of the different polymer scaffolds, the weight fraction of MOF on each of the four samples that contributed to the observed rate was determined using the same procedure performed by Lee et al.²⁹ To do this, the rate of DMNP hydrolysis was first measured using various amounts of the pure MOF collected from each of the four-sample preparation, and the apparent rate constant (k_{app}) for each batch of MOF was calculated. The k_{app} values obtained are shown in Table 4.3, along with the approximate uncertainty from the data fit. The values for k_{app} are approximately the same, within experimental error.

Using the calculations shown in Lee et al., the MOF mass fraction was calculated from the apparent rate constant and was found to be 8.0, 3.0, 3.8, and 2.0% for PMMA/Ti(OH)₄@TiO₂@MOF, PVDF/Ti(OH)₄@TiO₂@MOF, PA-6@TiO₂@MOF, and PP@TiO₂@MOF, respectively, Table 4.3.²⁹ Compared with the work published by Lee et al. the apparent rate constants and the active MOF mass fraction for these samples were found to be lower. It is difficult to discern why the rates of these samples differ from the previously published work because each of the MOF powders that were tested were prepared as different batches and made with different substrates. The lower rates in this work are likely due to a difficulty in collecting pure MOF from the synthetic batches because of fiber flakes that would remain after filtration for these samples, PMMA/Ti(OH)₄@TiO₂@MOF specifically. Another significant difference is that the MOF prepared by Lee et al. was done without HCl modulation, whereas the MOF sample prepared in this work is. Typically, HCl modulation is done to introduce defects in the MOF structure resulting

in faster rates of hydrolysis. However, the effect of HCl modulation on MOF quality in the presence of different fibers substrates is not well studied, which may contribute to the differences in apparent rate constant found in this work. When comparing the MOF mass fraction determined from the apparent rate constant to that obtained from the SA calculation, it can be reasoned that significant portions of the MOF on PMMA/Ti(OH)₄@TiO₂@MOF, PVDF/Ti(OH)₄@TiO₂@MOF, and PA-6@TiO₂@MOF are not contributing to the hydrolysis of the DMNP simulant. This can be explained by the TEM images shown in Figure 4.6. The large spherical nodes of MOF on the surfaces of PVDF/Ti(OH)₄@TiO₂@MOF and PA-6@TiO₂@MOF likely prevent DMNP from reaching the MOF active sites buried within the nodes preventing much of the MOF from contributing to the reaction.

At first glance, one would expect to see that PMMA/Ti(OH)₄@TiO₂@MOF has the highest catalytically active MOF because of the more evenly distribution of the MOF along the surface of the structure. However, comparing the MOF mass fraction obtained from SA analysis (41.2 wt %) and from the apparent rate constant (8.0 wt %), there is about 33 wt % not accounted for which could be due to two possibilities. First, the SA calculations used do not account for the increased SA from the hollowing process which could lead to an inaccurate wt % calculation. Second, and more likely, is the active sites of the MOF could be poisoned from the PMMA polymer or whatever polymer byproducts are produced from the hollowing process as it is being removed during the solvothermal synthesis of MOF. This could explain the observed broadening in the MOF signals seen in the FTIR, Figure 4.7B. Although PP@TiO₂@MOF showed the slowest DMNP hydrolysis rate, it actually showed the best activity in terms of the amount of MOF utilized on the surface of material likely reaching 100%. This is potentially because of the better distribution of MOF on the surface when comparing with the samples with PVDF and PA-6, and because of the chemical

stability of the PP, there was no possibility of inhibition of the MOF active sites by any polymer byproducts. This concludes that the differences observed in the rate of DMNP degradation for the four samples were a direct result of the weight percent of active MOF on the surface of the fibers.

4.5. Conclusions

Conformal coating of TiO₂ as MOF nucleation sites on four different types of polymer fibers was tested successfully based on using the ALD growth process. Differences in chemical and physical stability of the polymer fiber substrates to the MOF synthetic condition resulted in different final composite structures. Fibers with stable components [i.e., PP, PA-6, and PVDF/Ti(OH)₄] tend to maintain their fiber structures (Figure 4.5A), whereas relatively unstable PMMA/Ti(OH)₄ fibers were found to yield hollow fibers of TiO₂ (from ALD) coated with UiO-66-NH₂ MOF crystals for PMMA/Ti(OH)₄@TiO₂ fibers. TEM results showed bulbous growth of MOF on the surfaces of the stable polymers PVDF/Ti(OH)₄@TiO₂, PA-6@TiO₂, and PP@TiO₂ while MOF grown on the surface of PMMA/Ti(OH)₄@TiO₂ did not show defined spherical shapes of MOF on the surface. The tube structures demonstrated a more uniform distribution of MOF on the surface because of the microroughness of the surface. Hollowed PMMA/Ti(OH)₄@TiO₂@MOF has the highest SA (264 m²/g_(MOF+fiber)) compared with those of the other three fiber samples. The catalytic studies of the four samples using the DMNP simulant revealed that PP@TiO₂@MOF had the slowest catalytic activity followed by PVDF/Ti(OH)₄@TiO₂@MOF and then PA-6@TiO₂@MOF; the hollowed PMMA/Ti(OH)₄@TiO₂@MOF gave the fastest rate of reaction. However, the PP@TiO₂@MOF sample utilized the highest percentage of MOF on its surface compared with the other three samples with PMMA/Ti(OH)₄@TiO₂@MOF utilizing the lowest percentage of its surface bound MOF. The

observed rates of reaction are directly related to the weight percent of active MOF grown on the surface of the fiber samples. Because of the hollowing process of PMMA/Ti(OH)₄@TiO₂@MOF, a significant percentage of the mass of the material is from the surface bound MOF. However, the hollow PMMA/Ti(OH)₄@TiO₂@MOF has low utilization of the surface bound MOF likely because of the interference of PMMA polymer or polymer byproducts with the active sites of the MOF. Even though the hollowed PMMA/Ti(OH)₄@TiO₂@MOF fibers do not utilize much of the MOF on its surface, it still has the fastest observed rate of degradation because of the huge mass loading of MOF showing great promise for agent decontamination. This work has also demonstrated the robustness of this technique for fabrication of UiO-66-NH₂ MOF onto both pure polymer substrates and polymer composites substrates.

4.6. Figures

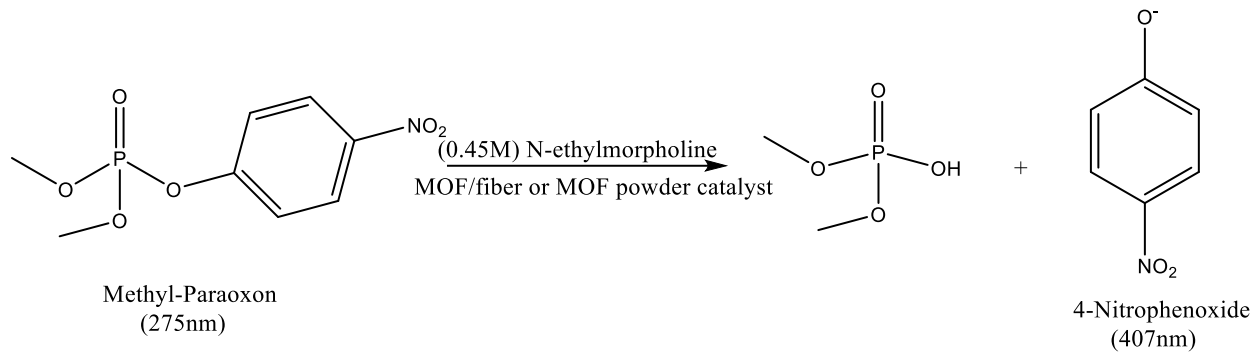


Figure 4.1. Reaction of decontamination of DMNP using MOF/fiber or MOF powder catalyst.

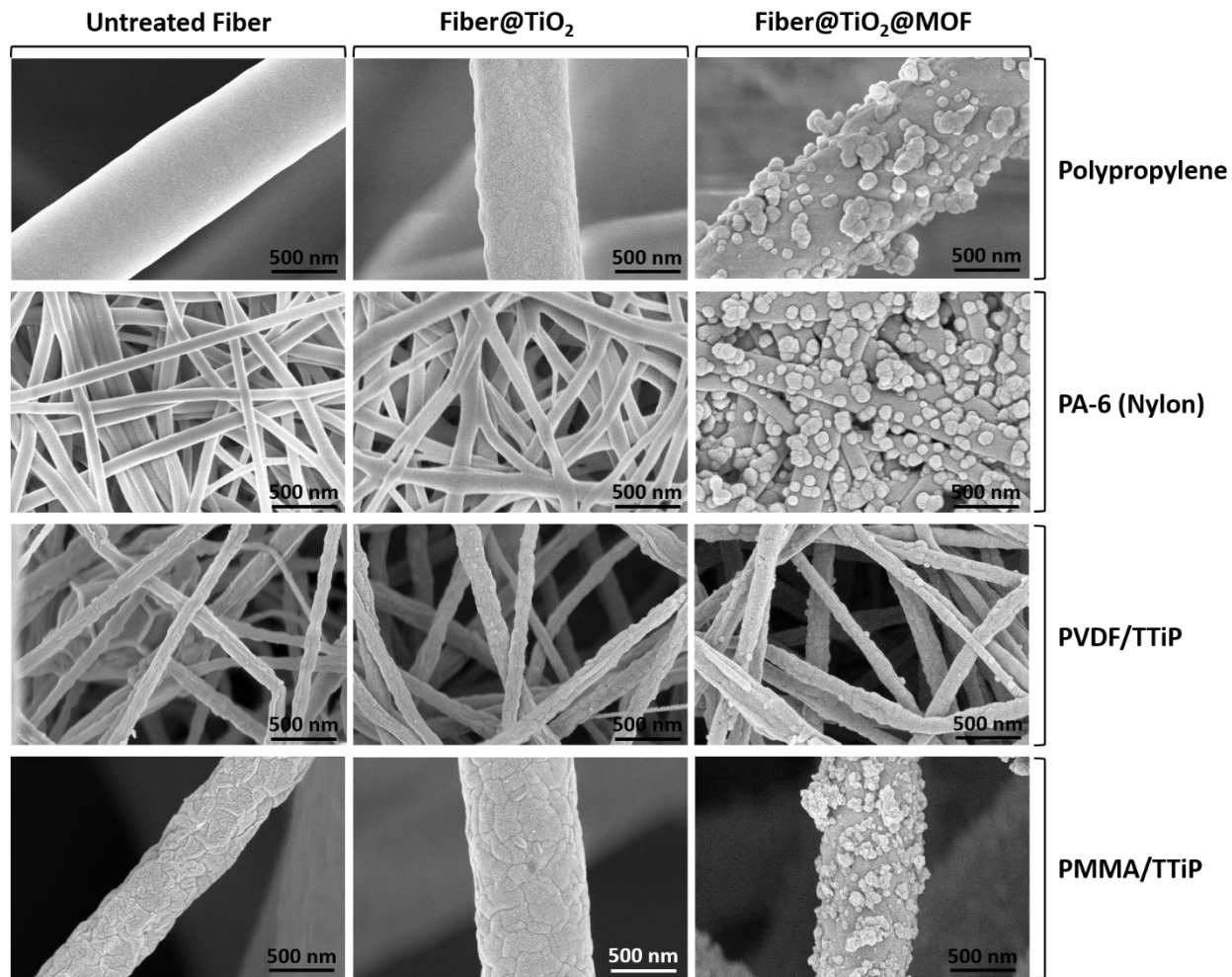


Figure 4.2. SEM images of untreated fibers, fibers after ALD treatment of TiO₂, and MOF/fiber samples after ALD and solvothermal synthesis of MOF.

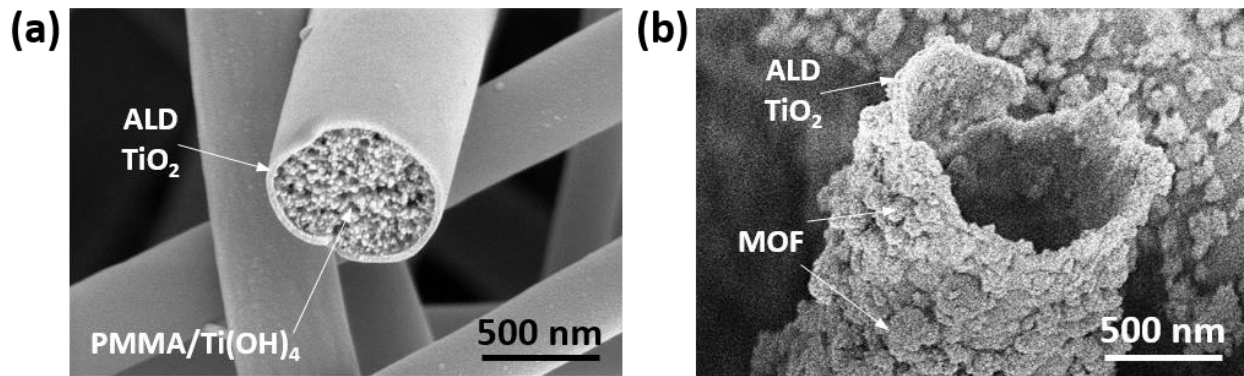


Figure 4.3. SEM images of PMMA/Ti(OH)₄@TiO₂ (A) and PMMA/ Ti(OH)₄@TiO₂@MOF (B).

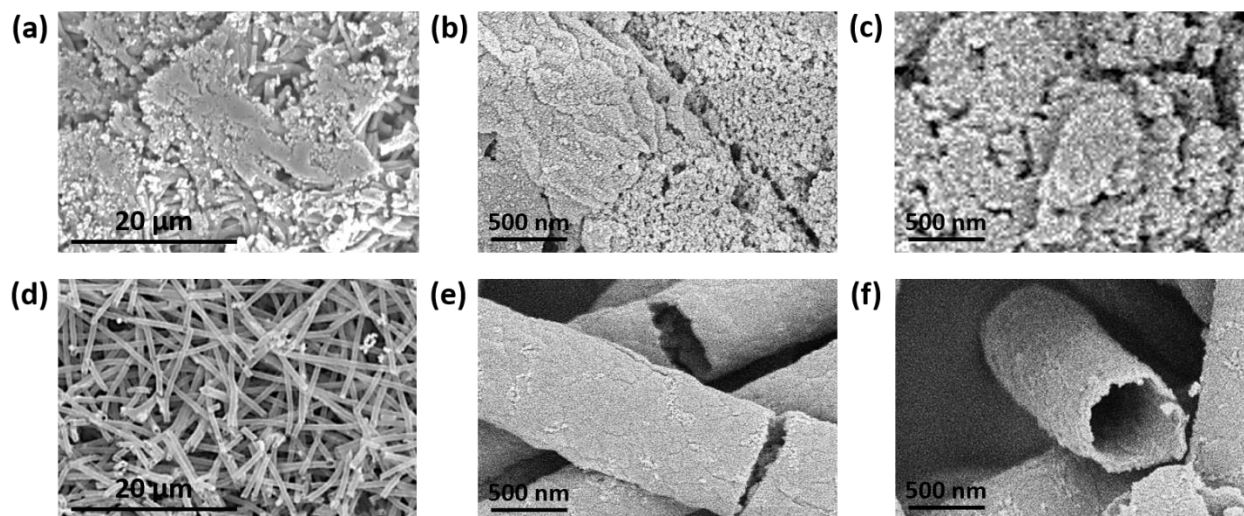


Figure 4.4. SEM images of PMMA/Ti(OH)₄ fibers (A-C) and PMMA/Ti(OH)₄@TiO₂ fibers (D-F) after solvothermal treatment without organic linker (i.e., 2-ATA) at 85 °C for 24 h.

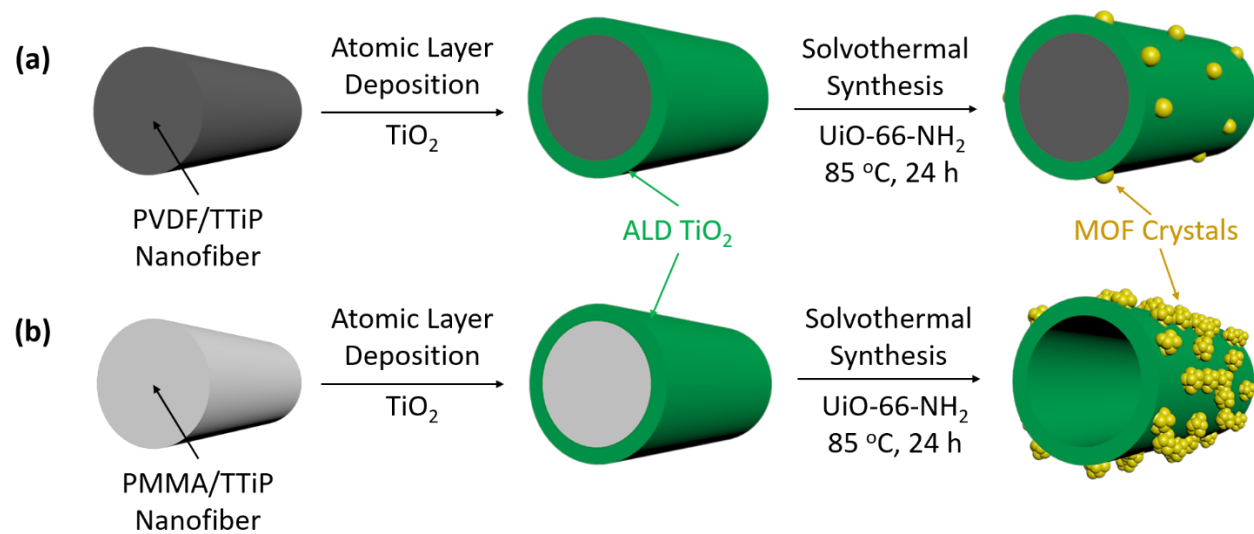


Figure 4.5. Schematic illustration of MOF integration procedures on PVDF/ Ti(OH)_4 (A) and PMMA/ Ti(OH)_4 (B) composite fibers.

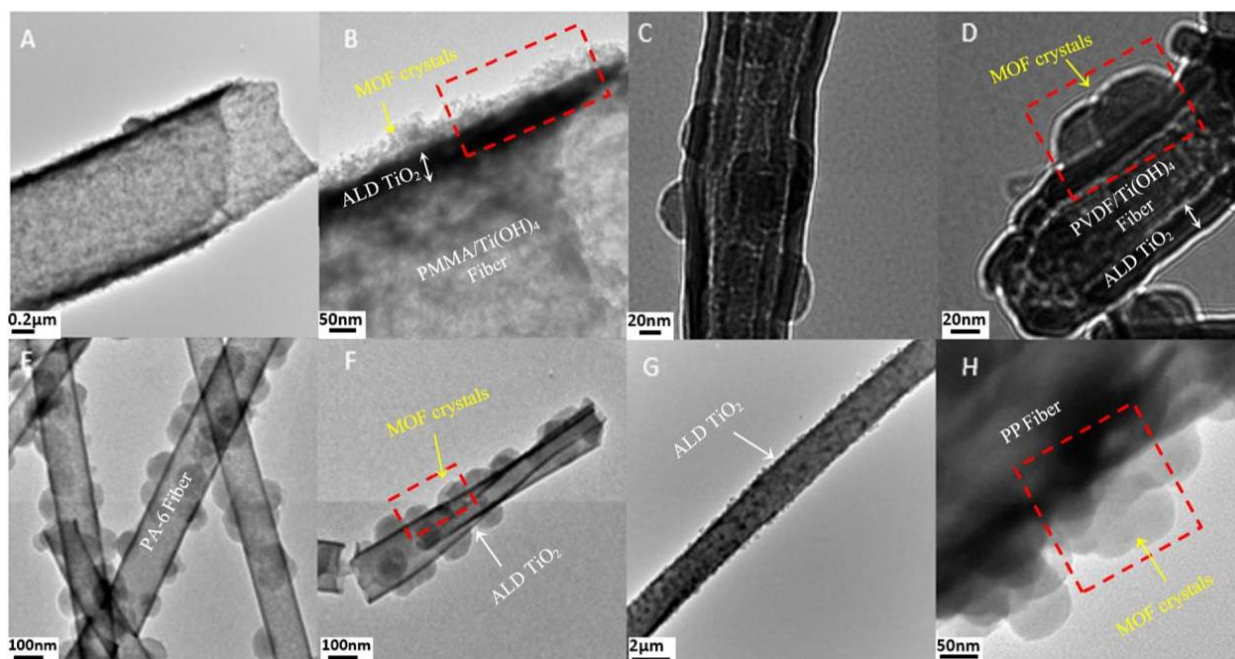


Figure 4.6. TEM images of hollowed PMMA/Ti(OH)₄@TiO₂@MOF (A,B), PVDF/Ti(OH)₄@TiO₂@MOF (C,D), PA-6@TiO₂@MOF (E,F), and PP@TiO₂@MOF (G,H).

Table 4.1. Raman Modes of UiO-66-NH₂, PMMA, PVDF, PA-6, and PP along with IR Modes of UiO-66-NH₂

Raman	Raman shift (cm ⁻¹)	mode
UiO-66-NH ₂	1012	benzene ring deformation ³⁹
	1270	C–O stretching ³⁹
	1456–1436	OCO symmetric stretching in-phase ³⁹
	1632	C=C stretching of aromatic rings ³⁹
	3078	CH stretching ³⁹
PMMA	1721	$\nu(\text{C}=\text{O})$ of (C–COO) ³⁸
	2836	O–CH ₃ combination band ³⁸
	2948	$\nu_s(\text{C}-\text{H})$ of α -CH ₃ , $\nu_a(\text{CH}_2)$ with $\nu_s(\text{C}-\text{H})$ of O–CH ₃ ³⁸
PVDF	2994	$\nu_a(\text{C}-\text{H})$ of O–CH ₃ and α -CH ₃ ³⁸
	2974	$\nu_s(\text{CH}_2)$ ³⁵
	3014	$\nu_a(\beta\text{-CH}_2)$ ³⁵
PA-6	1436	$\phi(\text{H}-\text{C}-\text{N})$ ³⁷
	2860, 2901, 2922	$\nu(\text{C}_6-\text{H})$, $\nu(\text{C}_2-\text{H})$, $\nu(\text{C}-\text{H})$ ³⁷
PP	2837, 2880	$\nu_s(\text{CH}_3)$ ³⁴
	2950	$\nu_a(\text{CH}_3)$ ³⁴
IR	wavenumber (cm ⁻¹)	mode
UiO-66-NH ₂	1648	C–NH ₂ ³⁶
	1569, 1430	COO ⁻³⁶
	1492, 1335	C _{ar} =C _{ar} ³⁶
	1256	C–N ³⁶
	764	Zr–O ³⁶

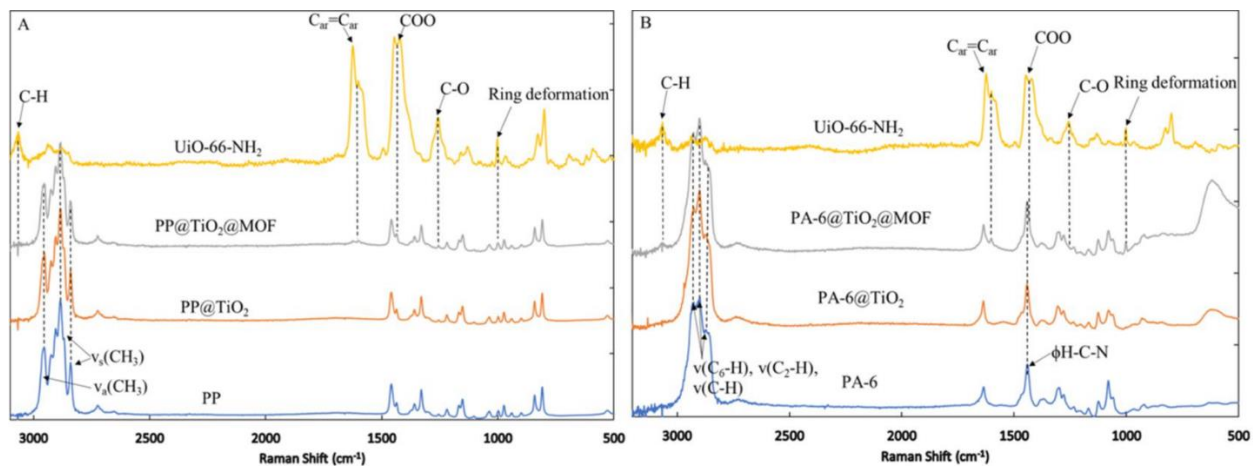


Figure 4.8. Raman spectra of PP@TiO₂@MOF (A) and PA-6@TiO₂@MOF (B).

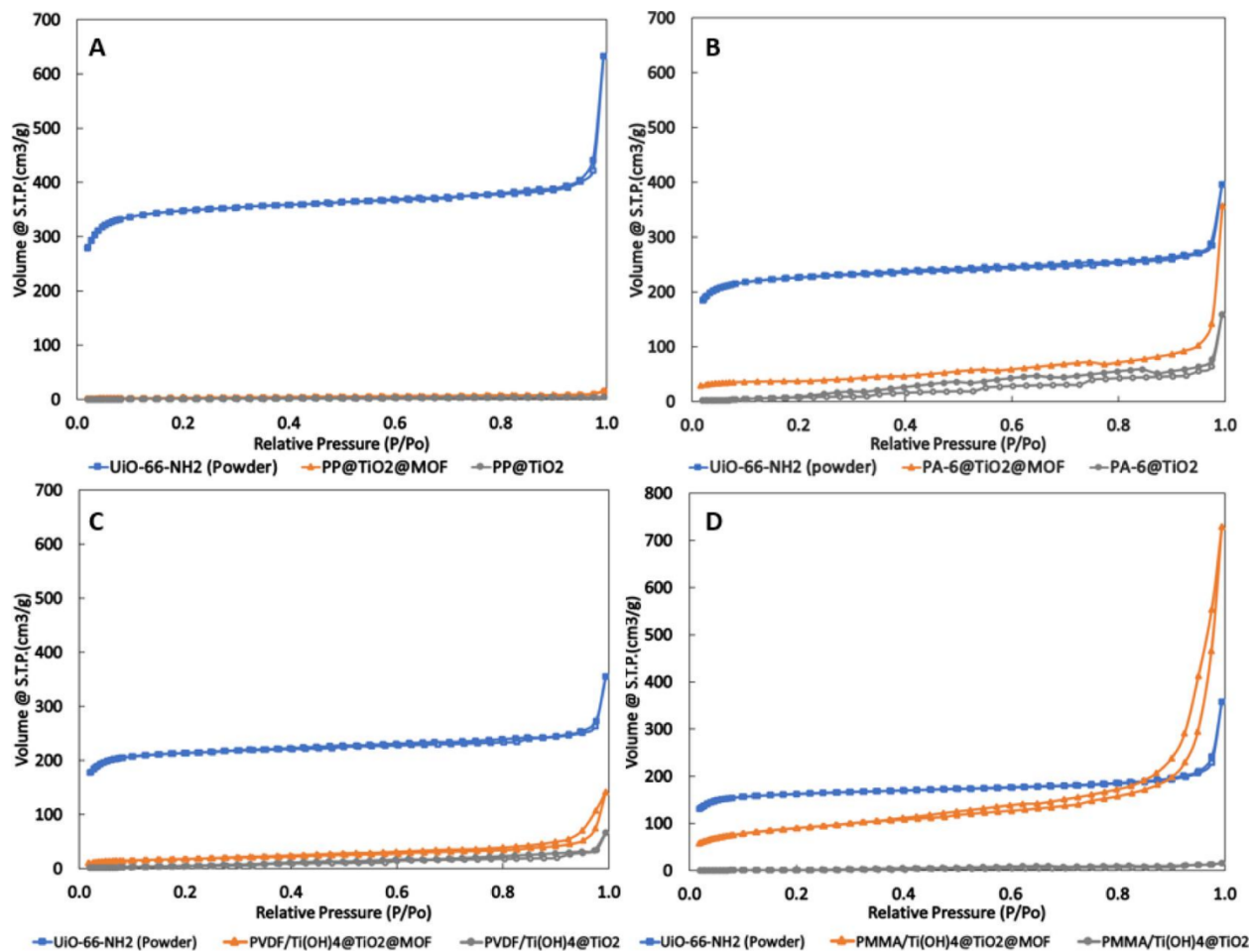
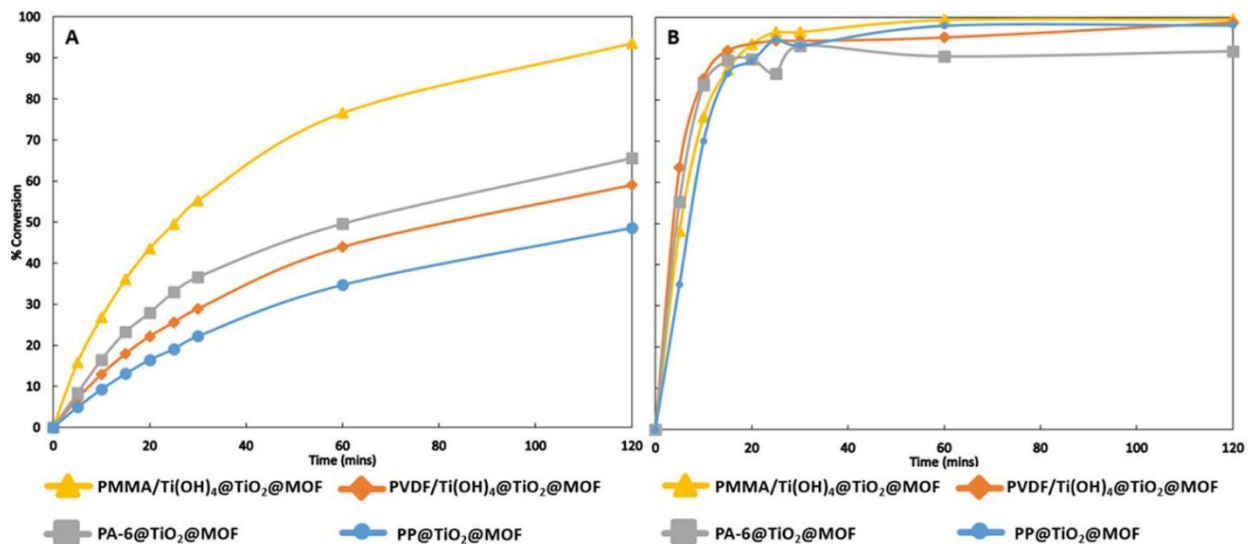


Figure 4.9. N_2 isotherms of $PP@TiO_2@MOF$ (A), $PA-6@TiO_2@MOF$ (B), $PVDF/Ti(OH)_4@TiO_2@MOF$ (C), and $PMMA/Ti(OH)_4@TiO_2@MOF$ (D) with corresponding MOF powder.

Table 4.2. BET SA Results of Fibers Samples and MOF Powders along with Calculated Weight Percent Based on SA Analysis

	BET SA (m ² /g)	MOF wt %
PP@TiO ₂ @MOF	8	0.6
MOF powder	1411	
PA-6@TiO ₂ @MOF	158	17.6
MOF powder	900	
PVDF/Ti(OH) ₄ @TiO ₂ @MOF	84	9.8
MOF powder	861	
PMMA/Ti(OH) ₄ @TiO ₂ @MOF	264	41.2
MOF powder	641	



	PMMA/Ti(OH) ₄ @TiO ₂ @MOF	PVDF/Ti(OH) ₄ @TiO ₂ @MOF	PA-6@TiO ₂ @MOF	PP@TiO ₂ @MOF
Rate (min ⁻¹)	0.0264	0.0113	0.0153	0.0083
t _{1/2} (mins)	26	61	45	83
	UiO-66-NH ₂	UiO-66-NH ₂	UiO-66-NH ₂	UiO-66-NH ₂
Rate (min ⁻¹)	0.1348	0.1148	0.0850	0.1196
t _{1/2} (mins)	5.1	6.0	8.2	5.8

Figure 4.10. DMNP results for fibers samples (12 mg) (A) and corresponding MOF powders (3 mg) (B) with table of kinetic data.

Table 4.3. Apparent Rate Constant of Each MOF Powder Sample and the Mass Fraction of Active MOF for Each MOF/Fiber Sample

	$K_{app} \text{ M}^{-1} \text{ min}^{-1}$	calculated active MOF mass fraction (%)
UiO-66-NH ₂ (PMMA)	47.6 ± 6.5	8.0
UiO-66-NH ₂ (PVDF)	54.8 ± 1.7	3.0
UiO-66-NH ₂ (PA-6)	58.4 ± 7.1	3.8
UiO-66-NH ₂ (PP)	61.6 ± 6.6	2.0

4.7. References

- (42) Raushel, F. M. Catalytic Detoxification. *Nature* **2011**, *469*, 310–311.
- (43) Singh, B.; Madhusudhanan, S.; Dubey, V.; Nath, R.; Rao, N. B. S. N. Active Carbon for Removal of Toxic Chemicals from Contaminated Water. *Carbon* **1996**, *34*, 327–330.
- (44) Osovsky, R.; Kaplan, D.; Nir, I.; Rotter, H.; Elisha, S.; Columbus, I. Decontamination of Adsorbed Chemical Warfare Agents on Activated Carbon Using Hydrogen Peroxide Solutions. *Environ. Sci. Technol.* **2014**, *48*, 10912–10918.
- (45) Tusek, D.; Asperger, D.; Bacic, I.; Curkovic, L.; Macan, J. Environmentally Acceptable Sorbents of Chemical Warfare Agent Simulants. *J. Mater. Sci.* **2017**, *52*, 2591–2604.
- (46) Meng, Q.; Doetschman, D. C.; Rizos, A. K.; Lee, M.-H.; Schulte, J. T.; Spyros, A.; Kanyi, C. W. Adsorption of Organophosphates into Microporous and Mesoporous NaX Zeolites and Subsequent Chemistry. *Environ. Sci. Technol.* **2011**, *45*, 3000–3005.
- (47) Sadeghi, M.; Yekta, S.; Ghaedi, H. Synthesis and application of Pb-MCM-41/ZnNiO₂ as a novel mesoporous nanocomposite adsorbent for the decontamination of chloroethyl phenyl sulfide (CEPS). *Appl. Surf. Sci.* **2017**, *400*, 471–480.
- (48) de Koning, M. C.; van Grol, T.; Breijaert, T. Degradation of Paraoxon and the Chemical Warfare Agents VX, Tabun, and Soman by the Metal-Organic Frameworks UiO-66-NH₂, MOF-808, NU-1000, and PCN-777. *Inorg. Chem.* **2017**, *56*, 11804–11809.
- (49) Gil-San-Millan, R.; López-Maya, E.; Hall, M.; Padial, N. M.; Peterson, G. W.; DeCoste, J. B.; Rodríguez-Albelo, L. M.; Oltra, J. E.; Barea, E.; Navarro, J. A. R. Chemical Warfare Agents Detoxification Properties of Zirconium Metal-Organic Frameworks by Synergistic Incorporation of Nucleophilic and Basic Sites. *ACS Appl. Mater. Interfaces* **2017**, *9*, 23967–23973.

- (50) Furukawa, H.; Cordova, K. E.; O’Keeffe, M.; Yaghi, O. M. The Chemistry and Applications of Metal-Organic Frameworks. *Science* **2013**, *341*, 1230444.
- (10) Hendon, C. H.; Rieth, A. J.; Korzynski, M. D.; Dinca, M. Grand Challenges and Future Opportunities for Metal-Organic Frameworks. *ACS Cent. Sci.* **2017**, *3*, 554–563.
- (11) Karmakar, A.; Samanta, P.; Desai, A. V.; Ghosh, S. K. Guest-Responsive Metal-Organic Frameworks as Scaffolds for Separation and Sensing Applications. *Acc. Chem. Res.* **2017**, *50*, 2457–2469.
- (12) Mondloch, J. E.; Katz, M. J.; Planas, N.; Semrouni, D.; Gagliardi, L.; Hupp, J. T.; Farha, O. K. Are Zr₆-based MOFs water stable? Linker hydrolysis vs. capillary-force-driven channel collapse. *Chem. Commun.* **2014**, *50*, 8944–8946.
- (13) Mondloch, J. E.; Katz, M. J.; Isley, W. C., III; Ghosh, P.; Liao, P.; Bury, W.; Wagner, G. W.; Hall, M. G.; DeCoste, J. B.; Peterson, G. W.; Snurr, R. Q.; Cramer, C. J.; Hupp, J. T.; Farha, O. K. Destruction of Chemical Warfare Agents using Metal-Organic Frameworks. *Nat. Mater.* **2015**, *14*, 512–516.
- (14) Katz, M. J.; Moon, S.-Y.; Mondloch, J. E.; Beyzavi, M. H.; Stephenson, C. J.; Hupp, J. T.; Farha, O. K. Exploiting parameter space in MOFs: a 20-fold enhancement of phosphate-ester hydrolysis with UiO-66-NH₂. *Chem. Sci.* **2015**, *6*, 2286–2291.
- (15) Lu, A. X.; McEntee, M.; Browe, M. A.; Hall, M. G.; DeCoste, J. B.; Peterson, G. W. MOFabric: Electrospun Nanofiber Mats from PVDF/UiO-66-NH₂ for Chemical Protection and Decontamination. *ACS Appl. Mater. Interfaces* **2017**, *9*, 13632–13636.

- (16) Zhao, J.; Lee, D. T.; Yaga, R. W.; Hall, M. G.; Barton, H. F.; Woodward, I. R.; Oldham, C. J.; Walls, H. J.; Peterson, G. W.; Parsons, G. N. Ultra-Fast Degradation of Chemical Warfare Agents Using MOF-Nanofiber Kebabs. *Angew. Chem., Int. Ed.* **2016**, *55*, 13224–13228.
- (17) McCarthy, D. L.; Liu, J.; Dwyer, D. B.; Troiano, J. L.; Boyer, S. M.; DeCoste, J. B.; Bernier, W. E.; Jones, W. E., Jr. Electrospun metal-organic framework polymer composites for the catalytic degradation of methyl paraoxon. *New J. Chem.* **2017**, *41*, 8748–8753.
- (18) Zhang, Y.; Feng, X.; Yuan, S.; Zhou, J.; Wang, B. Challenges and Recent Advances in MOF-polymer Composite Membranes for Gas Separation. *Inorg. Chem. Front.* **2016**, *3*, 896–909.
- (19) Chen, Y.; Li, S.; Pei, X.; Zhou, J.; Feng, X.; Zhang, S.; Cheng, Y.; Li, H.; Han, R.; Wang, B. A Solvent-Free Hot-Pressing Method for Preparing Metal-Organic-Framework Coatings. *Angew. Chem., Int. Ed.* **2016**, *55*, 3419–3423.
- (20) Neufeld, M. J.; Harding, J. L.; Reynolds, M. M. Immobilization of Metal-Organic Framework Copper(II) Benzene-1,3,5-tricarboxylate (CuBTC) onto Cotton Fabric as a Nitric Oxide Release Catalyst. *ACS Appl. Mater. Interfaces* **2015**, *7*, 26742–26750.
- (21) Parsons, G. N.; Atanasov, S. E.; Dandley, E. C.; Devine, C. K.; Gong, B.; Jur, J. S.; Lee, K.; Oldham, C. J.; Peng, Q.; Spagnola, J. C.; Williams, P. S. Mechanisms and Reactions during Atomic Layer Deposition on Polymers. *Coord. Chem. Rev.* **2013**, *257*, 3323–3331.
- (22) Brozena, A. H.; Oldham, C. J.; Parsons, G. N. Atomic Layer Deposition on Polymer Fibers and Fabrics for Multifunctional and Electronic Textiles. *J. Vac. Sci. Technol., A* **2016**, *34*, 010801.
- (23) Hyde, G. K.; Park, K. J.; Stewart, S. M.; Hinstroza, J. P.; Parsons, G. N. Atomic Layer Deposition of Conformal Inorganic Nanoscale Coatings on three-dimensional Natural Fiber

- systems: Effect of Surface Topology on Film Growth Characteristics. *Langmuir* **2007**, *23*, 9844–9849.
- (24) Jur, J. S.; Spagnola, J. C.; Lee, K.; Gong, B.; Peng, Q.; Parsons, G. N. Temperature-Dependent Subsurface Growth during Atomic Layer Deposition on Polypropylene and Cellulose Fibers. *Langmuir* **2010**, *26*, 8239–8244.
- (25) Spagnola, J. C.; Gong, B.; Arvidson, S. A.; Jur, J. S.; Khan, S. A.; Parsons, G. N. Surface and Sub-surface Reactions during Low Temperature Aluminium Oxide Atomic Layer Deposition on Fiber-forming Polymers. *J. Mater. Chem.* **2010**, *20*, 4213–4222.
- (26) Zhao, J.; Gong, B.; Nunn, W. T.; Lemaire, P. C.; Stevens, E. C.; Sidi, F. I.; Williams, P. S.; Oldham, C. J.; Walls, H. J.; Shepherd, S. D.; Browe, M. A.; Peterson, G. W.; Losego, M. D.; Parsons, G. N. Conformal and Highly Adsorptive Metal-organic Framework Thin Films via Layer-by-layer growth on ALD-coated fiber mats. *J. Mater. Chem. A* **2015**, *3*, 1458–1464.
- (27) Lee, D. T.; Zhao, J.; Peterson, G. W.; Parsons, G. N. Catalytic MOF-Cloth Formed via Directed Supramolecular Assembly of UiO-66-NH₂ Crystals on Atomic Layer Deposition-Coated Textiles for Rapid Degradation of Chemical Warfare Agent Simulants. *Chem. Mater.* **2017**, *29*, 4894–4903.
- (28) Zhao, J.; Losego, M. D.; Lemaire, P. C.; Williams, P. S.; Gong, B.; Atanasov, S. E.; Blevins, T. M.; Oldham, C. J.; Walls, H. J.; Shepherd, S. D.; Browe, M. A.; Peterson, G. W.; Parsons, G. N. Highly Adsorptive, MOF-Functionalized Nonwoven Fiber Mats for Hazardous Gas Capture Enabled by Atomic Layer Deposition. *Adv. Mater. Interfaces* **2014**, *1*, 1400040.
- (29) Lee, D. T.; Zhao, J.; Oldham, C. J.; Peterson, G. W.; Parsons, G. N. UiO-66-NH₂ Metal-Organic Framework (MOF) Nucleation on TiO₂, ZnO, and Al₂O₃ Atomic Layer Deposition-Treated Polymer Fibers: Role of Metal Oxide on MOF Growth and Catalytic

- Hydrolysis of Chemical Warfare Agent Simulants. *ACS Appl. Mater. Interfaces* **2017**, *9*, 44847–44855.
- (30) Katz, M. J.; Mondloch, J. E.; Totten, R. K.; Park, J. K.; Nguyen, S. T.; Farha, O. K.; Hupp, J. T. Simple and Compelling Biomimetic Metal-Organic Framework Catalyst for the Degradation of Nerve Agent Simulants. *Angew. Chem., Int. Ed.* **2014**, *53*, 497–501.
- (31) Tulig, K.; Walton, K. S. An Alternative UiO-66 Synthesis for HCl-sensitive Nanoparticle Encapsulation. *RSC Adv.* **2014**, *4*, 51080–51083.
- (32) Safety Data Sheet, Titanium (IV)isopropoxide; 546-68-9; Sigma-Aldrich: 400 Summit Drive, Burlington, MA 01803, revision date 09/ 22/2017, print date 01/13/2018.
- (33) Baharvandi, H. R.; Talebzadeh, N.; Ehsani, N.; Aghand, F. Synthesis of B4C-Nano TiB2 Composite Powder by Sol-Gel Method. *J. Mater. Eng. Perform.* **2009**, *18*, 273–277.
- (34) Andreassen, E. Infrared and Raman spectroscopy of polypropylene. In *Polypropylene; Polymer Science and Technology Series*; Karger-Kocsis, J., Ed.; Springer: Dordrecht, 1999; Vol. 2, pp 320–328.
- (35) Constantino, C. J. L.; Job, A. E.; Simões, R. D.; Giacometti, J. A.; Zucolotto, V.; Oliveira, O. N.; Gozzi, G.; Chinaglia, D. L. Phase Transition in Poly(vinylidene fluoride) investigated with Micro-Raman Spectroscopy. *Appl. Spectrosc.* **2005**, *59*, 275–279.
- (36) Lemaire, P. C.; Lee, D. T.; Zhao, J.; Parsons, G. N. Reversible Low-Temperature Metal Node Distortion during Atomic Layer Deposition of Al₂O₃ and TiO₂ on UiO-66-NH₂ Metal-Organic Framework Crystal Surfaces. *ACS Appl. Mater. Interfaces* **2017**, *9*, 22042–22054.
- (37) Shukla, S. K.; Kumar, N.; Tandon, P.; Gupta, V. D. Vibrational Dynamics of Gamma Form of Nylon 6 (gamma NY6). *J. Appl. Polym. Sci.* **2010**, *116*, 3202–3211.

- (38) Thomas, K. J.; Sheeba, M.; Nampoory, V. P. N.; Vallabhan, C. P. G.; Radhakrishnan, P. Raman Spectra of Polymethyl Methacrylate Optical Fibres Excited by a 532nm Diode Pumped Solid State Laser. *J. Opt. A: Pure Appl. Opt.* **2008**, *10*, 055303.
- (39) Atzori, C.; Shearer, G. C.; Maschio, L.; Civalleri, B.; Bonino, F.; Lamberti, C.; Svelle, S.; Lillerud, K. P.; Bordiga, S. Effect of Benzoic Acid as a Modulator in the Structure of UiO-66: An Experimental and Computational Study. *J. Phys. Chem. C* **2017**, *121*, 9312–9324.
- (40) Ye, L.; Yang, C.; Tian, L.; Zan, L.; Peng, T. Tunable photocatalytic selectivity of fluoropolymer PVDF modified TiO₂. *Appl. Surf. Sci.* **2011**, *257*, 8072–8077.

CHAPTER 5

Rapid Photocatalytic Detoxification of Mustard-Gas Simulant Using Porphyrin-based Al-PMOF/fiber Textiles Prepared by Atomic Layer Deposition and Cosolvent System Approach

CHAPTER 5 is a manuscript unpublished yet

Dennis T. Lee,[†] Jovenal D. Jamir,[†] Gregory W. Peterson,[‡] and Gregory N. Parsons^{†,*}

[†]Department of Chemical & Biomolecular Engineering, North Carolina State University, 911 Partners Way, Raleigh, NC 27695, United States

[‡]Edgewood Chemical Biological Center, 5183 Blackhawk Road, Aberdeen Proving Ground, MD 21010, United States

5.1. Abstract

Detoxifying hazardous chemicals using metal-organic frameworks (MOFs) catalysts has made substantial progress, but variations in synthetic conditions and MOF integration methods upon materials necessitate better understanding of crystal growth mechanism to make MOF-functionalized systems. In this report, we for the first time discover an exceptional photocatalytic reactivity of Al-PMOF, comprised of an Earth-abundant metal-contained $\text{Al}(\text{OH})\text{O}_4$ clusters bridged by H_2TCCP (5,10,15,20-tetrakis(4-carboxyphenyl)porphyrin) chromophores, against mustard gas simulant, 2-chloroethyl ethyl sulfide (CEES) under visible light irradiation. Furthermore, the Al-PMOF immobilization into polymeric fibers is demonstrated via a well-controlled Al_2O_3 solid film conversion method with cosolvent system containing DMF and water. The approach enables a secure integration of conformal Al-PMOF films into fibers at a relatively low temperature (120 °C). Polymeric fiber substrates would decompose under conventional synthetic temperature (180 °C) otherwise. In addition, on a per unit mass of MOF basis, the surface-bound Al-PMOF thin films substantially enhance CEES detoxification turn-over-frequency ($\text{mol}_{\text{CEES}} \cdot \text{mol}_{\text{chromophore}}^{-1} \cdot \text{min}^{-1}$) by a factor of 19 compared to their powder counterparts prepared via a conventional solvothermal method. Importantly, the use of chemical protective textiles is explored for other practical applications including a colorimetric pH sensing and a selective removal of chloroform contaminants from water.

5.2. Introduction

Despite of international prohibition on their use and stockpiling, various chemical warfare agents (CWAs) are still present and keep posing substantial threats not only to military populations but also to civilians up to date.^[1] Sulfur mustard (mustard gas or HD), which gained notoriety as a chemical weapon for mass destruction since its first large-scale production during World War I, is blistering agent which causes intensive and irreversible damage to contacted skin, eyes, and respiratory system.^[2] There are three major strategies to detoxify HD, including hydrolysis,^[3] dehydrohalogenation,^[4] and oxidation.^[5] Among these, selective oxidation of HD into less toxic HDO (bis(2-chloroethyl)sulfoxide)^[6] over toxic sulfone derivatives using a reactive singlet oxygen ($^1\text{O}_2$) has proved to be considerably effective.^[7] This is because the partial oxidation of HD with oxidizable bivalent sulfur by $^1\text{O}_2$ exhibits fast reaction kinetics and produces no harmful byproducts compared to the other detoxification routes.^[8]

Zr-based metal-organic frameworks (MOFs), comprised of Zr-clusters bridged by organic linkers, have been actively used as heterogeneous catalysts or adsorbents for a range of nerve agents,^[9,10] blistering agents,^[11] and their simulants^[12–14] due to robust chemical stability and high porosity of the MOFs.^[15] Especially, porphyrin-based Zr-MOFs have been recently regarded as promising photocatalysts because porphyrin moieties within MOF structure are capable of generating $^1\text{O}_2$ under visible light, which is an environmental friendly and energy efficient way of detoxifying HD and its simulants.^[7,16–19] However, many of such catalytic study and performance are based on free-standing powders which are not ideal protective systems for practical use in realistic field environments.

To advance a practical effectiveness of MOFs, synthesis with diverse insoluble metal precursors (e.g., zero-valent metals,^[20] metal oxides,^[21–23] metal hydroxides,^[22,24] hydroxy double

salts,^[25–27] and metal carbides^[28]) and vapor-assisted synthetic approaches^[29,30] have been recently reported to provide a more flexible and controllable MOF production, which can also facilitate surface-anchored MOF film.^[31–34] However, a selective and rapid destruction of HD and its effective simulant, 2-chloroethyl ethyl sulfide (CEES),^[18] using textiles functionalized with porphyrin-based MOFs is still missing despite of such creative efforts.

In this study, for the first time we focus on thermally and chemically stable Al-PMOF,^[35] which is comprised of aluminum, the most abundant metallic element in the Earth's crust, and H₂TCPP (5,10,15,20-tetrakis(4-carboxyphenyl)porphyrin]) photosensitizer,^[36] as an alternative catalyst for a rapid detoxification of CEES. Furthermore, we demonstrate a successful integration of Al-PMOF into polypropylene (PP) fiber (PP@Al-PMOF) by leveraging an atomic layer deposition (ALD) technique and a cosolvent (DMF and water)-assisted synthetic approach. To achieve this outcome, we had to overcome the problem of relatively high reaction temperature required for Al-PMOF synthesis, which can cause structural decomposition of fiber substrates during the integration process.

Furthermore, we discovered that amorphous ALD Al₂O₃ film conformally deposited on PP can provide the metal source reacting with H₂TCPP dissolved in solution phase to form MOF film on the fiber, and acts as a strong adhesive layer between fiber substrate and the MOF film. It should be noted that a well-controlled DMF to water cosolvent ratio is essential to proceed with the heterogeneous nucleation and growth of high-quality Al-PMOF in our synthetic condition. The significant advantage of our approach is clearly substantiated by comparison with various conventional methods tested in this work, which result in poor crystallization and adhesion of the MOF crystals to substrates. This report is first to facilitate Al-PMOF integration into polymeric fiber substrate and to verify that the MOF/fiber composites are versatile not only in fast

neutralization of CEES, but also in colorimetric pH sensing and selective organic contaminant removal.

5.3. Experimental Section

Materials. All reagents were purchased from commercial sources and used without further treatment. Aluminum chloride hexahydrate ($\text{AlCl}_3 \cdot 6\text{H}_2\text{O}$, 99%, Sigma-Aldrich), aluminum oxide (Al_2O_3 , Sigma-Aldrich), tri-methyl aluminum (TMA, 98% STREM Chemicals, Inc.), titanium (IV) chloride (TiCl_4 , 99%, STREM Chemicals), meso-Tetra(4-carboxyphenyl)porphine (H_2TCPP , >97% Frontier Scientific), N,N-dimethylformamide (DMF, Fisher), deionized water (DI water), anhydrous ethanol (200 proof, VWR), 2-chloroethyl ethyl sulfide (CEES, 97%, Sigma-Aldrich), 1-bromo-3,5-difluorobenzene (99%, Oakwood Chemical), and dichloromethane (DCM, 99.9%, ACROS OrganicsTM).

Polymeric fibrous scaffolds. Non-woven polypropylene (PP) micro-fibrous mats (40 gsm) were used as received from Nonwovens Cooperative Research Center (NCRC), North Carolina State University.^[1] The polymeric fibrous mats are 0.30 mm thick and 1.0-9.0 μm diameter for 40 gsm fiber mats.

Atomic layer deposition (ALD) on PP microfibers and on Si wafers. Non-woven polypropylene (PP) fibrous mats were conformally coated with inorganic Al_2O_3 or TiO_2 using a home built hot-wall viscous-flow atomic layer deposition reactor. The reactor design for the processes was described in previous work. ALD deposition with the inorganic materials was conducted at 90°C under ~1.8 Torr. The sequence times (in second) of x exposure/ N_2 purge/ H_2O exposure/ N_2 purge were 1/30/1/30 for Al_2O_3 and 1/40/1/40 for TiO_2 , where x is TMA, TiCl_4 , respectively. These samples are referred to as PP@ Al_2O_3 and PP@ TiO_2 , respectively.

Silicon wafers with thin native oxide (~2 nm) (Si/SiO₂) were also placed together with PP fibrous mats inside the reactor under the same ALD condition. PP scaffolds were treated with 300 cycles of ALD Al₂O₃ or of TiO₂ on PP fibrous mats. Si wafer monitors were also used to measure thickness of the ALD coatings along with PP substrates. Around 30 nm of inorganic film on the Si@SiO₂ was confirmed from a J.A. Woollam alpha-spectroscopic ellipsometry (SE) ellipsometer at an incidence angle of 70°. These samples are referred to as Si/SiO₂@Al₂O₃ and Si/SiO₂@TiO₂, respectively.

Synthesis of Al-PMOF (Powder).

Conventional hydrothermal synthesis with AlCl₃·6H₂O and porphyrin linkers. Al-PMOF MOF powders were hydrothermally synthesized by using a method previously reported with some modifications.^[2] 0.1 g (0.13 mmol) of meso-Tetra(4-carboxyphenyl)porphine (H₂TCPP) and 0.03 g (0.13 mmol) of AlCl₃·6H₂O were both added into 40 mL of deionized water (DI-water), followed with 5 min of sonication at ambient temperature for a complete dispersion. The as-prepared precursor mixture was then introduced into a 60 mL Teflon lined autoclave and heated at 180°C for 20 hours. The Al-PMOF solid product was then recovered by filtering out unreacted precursor components, by-products, and residual solvent through polypropylene membrane (0.45 µm pore size, Whatman). After that, the filtered solid was washed with DI-water (3 × 80 mL) and with ethanol (3 × 80 mL). Eventually, the final solid in maroon color was obtained via filtration system and dried at room temperature at reduced pressure for 12 h. The well dried Al-PMOF MOF powder was stored in a desiccator until being used for further characterizations.

Hydro/solvothermal synthesis with AlCl₃·6H₂O and H₂TCPP in cosolvent systems. Al-PMOF MOF powders were synthesized in varied cosolvent systems containing DMF and DI-water to investigate cosolvent influence on the MOF synthesis at relatively low temperature (120°C). 0.1

g (0.13 mmol) of H₂TCPP and 0.03 g (0.13 mmol) of AlCl₃·6H₂O were both added into a solvent mixture with 30 mL of DMF and 10 mL of DI-water (D:W=3:1), a mixture with 20 mL of DMF and 20 mL of DI-water (D:W=1:1), or a mixture with 10 mL of DMF and 30 mL of DI-water (D:W=1:3), respectively. In addition, we also prepared precursor solutions with 40 mL of pure water and with 40 mL of pure DMF solvent, respectively. Each prepared precursor solution was sonicated for 5 min at ambient temperature for a complete dispersion. The as-prepared precursor mixture was then introduced into a 60 mL Teflon lined autoclave and heated at 120°C for 20 hours. The solid product obtained was then recovered by filtering out unreacted precursor components, by-products, and residual solvent through polypropylene membrane (0.45 μm pore size, Whatman). After that, the filtered solid was washed with DMF (3 × 80 mL) and with ethanol (3 × 80 mL). Eventually, the final solid was collected via filtration system and dried at room temperature at reduced pressure for 12 h. The well dried solid powder was stored in a desiccator until being used for further characterizations.

Solvothermal synthesis with Al₂O₃ powder and H₂TCPP in an optimized cosolvent system. Solid Al₂O₃ powder was used in place of AlCl₃·6H₂O and reacted with H₂TCPP to find an effect of the type of aluminum precursor on Al-PMOF synthesis. 0.1 g (0.13 mmol) of H₂TCPP and 0.013 g (0.13 mmol) of Al₂O₃ were both added into an optimized solvent mixture with 10 mL of DMF and 30 mL of DI-water (D:W=1:3), followed with sonication for 5 min at ambient temperature for a complete dispersion. The as-prepared precursor mixture was then introduced into a 60 mL Teflon lined autoclave and heated at 120°C for 20 hours. The solid product obtained was then recovered by filtering out unreacted precursor components, by-products, and residual solvent through polypropylene membrane (0.45 μm pore size, Whatman). After that, the filtered solid was washed with DMF (3 × 80 mL) and with ethanol (3 × 80 mL). Eventually, the final solid was

collected via filtration system and dried at room temperature at reduced pressure for 12 h. The well dried solid powder was stored in a desiccator until being used for further characterizations.

Synthesis of surface-bound Al-PMOF film on substrates (Composites).

Synthesis of PP@Al-PMOF and Si/SiO₂@Al-PMOF composites using ALD Al₂O₃ coated substrates (Direct conversion of Al₂O₃ to Al-PMOF). 0.05 g (0.062 mmol) of H₂TCPP was first dispersed in 5 mL of DMF, followed with sonication for 5 min at ambient temperature for a better dissolution. 15 mL of DI-water was then introduced into the prepared solution under stirring (~500 rpm), followed by another 5 min of sonication at ambient temperature for a complete dissolution. The as-prepared precursor mixture was then added to a 60 mL Teflon lined autoclave. Subsequently, ALD Al₂O₃ coated PP micro fibrous mat (i.e., PP@Al₂O₃, 1" × 2" swatch size) or Al₂O₃ coated silicon wafer (i.e., Si/SiO₂@Al₂O₃, 0.6" × 0.6" wafer size) was fully soaked in the prepared solution, respectively. Autoclave with each sample was heated at 120°C for 20 hours. After the synthesis is done, the MOF functionalized substrates (i.e., PP@Al-PMOF or Si/SiO₂@Al-PMOF) were rinsed 3 times with 20 mL of DMF, followed by another 3 times-anhydrous ethanol washing and soaked in anhydrous ethanol for 1 day. The MOF/fiber samples were finally dried at room temperature at a reduced pressure for 12 h. The well dried PP@Al-PMOF textiles were stored in a desiccator until being used for further characterizations or for subsequent experimental steps.

Synthesis of Al-PMOF film onto ALD TiO₂ coated Si/SiO₂ (Direct synthesis of Al-PMOF on TiO₂ surface). Direct growth of Al-PMOF onto stable ALD TiO₂ surface using AlCl₃·6H₂O and H₂TCPP was conducted to confirm a difference in MOF growth behavior compared to the Al-PMOF formation driven by reaction between Al₂O₃ film and H₂TCPP. 0.05 g (0.062 mmol) of H₂TCPP was first dispersed in 5 mL of DMF, followed with sonication for 5 min at ambient

temperature for a better dissolution. 15 mL of DI-water was then introduced into the prepared solution under stirring (~500 rpm), followed by another 5 min of sonication at ambient temperature for a complete dissolution. The as-prepared precursor mixture was then added to a 60 mL Teflon lined autoclave. Subsequently, ALD TiO₂ coated silicon wafer (i.e., Si/SiO₂@TiO₂, 0.6" × 0.6" wafer size) was fully immersed in the prepared solution, and the autoclave with sample was then heated at 120°C for 20 hours. After the synthesis is done, the MOF functionalized substrates (i.e., Si/SiO₂@TiO₂@Al-PMOF) were rinsed 3 times with 20 mL of DMF, followed by another 3 times-anhydrous ethanol washing and soaked in anhydrous ethanol for 1 day. The MOF coated silicon wafer samples were finally dried at room temperature at a reduced pressure for 12 h. The well dried samples were stored in a desiccator until being used for further characterizations or for subsequent experimental steps.

Photocatalytic oxidation for CEES.

Oxidation experiments with powder catalysts. Al-PMOF (1.2 mg_{MOF}, 0.7 mol%), or H₂TCPP (1.2 mg_{linker}, 0.8 mol%) powder was introduced into a 250 mL glass microwave tube and was subsequently dispersed in 1 mL methanol by sonicating the tube with mixture for 20 min at ambient temperature. After purging with O₂ for 10 min, 23 µL (0.2 mmol) 2-chloroethyl ethyl sulfide (CEES) and 10 µL (0.08 mmol) internal standard (1-bromo-3,5-difluorobenzene) were added to the microwave tube using a microsyringe. The microwave tube was then irradiated with an LED (blue). Aliquots were taken from the reaction solution at a certain time interval, filtered, and diluted with dichloromethane (DCM). The reaction kinetics was monitored, and the final products were analyzed by gas chromatography–mass spectrometry (GC-MS). The catalyst loading (mol%) was calculated based on moles of porphyrins in Al-PMOF.

Oxidation experiments with MOF/fiber catalysts. 8.5 mg of PP@Al-PMOF textile (0.3 mg_{MOF}, 0.2 mol%) was completely soaked in 1 mL of methanol which had been introduced into a 250 mL glass microwave tube. Unlike photocatalytic experiments with powder catalysts, no O₂ purging step was included with textile catalysts. This was because there was no need to worry about MOF aggregation or sedimentation during the reaction for surface-bound MOF thin film on fiber substrates. Therefore, 23 μ L (0.2 mmol) 2-chloroethyl ethyl sulfide (CEES) and 10 μ L (0.08 mmol) internal standard (1-bromo-3,5-difluorobenzene) were directly added to the microwave tube using a microsyringe. The microwave tube was then irradiated with an LED (blue). Aliquots were taken from the reaction solution at a certain time interval, filtered, and diluted with dichloromethane (DCM). The reaction kinetics was monitored, and the final products were analyzed by gas chromatography–mass spectrometry (GC-MS).

Characterization. Scanning electron microscopic (SEM) and energy dispersive X-ray analysis (EDX) were conducted using a FEI Verios 460 L field emission SEM. A thin layer of Au-Pd (5~10 nm) was sputter-coated onto the prepared samples before SEM imaging. The cross sections of the Al-PMOF coated silicon wafers were prepared with a FEI Quanta 3D FEG focused ion beam (FIB), and imaged with an FEI Titan 80-300 probe aberration corrected scanning transmission electron microscope (STEM). High-resolution EDX was analyzed using the SuperX Energy Dispersive Spectrometry (SuperX EDS) system installed on the FEI Titan STEM. X-ray diffraction (XRD) was implemented with a Rigaku SmartLab X-ray diffraction tool (Cu K α X-ray source) for crystalline phase analysis. Micromeritics 3Flex Surface Characterization Analyzer were used for measuring N₂ adsorption-desorption isotherms at 77 K. Water vapor adsorption-desorption isotherms were measured using Micromeritics 3Flex Surface Characterization Analyzer at 298 K. The fabric-based samples were dried in vacuum ($\sim 1 \times 10^{-5}$ Torr) in BET

instrument at room temperature for 1 h and at 110°C for 24 h in a consecutive manner before both N₂ adsorption-desorption and water vapor adsorption-desorption measurement. BET surface area was calculated based on the N₂ adsorption data within a relative pressure range of $P/P_0 = 0.02 \sim 0.08$.^[3,4] A Thermo Scientific Nicolet 6700 Fourier transform infrared spectrometer was used for analyzing MOF growth on IR silicon wafers coated with ALD metal oxides (i.e., Al₂O₃ or TiO₂). Fluorescence microscopy (BX-61 microscope, Olympus) was used to confirm uniformity of Al-PMOF film on PP fiber substrates.

5.4. Results and Discussion

Previous results showed conventional hydrothermal synthesis of Al-PMOF powder using AlCl₃·6H₂O and H₂TCPP at 180 °C in water.^[35] However, reducing the synthetic temperature down to less than 130 °C is inevitable to integrate MOF crystals on polymeric fiber substrates (e.g., polypropylene (PP)) with maintaining the fibrous structures during the reaction.^[37] We know that DMF miscible with water can help MOF crystallization of precursors containing hydrophobic organic compounds at low temperature.^[23] Therefore, we hypothesize that DMF or DMF-water mixtures may enable lower temperature growth of Al-PMOF powder. We also hypothesize that low temperature Al-PMOF growth with solvent mixtures may be possible on fiber substrates using ALD Al₂O₃ as an Al-source material in place of the common water-soluble AlCl₃·6H₂O precursor. To test our hypotheses we performed a set of experiments using a range of DMF-water solvent ratios combined with various sources of Al, including AlCl₃·6H₂O, Al₂O₃ powder, and ALD Al₂O₃ thin films.

Figure 5.1a illustrates the procedure of fabricating Al-PMOF/fiber composites. After polymer fibers are coated with a conformal ALD Al₂O₃ film (~30 nm),^[26,31] the Al₂O₃ reacts with

H₂TCPP linkers dissolved in solvent to form porous Al-PMOF film. Al-PMOF is comprised of infinite Al(OH)O₄ chains running along the *b*-axis and bridged by the H₂TCPP units (Figure 5.1b).^[35] As a first test, we compared pure water and 1:3 (v/v) mixture of DMF and water (i.e., D:W=1:3) as a solvent for Al-PMOF crystallization at low temperature (i.e., 120 °C) using AlCl₃·6H₂O and H₂TCPP precursors.

As confirmed by X-ray diffraction (XRD) and N₂ isotherms at 77 K (Figure 5.1c-d), the solid powder obtained at 120 °C with pure water shows non-porous and apparently different crystallinity compared to both solid powder made via conventional high temperature synthesis and its simulated pattern. On the other hand, the solid powder synthesized in the cosolvent system (D:W=1:3) at 120 °C exhibits almost identical crystalline patterns and slightly higher Brunauer-Emmett-Teller (BET) surface area of 1728 ± 250 m²/g compared to the MOF reported with 1200^[38] or 1400 m²/g^[35,39] obtained from the conventional high temperature method with pure water.

The UV-vis spectra^[38] and XRD patterns were measured on the products obtained and pure H₂TCPP powder to verify their optical and structural identity. We found that the solid powder made with pure water was pure H₂TCPP salt, while the solid synthesized with solvent mixture (D:W=1:3) was high quality Al-PMOF (Figure S5.1). Water vapor isotherms collected at 298 K (Figure 5.1e) on the highly porous solids, produced with mixed solvent, show a sigmoidal isotherm curves with hysteresis. This is generally featured in flexible MOFs, such as MIL-53(Al) comprised of Al(OH)O₄ connected by terephthalic acid linkers.^[28]

As a next experiment, we tested with relatively insoluble Al₂O₃ powder in place of AlCl₃·6H₂O as an alternative metal source to react with H₂TCPP in the cosolvent system (D:W=1:3) at 120 °C; however, it gave rise to a partial reaction with H₂TCPP and created non-porous solids with complex crystallinity (Figure S5.2-3).

To systematically investigate the influence of metal source types and solvent systems on the Al-PMOF formation at 120 °C, we compared Al-PMOF powder samples and MOF thin films on substrates synthesized in varied solvent systems (pure DMF (D), D:W=3:1, D:W=1:1, D:W=1:3, or pure water (W)).

Figure 5.2a shows scanning electron microscope (SEM) images of Al-PMOF powder samples synthesized with $\text{AlCl}_3 \cdot 6\text{H}_2\text{O}$ and H_2TCCP dissolved in diverse solvent systems. Solids synthesized in pure DMF or in cosolvent systems all display Al-PMOF crystals, while the synthesis with pure water results in only assembled H_2TCCP salts (Figure S5.1). XRD patterns and N_2 isotherms for the solids obtained with pure DMF, D:W=3:1, or D:W=1:1 indicate relatively less-defined crystal domains and almost half powder surface area compared to the powder produced with D:W=1:3 solvent system (Figure S5.4).

We think that this has something to do with MOF formation kinetics controlled by solvent composition.^[40] In the mixed solvent system, compared to water, DMF possesses stronger solvation properties^[41] with the MOF primary building blocks (i.e., metal ions and linker molecules) so that MOF lattice formation rate can be retarded with an increase in the DMF content. For these reasons, the D:W=1:3 cosolvent, among other cosolvent systems tested, enables both solubilization of the MOF primary building blocks and relatively fast MOF crystallization kinetics even at low synthetic temperature (i.e., 120 °C), thereby forming high quality Al-PMOF.

The same synthetic approach, instead of soluble $\text{AlCl}_3 \cdot 6\text{H}_2\text{O}$, was conducted with H_2TCCP linkers and insoluble ALD Al_2O_3 film (~30 nm) deposited on Si wafer (Si/SiO₂) (Figure 5.2b) and on polymeric fiber substrate (PP) (Figure 5.2c) to explore Al-PMOF formation behavior and corresponding film properties on the substrates upon the variation in the cosolvent systems.

The cosolvent systems (DMF and water mixture) only facilitated 2D Al-PMOF growth on the either substrate, whereas no crystalline structures were found on the synthesis with single solvent systems (DMF or water). The visibly clean surface of both silicon- and fiber-based substrates after the reaction with H₂TCPP dissolved in pure DMF is probably due to high resistance of Al₂O₃ coated on substrates to DMF solvent.^[28]

As observed in the powder synthesis, the D:W=1:3 cosolvent system rendered the most dense packing of surface-bound 2D nanometer-thick Al-PMOF film with remarkably large (micron-sized) lateral dimension (Figure 5.2b-c) compared to its powder (<500 nm) (Figure 5.2a) produced under the same synthetic condition.

We also evaluated the film quality formed on fiber substrates via XRD and N₂ isotherms for fiber-based materials, and via Fourier transform infrared (FTIR) and X-ray photoelectron spectroscopy (XPS) for Si wafer-based counterparts (Figure 5.3). As represented by SEM images in Figure 5.2c, the film integrated into PP fibers with the cosolvent system (D:W=1:3) showed markedly pronounced XRD peaks (Figure 5.3a), which agree well with both the corresponding Al-PMOF powders and its simulated pattern (Figure 5.1c). On the other hand, other cosolvent systems (D:W=3:1 and D:W=1:1) only display a small hump at 7.8° 2θ, indicative of evidently less-defined crystallinity of the film, and even no peaks relevant to MOF integrity were observed from single solvent system-driven materials (Figure 5.3a).

BET surface area of the fiber-based materials calculated from N₂ isotherms also supports that in our synthetic condition the D:W=1:3 solvent system promotes microporous Al-PMOF film formation on fiber with 233 m²/g_(MOF+fiber), whereas other solvent systems tested create non-porous or less-defined structures (i.e., 2, 45, 8, and 10 m²/g_(MOF+fiber) for pure DMF, D:W=3:1, D:W=1:1, D:W=1:3, and pure water, respectively) (Figure 5.3b).

Furthermore, FTIR studies of Al-PMOF film on Al₂O₃-coated Si/SiO₂ substrate made with the cosolvent system (D:W=1:3) show characteristic vibrational modes of the coordination ($\nu_{\text{asym}}[\text{C}=\text{O}]$ (1612 cm⁻¹) and $\nu_{\text{sym}}[\text{C}=\text{O}]$ (1442 cm⁻¹)) between Al(OH)O₄ clusters and the carboxyl groups of H₂TCPP which can be achieved within 10 h of the reaction (Figure 5.3c and Figure S5.5).^[38] The presence of Al-based secondary building units (SBUs) created during the MOF synthesis is indicative of O-H (3700 cm⁻¹) and Al-O/Al-OH stretching and bending modes^[42] in the range 400-800 cm⁻¹. In addition, general symmetric and asymmetric stretching modes of aromatic $\nu(\text{C}-\text{C})$, $\nu(\text{C}=\text{N})$, $\nu(\text{C}-\text{N})$, and $\nu(\text{C}-\text{H})$ of H₂TCPP as well as N-H band of the pyrrole ring are exclusively observed compared to the films formed with other single or cosolvent systems (D:W=3:1 and D:W=1:1).^[27,43]

As for the reaction with the single solvent systems (pure DMF or water), no inherent chemical identities of Al-PMOF are found. Instead, small peaks (1300-1600 cm⁻¹) of free H₂TCPP and clear broad peaks (400-600 cm⁻¹) of hydrated Al₂O₃ are present in the material prepared with pure water, whereas no other peaks are observed from the sample made with pure DMF (Figure 5.3c). We believe this is associated with poor stability of ALD Al₂O₃ to water^[44] and robust resistance to DMF.^[28]

XPS analyses (Figure 5.3d-f) measured on Al-PMOF film on Si/SiO₂ substrate made with the cosolvent system (D:W=1:3) indicate similar elemental compositions to reported Al-PMOF^[38] and MIL-53(Al)^[31] which are comprised of infinite chains of *trans*-connected AlO₆ polyhedra linked to each other via organic ligands. The high resolution O 1s peak at 532.4 eV and Al 2p peak at 74.8 eV are corresponding to the coordination of the Al cations with the oxygen anions of the H₂TCPP linker. Smaller humps at 534 eV in O 1s and 76.2 eV in Al 2p are also observed, which

is attributed to the presence of dangling carboxylic groups, byproduct of Al-O/-OH, or defective sites in MOFs produced during the synthesis.

As a control experiment, we also performed a heterogeneous Al-PMOF growth on highly stable ALD TiO₂ surface coated on silicon wafer (Si/SiO₂@TiO₂) using AlCl₃·6H₂O and H₂TCPP with solvent mixture (D:W=1:3) at 120 °C. The direct MOF growth approach resulted in a sparse coating of Al-PMOF crystals with a later dimension less than 500 nm as opposed to highly uniform and micron-sized Al-PMOF film with good crystallinity obtained with ALD Al₂O₃ film and H₂TCPP in the same synthetic condition (Figure S5.6).

Through the systematic investigation on solvent effects coupled with diverse Al metal sources, we demonstrated that a simple variation in solvent mixture composition (DMF and water) without any additives can initiate surface-immobilized MOF growth at relatively low temperature and control its crystallization kinetics that single solvent system cannot facilitate.

Figure 5.4a-b illustrate a proposed mechanism for the Al-PMOF formation driven by ALD Al₂O₃ film and H₂TCPP in cosolvent system (DMF and water). The Al₂O₃ dissolution is initiated by a rapid hydration of the metal oxide surface, followed with release of Al³⁺ ions near the surface by reacting with protons (H⁺) and water molecules (H₂O) present in the solvent system.^[45,46] The possible hydrated species obtained from our thermodynamic calculations are mainly aluminum oxide hydroxides including diaspore (AlO(OH)(D)) and boehmite (AlO(OH)(B)), and aluminum hydroxides (Al(OH)₃) (Supporting Information), all of which can convert to Al-based MOFs in hydrothermal conditions.^[22] Our modeling calculation also indicates that in our synthetic condition the release of Al³⁺ and subsequent formation of aluminum aqua complexes ([Al(H₂O)₆]³⁺) by a reaction, for instance, between Al(OH)(D) and H⁺ in water ([AlO(OH)(D)](s) + 4H₂O(l) + 3H⁺(aq) → Al³⁺(aq) + 6H₂O(l)) is thermodynamically favorable at 120 °C with ΔG = -21.6 kJ per

mol of AlO(OH)(D) (Supporting Information). The coordination between the released Al³⁺ ions and H₂TCPP linkers solubilized well by DMF can facilitate Al₂(OH)₂(H₂TCPP) nucleation on the surface and promotes further MOF film growth.

We also find that no reaction occurs between H₂TCPP dissolved in pure DMF and hydrated alumina film due to a strong resistance of the film to DMF, whereas Al-PMOF film forms with H₂TCPP dissolved in water-contained cosolvent (Figure S5.7).

As a result, we can conclude that the cosolvent system (DMF and water) plays a significant role in that water dissolves Al₂O₃ into Al³⁺ ions while DMF solubilizes H₂TCPP linkers to facilitate the Al-PMOF lattice formation at relatively low temperature, 120 °C. The MOF film growth kinetics can be also controlled by cosolvent ratio^[40,47] and concentration of organic linkers (Figure S5.8) together with other synthetic parameters, such as reaction temperature and pH of the initial reaction mixture.^[46]

The mechanism is further supported by a cross-section analysis of the Al-PMOF film obtained by high-angle annular dark-field scanning transmission electron microscopy (HAADF-STEM, Figure 5.4c-d). In addition, the elemental distribution in the cross section was analyzed by high-resolution EDX mapping to confirm the interface components (Figure 5.4e-h). Figure 5.4c-d show that the distinct interface (~40 nm) between Al-PMOF and the Si substrate is rough, porous, and slightly swollen compared to the starting dense and seamless ALD Al₂O₃ film.^[44] Strong signals of Al and O together with a weak C signal in Figure 5.4e-h present that the interface formed during the synthesis would be an intermediate layer dominantly composed of porous hydrated alumina (i.e., AlO(OH) and Al(OH)₃).

To prove the catalytic performance of Al-PMOF/fiber textile, we investigated CEES photooxidation in contact with powder or composite catalyst under O₂ rich and LED irradiation

environment (Figure 5.5a). The CEES oxidation study with powder samples was conducted by dispersing solid powder in methanol with 20 min of sonication, which was sealed in a glass microwave tube. After the sonication process, the mixture was purged with O₂ for 10 min, followed with adding 10 μL of 1-bromo-3,5-difluorobenzene as an internal standard (IS) and CEES (23 μL, 0.2 mmol) to the tube, and the oxidation reaction was monitored by GC-MS (Figure S5.9-10). The sonication step was left off when MOF/fiber catalysts were used in place of powder samples. Instead, the MOF/fiber textile was simply submerged in methanol, followed directly by 10 min O₂ purging, subsequent IS and CEES addition to the tube. Figure 5.5b displays oxidation profiles of CEES over time in the presence of Al-PMOF powder (1.2 mg_{MOF}, 0.7 mol%), H₂TCP (1.2 mg_{linker}, 0.8 mol%), or 8.5 mg_(MOF+fiber) of PP@Al-PMOF (0.3 mg_{MOF}, 0.2 mol%) with calculated simulant half lives of 16, 6, and 4 min, respectively. Corresponding GC-MS spectra and kinetic analysis to obtain simulant half-lives are also included in Supporting Information (Figure S5.11-12). The catalyst loading (mol%) is calculated based on moles of porphyrins in Al-PMOF (calculation of the catalyst loading is described in Supporting Information).

As confirmed by GC-MS spectra in Figure 5.5c, the only product during the oxidation was the nontoxic CEESO without toxic CEESO₂, exhibiting a highly selective oxidation process in our photocatalytic system (Figure S5.9-11). Almost negligible CEES oxidation was observed for 120 min from 10 mg_{fiber} of PP coated with ALD Al₂O₃, revealing that only Al-PMOF component acts as a photocatalyst (Figure 5.5b). The result evidently indicates that Al-PMOF is capable of absorbing the light, generating ¹O₂, and rapidly oxidizing CEES to CEESO as other Zr₆-based MOFs perform (e.g., PCN-222/MOF545,^[18,48] NU-1000,^[17,48] and UMCM-313^[48]). We also found a complete deactivation of photocatalytic oxidation of CEES in the dark (Figure S5.13).

Turnover frequencies (TOF) for CEES oxidation were calculated to identify and compare the catalytic efficacy of our products with reported performances of other MOF-based materials^[48] (calculation of TOFs and simulant half lives of CEES is described in Supporting Information). Al-PMOF bulk powder, H₂TCPP powder, and Al-PMOF thin film on PP fiber exhibits 9, 22, and 170 mol_{CEES}·mol_{chromophore}⁻¹·min⁻¹ TOF, respectively. This signifies that catalytic activity of porphyrin linker and Al-PMOF film are 2.5-fold and 19-fold higher than Al-PMOF powder counterpart, respectively. 10-fold enhancement in TOF was recently demonstrated on UMCM-313 film solvothermally grown on FTO substrate compared to MOF powder counterpart.^[48] Importantly, our Al-PMOF film on fiber substrate shows even 1.7-fold higher photocatalytic activity than UMCM-313 film on flat substrate. This conspicuous enhancement in catalytic performance is probably because 2D Al-PMOF nanosheet crystals are radially grown and effectively arranged with no aggregation on fiber surface (Figure S5.14), thus leading to greater local concentration of CEES per gram of MOF compared to micron-sized Zr₆-based MOF films on flat surface.^[27] This distinct feature also enables a substantial exposure of Al-PMOF film to incident light with less light scattering,^[49] therefore effectively generating ¹O₂ to oxidize CEES. To the best of our knowledge, this is the first to both substantiate a great promise of Al-based MOF as a promising photocatalyst, and demonstrate Al-PMOF/fiber catalyst with prominently enhanced photocatalytic activity in CEES detoxification.

The practical effectiveness of Al-PMOF/fiber composite can be extended to a colorimetric textile pH sensor, showing an instant and dramatic color change from brown to green upon HCl vapor exposure (Figure 5.5d). The greenish color can immediately return to the original brown color upon exposure to NH₃ vapor given off from NH₄OH solution (Figure 5.5d). The reversible color change is attributed to protonation/deprotonation of the nitrogen Lewis basic sites on the

H₂TCPP linker in Al-PMOF.^[39] The structural robustness of the Al-PMOF after HCl exposure was also verified in a previous report.^[39] The systematic exploration on reversible colorimetric and switchable pH response was implemented with PCN-222 containing H₂TCPP as a linker.^[50]

The Al-PMOF/fiber textile can be also exploited as an efficient adsorbent for organic solvents with high selectivity. As shown in Figure 5.5e, the chloroform droplets contaminated in water was rapidly absorbed by the MOF/fiber composite upon contact. The selective and immediate organic solvent suction over water is due to relatively hydrophobic nature of the Al-PMOF film as demonstrated in the water isotherms of the MOF (Figure 5.1d) and in a simple test with water droplets cast on the composite surface (Figure 5.5e).

5.5. Conclusions

In summary, we for the first time found Al-PMOF as a promising photocatalyst to efficiently generate reactive singlet oxygen under LED irradiation, therefore rapidly and selectively oxidizing toxic CEES into non-hazardous CEESO. We further demonstrated surface-immobilized Al-PMOF thin films on polymeric non-woven textile substrates at relatively low temperature (120 °C) by using a solid Al₂O₃ film conversion approach in cosolvent system of DMF and water. The minimization of light scattering driven by finely controlled MOF thin film growth on macroporous fiber network gave rise to highly effective exposure of the catalyst film to the incident light, thus substantially enhancing the singlet oxygen (¹O₂) generation yield. In addition, the MOF/fiber composite architecture further helps efficacious exposure of CEES molecules to singlet oxygen abundant near the catalyst film. These significant benefits of the Al-PMOF/fiber photocatalyst with only 0.2 mol% of MOF enabled CEES half lives of 4 min under blue LED light irradiation, corresponding to 170 mol_{CEES} · mol_{chromophore}⁻¹ · min⁻¹ TOF. To the best of our knowledge,

the photocatalytic performance out of fiber-surface-bound Al-PMOF thin film is the most efficient among other MOF thin film systems reported. We also further demonstrated the multifunctionality of the MOF/fiber textiles as a reversible colorimetric pH sensing and a selective absorption of organic solvents from contaminated water. Therefore, these prominent results reported here can be readily extended to other smart textile systems with more effective functional performance in wider application areas.

5.6. Figures

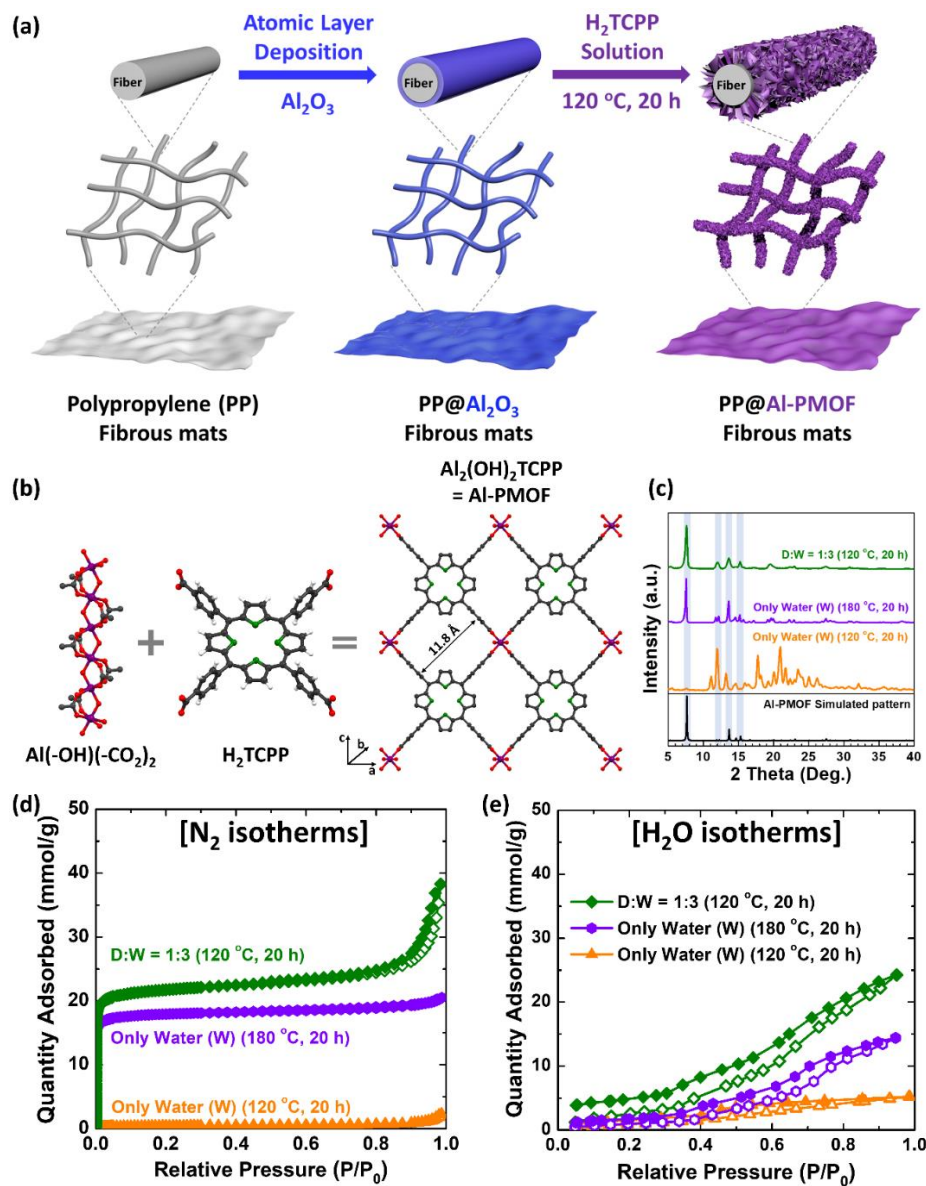


Figure 5.1. (a) Schematic illustration of a synthetic procedure of MOF/fiber textiles using ALD Al_2O_3 -treated PP fibers, followed by reacting with H_2TCPP organic linkers. (b) Crystal structure of $\text{Al}_2(\text{OH})_2\text{TCPP}$ MOF (i.e., Al-PMOF), consisting of octahedral $\text{Al}(\text{OH})$ clusters interconnected to H_2TCPP organic linkers. (c) XRD patterns, (d) N_2 sorption isotherms at 77 K, and (e) water vapor isotherms at 298 K of Al-PMOF powders prepared with $\text{AlCl}_3 \cdot 6\text{H}_2\text{O}$ and H_2TCPP under varied synthetic conditions.

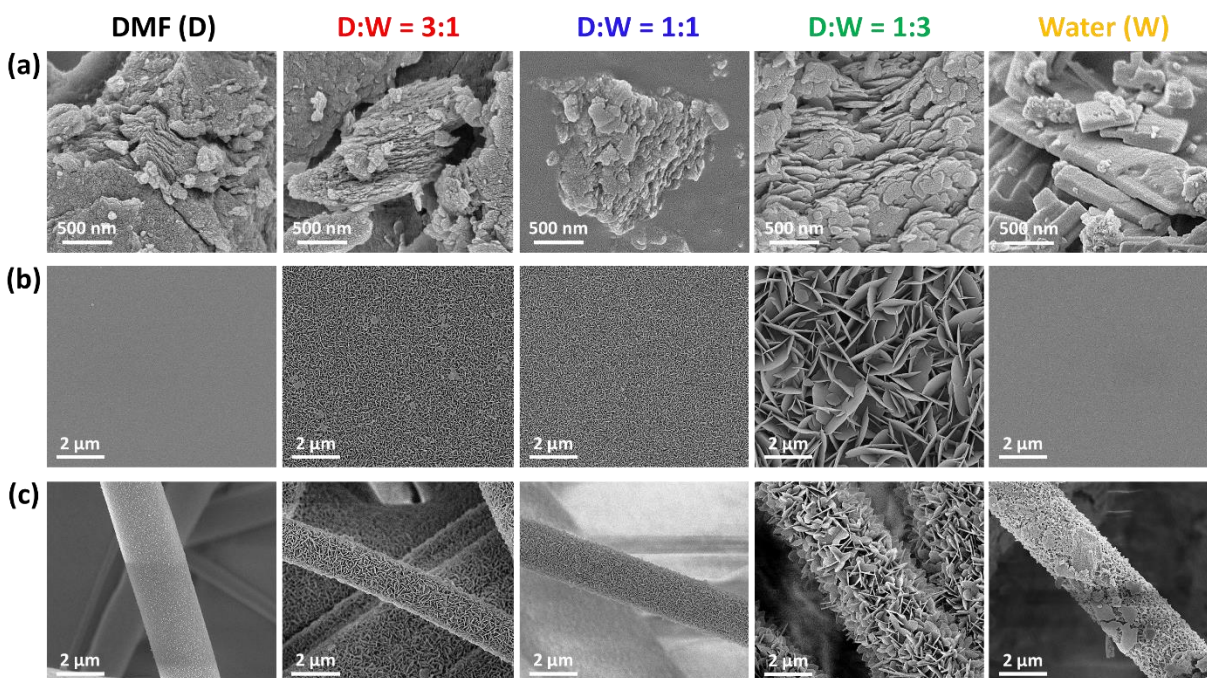


Figure 5.2. SEM images of (a) Al-PMOF powder, (b) Si/SiO₂@Al-PMOF, and (c) PP@Al-PMOF obtained with different ratios of solvents (DMF:Water) at 120 °C for 20 h. MOF powder was synthesized by AlCl₃·6H₂O and H₂TCPP, and MOF on solid substrates was driven by reaction of ALD Al₂O₃ on the substrates with H₂TCPP.

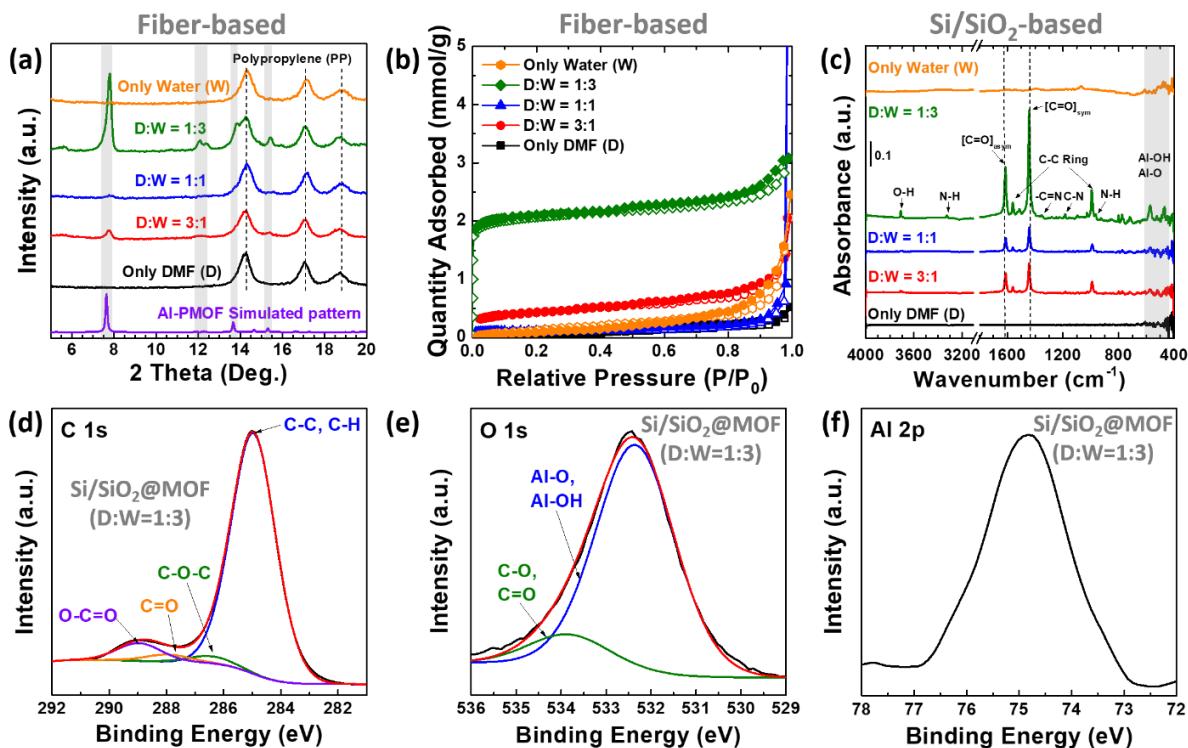


Figure 5.3. (a) XRD patterns and (b) N₂ sorption isotherms at 77 K of PP@Al-PMOF, and (c) FTIR spectra of Si/SiO₂@Al-PMOF (Si/SiO₂@Al₂O₃ as a background for each sample). The samples are synthesized using ALD Al₂O₃-coated substrates with H₂TCPP linkers dissolved in varied ratios of solvent mixtures (DMF:Water) at 120 °C for 20 h. XPS data for (d) C 1s, (e) O 1s, and (f) Al 2p for Si/SiO₂@Al-PMOF made from ALD Al₂O₃-coated substrates and H₂TCPP linkers dissolved in a solvent mixture (DMF:Water=1:3).

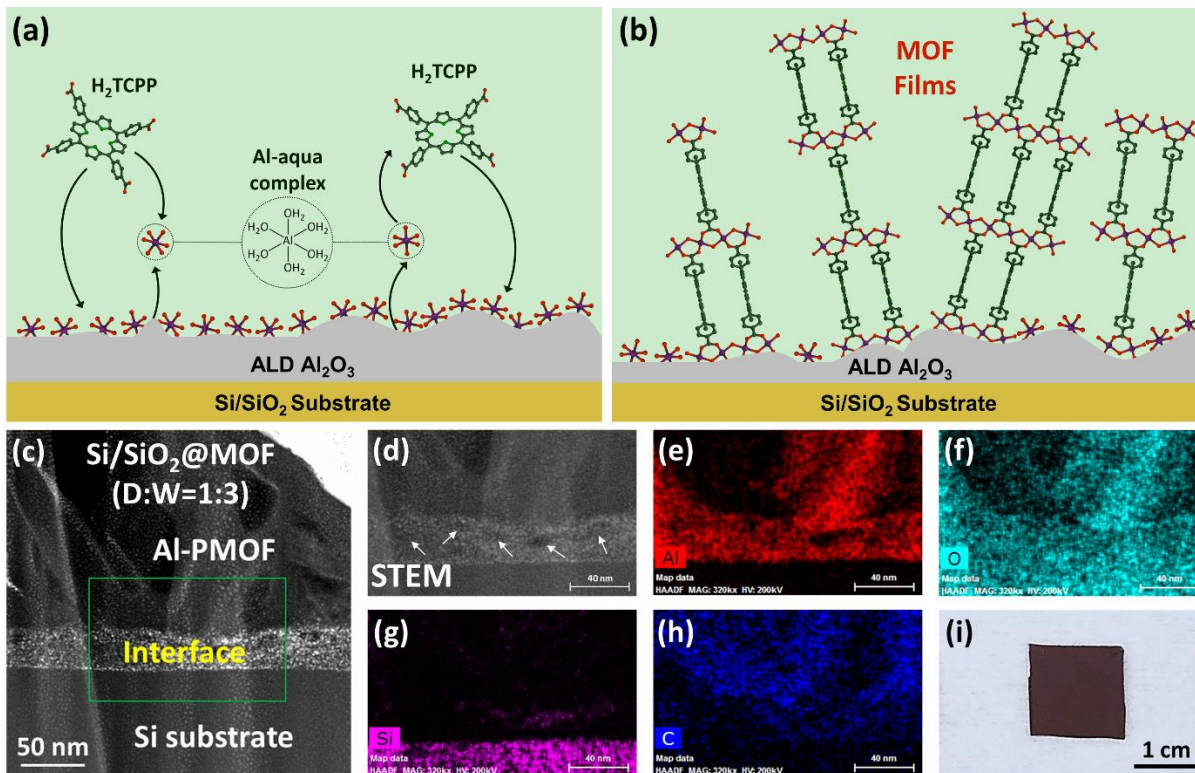


Figure 5.4. (a, b) Schematic illustration of Al-PMOF film formation mechanism in cross-sectional view and (c, d) HAADF-STEM images for a cross section of the Al-PMOF formed on ALD Al₂O₃-coated Si wafer (Si/SiO₂@Al-PMOF). The green box in (c) indicates the location of (d–h). (e–h) High-resolution EDX mapping images of the cross section. (i) A digital photograph of the actual sample measured, Si/SiO₂@Al-PMOF (DMF:Water=1:3). Arrows in (d) are indicative of voids in alumina film, which are generated during the film dissolution process by water.

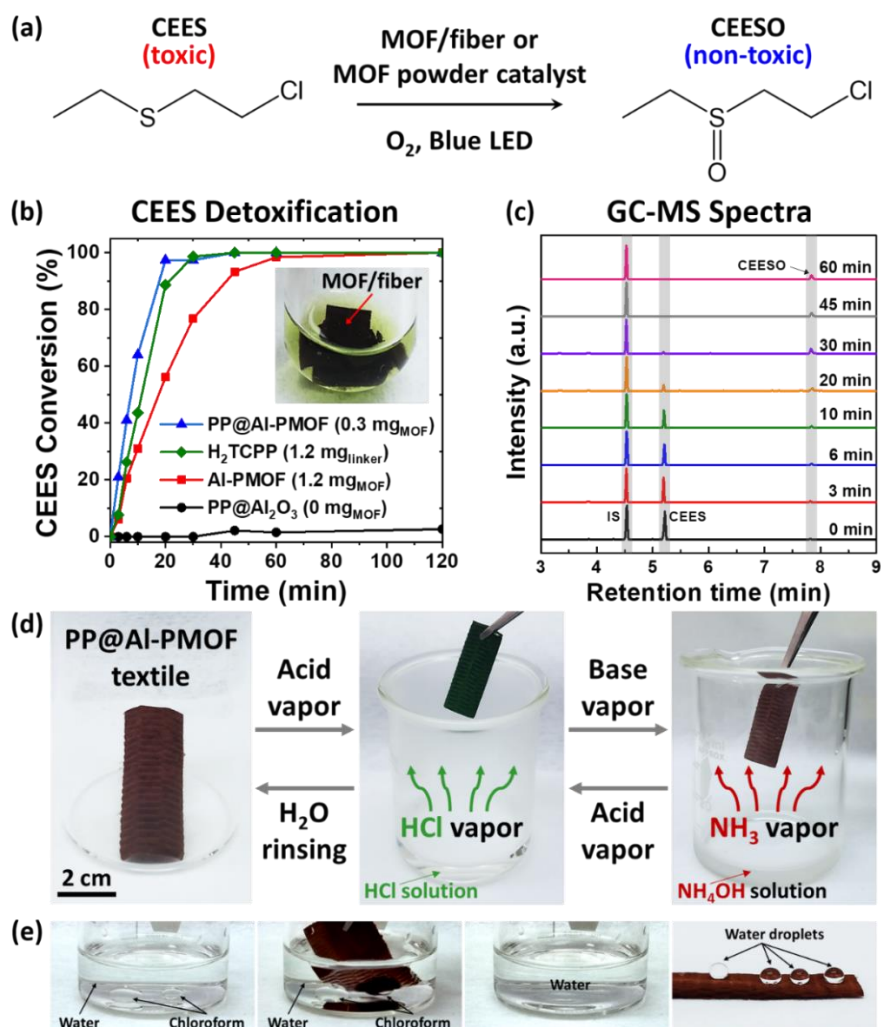


Figure 5.5. Multifunctionality of Al-PMOF/fiber textiles. (a) Selective photo-oxidation of 2-chloroethyl ethyl sulfide (CEES) under blue LED irradiation and O₂ environment catalyzed by MOF-based catalysts. (b) Oxidation profiles of CEES to CEESO conversion over time using varied photo-catalysts. (c) Gas chromatography (GC) signals exhibiting the selective oxidation progress of CEES (5.2 min) to CEESO (7.8 min) in the presence of Al-PMOF powder. 1-bromo-3,5-difluorobenzene was used as an internal standard (IS) during the reaction. (d) A colorimetric MOF/fiber textile pH sensor. (e) Snapshots of selective removal of chloroform contaminants from water using MOF/fiber textiles (left to right). The rightmost picture in (d) shows a hydrophobic feature of the MOF/fiber textiles.

5.7. References

- [1] N. S. Bobbitt, M. L. Mendonca, A. J. Howarth, T. Islamoglu, J. T. Hupp, O. K. Farha, R. Q. Snurr, *Chem. Soc. Rev.* **2017**, *46*, 3357.
- [2] G. J. Fitzgerald, *Am. J. Public Health* **2008**, *98*, 611.
- [3] H. Li, R. Muir, N. R. McFarlane, R. J. Soilleux, X. Yu, I. P. Thompson, S. A. Jackman, *Biodegradation* **2013**, *24*, 125.
- [4] G. W. Wagner, O. B. Koper, E. Lucas, S. Decker, K. J. Klabunde, *J. Phys. Chem. B* **2000**, *104*, 5118.
- [5] C. R. Ringenbach, S. R. Livingston, D. Kumar, C. C. Landry, *Chem. Mater.* **2005**, *17*, 5580.
- [6] J. Hirade, A. Ninomiya, *J. Biochem.* **1950**, *37*, 19.
- [7] A. J. Howarth, C. T. Buru, Y. Liu, A. M. Ploskonka, K. J. Hartlieb, M. McEntee, J. J. Mahle, J. H. Buchanan, E. M. Durke, S. S. Al-Juaid, J. F. Stoddart, J. B. DeCoste, J. T. Hupp, O. K. Farha, *Chem. – A Eur. J.* **2017**, *23*, 214.
- [8] H. Wang, G. W. Wagner, A. X. Lu, D. L. Nguyen, J. H. Buchanan, P. M. McNutt, C. J. Karwacki, *ACS Appl. Mater. Interfaces* **2018**, *10*, 18771.
- [9] J. E. Mondloch, M. J. Katz, W. C. Isley III, P. Ghosh, P. Liao, W. Bury, G. W. Wagner, M. G. Hall, J. B. DeCoste, G. W. Peterson, R. Q. Snurr, C. J. Cramer, J. T. Hupp, O. K. Farha, *Nat. Mater.* **2015**, *14*, 512.
- [10] S.-Y. Moon, G. W. Wagner, J. E. Mondloch, G. W. Peterson, J. B. DeCoste, J. T. Hupp, O. K. Farha, *Inorg. Chem.* **2015**, *54*, 10829.
- [11] R. Gil-San-Millan, E. López-Maya, M. Hall, N. M. Padial, G. W. Peterson, J. B. DeCoste, L. M. Rodríguez-Albelo, J. E. Oltra, E. Barea, J. A. R. Navarro, *ACS Appl. Mater. Interfaces* **2017**, *9*, 23967.

- [12] S.-Y. Moon, Y. Liu, J. T. Hupp, O. K. Farha, *Angew. Chemie Int. Ed.* **2015**, *54*, 6795.
- [13] M. J. Katz, S.-Y. Moon, J. E. Mondloch, M. H. Beyzavi, C. J. Stephenson, J. T. Hupp, O. K. Farha, *Chem. Sci.* **2015**, *6*, 2286.
- [14] A. M. Ploskonka, J. B. DeCoste, *ACS Appl. Mater. Interfaces* **2017**, *9*, 21579.
- [15] A. J. Howarth, Y. Liu, P. Li, Z. Li, T. C. Wang, J. T. Hupp, O. K. Farha, *Nat. Rev. Mater.* **2016**, *1*, 15018.
- [16] A. Atilgan, T. Islamoglu, A. J. Howarth, J. T. Hupp, O. K. Farha, *ACS Appl. Mater. Interfaces* **2017**, *9*, 24555.
- [17] Y. Liu, C. T. Buru, A. J. Howarth, J. J. Mahle, J. H. Buchanan, J. B. DeCoste, J. T. Hupp, O. K. Farha, *J. Mater. Chem. A* **2016**, *4*, 13809.
- [18] Y. Liu, A. J. Howarth, J. T. Hupp, O. K. Farha, *Angew. Chemie Int. Ed.* **2015**, *54*, 9001.
- [19] Y. Liu, S.-Y. Moon, J. T. Hupp, O. K. Farha, *ACS Nano* **2015**, *9*, 12358.
- [20] J. Kim, S. Lee, J. Kim, D. Lee, *Adv. Funct. Mater.* **2019**, *0*, 1808466.
- [21] K. Khaletskaya, S. Turner, M. Tu, S. Wannapaiboon, A. Schneemann, R. Meyer, A. Ludwig, G. Van Tendeloo, R. A. Fischer, *Adv. Funct. Mater.* **2014**, *24*, 4804.
- [22] Z. Li, Y. Wu, J. Li, Y. Zhang, X. Zou, F. Li, *Chem. – A Eur. J.* **2015**, *21*, 6913.
- [23] Y. Zhao, N. Kornienko, Z. Liu, C. Zhu, S. Asahina, T.-R. Kuo, W. Bao, C. Xie, A. Hexemer, O. Terasaki, P. Yang, O. M. Yaghi, *J. Am. Chem. Soc.* **2015**, *137*, 2199.
- [24] K. Okada, R. Ricco, Y. Tokudome, M. J. Styles, A. J. Hill, M. Takahashi, P. Falcaro, *Adv. Funct. Mater.* **2014**, *24*, 1969.
- [25] M. Zhang, L. Ma, L. Wang, Y. Sun, Y. Liu, *ACS Appl. Mater. Interfaces* **2018**, *10*, 2259.

- [26] J. Zhao, M. D. Losego, P. C. Lemaire, P. S. Williams, B. Gong, S. E. Atanasov, T. M. Blevins, C. J. Oldham, H. J. Walls, S. D. Shepherd, M. A. Browe, G. W. Peterson, G. N. Parsons, *Adv. Mater. Interfaces* **2014**, *1*, 1400040.
- [27] D. T. Lee, J. D. Jamir, G. W. Peterson, G. N. Parsons, *Small* **2019**, *Accepted*.
- [28] C. M. Moran, J. N. Joshi, R. M. Marti, S. E. Hayes, K. S. Walton, *J. Am. Chem. Soc.* **2018**, *140*, 9148.
- [29] I. Stassen, M. Styles, G. Greci, H. V. Gorp, W. Vanderlinden, S. D. Feyter, P. Falcaro, D. De Vos, P. Vereecken, R. Ameloot, *Nat. Mater.* **2015**, *15*, 304.
- [30] X. Ma, P. Kumar, N. Mittal, A. Khlyustova, P. Daoutidis, K. A. Mkhoyan, M. Tsapatsis, *Science (80-.)*. **2018**, *361*, 1008 LP.
- [31] D. T. Lee, J. Zhao, C. J. Oldham, G. W. Peterson, G. N. Parsons, *ACS Appl. Mater. Interfaces* **2017**, *9*, 44847.
- [32] J. Zhao, D. T. Lee, R. W. Yaga, M. G. Hall, H. F. Barton, I. R. Woodward, C. J. Oldham, H. J. Walls, G. W. Peterson, G. N. Parsons, *Angew. Chemie Int. Ed.* **2016**, *55*, 13224.
- [33] D. T. Lee, J. Zhao, G. W. Peterson, G. N. Parsons, *Chem. Mater.* **2017**, *29*, 4894.
- [34] M. Bechelany, M. Drobek, C. Vallicari, A. Abou Chaaya, A. Julbe, P. Miele, *Nanoscale* **2015**, *7*, 5794.
- [35] A. Fateeva, P. A. Chater, C. P. Ireland, A. A. Tahir, Y. Z. Khimyak, P. V Wiper, J. R. Darwent, M. J. Rosseinsky, *Angew. Chemie Int. Ed.* **2012**, *51*, 7440.
- [36] C. Y. Lee, O. K. Farha, B. J. Hong, A. A. Sarjeant, S. T. Nguyen, J. T. Hupp, *J. Am. Chem. Soc.* **2011**, *133*, 15858.

- [37] G. K. Hyde, G. Scarel, J. C. Spagnola, Q. Peng, K. Lee, B. Gong, K. G. Roberts, K. M. Roth, C. A. Hanson, C. K. Devine, S. M. Stewart, D. Hojo, J.-S. Na, J. S. Jur, G. N. Parsons, *Langmuir* **2010**, *26*, 2550.
- [38] N. Sadeghi, S. Sharifnia, T.-O. Do, *J. Mater. Chem. A* **2018**, *6*, 18031.
- [39] O. T. Wilcox, A. Fateeva, A. P. Katsoulidis, M. W. Smith, C. A. Stone, M. J. Rosseinsky, *Chem. Commun.* **2015**, *51*, 14989.
- [40] R. Ameloot, E. Gobechiya, H. Uji-i, J. A. Martens, J. Hofkens, L. Alaerts, B. F. Sels, D. E. De Vos, *Adv. Mater.* **2010**, *22*, 2685.
- [41] I. Persson, *Pure Appl. Chem.* **1986**, *58*, 1153.
- [42] A. E. J. Hoffman, L. Vanduyfhuys, I. Nevjestic, J. Wieme, S. M. J. Rogge, H. Depauw, P. Van Der Voort, H. Vrielinck, V. Van Speybroeck, *J. Phys. Chem. C* **2018**, *122*, 2734.
- [43] R. Rahimi, S. Shariatnia, S. Zargari, M. Yaghoubi Berijani, A. Ghaffarinejad, Z. S. Shojaie, *RSC Adv.* **2015**, *5*, 46624.
- [44] G. C. Correa, B. Bao, N. C. Strandwitz, *ACS Appl. Mater. Interfaces* **2015**, *7*, 14816.
- [45] J. Reboul, S. Furukawa, N. Horike, M. Tsotsalas, K. Hirai, H. Uehara, M. Kondo, N. Louvain, O. Sakata, S. Kitagawa, *Nat. Mater.* **2012**, *11*, 717.
- [46] H. Robotjazi, D. Weinberg, D. F. Swearer, C. Jacobson, M. Zhang, S. Tian, L. Zhou, P. Nordlander, N. J. Halas, *Sci. Adv.* **2019**, *5*, eaav5340.
- [47] W. Zhan, Q. Kuang, J. Zhou, X. Kong, Z. Xie, L. Zheng, *J. Am. Chem. Soc.* **2013**, *135*, 1926.
- [48] C. T. Buru, M. B. Majewski, A. J. Howarth, R. H. Lavroff, C.-W. Kung, A. W. Peters, S. Goswami, O. K. Farha, *ACS Appl. Mater. Interfaces* **2018**, *10*, 23802.
- [49] L. Heinke, C. Wöll, *Adv. Mater.* **2019**, *0*, 1806324.
- [50] B. J. Deibert, J. Li, *Chem. Commun.* **2014**, *50*, 9636.

5.8. Supporting Information

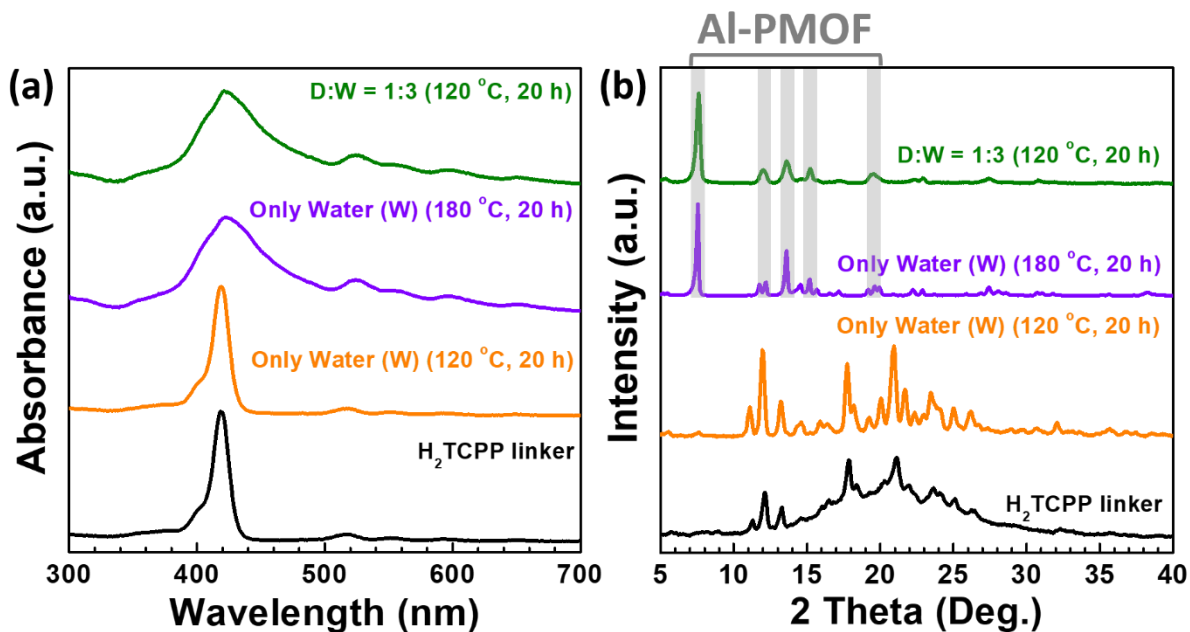


Figure S5.1. (a) UV-Vis absorption spectra and (b) XRD patterns of H₂TCPP linker and powder samples synthesized with AlCl₃·6H₂O and H₂TCPP in pure water at 120 °C for 20 h, in pure water at 180 °C for 20 h, and in cosolvent (DMF:Water=1:3) at 120 °C for 20 h, respectively (from bottom to top).

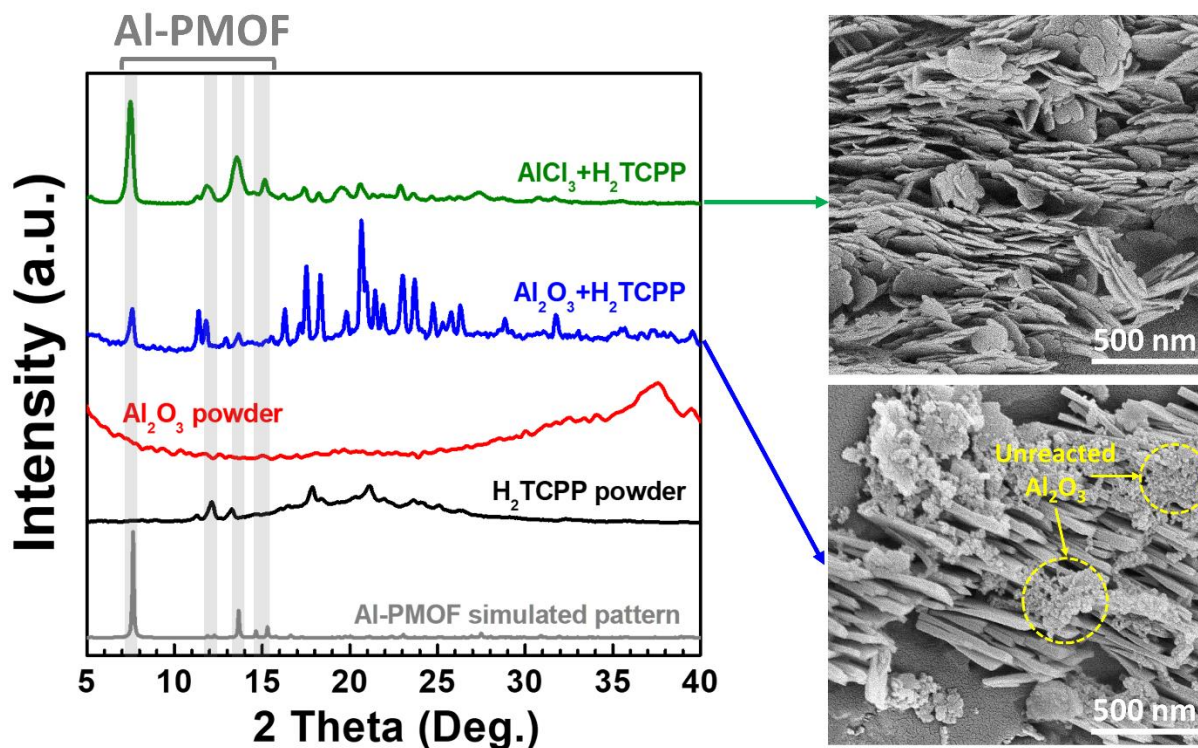


Figure S5.2. XRD patterns (left) of Al-PMOF simulated pattern, H₂TCPP linker, Al₂O₃ solid powder, and synthesized powders made with Al₂O₃ powder and H₂TCPP, and with AlCl₃·6H₂O and H₂TCPP in cosolvent (DMF:Water=1:3) at 120 °C for 20 h, respectively (from bottom to top). SEM images (right) of solid products after corresponding reactions. Well-defined Al-PMOF crystals (top), made with AlCl₃·6H₂O, were observed, whereas unreacted Al₂O₃ solids and nonporous assembled H₂TCPP salts were dominantly found when Al₂O₃ powder was used as a metal source.

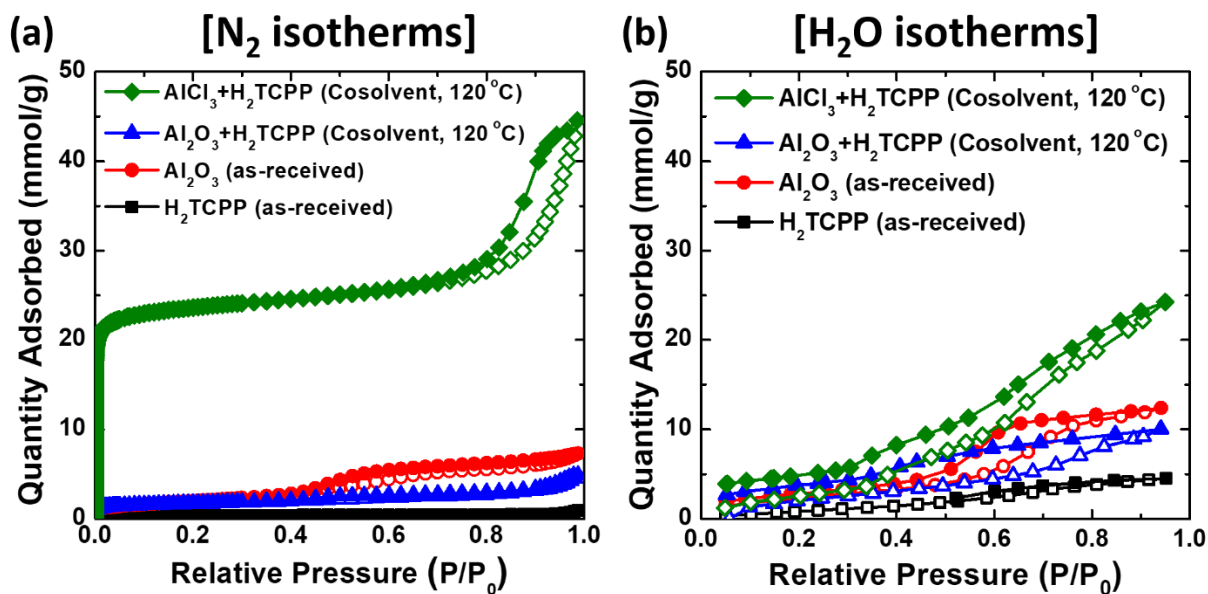


Figure S5.3. (a) N₂ sorption isotherms at 77 K, and (b) water vapor isotherms at 298 K of H₂TCPP linker, Al₂O₃ solid powder, and synthesized powders made with Al₂O₃ powder and H₂TCPP, and with AlCl₃·6H₂O and H₂TCPP in cosolvent (DMF:Water=1:3) at 120 °C for 20 h, respectively.

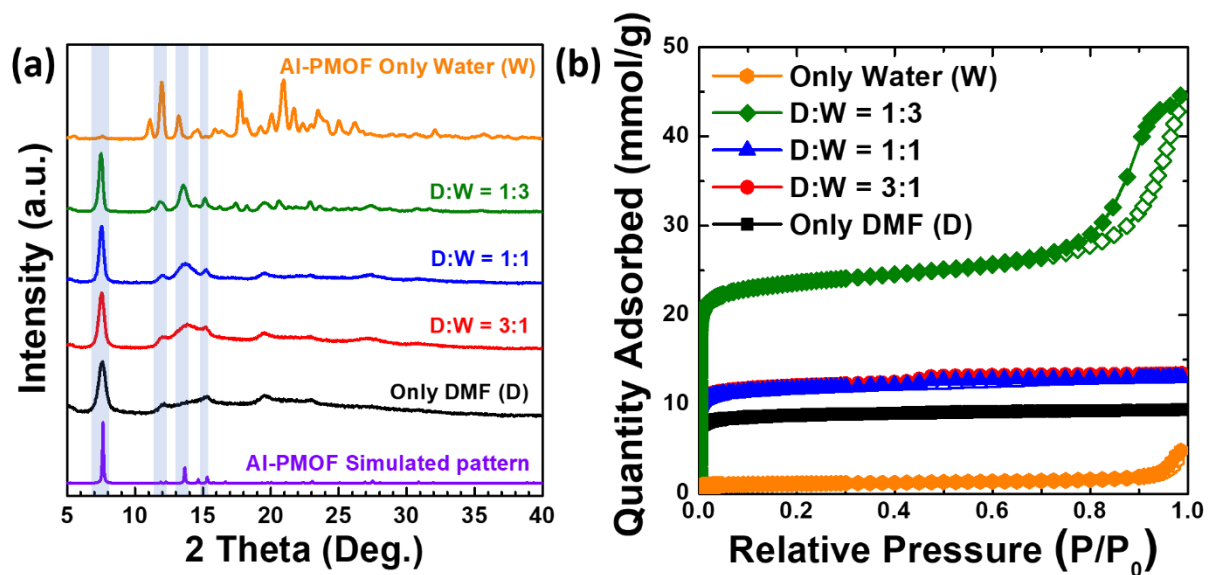


Figure S5.4. (a) XRD patterns and (b) N₂ sorption isotherms at 77 K of powder samples synthesized with different ratios of solvents (DMF:Water) at 120 °C for 20 h. MOF powder was synthesized with AlCl₃·6H₂O and H₂TCPP precursors.

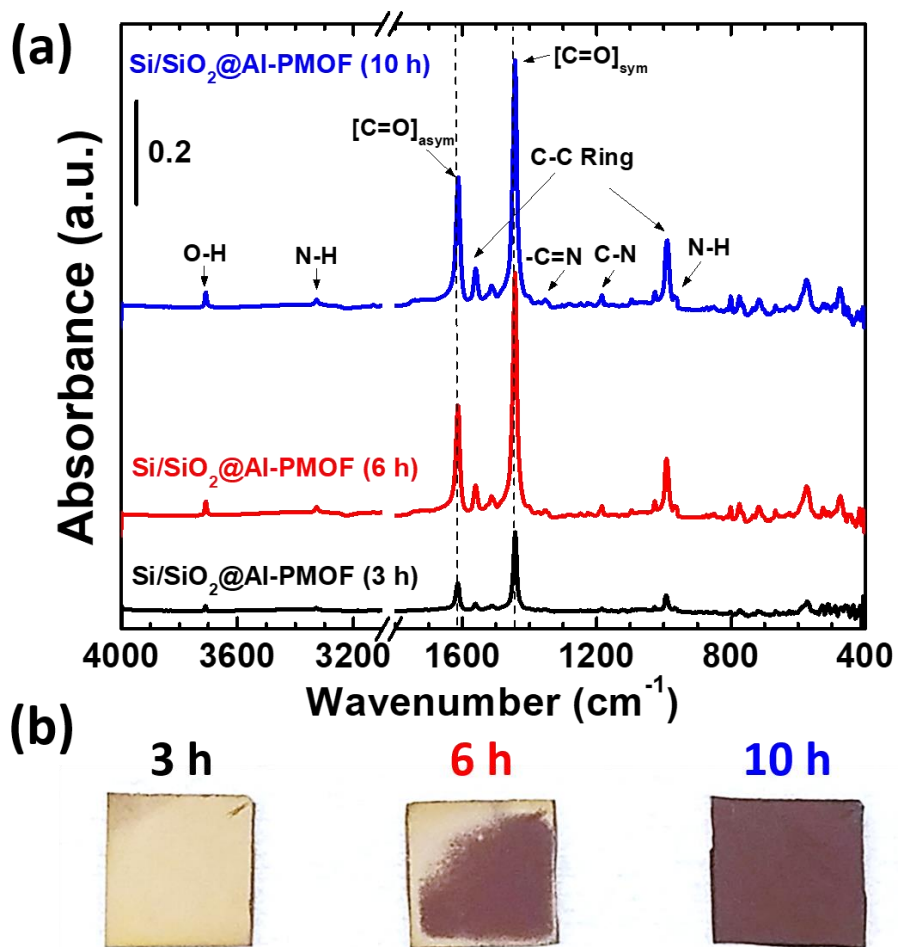


Figure S5.5. (a) FTIR spectra of progressive Al-PMOF film formation on Si/SiO₂ substrate (Si/SiO₂@Al-PMOF) over time of reaction between Si/SiO₂ coated with ALD Al₂O₃ (Si/SiO₂@Al₂O₃) and H₂TCPP dissolved in cosolvent (DMF:Water=1:3) at 120 °C. Note that Si/SiO₂@Al₂O₃ was used as a background for all FTIR spectra. (b) Optical photographs of each sample collected at 3 h, 6 h, and 10 h of corresponding reaction.

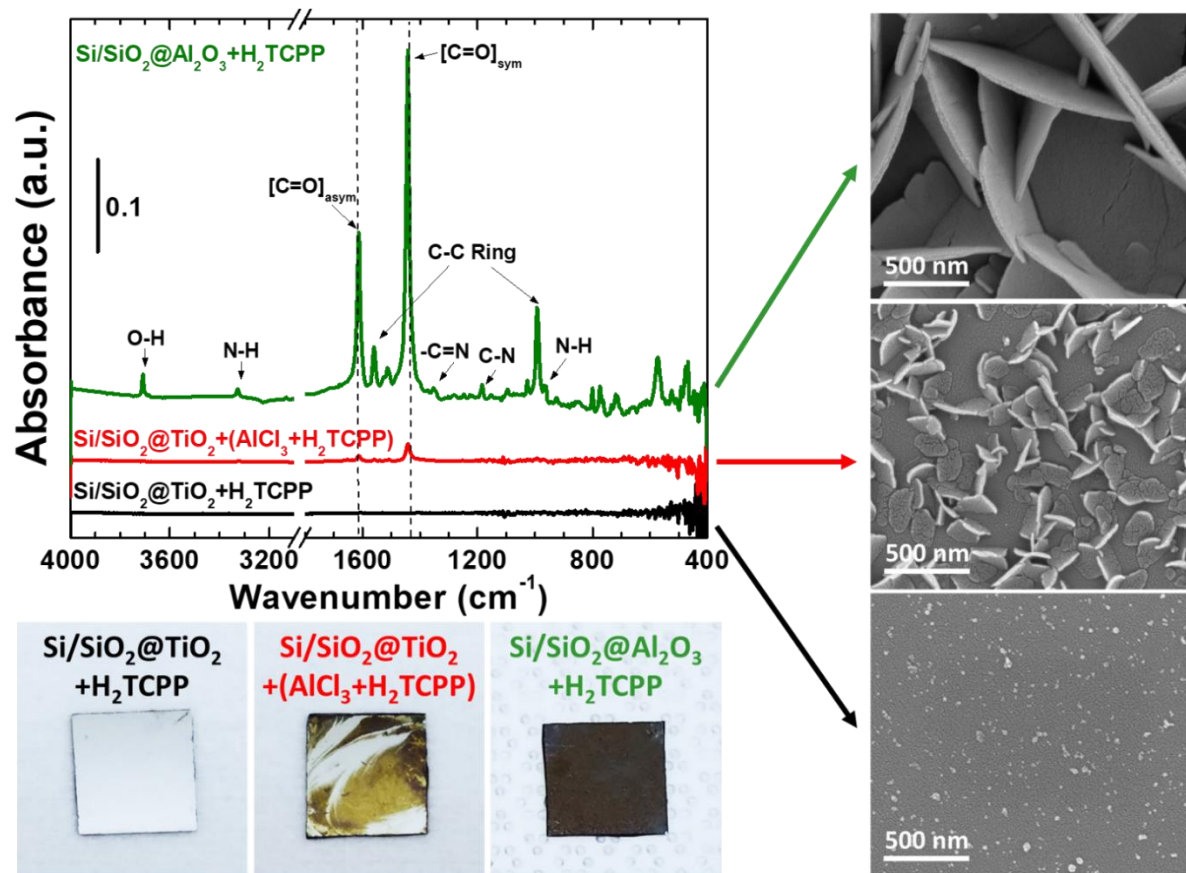


Figure S5.6. FTIR spectra captured in differential mode. For the spectra obtained here, the Si/SiO₂@TiO₂ and Si/SiO₂@Al₂O₃ were subtracted as a background for first two samples from the bottom (black and red) and for the sample on top (green), respectively. The reaction condition for the samples here were conducted with (DMF:Water=1:3) mixture at 120 °C for 20 h. The spectrum on Si/SiO₂@TiO₂+H₂TCPP (black) after a background subtraction shows that ALD TiO₂ remained intact and no reaction occurred with H₂TCPP in the synthetic condition. AlCl₃·6H₂O and H₂TCPP can form Al-PMOF film on stable TiO₂ surface but poor film uniformity was obtained (Si/SiO₂@TiO₂+AlCl₃+H₂TCPP, red). The well-defined and densely coated Al-PMOF film was observed by the optimal synthetic route with Si/SiO₂@Al₂O₃ reacting with H₂TCPP (Si/SiO₂@Al₂O₃+H₂TCPP, green) in the synthetic condition. Optical photographs and SEM images of each sample are shown on the bottom and on the right side, respectively.

Thermodynamic Calculations (reactions at equilibrium)

[Possible Al₂O₃ hydration reactions at 120 °C]

- Al₂O₃(s) + H₂O(l) → 2AlO(OH)(D)(s), ΔG = -22.068 kJ
- Al₂O₃(s) + H₂O(l) → 2AlO(OH)(B)(s), ΔG=-12.673 kJ
- Al₂O₃(s) + 3H₂O(l) → 2Al(OH)₃(s), ΔG=-3.552 kJ

Here, two types of main aluminum hydroxides are obtained via thermodynamic modeling: diaspore (AlO(OH)(D)) and boehmite (AlO(OH)(B)).

[Possible hydrated alumina dissolution reactions at 120 °C]

- AlO(OH)(D)(s) + 4H₂O(l) + 3H⁺(aq) → Al³⁺(aq) + 6H₂O(l), ΔG = -21.562 kJ
- AlO(OH)(B)(s) + 4H₂O(l) + 3H⁺(aq) → Al³⁺(aq) + 6H₂O(l), ΔG = -26.260 kJ
- Al(OH)₃(s) + 3H⁺(aq) + 3H₂O(l) → Al³⁺(aq) + 6H₂O(l), ΔG = -30.820 kJ

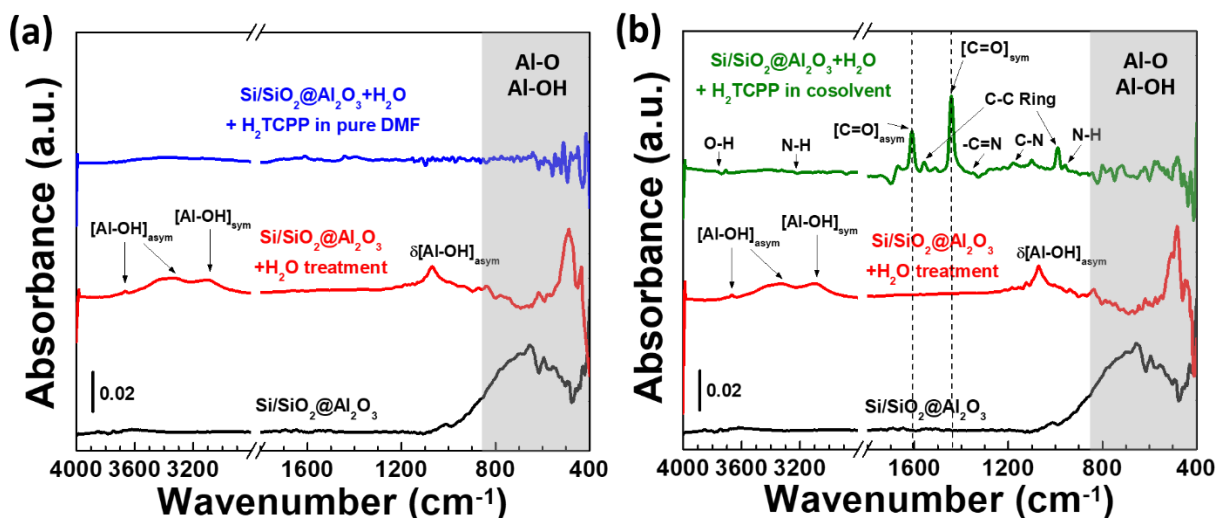


Figure S5.7. (a) Difference FTIR spectra following sequential ALD Al_2O_3 (black), H_2O treatment (red), and reaction with H_2TCPP in pure DMF (blue) on Si/SiO_2 substrate. (b) Difference FTIR spectra following sequential ALD Al_2O_3 (black), H_2O treatment (red), and reaction with H_2TCPP in the optimized cosolvent (DMF:Water=1:3) (green). The IR spectra of $\text{Si}/\text{SiO}_2@/\text{Al}_2\text{O}_3$ (black) was obtained by subtracting the spectrum of Si/SiO_2 as a background from the spectrum collected after ALD Al_2O_3 to $\text{Si}@/\text{SiO}_2$. H_2O treatment was conducted by submerging $\text{Si}/\text{SiO}_2@/\text{Al}_2\text{O}_3$ in liquid water at 90°C for 1 h. The reactions with H_2TCPP in pure DMF or in the optimized cosolvent was carried out at 120°C for 20 h.

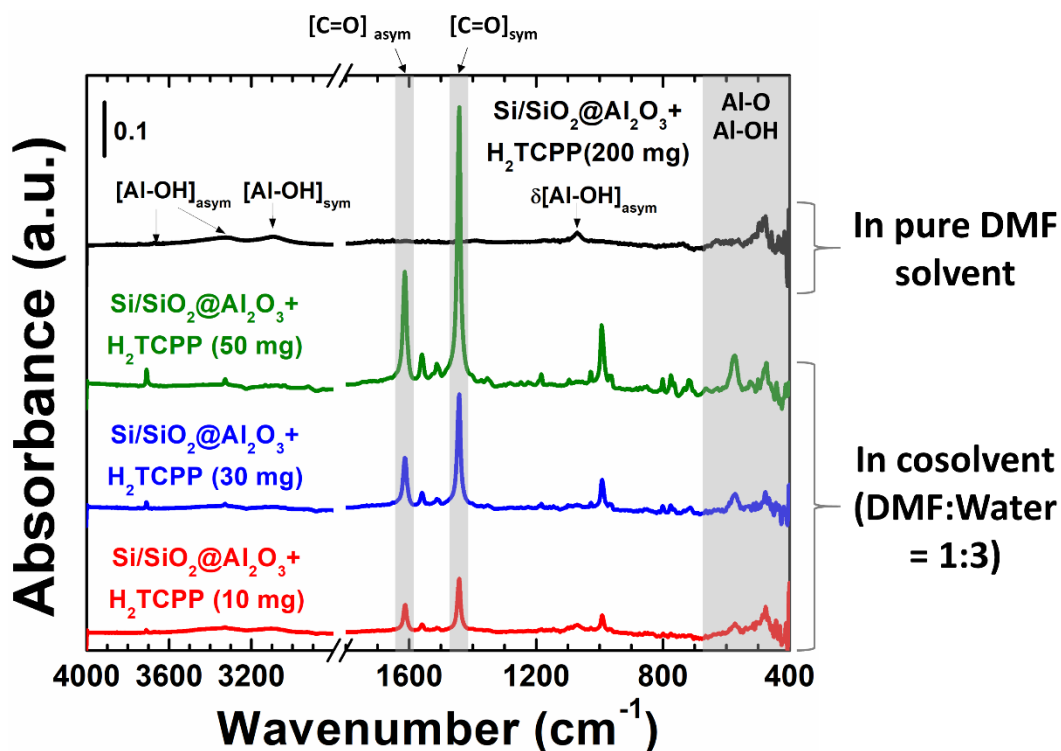


Figure S5.8. FTIR spectra captured in differential mode. The spectra of each Si/SiO₂@Al₂O₃ was subtracted as a background for the entire sample after reacting with H₂TCPP solutions. The reactions for Si/SiO₂@Al₂O₃+H₂TCPP (10, 30, or 50 mg (from bottom)) and for Si/SiO₂@Al₂O₃+H₂O treatment+H₂TCPP (200 mg, topmost) were implemented with (DMF:Water=1:3) mixture and pure DMF at 120 °C for 20 h, respectively. H₂O treatment was conducted by submerging Si/SiO₂@Al₂O₃ in liquid water at 90 °C for 1 h.

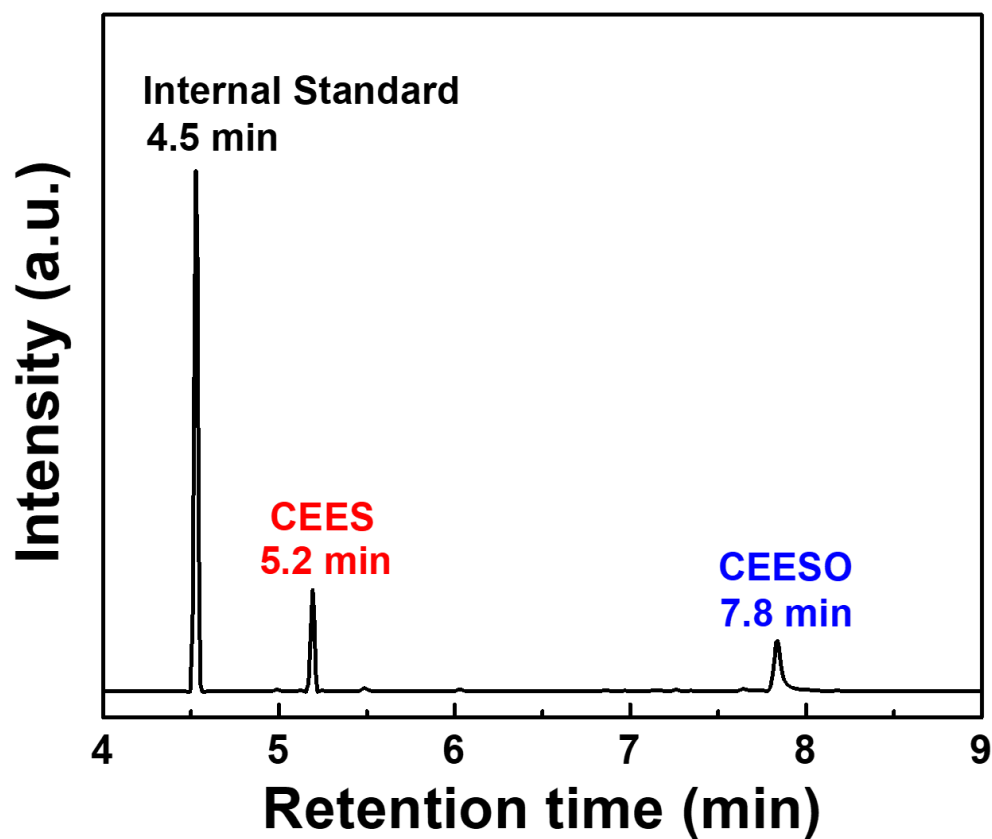
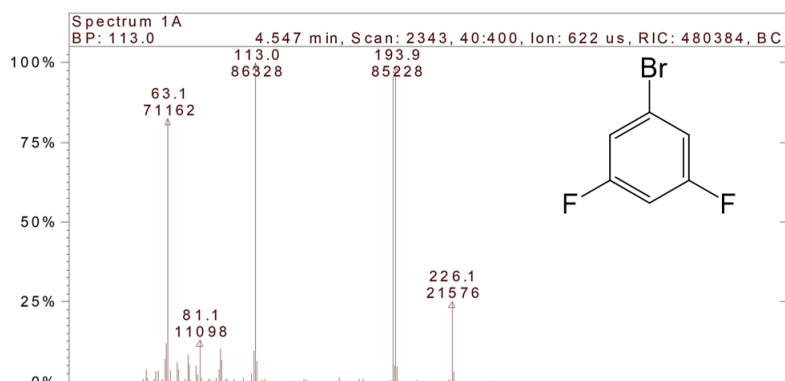


Figure S5.9. GC-MS spectra monitored at 10 min of CEES oxidation using Al-PMOF powder catalyst. Selective oxidation of CEES ($t = 5.2$ min) into 2-chloroethyl ethyl sulfoxide (CEESO, $t = 7.8$ min) was observed. 1-bromo-3,5-difluorobenzene was used as an internal standard (IS, $t = 4.5$ min).

(a) Internal Standard (4.5 min)



(b) 2-chloroethyl ethyl sulfide (CEES, 5.2 min)



(c) 2-chloroethyl ethyl sulfoxide (CEESO, 7.8 min)

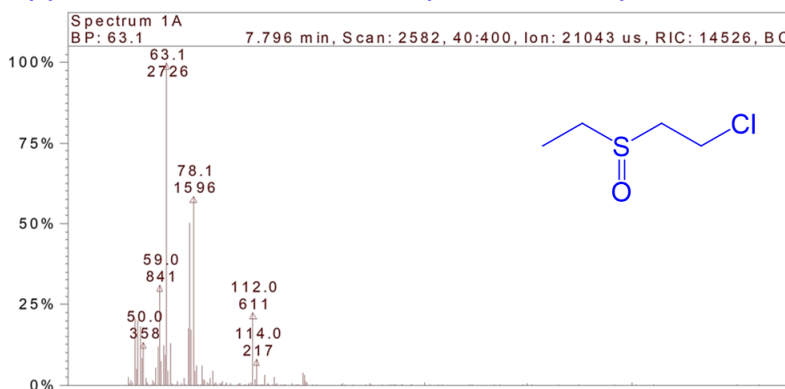


Figure S5.10. Mass spectrometry of (a) 1-bromo-3,5-difluorobenzene as an internal standard (IS), (b) CEES as a blistering agent simulant, and (c) CEESO as the only product obtained from the photooxidation of CEES with Al-PMOF powder catalyst.

Calculation of the catalyst loading (mol%) used for the CEES photooxidation experiments

(The catalyst loading (mol%) is calculated based on moles of porphyrins)

Powder samples

- **Al-PMOF (1.2 mg_{MOF})**

Chemical formula: Al₂(OH)₂(H₂TCPP) (878.77 g/mol)

Porphyrin (=chromophore) mass fraction in Al-PMOF = 0.9

$$\text{"mol of chromophore"} = \frac{1.2 \text{ mg} \times (0.9)}{790.77 \frac{\text{g}}{\text{mol}}} \times \frac{\text{g}}{10^3 \text{ mg}} = 1.37 \times 10^{-3} \text{ mmol} \quad (1)$$

$$\text{"catalyst loading(\%)"} = \frac{1.37 \times 10^{-3} \text{ mmol}}{(1.37 \times 10^{-3} + 0.2) \text{ mmol}} \times 100 (\%) \approx \mathbf{0.7 \text{ mol}\%} \quad (2)$$

Here, 0.2 mmol is the amount of CEES (23 μL) added to the reaction system.

- **H₂TCPP (1.2 mg_{chromophore})**

Chemical formula: H₂TCPP (790.77 g/mol)

Porphyrin (=chromophore) mass fraction in Al-PMOF = 1.0

$$\text{"mol of chromophore"} = \frac{1.2 \text{ mg} \times (1.0)}{790.77 \frac{\text{g}}{\text{mol}}} \times \frac{\text{g}}{10^3 \text{ mg}} = 1.52 \times 10^{-3} \text{ mmol} \quad (3)$$

$$\text{"catalyst loading (\%)"} = \frac{1.52 \times 10^{-3} \text{ mmol}}{(1.52 \times 10^{-3} + 0.2) \text{ mmol}} \times 100 (\%) \approx \mathbf{0.8 \text{ mol}\%} \quad (4)$$

Here, 0.2 mmol is the amount of CEES (23 μL) added to the reaction system.

MOF/fiber composite samples

- **PP@Al-PMOF (8.5 mg_(MOF+fiber))**

$$\text{"MOF mass fraction (\%)"} = \frac{\text{BET SA of PP@MOF}}{\text{BET SA of MOF powder}} = \frac{52 \frac{\text{m}^2}{\text{g}_{(\text{MOF}+\text{fiber})}}}{1929 \frac{\text{m}^2}{\text{g}_{(\text{MOF})}}} \times 100 (\%)$$

$$\approx 3 \text{ wt}\% \text{ of MOF in PP@MOF} \quad (5)$$

$$\text{"mol of chromophore"} = \frac{8.5 \text{ mg} \times (0.03) \times (0.9)}{790.77 \frac{\text{g}}{\text{mol}}} \times \frac{\text{g}}{10^3 \text{ mg}} = 0.3 \times 10^{-3} \text{ mmol} \quad (6)$$

$$\text{"catalyst loading (\%)} = \frac{0.3 \times 10^{-3} \text{ mmol}}{(0.3 \times 10^{-3} + 0.2) \text{ mmol}} \times 100 (\%) \approx \mathbf{0.2 \text{ mol\%}} \quad (7)$$

Here, 0.2 mmol is the amount of CEES (23 μL) added to the reaction system.

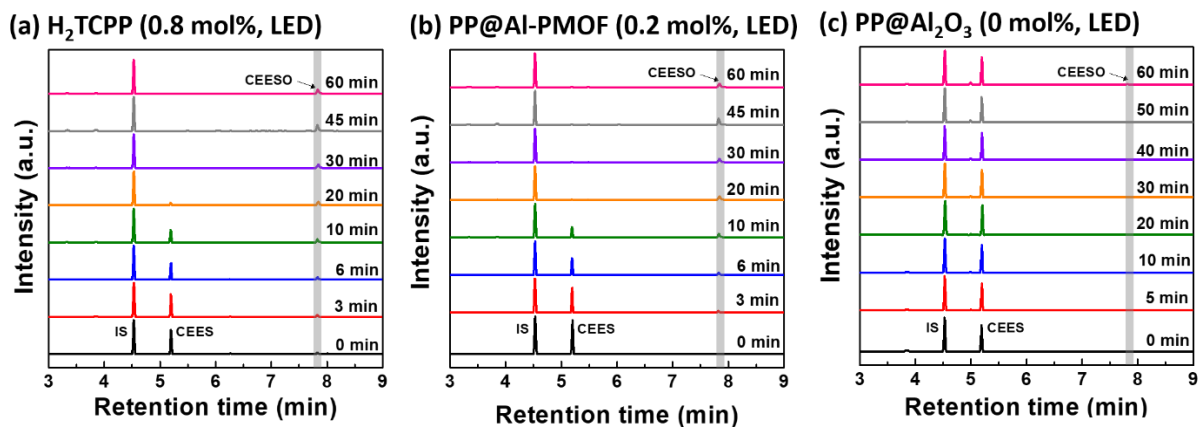


Figure S5.11. GC-MS spectra monitored during CEES photooxidation with (a) H₂TCPP (0.8 mol%), (b) with PP@Al-PMOF (0.2 mol%), or (c) with PP@Al₂O₃ (0 mol%). The catalyst loading (mol%) is calculated based on moles of porphyrins in Al-PMOF. No CEESO was observed in the catalytic reaction with PP@Al₂O₃ due to the absence of porphyrin-contained components functioning as catalysts.

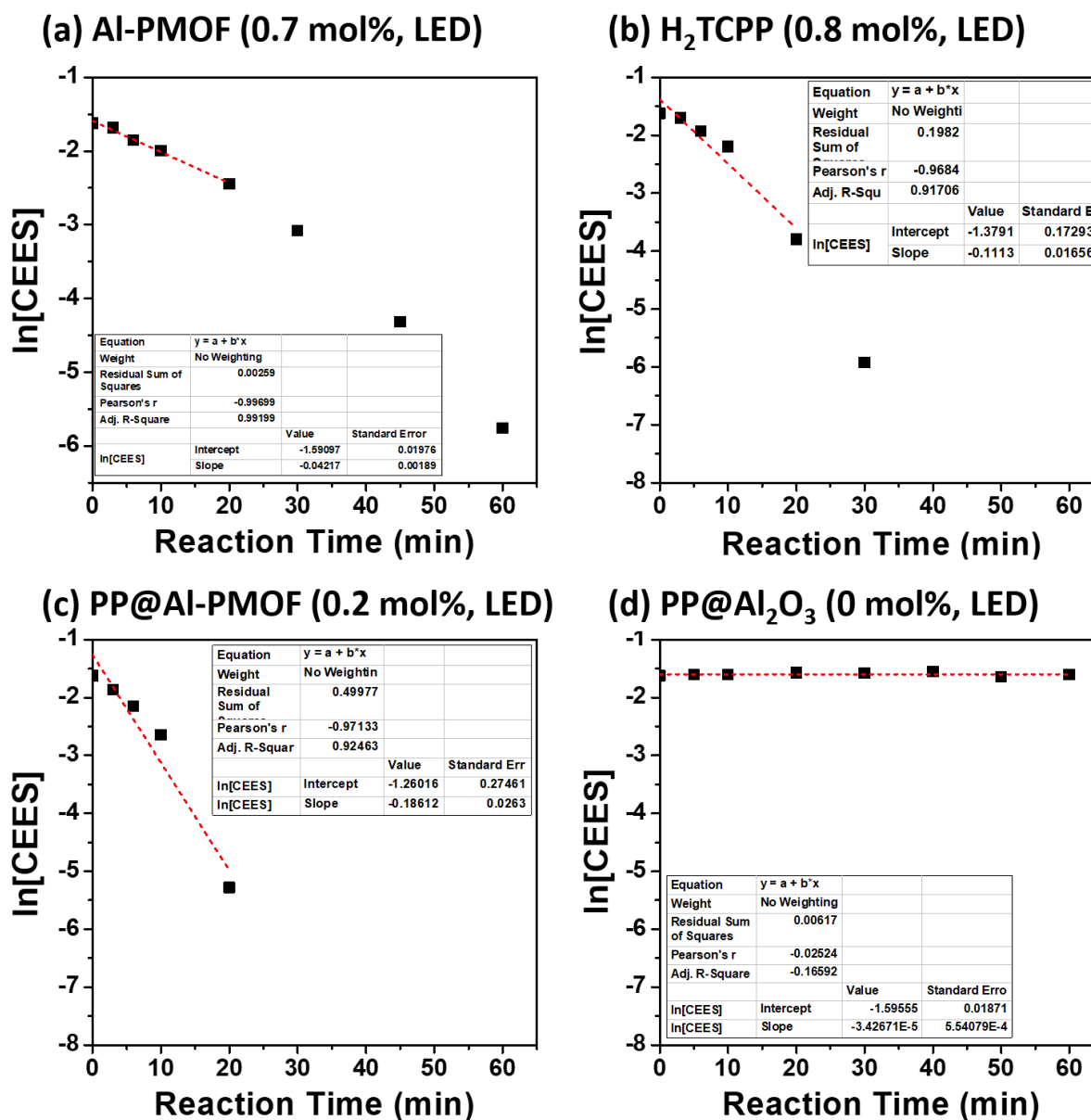


Figure S5.12. Kinetic analysis of oxidative detoxification profiles of CEES using (a) Al-PMOF powder (0.7 mol%), (b) H₂TCPP powder (0.8 mol%), (c) PP@Al-PMOF (0.2 mol%), or (d) PP@Al₂O₃ (0 mol%). The profiles were fit to a first-order kinetic model. The catalyst loading (mol%) is calculated based on moles of porphyrins in Al-PMOF.

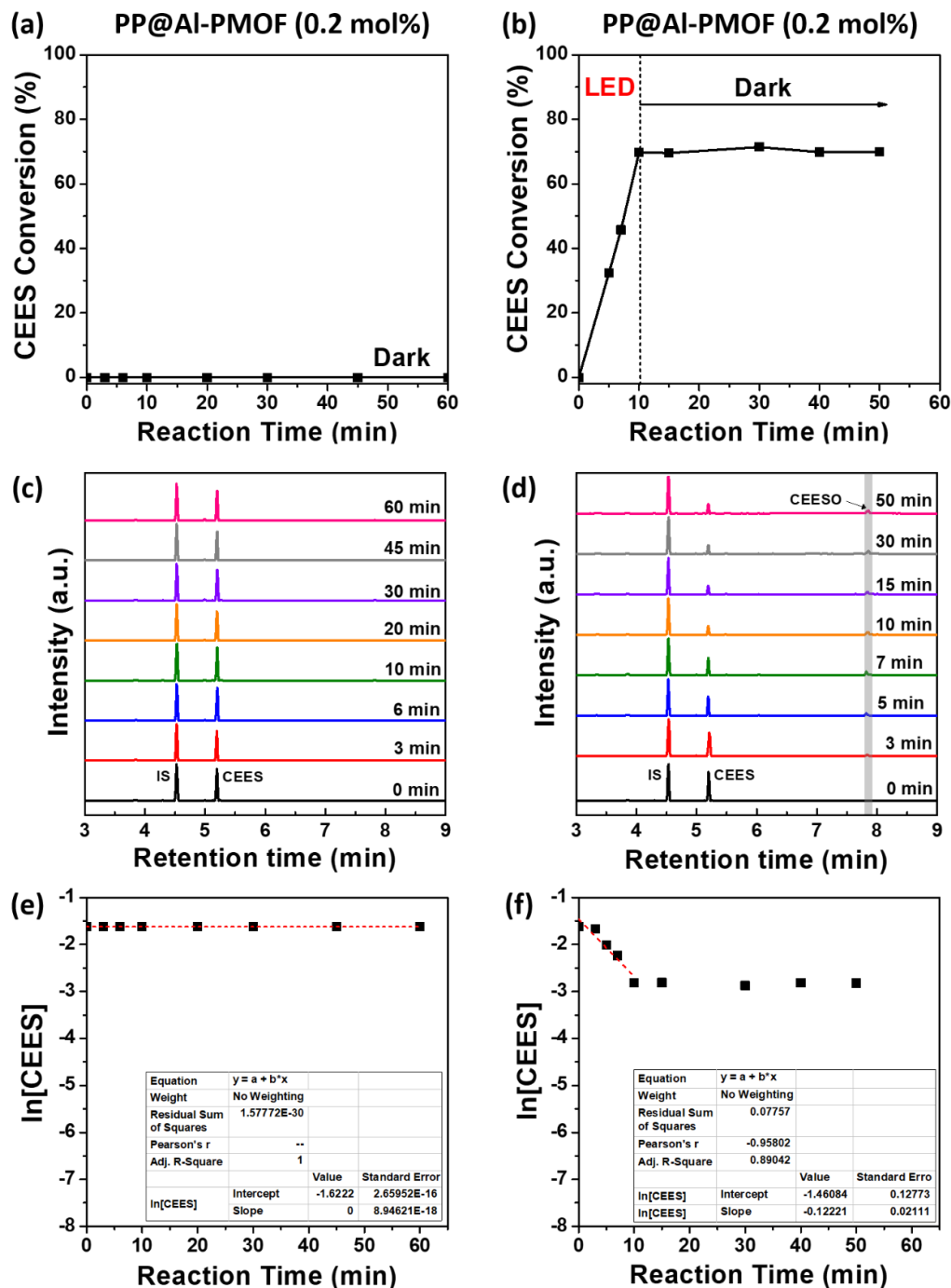


Figure S5.13. Effect of LED light irradiation on the rate of CEES oxidation using textile catalysts.

(a) CEES degradation profile, (c) GC-MS spectra, and (e) kinetic analysis obtained in the dark. (b) CEES degradation profile, (d) GC-MS spectra, and (f) kinetic analysis monitored with light irradiation (0 - 10 min) and subsequently in the dark (10 - 50 min).

Calculation of turnover frequency (TOF) for CEES oxidation

$$TOF = \frac{mol_{CEES}}{mol_{chromophore} \cdot min_{half\ life}} \quad (8)$$

- **Al-PMOF (1.2 mg_{MOF}, 1.37×10⁻³ mmol from “equation 1”)**

$$TOF = \frac{0.2\ mmol}{1.37 \times 10^{-3}\ mmol \times 16.5\ min} \approx 9\ min^{-1} \quad (9)$$

Here, $t_{1/2} = \frac{\ln 2}{-slope} = \frac{\ln 2}{-0.042} = 16.5\ min$; the slope value is obtained from kinetic analysis (Figure

S5.12a)

- **H₂TCPP (1.2 mg_{chromophore}, 1.52×10⁻³ mmol from “equation 3”)**

$$TOF = \frac{0.2\ mmol}{1.52 \times 10^{-3}\ mmol \times 6.2\ min} \approx 22\ min^{-1} \quad (10)$$

Here, $t_{1/2} = \frac{\ln 2}{-slope} = \frac{\ln 2}{-0.111} = 6.2\ min$; the slope value is obtained from kinetic analysis (Figure

S5.12b)

- **PP@Al-PMOF (8.5 mg_(MOF+fiber), 0.3×10⁻³ mmol from “equation 6”)**

$$TOF = \frac{0.2\ mmol}{0.3 \times 10^{-3}\ mmol \times 4\ min} \approx 170\ min^{-1} \quad (11)$$

Here, $t_{1/2} = \frac{\ln 2}{-slope} = \frac{\ln 2}{-0.186} = 4\ min$; the slope value is obtained from kinetic analysis

(Figure S5.12c)

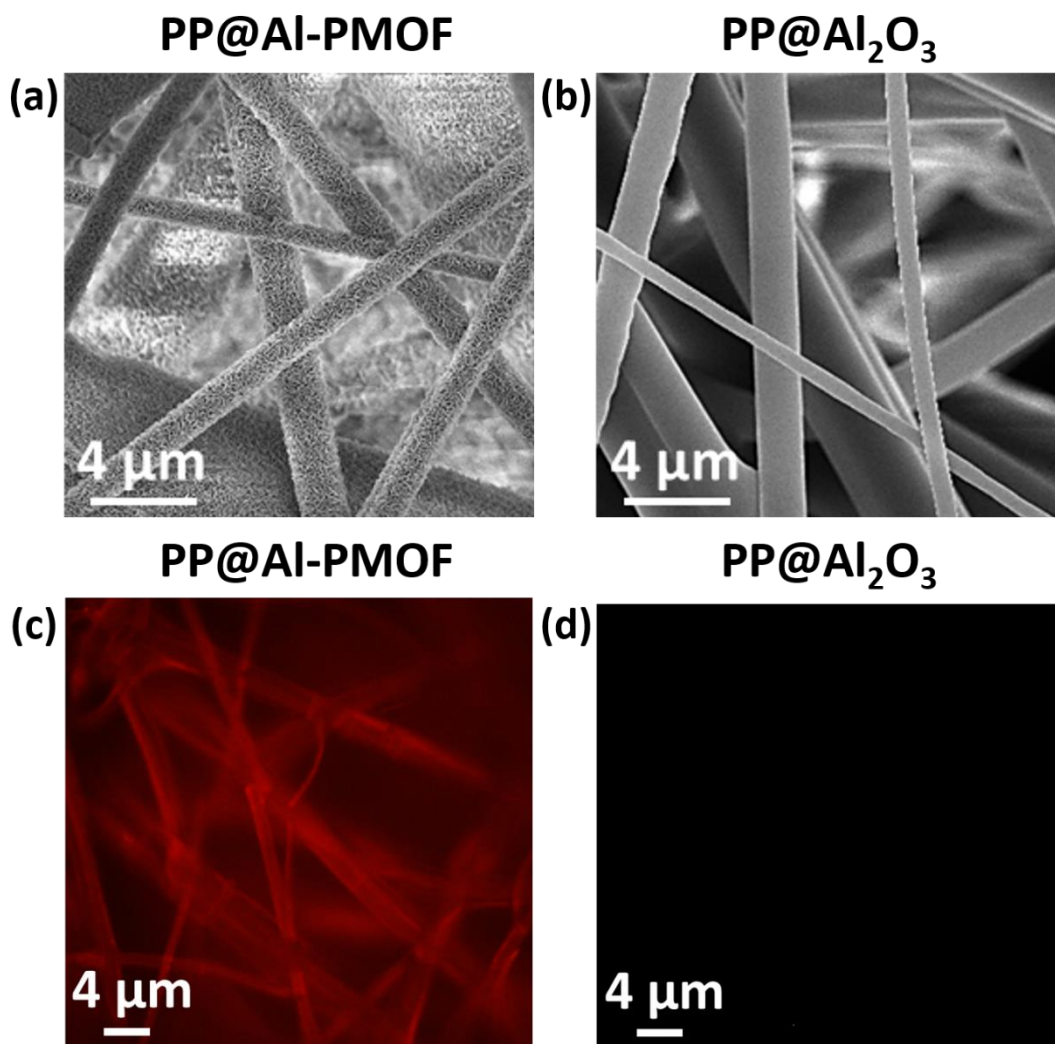


Figure S5.14. SEM images of (a) PP@Al-PMOF and (b) PP@Al₂O₃. Fluorescence imaging of (c) PP@Al-PMOF and (d) PP@Al₂O₃. The fluorescence imaging results indicate that Al-PMOF integrated into PP fiber surface is uniform and functions well in visible light.

References

- [1] G. K. Hyde, K. J. Park, S. M. Stewart, J. P. Hinstroza, G. N. Parsons, *Langmuir* **2007**, *23*, 9844.
- [2] A. Fateeva, P. A. Chater, C. P. Ireland, A. A. Tahir, Y. Z. Khimyak, P. V Wiper, J. R. Darwent, M. J. Rosseinsky, *Angew. Chemie Int. Ed.* **2012**, *51*, 7440.
- [3] A. G. Wong-Foy, A. J. Matzger, O. M. Yaghi, *J. Am. Chem. Soc.* **2006**, *128*, 3494.
- [4] K. S. Walton, R. Q. Snurr, *J. Am. Chem. Soc.* **2007**, *129*, 8552.

CHAPTER 6

Water-Stable Chemical-Protective Textiles via Euhedral Surface-Oriented 2D Cu-TCPP

Metal-Organic Frameworks

CHAPTER 6 is a reprint of a manuscript published in *Small*

Dennis T. Lee,[†] Jovenal D. Jamir,[†] Gregory W. Peterson,[‡] and Gregory N. Parsons^{†,*}

[†]Department of Chemical & Biomolecular Engineering, North Carolina State University, 911

Partners Way, Raleigh, NC 27695, United States

[‡]Edgewood Chemical Biological Center, 5183 Blackhawk Road, Aberdeen Proving Ground, MD

21010, United States

6.1. Abstract

Abatement of chemical hazards using adsorptive metal-organic frameworks (MOFs) attracts substantial attention, but material stability and crystal integration into functional systems remain key challenges. Herein, water stable, polymer fiber-surface-oriented M-TCPP [M = Cu, Zn, and Co, H₂TCPP = 5,10,15,20-tetrakis(4-carboxyphenyl)porphyrin] 2D MOF crystals are fabricated using a facile hydroxy double salt (HDS) solid-source conversion strategy. For the first time, Cu-TCPP is formed from a solid source and confirmed to be highly adsorptive for NH₃ and 2-chloroethyl ethyl sulfide (CEES), a blistering agent simulant, in humid (80% RH) conditions. Moreover, the solid HDS source is found as a unique new approach to control MOF thin film crystal orientation, thereby facilitating radially-arranged MOF crystals on fibers. On a per unit mass of MOF basis in humid conditions, the MOF/fiber composite enhances NH₃ adsorptive capacity by a factor of 3 compared to conventionally-prepared MOF powders. The synthesis route extends to other MOF/fiber composite systems, therefore providing a new route for chemically protective materials.

6.2. Introduction

Toxic industrial chemicals (TICs) and chemical warfare agents (CWAs) pose an increasing threat to personal safety and security.^[1] Metal organic frameworks (MOFs)^[2,3] are comprised of inorganic metal centers interconnected by organic linkers. Their high surface area, large pore volume, ordered crystalline structure, and tunable functionality make them attractive for adsorption^[4,5] and catalytic decontamination of harmful agents.^[6,7]

Open coordination sites (OCSs) in MOFs play a significant role in removing diverse polar toxic compounds, such as H₂S, NH₃, NO_x, and SO₂, from liquid and vapor phases.^[8] However, competitive adsorption of water and decaying structural robustness of MOFs under humid conditions impede their practical use.^[1] Therefore, considerable research is now addressing stable MOFs capable of selectively adsorbing hazardous organic compounds in humid conditions.^[9] Especially Zr-based MOFs (e.g., UiO-type,^[10] MOF-808,^[11] PCN-222/MOF-545,^[12] NU-1000,^[13] and UMCM-313^[14]) and hybrid materials (e.g., PW₁₂@NU-1000^[15] and BODIPY@NU-1000^[16]) have exhibited promising performance of catalytic detoxification for CWAs and their simulants. Various composite materials including MOF-polymer MMMs,^[17] MOF/fiber,^[18,19] BODIPY/fiber,^[20] and MOFwich^[21] have been recently explored as protective systems for practical deployment, collection, and recycle. However, aggregation of active materials within encasing components still limits their performance and use in the long run.^[20]

In this regard, we focus on water stable 2D Cu-TCPP MOF composed of both OCSs and hydrophobic porphyrin linkers to capture both polar and water immiscible toxins in humid conditions. While Cu-TCPP has been previously studied,^[22,23] this report is the first to describe its synthesis with controlled crystal arrangement, and the first to document its strong adsorptive capacity for NH₃ and 2-chloroethyl ethyl sulfide (CEES) under humid (80% RH) conditions. Low

temperature synthesis at 40°C using a hydroxy double salt (HDS) intermediate,^[24] formed from atomic layer deposition (ALD) ZnO on polypropylene (PP) fibers, yielded dense and strongly adhered MOFs on fibers with no aggregation. The resulting MOF/fiber composite had 3x higher NH₃ adsorptive performance and showed almost retained CEES adsorptive capacity in humid conditions compared to the bulk powder MOFs. The “needle-like” HDS film facilitates radially-directed euhedral MOF film with no aggregation, otherwise anhedral MOF stacks with poor adhesion to substrates. This work is the first to report synthesis of a porphyrin-based MOF from a solid-oxide source; and it directly demonstrates novel and a unique approach to MOF crystal orientation control which is a common challenge in MOF thin film growth.

6.3. Experimental Section

Materials. All reagents were purchased from commercial sources and used without further treatment. Diethylzinc (DEZ, 95% STREM Chemicals, Inc.), copper nitrate trihydrate (Cu(NO₃)₂·3H₂O, 99-104%, Sigma-Aldrich), 1,2,3-benzenetricarboxylic acid (H₃BTC, 95%, Aldrich), meso-Tetra(4-carboxyphenyl)porphine (H₂TCPP, >97% Frontier Scientific), zinc acetate dihydrate (Zn(CH₃CO₂)₂·2H₂O, ≥99%, Sigma-Aldrich), cobalt nitrate hexahydrate (Co(NO₃)₂·6H₂O, ≥99%, Sigma-Aldrich), N,N-dimethylformamide (DMF, Fisher), deionized water (DI water), anhydrous ethanol (200 proof, VWR).

Polymeric fibrous scaffolds. Non-woven polypropylene (PP) micro-fibrous mats with two different densities (1) 40 gsm and 2) 75 gsm)) were used as received from Nonwovens Cooperative Research Center (NCRC), North Carolina State University.^[1] The polymeric fibrous mats are 0.30 mm thick and 1.0-9.0 μm diameter for 40 gsm fiber mats, and 0.60 mm thick and 20-25 μm diameter for 75 gsm fiber mats, respectively.

Atomic layer deposition (ALD) for ZnO thin film on PP microfibers. Free-standing non-woven polypropylene (PP) fibrous mats (1" × 2" or 2" × 2") were placed in a home built hot-wall viscous-flow atomic layer deposition reactor. The detailed reactor design for the process was depicted in the previous work.^[2] ALD ZnO deposition was implemented at 90°C under ~1.8 Torr. In the ALD ZnO cycle, the sequence time (in second) of diethyl zinc (DEZ) exposure/N₂ purge/H₂O exposure/N₂ purge was 2/60/2/60. 200 cycles of ALD ZnO was carried out to prepare ZnO coated PP fibrous mats (PP@ZnO). Silicon wafers with thin native oxide (~2 nm) (Si@SiO₂) were also placed along with PP fibrous mats inside the reactor under the same ALD ZnO condition. Si wafer monitors were also used to measure thickness of the ALD coatings together with PP fibrous mats. Around 20 nm of inorganic film on the Si@SiO₂ was confirmed from a J.A. Woollam alpha-spectroscopic ellipsometry (SE) ellipsometer at an incidence angle of 70°.

Synthesis of 2D Cu-TCPP MOFs (powder). 2D Cu-TCPP MOFs were solvothermally synthesized by using a method previously reported with some modifications.^[3] 0.038 g (0.157 mmol) of Cu(NO₃)·3H₂O was first added to 20 mL glass scintillation vial and dissolved in 20 mL of DMF under magnetic stirring (~500 rpm) for 5 min. 0.125 g (0.157 mmol) of H₂TCPP was subsequently added to the prepared solution under stirring (~500 rpm), followed by 5 min of sonication at ambient temperature for a well dispersion. This as-prepared mixture was heated at 80°C for 24 h in a box furnace (Thermo Scientific). The Cu-TCPP MOF product was then selectively obtained by filtering out by-products, unreacted precursor components, and residual DMF through polypropylene membrane (0.45 μm pore size, Whatman). After that, the filtered solid was vigorously rinsed with 80 mL of DMF in a 100 mL beaker under magnetic stirring (~500 rpm) for 24 h. After collecting only solid product by filtering out the solution, 80 mL of anhydrous ethanol was used to perform a solvent exchange by using the same way as DMF rinsing method.

Eventually, the final solid in light purple color was obtained via filtration system and dried at room temperature at reduced pressure for 12 h. The well dried Cu-TCPP MOF powder was stored in a desiccator until being used for further characterizations.

Synthesis of hydroxy double salt coating onto PP micro fibrous mats.

Hydroxy double salt (Zn,Cu) (PP@HDS(Zn,Cu))

0.87 g (3.601 mmol) of $\text{Cu}(\text{NO}_3)_2 \cdot 3\text{H}_2\text{O}$ was dispersed in 18 mL mixture of DI water (9 mL) and anhydrous ethanol (9 mL) in 20 mL scintillation vial. Subsequently, PP micro fibrous mats (1" × 2") coated with 200 cycles of ALD ZnO (PP@ZnO) are soaked in the prepared solution at ambient temperature for 2 min. After the reaction done, the HDS(Zn,Cu) coated fibers were rinsed 3 times with 20 mL of anhydrous ethanol and soaked in the solvent for 1 day. The products were eventually dried at room temperature at a reduced pressure for 12 h. The well dried HDS(Zn,Cu) coated fibers were stored in a desiccator until being used for further characterizations or for subsequent experimental steps.

Hydroxy double salt (Zn,Zn) (PP@HDS(Zn,Zn))

1.98 g (9.02 mmol) of $\text{Zn}(\text{CH}_3\text{CO}_2)_2 \cdot 2\text{H}_2\text{O}$ was dispersed in 18 mL mixture of DI water (9 mL) and anhydrous ethanol (9 mL) in 20 mL scintillation vial. Subsequently, PP micro fibrous mats (1" × 2") coated with 200 cycles of ALD ZnO (PP@ZnO) are soaked in the prepared solution at ambient temperature for 10 min. After the reaction done, the HDS(Zn,Zn) coated fibers were rinsed 3 times with 20 mL of anhydrous ethanol and soaked in the solvent for 1 day. The products were eventually dried at room temperature at a reduced pressure for 12 h. The well dried HDS(Zn,Zn) coated fibers were stored in a desiccator until being used for further characterizations or for subsequent experimental steps.

Hydroxy double salt (Zn,Co) (PP@HDS(Zn,Co))

1.572 g (5.401 mmol) of $\text{Co}(\text{NO}_3)_2 \cdot 6\text{H}_2\text{O}$ was dispersed in 18 mL mixture of DI water (9 mL) and anhydrous ethanol (9 mL) in 20 mL scintillation vial. Subsequently, PP micro fibrous mats (1" \times 2") coated with 200 cycles of ALD ZnO (PP@ZnO) were soaked in the prepared solution. This as-prepared mixture was heated at 80 °C for 12 h in a box furnace (Thermo Scientific). After the reaction done, the HDS(Zn,Co) coated fibers were rinsed 3 times with 20 mL of anhydrous ethanol and soaked in the solvent for 1 day. The products were eventually dried at room temperature at a reduced pressure for 12 h. The well dried HDS(Zn,Co) coated fibers were stored in a desiccator until being used for further characterizations or for subsequent experimental steps.

Direct synthesis of metal-TCPP MOF onto ALD ZnO coated PP micro fibrous mats. For the preparation of PP@Cu-TCPP sample using ALD ZnO coated PP (PP@ZnO), 0.03 g (0.124 mmol) of $\text{Cu}(\text{NO}_3)_2 \cdot 3\text{H}_2\text{O}$ was first added to 16 mL glass scintillation vial and dissolved in 20 mL of DMF under magnetic stirring (~500 rpm) for 5 min. 0.05 g (0.063 mmol) of H_2TCPP was subsequently added to the prepared solution under stirring (~500 rpm), followed by 5 min of sonication at ambient temperature for a well dispersion of the solution. Subsequently, PP micro fibrous mats (1" \times 2") coated with ALD ZnO (i.e., PP@ZnO) were fully soaked in the prepared solution. This as-prepared mixture with fabric was heated at $>40^\circ\text{C}$ (between 40 and 60°C) for 12 h in a box furnace (Thermo Scientific). After the solvothermal synthesis is complete, the MOF coated PP fibrous mats (i.e., PP@Cu-TCPP) were rinsed 3 times with 20 mL of DMF, followed by another 3 times-anhydrous ethanol washing and soaked in anhydrous ethanol for 1 day. The MOF/Fabric samples were finally dried at room temperature at a reduced pressure for 12 h. The

well dried 2D Cu-TCPP MOF coated fibers were stored in a desiccator until being used for further characterizations or for subsequent experimental steps.

A preparation for direct synthesis of Zn-TCPP MOF onto ALD ZnO coated PP micro fibrous mats (PP@Zn-TCPP) was conducted using the same method described above for PP@Cu-TCPP using PP@ZnO fabric. Here, however, $\text{Cu}(\text{NO}_3)_2 \cdot 3\text{H}_2\text{O}$ was not contained in the precursor solution, but only 0.05 g (0.063 mmol) of H_2TCPP was added.

Synthesis of 2D metal-TCPP MOF onto PP micro fibrous mats using Hydroxy double salt coated PP micro fibrous mats. Precursor solutions for 2D metal-TCPP growth on PP micro fibrous mats (i.e., PP@HDS+TCPP, here HDS can be 1) HDS(Zn,Cu) for Cu-TCPP, 2) HDS(Zn,Zn) for Zn-TCPP, or 3) HDS(Zn,Co)) were prepared by adding 0.05g (0.063 mmol) of meso-Tetra(4-carboxyphenyl)porphine (H_2TCPP) to 16 mL of DMF in 20 mL scintillation vial. After that, 5 min of sonication at ambient temperature was performed to the solution for a well dispersion of H_2TCPP in DMF. Sequentially, PP micro fibrous mats (1" × 2") coated with HDS (i.e., 1) PP@HDS(Zn,Cu) for PP@Cu-TCPP, 2) PP@HDS(Zn,Zn) for PP@Zn-TCPP, or 3) PP@HDS(Zn,Co)) were fully soaked in the prepared solution. This as-prepared mixture with fabric was heated at $>40^\circ\text{C}$ (between 40 and 60°C) for 12 h in a box furnace (Thermo Scientific). After the solvothermal synthesis is complete, the MOF coated PP fibrous mats (i.e., 1) PP@Cu-TCPP, 2) PP@Zn-TCPP, or 3) PP@Co-TCPP) were rinsed 3 times with 20 mL of DMF, followed by another 3 times-anhydrous ethanol washing and soaked in anhydrous ethanol for 1 day. The MOF/Fabric samples were finally dried at room temperature at a reduced pressure for 12 h. The well dried 2D metal-TCPP MOF coated fibers were stored in a desiccator until being used for further characterizations or for subsequent experimental steps.

Synthesis of PP@Cu-BTC composite materials using a rapid room temperature approach. This synthesis method is based on our previous method^[4] with some modifications. 0.435 g (1.8 mmol) of $\text{Cu}(\text{NO}_3)_2 \cdot 3\text{H}_2\text{O}$ was dissolved in 9 mL of DI water in 20 mL scintillation vial. In a separate vial, 0.210 g (1.0 mmol) of 1,2,3-benzenetricarboxylic acid (H_3BTC) was dissolved in 9 mL of anhydrous ethanol. After the H_3BTC was completely dissolved, the H_3BTC solution was gently added to the as-prepared $\text{Cu}(\text{NO}_3)_2 \cdot 3\text{H}_2\text{O}$ solution under stirring for 2 min at ambient temperature. Subsequently, PP micro fibrous mats (1" × 2") coated with 200 cycles of ALD ZnO (PP@ZnO) are dipped in the prepared solution at ambient temperature for 2 min. After the reaction done, the Cu-BTC coated fibers (PP@Cu-BTC) were rinsed 3 times with 20 mL of anhydrous ethanol and soaked in the solvent for 1 day. The products were eventually dried at room temperature at a reduced pressure for 12 h. The well dried Cu-BTC coated fibers (PP@Cu-BTC) were stored in a desiccator until being used for further characterizations or for subsequent experimental steps.

Breakthrough test for NH_3 and 2-chloroethyl ethyl sulfide (CEES). Untreated PP fibrous mats, Cu-TCPP MOF powder, MOF-coated fiber samples were evaluated for ammonia and 2-chloroethyl ethylsulfide (CEES) capacity using a microbreakthrough apparatus that has been described previously.^[5] Briefly, a small powder or composite was inserted into a 4 mm diameter fritted glass tube. Composite samples were compressed slightly to achieve an approximate bed height of 4 mm. Ammonia testing was conducted using a stainless-steel ballast charged with ammonia and pressurized to 20 psig. The stream was mixed with a dry (0% RH) or humidified (80% RH) air stream at a rate necessary to achieve a feed concentration of 2,000 mg/m^3 . The effluent was monitored continuously using a HP6890 gas chromatograph (GC) equipped with a photoionization detector with a 10.6 eV lamp. CEES was fed to the fritted glass tube using a

saturator cell with an air sweep gas and mixed with diluent streams at a flow rate necessary to achieve 4,000 mg/m³. The effluent was monitored continuously using a HP5890 GC equipped with a flame ionization detector.

Characterization. Scanning electron microscopic (SEM) and energy dispersive X-ray analysis (EDX) were conducted using a FEI Verios 460 L field emission SEM. A thin layer of Au-Pd (5~10 nm) was sputter-coated onto the prepared samples before SEM imaging. X-ray diffraction (XRD) was implemented with a Rigaku SmartLab X-ray diffraction tool (Cu K α X-ray source) for crystalline phase analysis. A Quantachrome Autosorb-1C surface area and pore size analyzer and Micromeritics 3Flex Surface Characterization Analyzer were used for measuring N₂ adsorption-desorption isotherms at 77 K. Water vapor adsorption-desorption isotherms were measured using Micromeritics 3Flex Surface Characterization Analyzer at 298 K. The fabric-based samples were dried in vacuum ($\sim 1 \times 10^{-5}$ Torr) in BET instrument at room temperature for 1 h and at 110°C for 24 h in a consecutive manner before both N₂ adsorption-desorption and water vapor adsorption-desorption measurement. BET surface area was calculated based on the N₂ adsorption data within a relative pressure range of $P/P_0 = 0.02 \sim 0.08$.^[6,7] A Thermo Scientific Nicolet 6700 Fourier transform infrared spectrometer was used for analyzing MOF growth on IR silicon wafers coated with ALD metal oxides (i.e., Al₂O₃, TiO₂, or ZnO). Attenuated total reflectance Fourier transform infrared (ATR-FTIR) spectra were obtained with a Bruker Tensor 27 FTIR using a Platinum ATR accessory and equipped with a single reflection diamond crystal. Measurements were made with an average of 16 scans over a range of 400 to 4,000 cm⁻¹ and a resolution of 2 cm⁻¹. Powder X-ray diffraction (PXRD) measurements were made using a Rigaku Miniflex 600 X-ray powder diffractometer equipped with a D/Tex detector. Samples were scanned over a 2 θ range of 2 to 50° at a rate of 5° min⁻¹.

6.4. Results and Discussion

Figure 6.1 illustrates synthetic routes to integrate Cu-TCPP or Zn-TCPP MOFs onto fiber mats. After coating fibers with ~ 20 nm of conformal ALD ZnO (Figure 6.1a), exposure to H₂TCPP converts the ZnO to Zn-TCPP, **1** (Figure 6.1b). Alternately, synthesis with Cu(NO₃)₂ and H₂TCPP yields Cu-TCPP on the ZnO, **2** (Figure 6.1c).

As a third approach, the smooth ALD ZnO is exposed to Cu(NO₃)₂ for 2 min at 25°C, converting it to HDS(Zn,Cu) with roughened texture, **3** (PP@HDS(Zn,Cu)) (Figure 6.1d).^[24] The HDS then undergoes anion exchange with H₂TCPP (40°C, 12h) forming Cu-TCPP on the fiber, **4** (PP@Cu-TCPP, Figure 6.1e and S6.1-S6.2). Crystalline nature of ALD ZnO, HDS(Zn,Cu), or Cu-TCPP film on PP is well consistent with that of corresponding powder samples (Figure S6.3).

Interestingly, the HDS(Zn,Cu) on the fiber yields radially oriented 2D platelet Cu-TCPP crystals, distinctly different from the crystals formed as described in Figure 6.2 and those reported in literature.^[25] Anhedral 2D MOFs, synthesized via the conventional method, horizontally conform to the polymer and are not well adhered (Figure S6.4), thus leading to poor distribution of MOF crystals on the fiber mats. (inset in Figure 6.2b)^[19] On the other hand, the 2D MOF, formed with HDS(Zn,Cu), is strongly bound to PP surface by means of ALD ZnO interface layer between MOF and fiber surface via physical and chemical bonds. While quantitative bonding force was not readily measurable, we observed that the MOF does not flake off of the PP substrates during common lab handling or when a nylon brush is swept across the MOF/fiber textile surface.^{[19][24][26]}

Figure 6.3a shows the integrity of Cu-TCPP on fiber as determined by X-ray diffraction (XRD). The experimental XRD pattern of **4** includes peaks from the Cu-TCPP (Figure S6.4),^[22,25,27] with no evidence for HDS(Zn,Cu)^[24,28] at 12.8° 2θ, observed for **3**. Furthermore, scanning electron microscope (SEM) images and X-ray photoelectron spectroscopy (XPS) also

confirm Cu-TCPP morphology, and plausible binding strengths between metal clusters and linkers, respectively (Figure S6.5).

Fourier transform infrared (FTIR) spectrum of **4**, made with a subsequent exposure of **3** to H₂TCPP solution at 40°C, shows intense peaks for $\nu_{\text{asym}}[\text{C}=\text{O}]$ (1630 cm⁻¹) and $\nu_{\text{sym}}[\text{C}=\text{O}]$ (1407 cm⁻¹), indicative of the successful coordination between the carboxyl groups of H₂TCPP and the Cu-based secondary building units (SBUs).^[27,29]

We also assessed Brunauer-Emmett-Teller (BET) surface area of fiber substrates, MOF/textile composites, and Cu-TCPP powder based upon the N₂ isotherms at 77 K (Figure 6.3c-d). The sorption curves for the Cu-TCPP powder mainly feature type I isotherms ($P/P_0 < 0.9$),^[30] indicating micropores. In addition, a prompt capillary condensation at high relative pressure ($P/P_0 > 0.9$) is due to meso- or macro-pores, ascribed to dense packing of surface-bound MOF crystals.^[31,32] As shown in Figure 6.3d, the BET surface area of Cu-TCPP powder is 520 ± 84 m²/g, comparable to its reported value^[30] of 485 m²/g and much higher than that of other 2D porous materials such as Cu-BDC^[33] and Zn₂(bim)₄^[34] nanosheets. The composite **4** with euhedral MOF crystals shows 220 m²/g_(MOF+fiber), a factor of 20x enhancement over the <10 m²/g_(MOF+fiber) for the anhedral structure **3**.

Further study on Cu-TCPP film formation on PP fiber surface proves that HDS(Zn,Cu) film first absorbs H₂TCPP linkers for 4 h, followed by crystalline MOF nuclei formation, and subsequent MOF growth until precursor consumption (Figure S6.6-S8). 40°C of processing temperature is at least required to drive the reaction between HDS(Zn,Cu) and H₂TCPP to form crystalline and porous Cu-TCPP structure on fiber substrate (Figure S6.9-S10).

To define water stability of Cu-TCPP on PP textiles, we submerged **4** in water at 25°C for 17 h (Figure 6.4). PP@Cu-BTC was also tested as a control. More robust PP fabric (75 vs 40 grams

per square meter (gsm)) was also used to prepare MOF/fiber composites. (Figure S6.11). We found that the difference in fiber density did not give rise to a substantial change in MOF growth mechanism on the fiber. As shown in SEM images (Figure 6.4a-d), Cu-BTC dominantly transforms into flat noodle structure, whereas Cu-TCPP completely maintains its original 2D structures after water treatment. This remarkable difference was also reflected in the color change of PP@Cu-BTC from deep blue to light blue, whereas **4** in purple was maintained after the water treatment. From the measured XRD (Figure S6.12), FTIR (Figure S6.13), and BET surface area (Figure S6.14), the structural integrity and porosity of Cu-TCPP/fiber composites (**4**) are found to remain intact, while Cu-BTC completely degraded into a non-porous structure.^[35]

The type-V water adsorption isotherms for **4** (Figure 6.4f and Figure S6.15) confirm that the hydrophobic H₂TCPP^[36] enables partially hydrophobic MOF/fabric composites with good water stability compared to the unstable hydrophilic Cu-BTC. The overall water uptake at 298 K by **4** is 7 mmol/g_{MOF} vs 39 mmol/g_{MOF} for the Cu-BTC/fabric.

We implemented, for the first time, microbreakthrough tests for Cu-TCPP powder and composite **4** to test our hypothesis that the hybrid textiles can be used for hazardous gas removal even under humid conditions (Figures 6.5 and S16). The adsorption capacities for challenge gases (i.e., NH₃ or CEES) are presented on a per unit mass of MOF (mol/kg_{MOF}) to readily compare the chemical adsorptive performance of MOF film on fiber and that of MOF powder. As shown in Figure 6.5a-b and Table S6.1, the euhedral Cu-TCPP on fibers (**4**) shows NH₃ uptake of 2.0 and 3.5 mol/kg_{MOF} under dry and wet conditions, respectively, compared to only 1.2 mol/kg_{MOF} for the Cu-TCPP powder with or without humidity present.^[37]

Moisture condensation on MOFs can promote NH₃ uptake.^[36] Compared to Cu-TCPP powder, which shows no enhancement due to moisture, the ~3x enhanced NH₃ uptake under humid

conditions for the euhedral Cu-TCPP on the fiber (**4**) is ascribed to increased external surface area, and therefore enhanced water interaction per unit MOF volume. This hypothesis is supported by water isotherms at 298 K (Figure S6.17), where the total water uptake in the MOF on fiber is 10 mmol/g_{MOF}, compared to 4.3 mmol/g_{MOF} for the MOF powder. The higher water uptake in MOF on fibers allows enhanced intermolecular hydrogen bonding^[30] between polar NH₃ and water film, thus increasing NH₃ uptake. The water interaction is sufficient to drive favorable enhancement of NH₃ uptake, whereas the horizontal stacks of Cu-TCPP in the bulk powder make the effect less pronounced. Moreover, data in Figure 6.4 and Figure S6.12-15 show that the favorable water interaction with the euhedral Cu-TCPP on fibers is not sufficient to decompose the MOF. On the other hand, rapid degradation of hydrophilic Cu-BTC with higher pore volume is due to massive water uptake and clustering around the Cu sites.^[38-40] The smaller pore volume for Cu-TCPP vs Cu-BTC (0.3 vs 1.1 cm³/g_{MOF}) correlates with reduced NH₃ adsorptive capacity, (3-4 vs 6-7 mol/kg_{MOF}),^[38] but leads to substantially enhanced stability.

These results prove that the arrangement/orientation of Cu-TCPP film on fiber made by our synthetic strategy is more beneficial than powder counterpart in interacting with polar NH₃ molecules and with water molecules, thereby leading to even substantial enhancement in adsorption capacity under humid conditions (80% RH).

Figure 6.5c-d and Table S6.1 present CEES uptake on **4** and the corresponding Cu-TCPP powder under wet and dry conditions. The adsorption capacity for CEES is nearly the same on the powder and MOF/fiber composites under wet and dry conditions. A slight decrease in CEES uptake under wet conditions is not caused by MOF degradation but rather due to partial inhibition of lipophilic CEES molecules from interacting with Cu-TCPP.^[41] The water-stable adsorptive capacity of Cu-TCPP is highly promising in view of other MOFs exhibiting detrimental chemical

interactions with CEES in the presence of moisture.^[42] Analysis by PXRD (Figure S6.18) and attenuated total reflectance-Fourier transform infrared (ATR-FTIR) (Figure S6.19) confirm the stability of Cu-TCPP against NH₃ and CEES under dry and wet conditions.

In addition to Cu-TCPP/fiber composites, we also successfully prepared HDS(Zn,Zn) and HDS(Zn,Co) on PP (Figure S6.20), allowing direct conversion to Zn-TCPP and Co-TCPP MOF on fibers, respectively (Figure S6.21). These MOFs show euhedral radial crystal orientation and robust adhesion similar to the Cu-TCPP (Figure S6.22-26). We believe that such water stable 2D MOF/polymer composites with a variety of metal clusters may allow even better abatement performance with other toxic chemicals, and possibly demonstrate exceptional performance in other applications.

6.5. Conclusions

We quantitatively compared ALD metal oxide surfaces including Al₂O₃, ZnO, and TiO₂ on polypropylene textiles as starting surfaces for heterogeneous nucleation of UiO-66-NH₂ MOF as catalysts for hydrolysis of DMNP, as chemical warfare agent simulant. Compared to ALD ZnO and Al₂O₃, the TiO₂ layers led to more uniform MOF coating with highest overall MOF loading and net surface area (m²/g_(MOF+Fiber)). We confirmed the MOFs on TiO₂ treated polypropylene catalyzed the DMNP hydrolysis with t_{1/2}= 15 min, comparable to previous results and appreciably faster than PP fibrous mats with only the ALD coating. The Al₂O₃ coated PP performed nearly the same as TiO₂ in MOF nucleation and growth, but the ALD ZnO was unstable under MOF solvothermal synthesis conditions, resulting in ZnO dissolution and more favorable homogeneous MOF nucleation, likely promoted by the presence of Zn²⁺ ions in solution. Faster homogeneous nucleation led to more MOF crystals entrapped within the fiber mat, and an overall net larger mass

loading. While the larger MOF loading increased the net rate of DMNP degradation ($t_{1/2} = 10$ min), we find the entrapped crystals are less robust under mechanical handling, and therefore likely less desirable than covalently-bound crystals obtained on the TiO_2 surface. Further work is needed to specifically identify the likely nucleation sites and reactive species that enable favorable MOF nucleation on metal oxide or other growth surfaces.

6.6. Figures

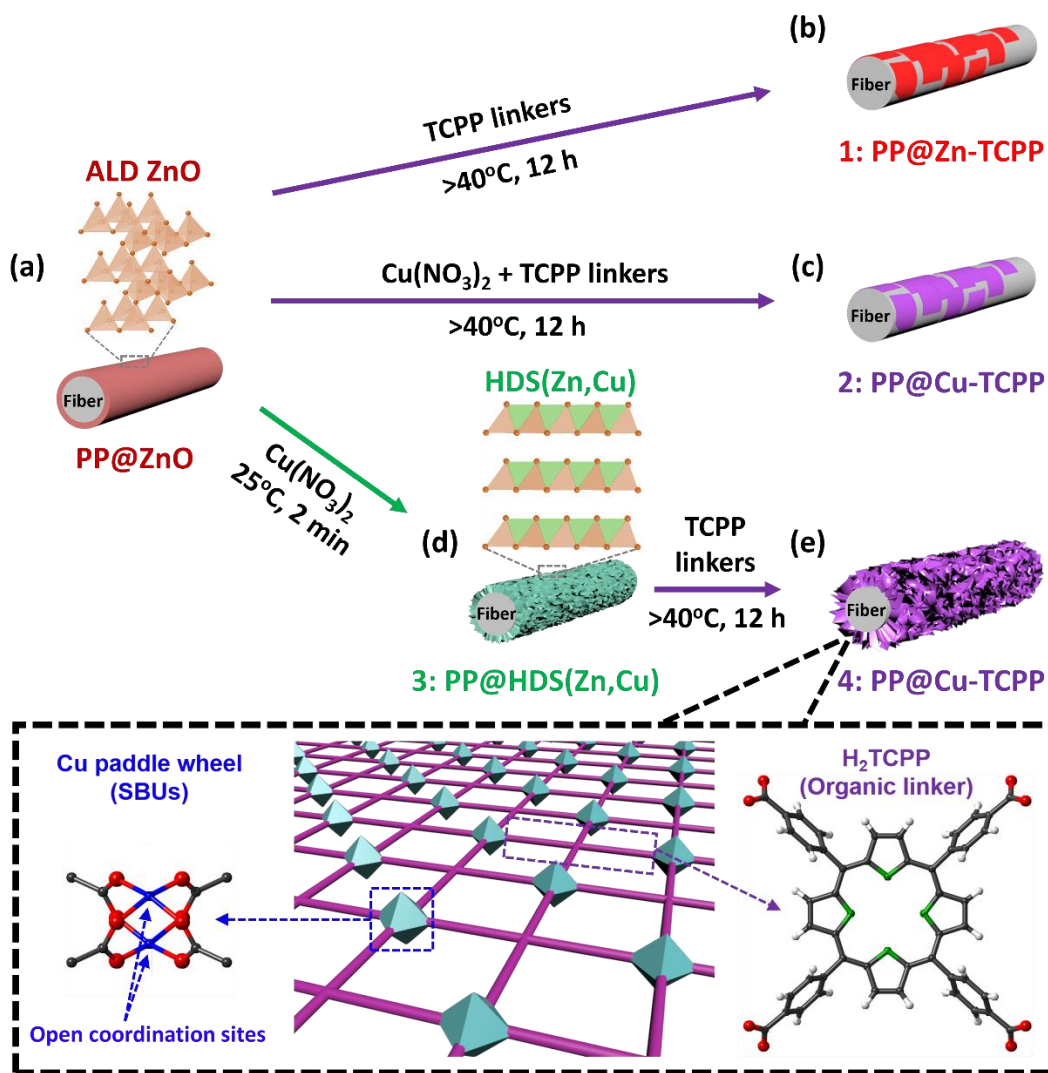


Figure 6.1. Schematic illustration of metal-TCPP MOF growth on PP fibers via different synthetic routes. (a) ALD ZnO-treated PP (PP@ZnO), (b) **1** (PP@Zn-TCPP), (c) **2** (PP@Cu-TCPP), (d) **3** (PP@HDS), and (e) **4** (PP@Cu-TCPP) composites. Components of Cu-TCPP are illustrated in the dashed box.

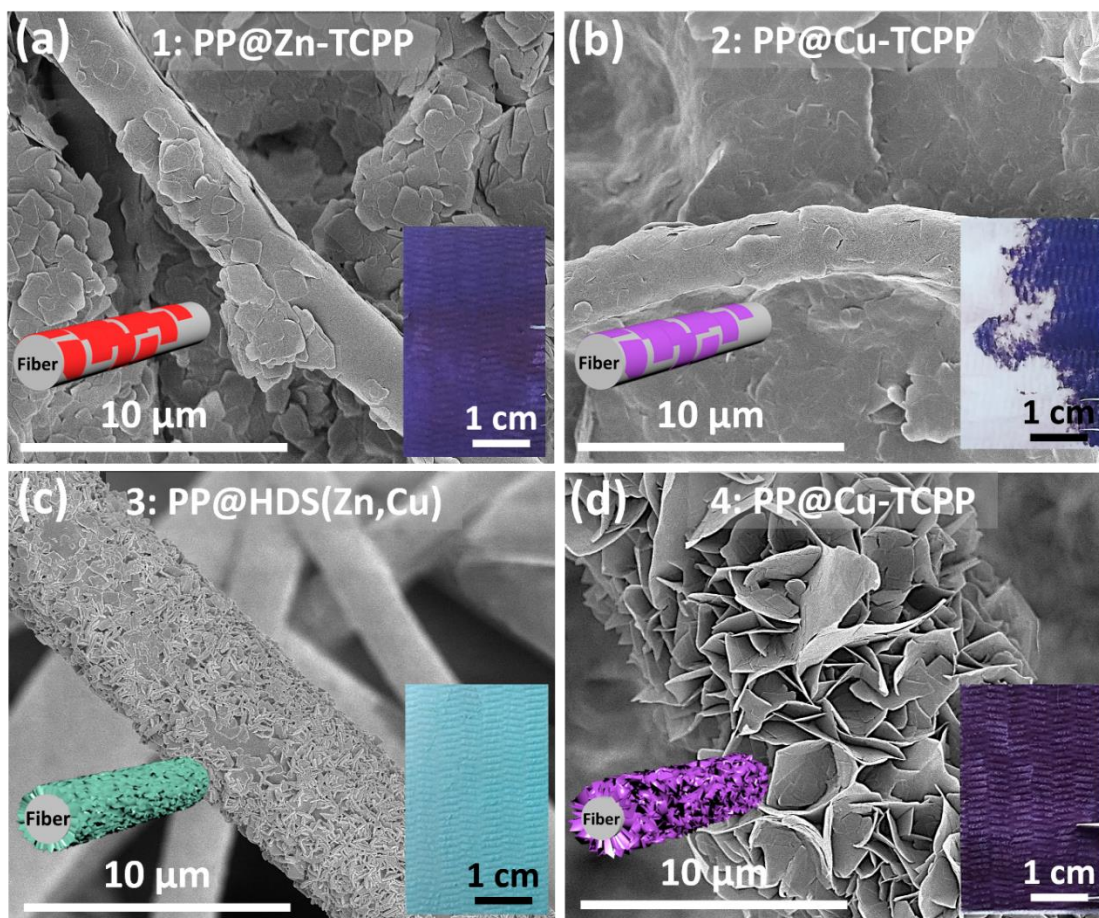


Figure 6.2. SEM images of (a) 1, (b) 2, (c) 3, and (d) 4 composites. The insets in the SEM images are corresponding schematic illustrations and digital photographs of the actual samples.

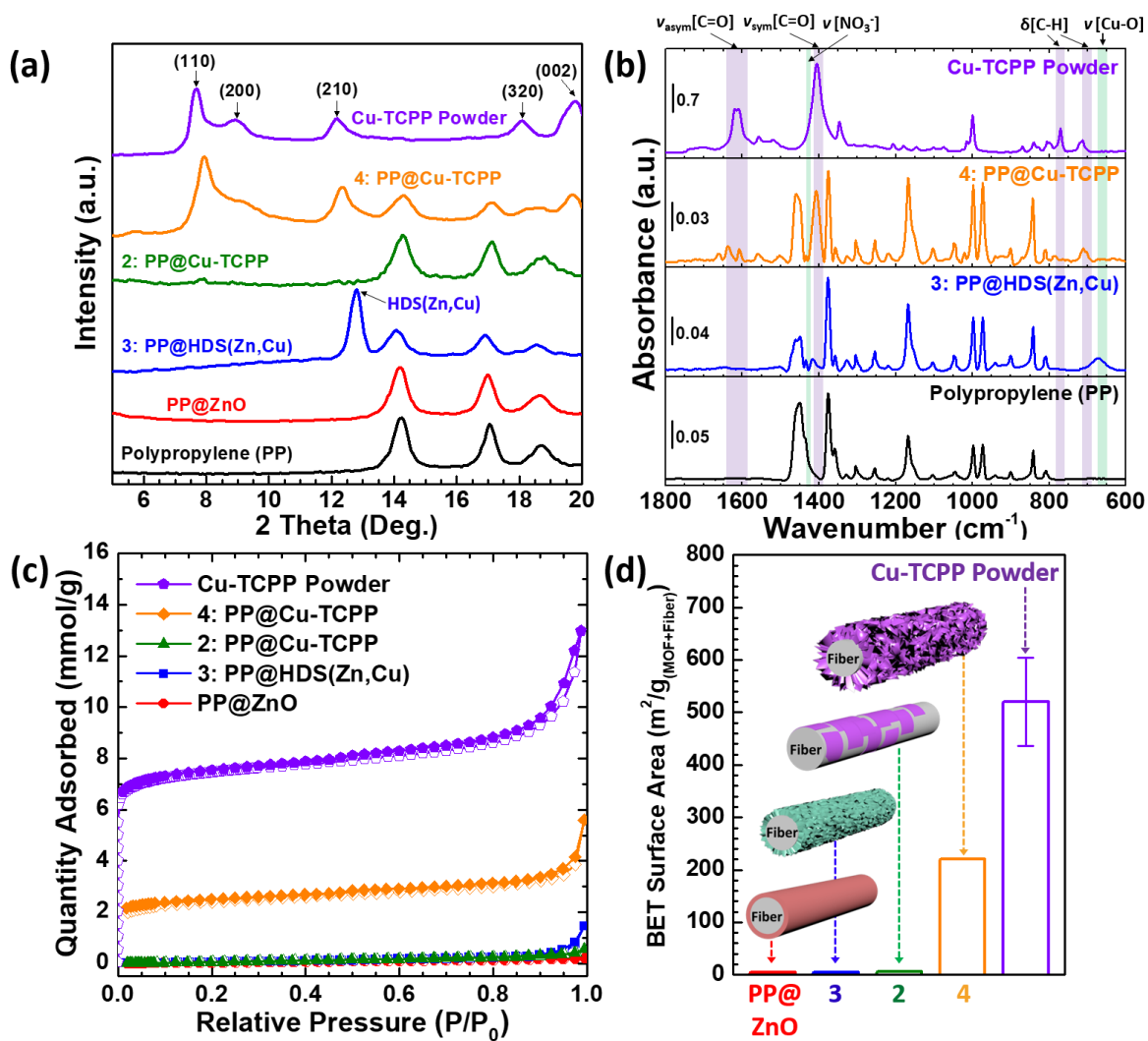


Figure 6.3. (a) XRD patterns for untreated PP, PP@ZnO, 3, 2, 4, and Cu-TCPP powder. (b) FTIR spectra for untreated PP, 3, 4, and Cu-TCPP powder. (c) N_2 isotherms at 77 K and (d) overall BET surface area ($\text{m}^2/\text{g}_{(\text{MOF}+\text{fiber})}$) for PP@ZnO, 3, 2, 4, and Cu-TCPP powder.

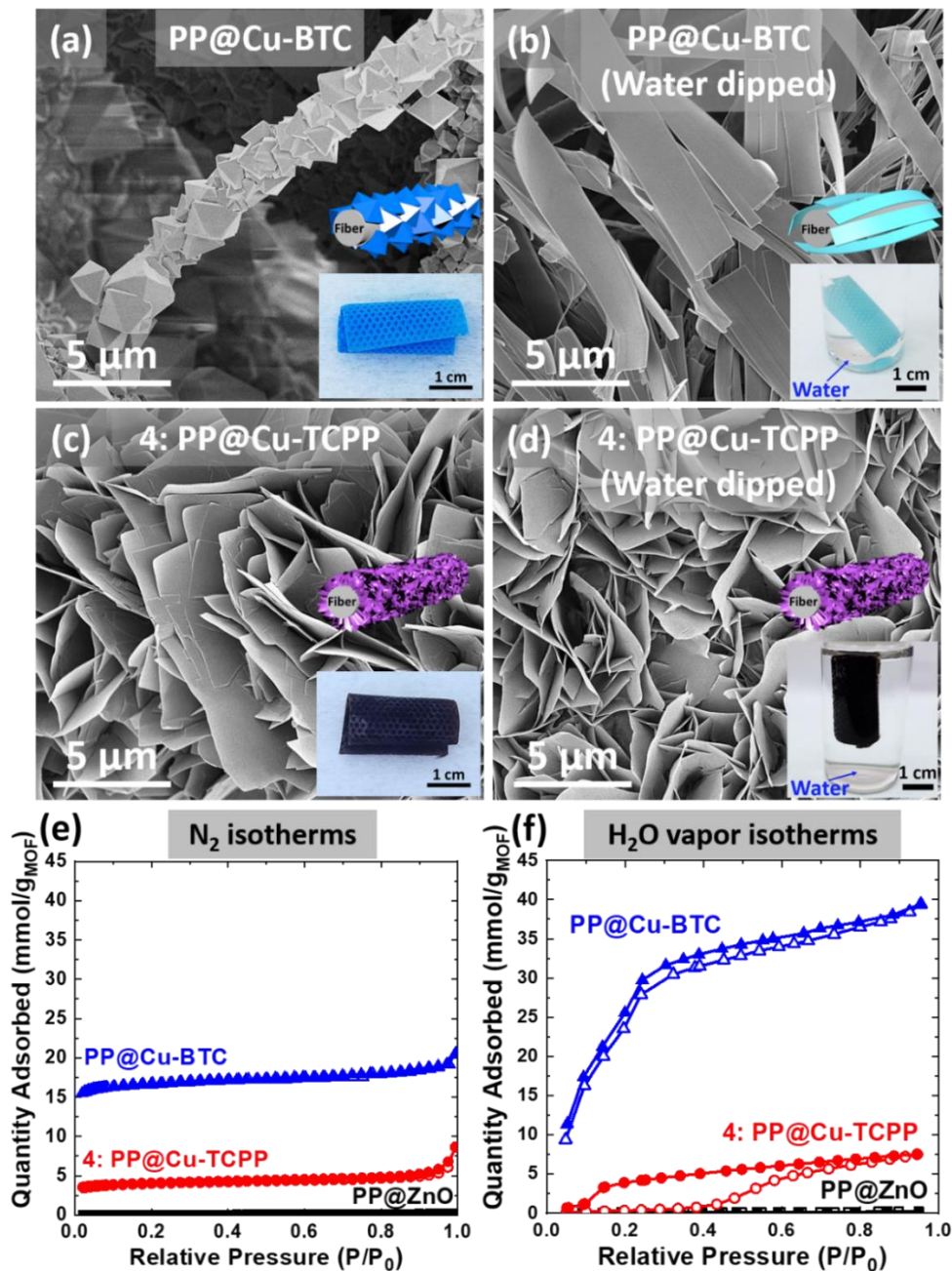


Figure 6.4. Water stability tests of PP@MOF textiles. SEM images for PP@Cu-BTC (a) before and (b) after submerged in water at 25 °C for 17 h (water treatment), and for **4** (c) before and (d) after the water treatment. The insets in Figure 4a-d are corresponding schematic illustrations and digital photographs of the actual samples. (e) N₂ isotherms at 77 K and (f) water vapor isotherms at 298 K before water treatment for PP@ZnO, PP@Cu-BTC, and **4** on a per gram of MOF basis.

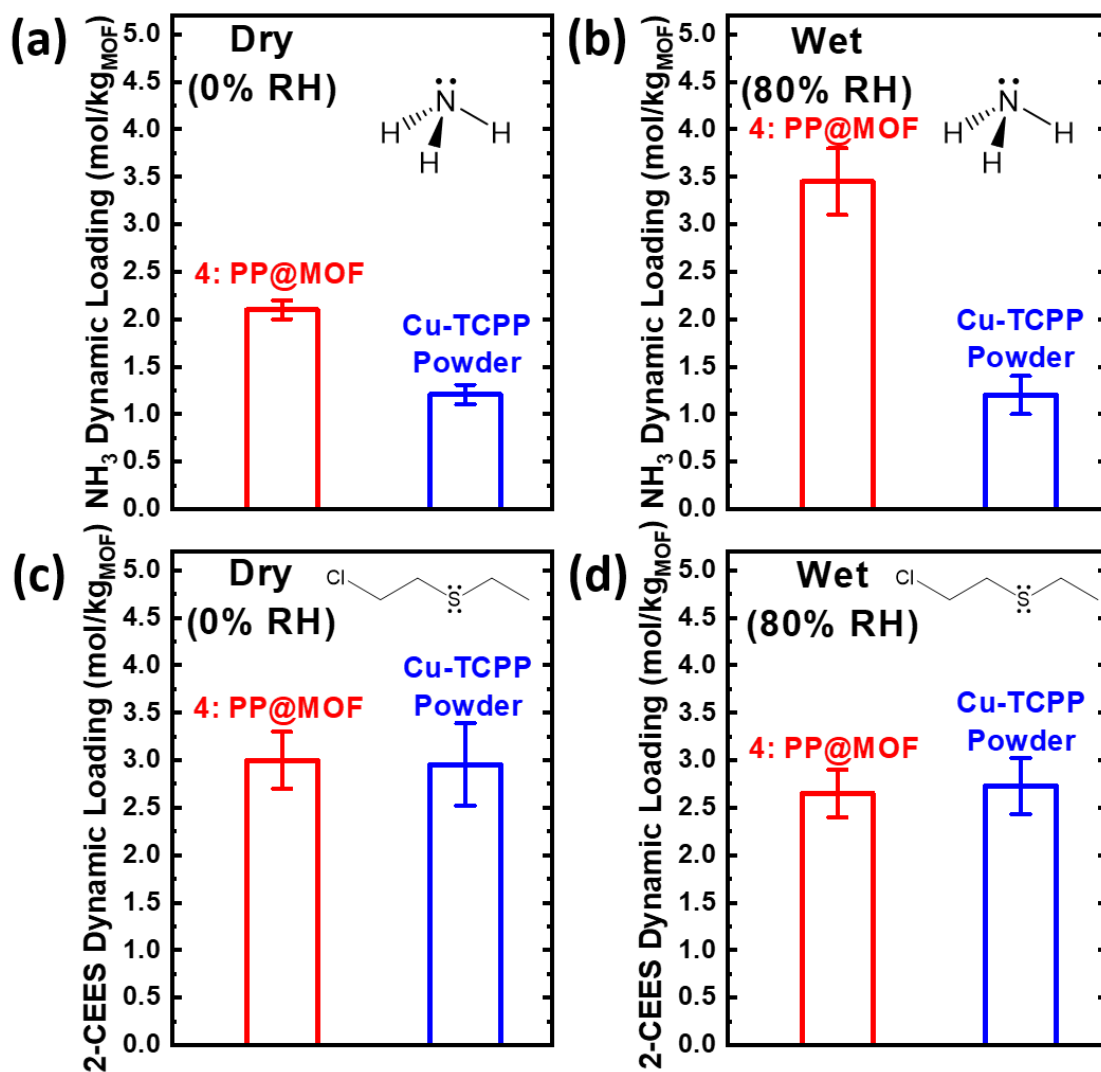


Figure 6.5. Dynamic loading (mol_(adsorbate)/kg_(MOF)) calculated from microbreakthrough tests. NH₃ dynamic loading for **4** and Cu-TCPP powder under (a) dry condition and (b) wet condition. CEES dynamic loading for **4** and Cu-TCPP powder under (c) dry condition and (d) wet condition. The insets are chemical structures of NH₃ and CEES.

6.7. References

- (1) N. S. Bobbitt, M. L. Mendonca, A. J. Howarth, T. Islamoglu, J. T. Hupp, O. K. Farha, R. Q. Snurr, *Chem. Soc. Rev.* **2017**, *46*, 3357.
- (2) H. Furukawa, K. E. Cordova, M. O’Keeffe, O. M. Yaghi, *Science* **2013**, *341*.
- (3) S. Li, F. Huo, *Small* **2014**, *10*, 4371.
- (4) Y. Peng, V. Krungleviciute, I. Eryazici, J. T. Hupp, O. K. Farha, T. Yildirim, *J. Am. Chem. Soc.* **2013**, *135*, 11887.
- (5) J. Zhao, M. D. Losego, P. C. Lemaire, P. S. Williams, B. Gong, S. E. Atanasov, T. M. Blevins, C. J. Oldham, H. J. Walls, S. D. Shepherd, M. A. Browe, G. W. Peterson, G. N. Parsons, *Adv. Mater. Interfaces* **2014**, *1*, 1400040.
- (6) J. Zhao, D. T. Lee, R. W. Yaga, M. G. Hall, H. F. Barton, I. R. Woodward, C. J. Oldham, H. J. Walls, G. W. Peterson, G. N. Parsons, *Angew. Chemie Int. Ed.* **2016**, *55*, 13224.
- (7) D. T. Lee, J. Zhao, G. W. Peterson, G. N. Parsons, *Chem. Mater.* **2017**, *29*, 4894.
- (8) N. A. Khan, Z. Hasan, S. H. Jung, *J. Hazard. Mater.* **2013**, *244–245*, 444.
- (9) N. M. Padial, E. Quartapelle Procopio, C. Montoro, E. López, J. E. Oltra, V. Colombo, A. Maspero, N. Masciocchi, S. Galli, I. Senkowska, S. Kaskel, E. Barea, J. A. R. Navarro, *Angew. Chemie Int. Ed.* **2013**, *52*, 8290.
- (10) M. J. Katz, J. E. Mondloch, R. K. Totten, J. K. Park, S. T. Nguyen, O. K. Farha, J. T. Hupp, *Angew. Chemie Int. Ed.* **2013**, *53*, 497.
- (11) S.-Y. Moon, Y. Liu, J. T. Hupp, O. K. Farha, *Angew. Chemie Int. Ed.* **2015**, *54*, 6795.
- (12) Y. Liu, A. J. Howarth, J. T. Hupp, O. K. Farha, *Angew. Chemie Int. Ed.* **2015**, *54*, 9001.

- (13) J. E. Mondloch, M. J. Katz, W. C. Isley III, P. Ghosh, P. Liao, W. Bury, G. W. Wagner, M. G. Hall, J. B. DeCoste, G. W. Peterson, R. Q. Snurr, C. J. Cramer, J. T. Hupp, O. K. Farha, *Nat. Mater.* **2015**, *14*, 512.
- (14) C. T. Buru, M. B. Majewski, A. J. Howarth, R. H. Lavroff, C.-W. Kung, A. W. Peters, S. Goswami, O. K. Farha, *ACS Appl. Mater. Interfaces* **2018**, *10*, 23802.
- (15) C. T. Buru, P. Li, B. L. Mehdi, A. Dohnalkova, A. E. Platero-Prats, N. D. Browning, K. W. Chapman, J. T. Hupp, O. K. Farha, *Chem. Mater.* **2017**, *29*, 5174.
- (16) A. Atilgan, T. Islamoglu, A. J. Howarth, J. T. Hupp, O. K. Farha, *ACS Appl. Mater. Interfaces* **2017**, *9*, 24555.
- (17) X. Zhang, Q. Zhang, D. Yue, J. Zhang, J. Wang, B. Li, Y. Yang, Y. Cui, G. Qian, *Small* **2018**, *14*, 1801563.
- (18) D. B. Dwyer, D. T. Lee, S. Boyer, W. E. Bernier, G. N. Parsons, W. E. Jones, *ACS Appl. Mater. Interfaces* **2018**, *10*, 25794.
- (19) D. T. Lee, J. Zhao, C. J. Oldham, G. W. Peterson, G. N. Parsons, *ACS Appl. Mater. Interfaces* **2017**, *9*, 44847.
- (20) H. Wang, G. W. Wagner, A. X. Lu, D. L. Nguyen, J. H. Buchanan, P. M. McNutt, C. J. Karwacki, *ACS Appl. Mater. Interfaces* **2018**, *10*, 18771.
- (21) G. W. Peterson, A. X. Lu, M. G. Hall, M. A. Browe, T. Tovar, T. H. Epps, *ACS Appl. Mater. Interfaces* **2018**, *10*, 6820.
- (22) G. Xu, T. Yamada, K. Otsubo, S. Sakaida, H. Kitagawa, *J. Am. Chem. Soc.* **2012**, *134*, 16524.
- (23) Y. Wang, M. Zhao, J. Ping, B. Chen, X. Cao, Y. Huang, C. Tan, Q. Ma, S. Wu, Y. Yu, Q. Lu, J. Chen, W. Zhao, Y. Ying, H. Zhang, *Adv. Mater.* **2016**, *28*, 4149.

- (24) J. Zhao, W. T. Nunn, P. C. Lemaire, Y. Lin, M. D. Dickey, C. J. Oldham, H. J. Walls, G. W. Peterson, M. D. Losego, G. N. Parsons, *J. Am. Chem. Soc.* **2015**, *137*, 13756.
- (25) S. Motoyama, R. Makiura, O. Sakata, H. Kitagawa, *J. Am. Chem. Soc.* **2011**, *133*, 5640.
- (26) A. H. Brozena, C. J. Oldham, G. N. Parsons, *J. Vac. Sci. Technol. A* **2015**, *34*, 10801.
- (27) R. Makiura, S. Motoyama, Y. Umemura, H. Yamanaka, O. Sakata, H. Kitagawa, *Nat. Mater.* **2010**, *9*, 565.
- (28) M. Meyn, K. Beneke, G. Lagaly, *Inorg. Chem.* **1993**, *32*, 1209.
- (29) R. Rahimi, S. Shariatinia, S. Zargari, M. Yaghoubi Berijani, A. Ghaffarinejad, Z. S. Shojaie, *RSC Adv.* **2015**, *5*, 46624.
- (30) G. Xu, K. Otsubo, T. Yamada, S. Sakaida, H. Kitagawa, *J. Am. Chem. Soc.* **2013**, *135*, 7438.
- (31) A. Corma, V. Fornes, S. B. Pergher, T. L. M. Maesen, J. G. Buglass, *Nature* **1998**, *396*, 353.
- (32) M. Choi, K. Na, J. Kim, Y. Sakamoto, O. Terasaki, R. Ryoo, *Nature* **2009**, *461*, 246.
- (33) T. Rodenas, I. Luz, G. Prieto, B. Seoane, H. Miro, A. Corma, F. Kapteijn, F. X. Llabrés i Xamena, J. Gascon, *Nat. Mater.* **2014**, *14*, 48.
- (34) Y. Peng, Y. Li, Y. Ban, H. Jin, W. Jiao, X. Liu, W. Yang, *Science* **2014**, *346*, 1356 LP.
- (35) G. Majano, J. Pérez-Ramírez, *Adv. Mater.* **2012**, *25*, 1052.
- (36) O. T. Wilcox, A. Fateeva, A. P. Katsoulidis, M. W. Smith, C. A. Stone, M. J. Rosseinsky, *Chem. Commun.* **2015**, *51*, 14989.
- (37) P. Ghosh, K. C. Kim, R. Q. Snurr, *J. Phys. Chem. C* **2014**, *118*, 1102.
- (38) G. W. Peterson, G. W. Wagner, A. Balboa, J. Mahle, T. Sewell, C. J. Karwacki, *J. Phys. Chem. C* **2009**, *113*, 13906.
- (39) N. Nijem, K. Fürsich, H. Bluhm, S. R. Leone, M. K. Gilles, *J. Phys. Chem. C* **2015**, *119*, 24781.

- (40) J. B. Decoste, G. W. Peterson, M. W. Smith, C. A. Stone, C. R. Willis, *J. Am. Chem. Soc.* **2012**, *134*, 1486.
- (41) G. W. Peterson, G. W. Wagner, *J. Porous Mater.* **2014**, *21*, 121.
- (42) G. W. Peterson, M. R. Destefano, S. J. Garibay, A. Ploskonka, M. McEntee, M. Hall, C. J. Karwacki, J. T. Hupp, O. K. Farha, *Chem. – A Eur. J.* **2017**, *23*, 15913.

6.8. Supporting Information

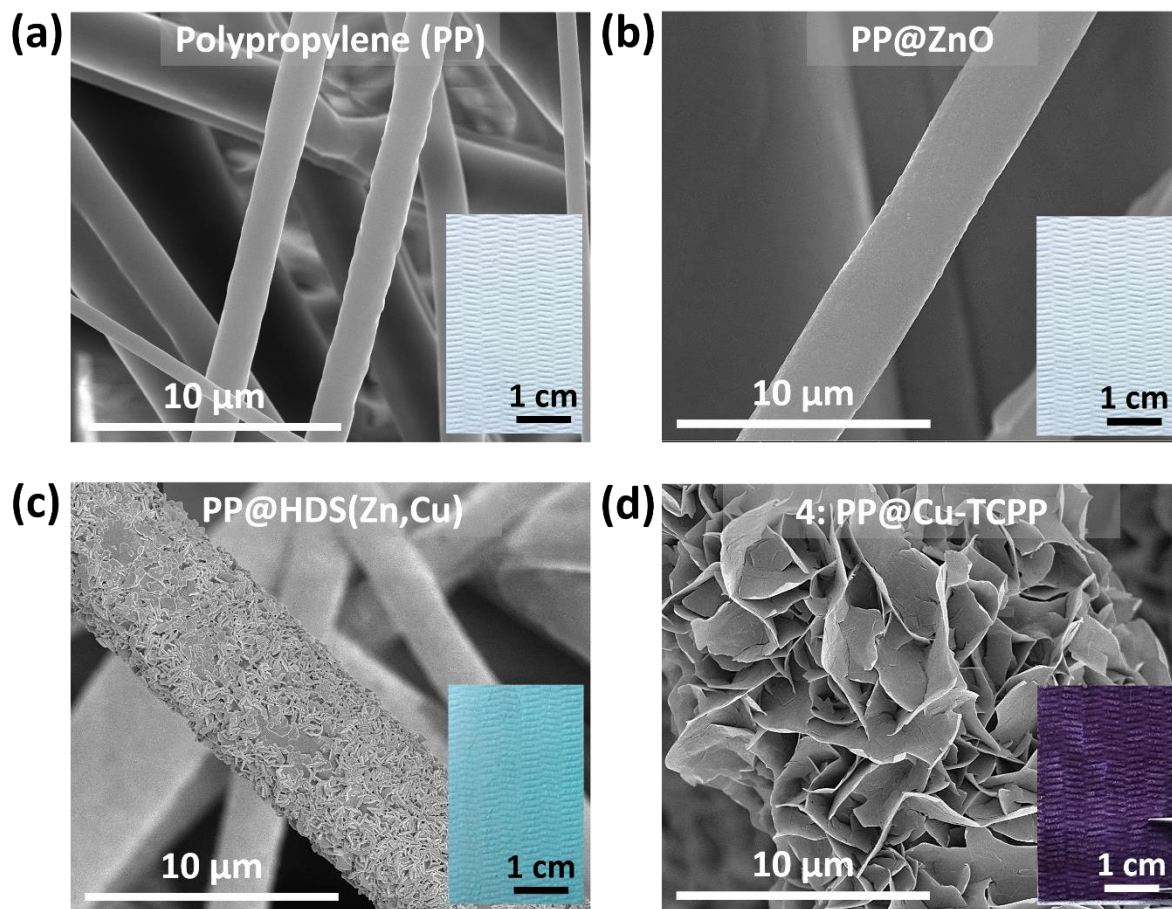


Figure S6.1. SEM images of (a) untreated polypropylene (PP) fibrous mats, (b) ALD ZnO-treated PP (PP@ZnO), (c) HDS(Zn,Cu) coated PP (PP@HDS), and (d) PP@Cu-TCPP composites made by reacting PP@HDS(Zn,Cu) and H₂TCPP linker solution (4: PP@Cu-TCPP) at 40°C for 12 h. The insets in the SEM images are digital photographs of corresponding actual samples.

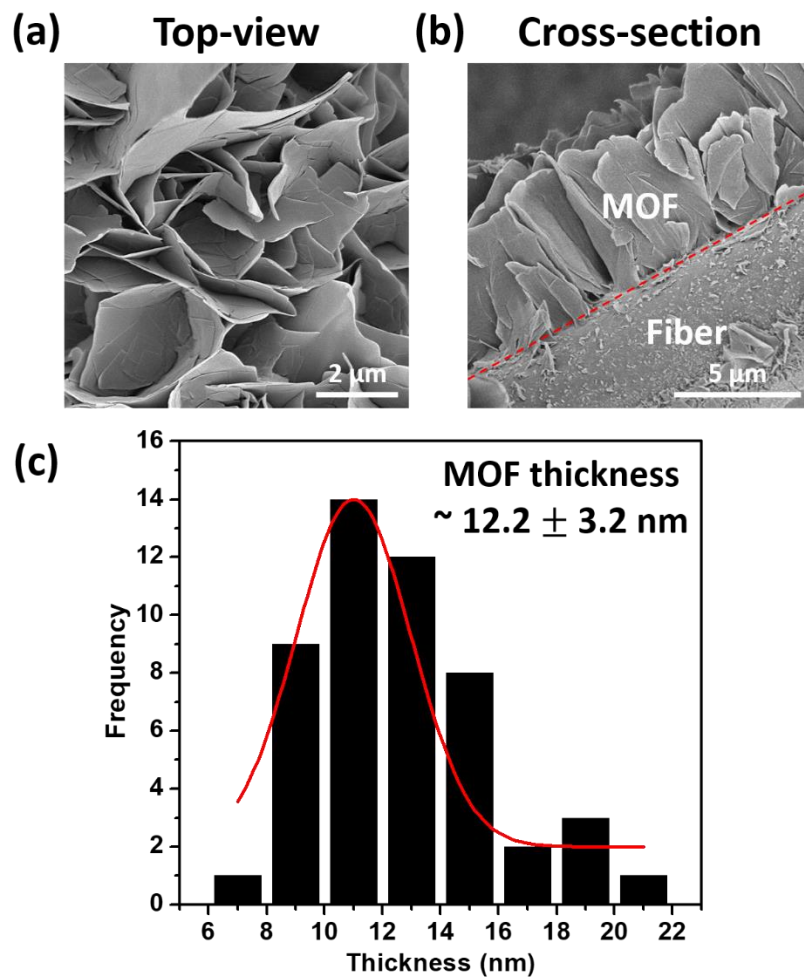


Figure S6.2. SEM images of vertically grown Cu-TCPP MOFs on PP micro-fibers (a) in a top-view and (b) a cross-sectional view. (c) MOF thickness distribution measured based on the SEM images.

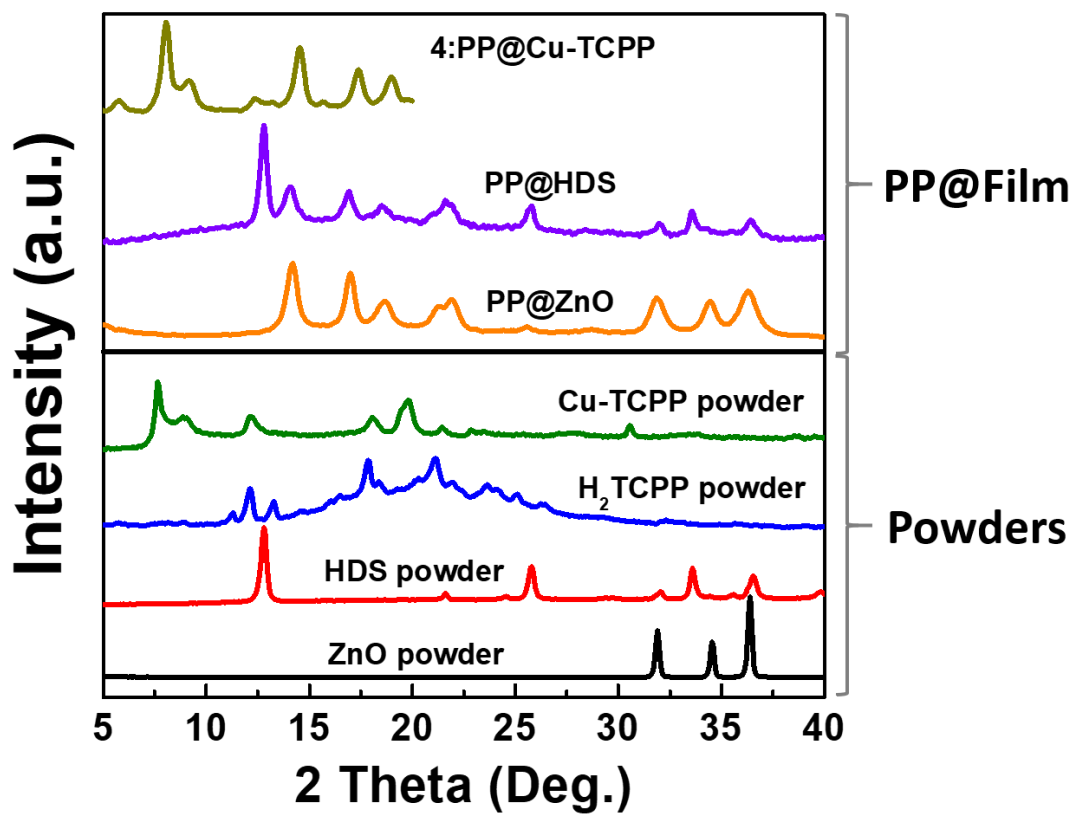


Figure S6.3. Measured XRD patterns of powder samples including ZnO, HDS(Zn,Cu), H₂TCPP, and Cu-TCPP, and PP@film composite materials including PP@ZnO, PP@HDS(Zn,Cu), and 4:PP@Cu-TCPP.

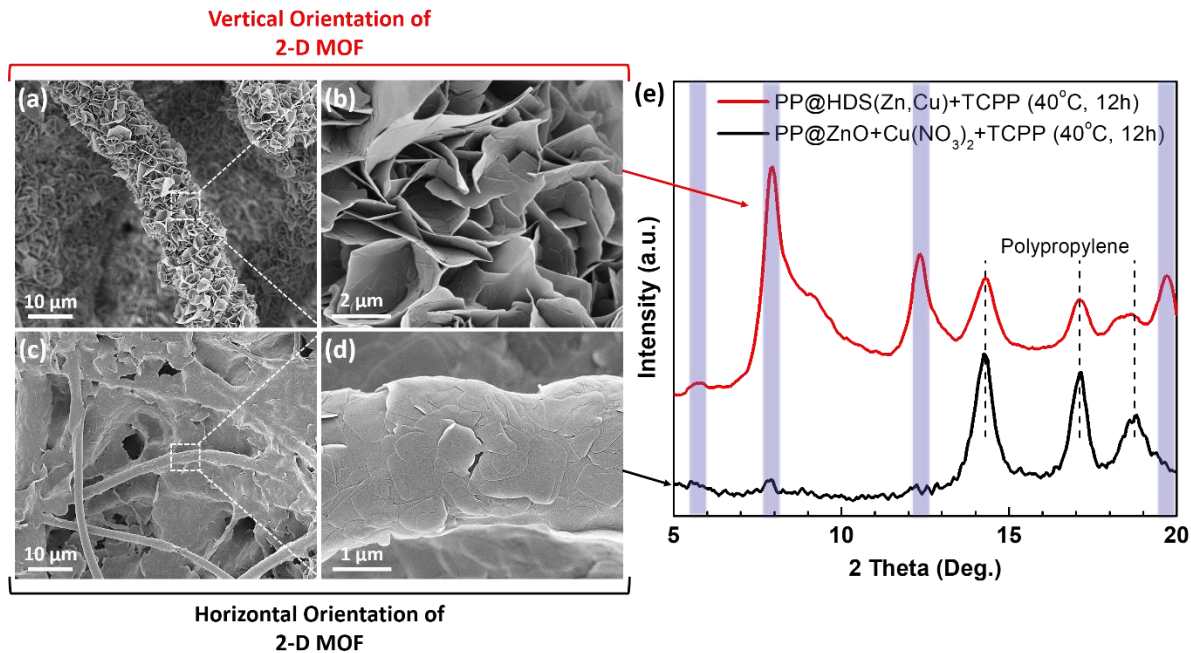


Figure S6.4. SEM images of Cu-TCPP MOFs grown on PP micro-fibers (a-b) ($\text{PP@HDS(Zn,Cu)+TCPP}$) in a vertical and (c-d) ($\text{PP@ZnO+Cu(NO}_3)_2\text{+TCPP}$) in a horizontal manner. (e) XRD patterns for both $\text{PP@HDS(Zn,Cu)+TCPP}$ and $\text{PP@ZnO+Cu(NO}_3)_2\text{+TCPP}$ composite materials. Synthetic condition for both samples was performed at 40°C for 12 h. $\text{PP@ZnO+Cu(NO}_3)_2\text{+TCPP}$ is equal to **3**: PP@Cu-TCPP . $\text{PP@HDS(Zn,Cu)+TCPP}$ is equal to **4**: PP@Cu-TCPP

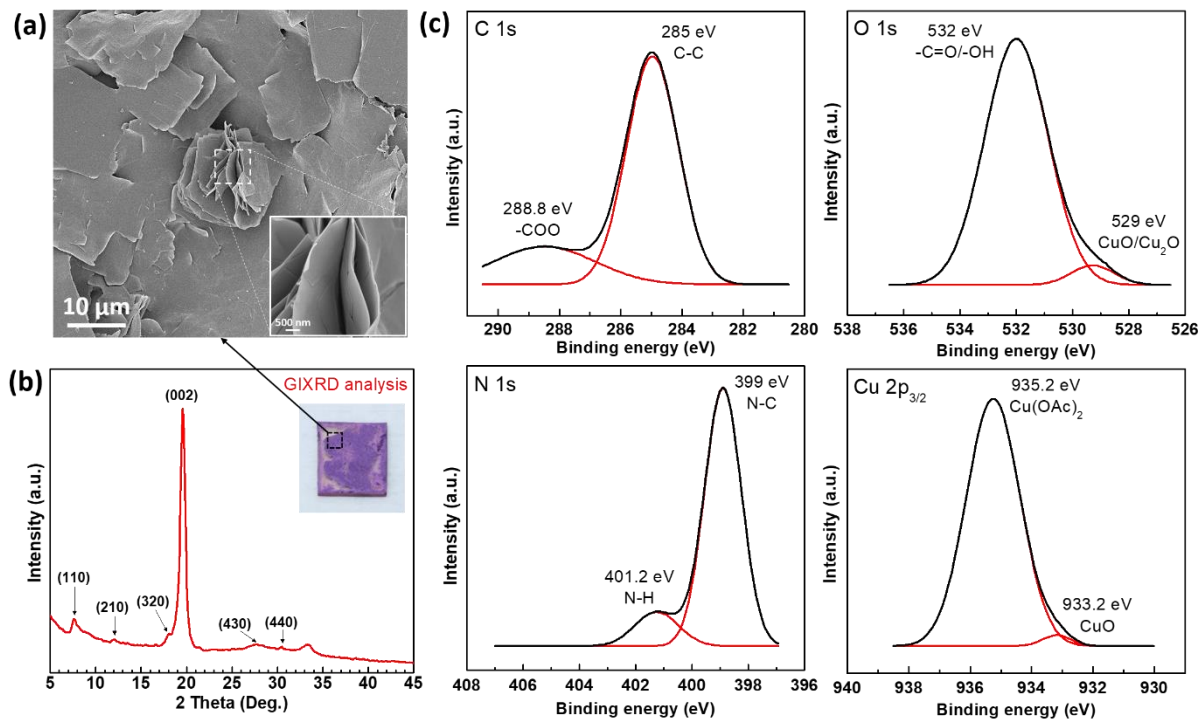


Figure S6.5 (a) SEM images and (b) XRD pattern of Cu-TCPP MOFs drop-cast on a flat glass substrate obtained by a grazing-incidence XRD (GIXRD) technique (the inset shows the actual sample measured). (c) XPS data collected on Cu-TCPP MOFs drop-cast on a piece of silicon wafer. Cu-TCPP MOF powder used was prepared by a conventional solvothermal method conducted at 80°C for 24 h.

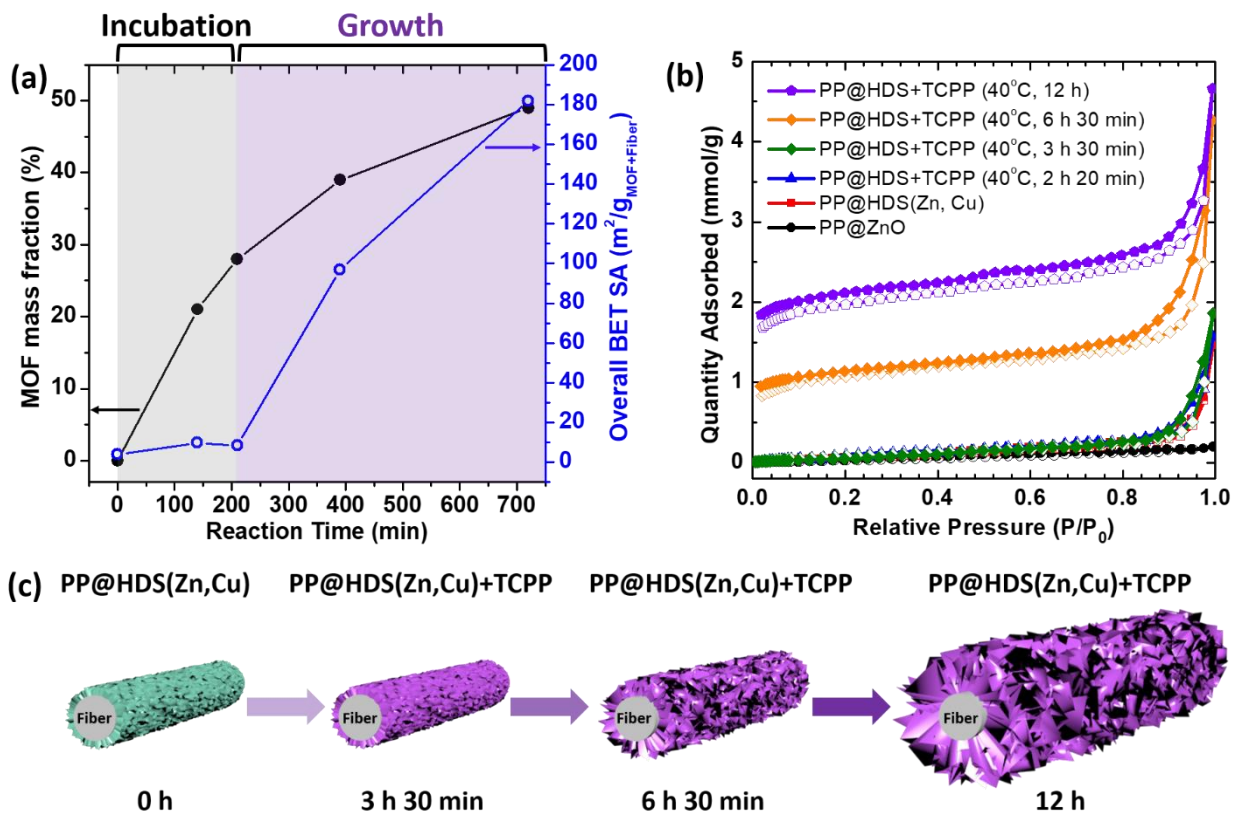


Figure S6.6. (a) A graph of MOF mass fraction (%) ($= \frac{m_{MOF+Fiber} - m_{Fiber}}{m_{MOF+Fiber}} \times 100$ (%)) and overall BET surface area ($m^2/g_{(MOF+fiber)}$) as a function of a varied reaction time (min), (b) N_2 isotherms for PP@ZnO, PP@HDS(Zn,Cu), PP@HDS(Zn,Cu) reacted with TCPP solution at 40°C for varied reaction time, and (c) schematic illustration of Cu-TCPP MOF growth mechanism onto PP@HDS(Zn,Cu). PP@HDS(Zn,Cu)+TCPP is equal to **4**: PP@Cu-TCPP.

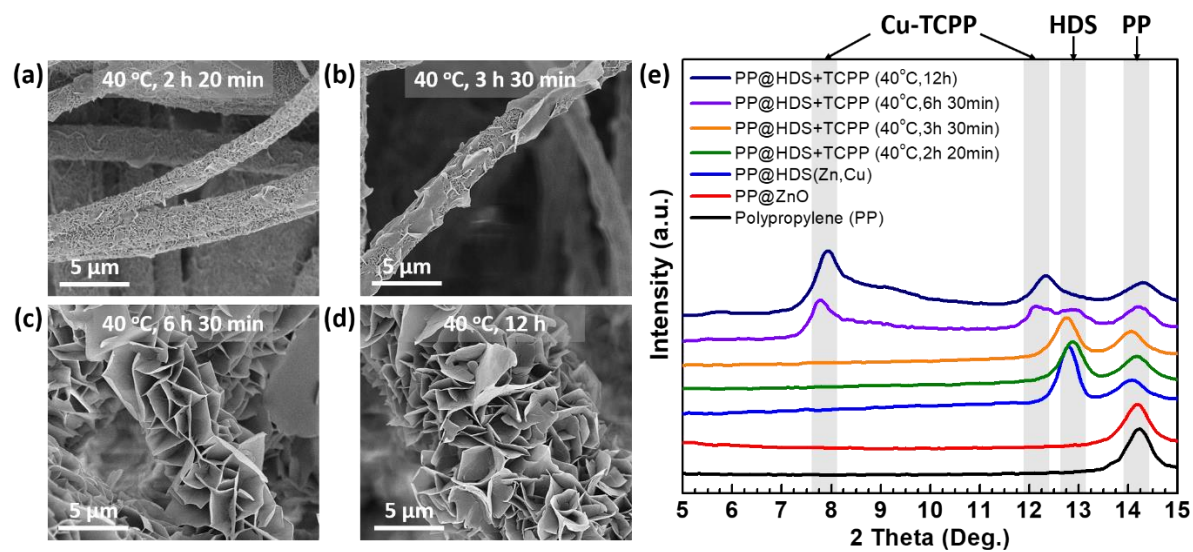


Figure S6.7. (a-d) SEM images and (e) XRD patterns captured at varied reaction time (i.e., 2h 20 min, 3h 30 min, 6h 30 min, and 12 h) for PP@HDS(Zn,Cu)+TCPP at 40°C. PP@HDS(Zn,Cu)+TCPP is equal to **4**: PP@Cu-TCPP.

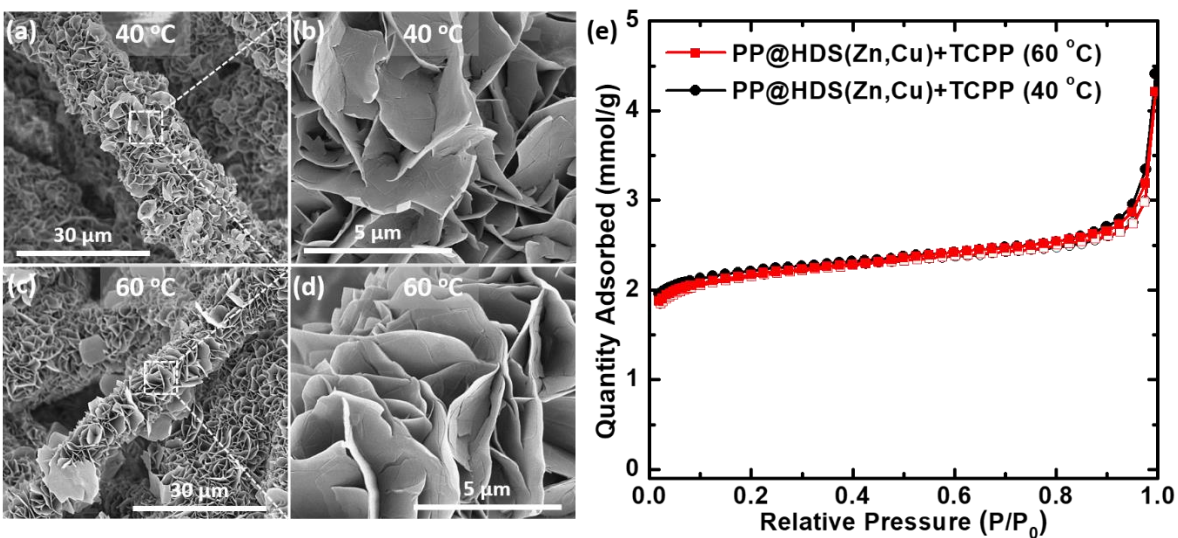


Figure S6.8. SEM images of (a-b) PP@HDS(Zn,Cu)+TCPP at 40°C for 12 h and (c-d) PP@HDS(Zn,Cu)+TCPP at 60°C for 12 h. (e) N₂ isotherms at 77 K for the samples imaged. This proves that a relatively low temperature, 40°C, is enough to grow good quality of 2D Cu-TCPP MOF crystals for PP@HDS(Zn,Cu)+TCPP. PP@HDS(Zn,Cu)+TCPP is equal to **4**: PP@Cu-TCPP.

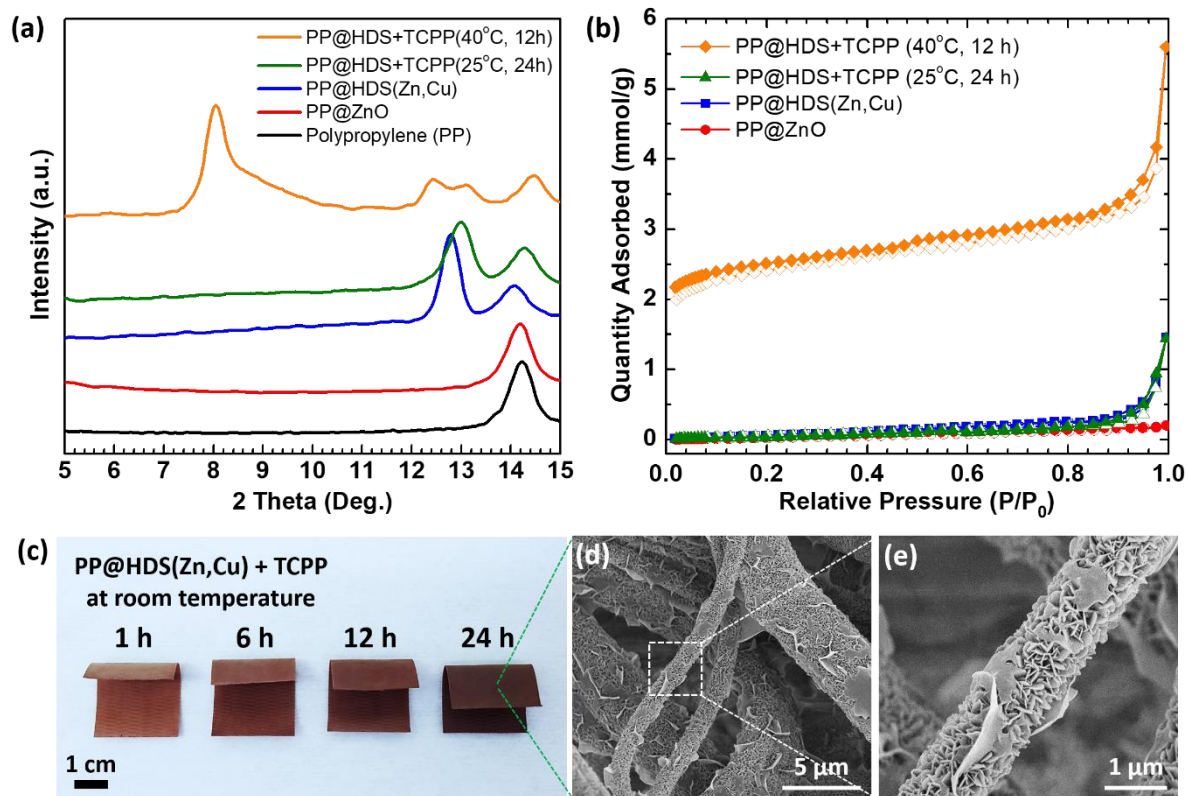


Figure S6.9. (a) XRD patterns and (b) N_2 isotherms at 77 K for PP fibrous mats, PP@ZnO, PP@HDS(Zn,Cu), PP@HDS(Zn,Cu)+TCPP synthesized at 25°C for 24 h, and PP@HDS(Zn,Cu)+TCPP synthesized at 40°C. (c) Actual PP@HDS(Zn,Cu)+TCPP samples collected at varied reaction time (1 h, 6 h, 12 h, and 24 h) conducted at room temperature. (d-e) SEM images of PP@HDS(Zn,Cu)+TCPP prepared at 25°C for 24 h. This result indicates that PP@HDS(Zn,Cu) swatch can absorb more amounts of H_2 TCPP organic linkers for a longer dipping time, but not enough to grow crystalline Cu-TCPP MOFs.

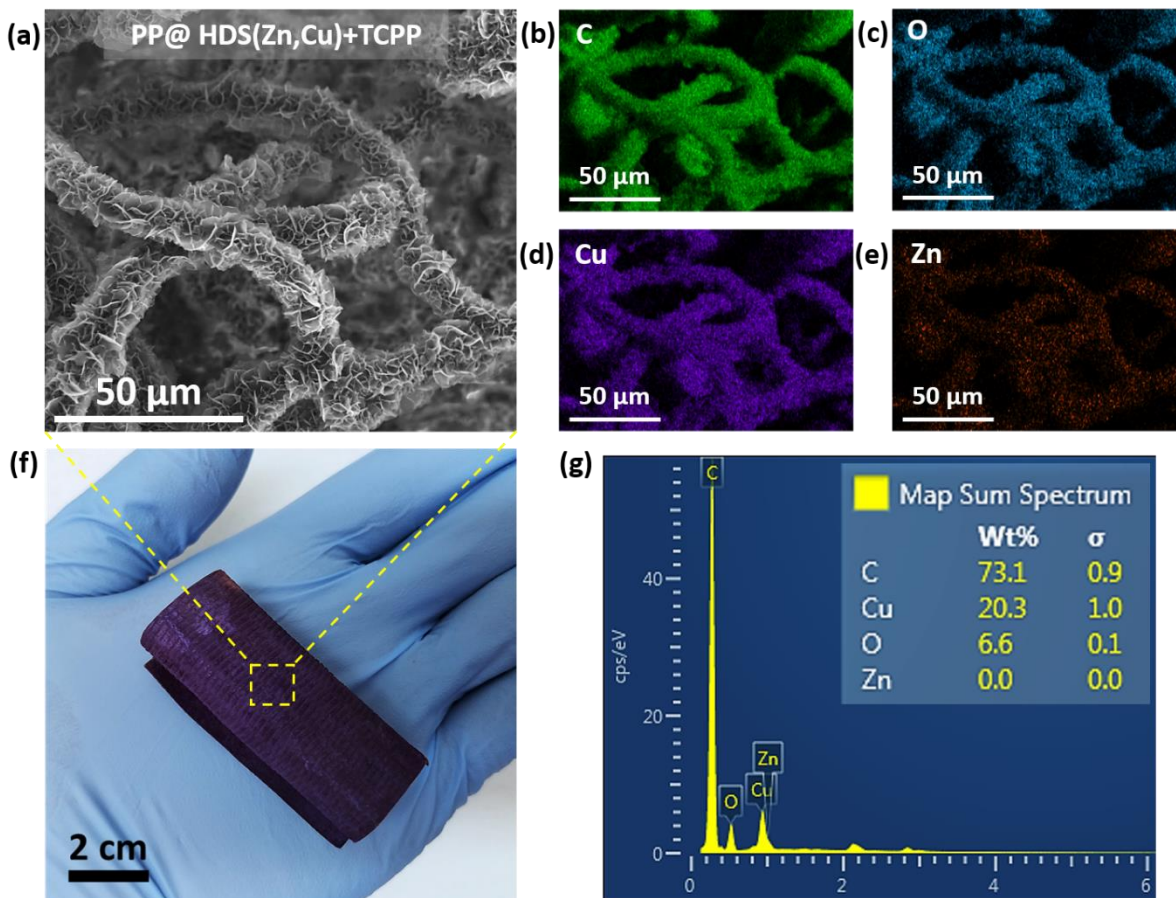


Figure S6.10. (a) SEM and (b-e) EDS mapping images of PP@HDS(Zn,Cu)+TCPP prepared at 40°C for 12 h. (f) A digital photograph of the actual sample (size: 2''x2'' composite swatch) and (g) its EDS spectra. PP@HDS(Zn,Cu)+TCPP is equal to **4**: PP@Cu-TCPP.

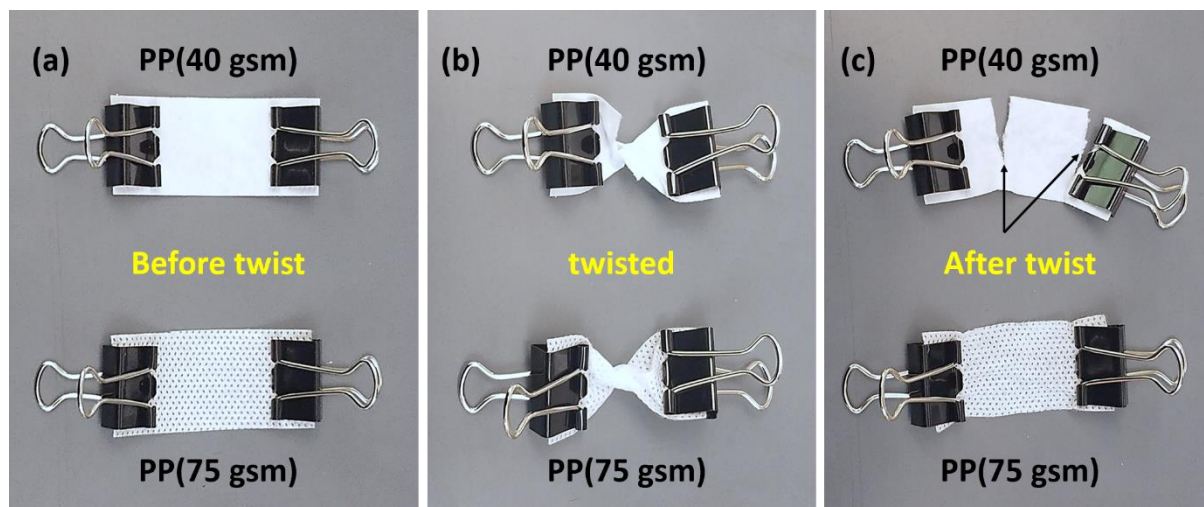


Figure S6.11. Digital photographs of the actual polypropylene (PP) substrates with 40 grams per square meter (gsm) or 75 gsm (a) before, (b) when, and (c) after twisted by binder clips. PP(75) swatch shows much higher mechanical strength compared to PP(40) polymeric fibrous mats.

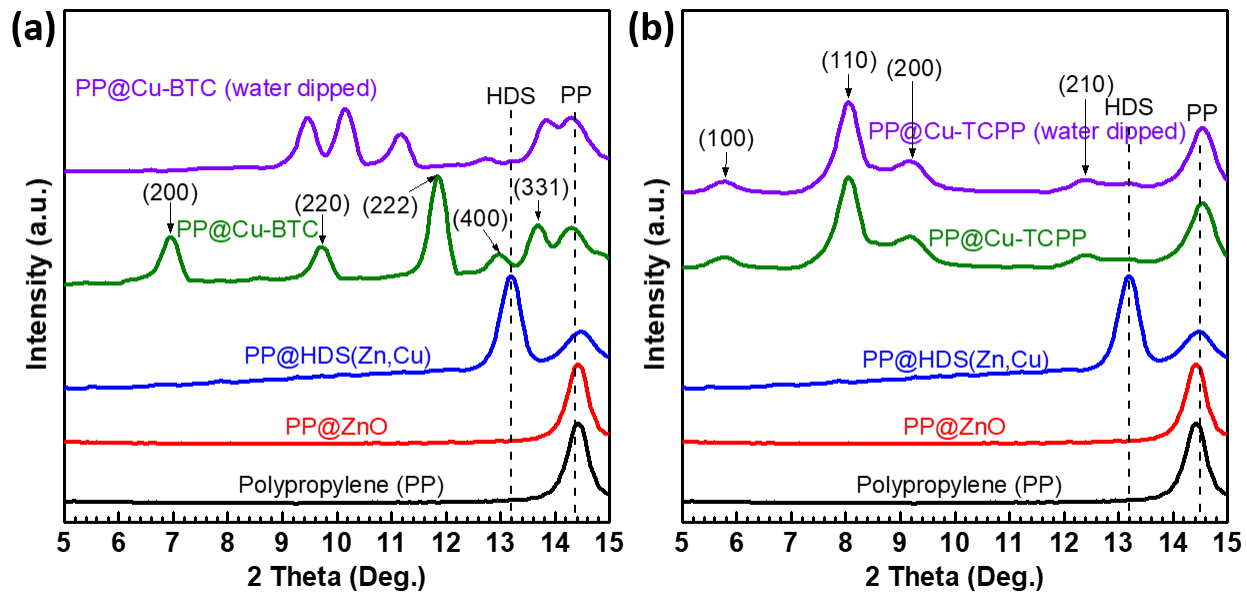


Figure S6.12. XRD patterns of (a) PP@Cu-BTC and (b) 4: PP@Cu-TCPP before and after the water stability test (17 h, ambient temperature) together with reference substrates including PP, PP@ZnO, PP@HDS(Zn,Cu).

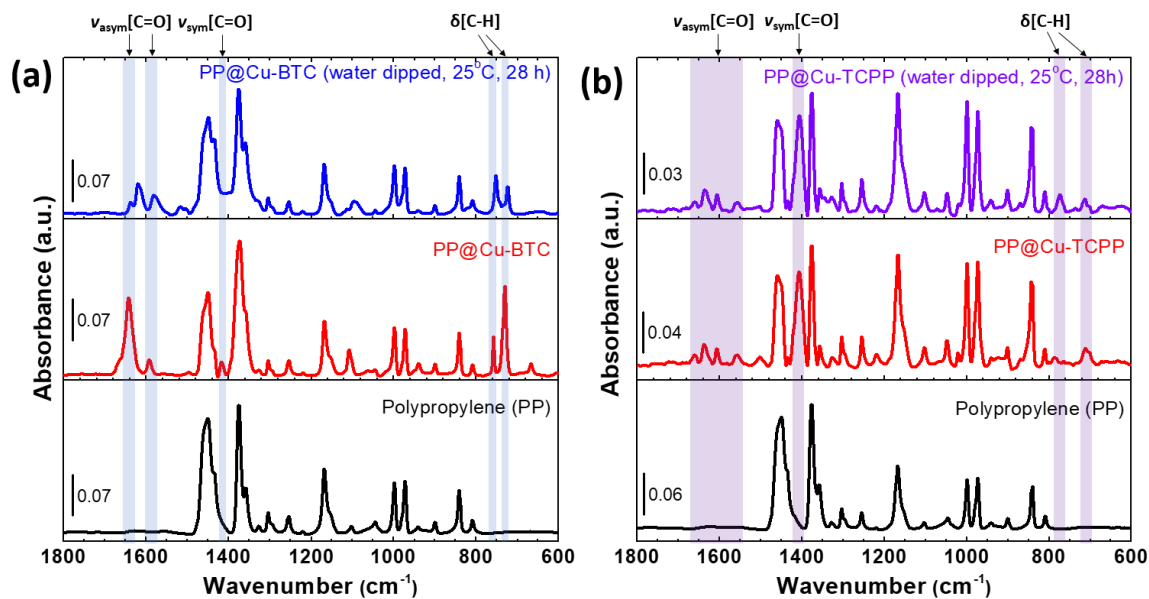


Figure S6.13. FTIR spectra for untreated PP fibers and PP@Cu-BTC before and after the water treatment, and for untreated PP fibers and **4**: PP@Cu-TCPP before and after the water treatment. The water treatment was done by dipping samples in liquid water for 28 h. PP@Cu-BTC was prepared by reacting PP@HDS(Zn,Cu) with H₃BTC solution at room temperature for 2 min. **4**: PP@Cu-TCPP was synthesized by reacting PP@HDS(Zn,Cu) with H₂TCPP solution at 40°C for 12 h.

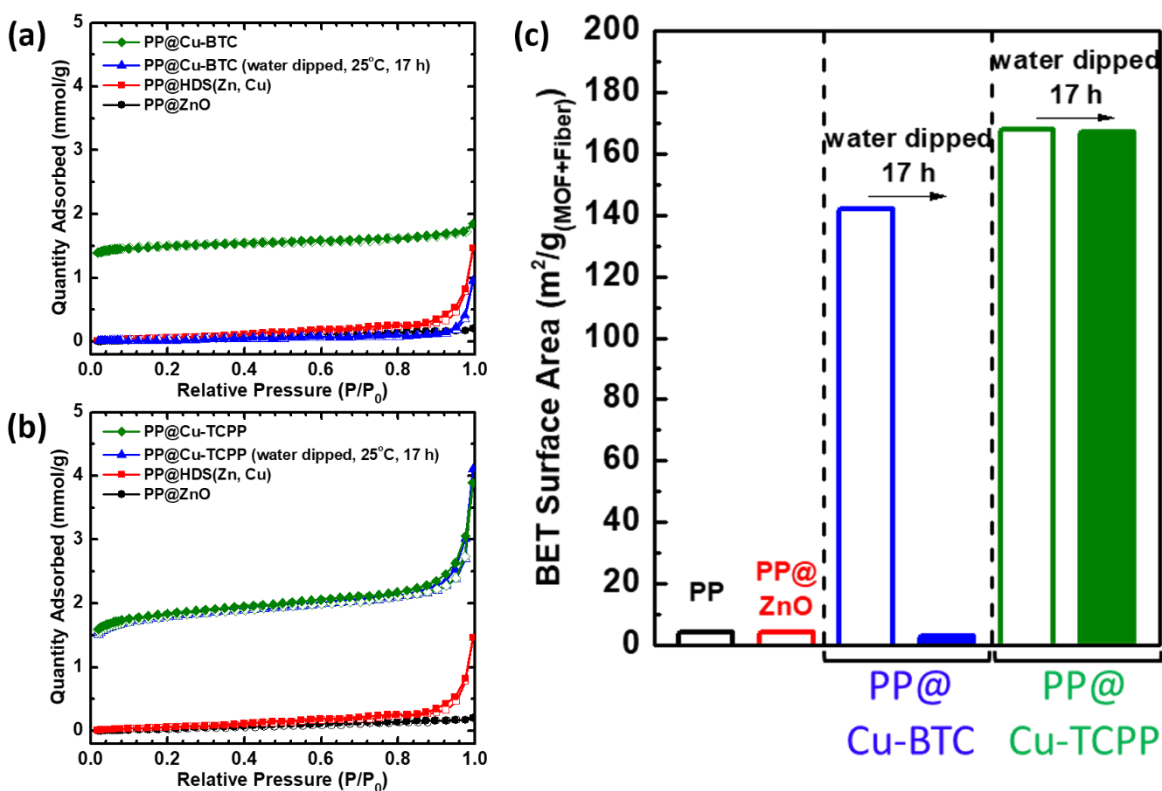


Figure S6.14. N₂ isotherms at 77 K for (a) PP@Cu-BTC and (b) **4**: PP@Cu-TCPP before and after a water stability test. (c) BET surface area (m²/g_(MOF+fiber)) for PP, PP@ZnO, and PP@Cu-BTC and **4**: PP@Cu-TCPP before and after the water stability test. The water stability test was performed by dipping samples in liquid water for 17 h. PP@Cu-BTC was prepared by reacting PP@HDS(Zn,Cu) with H₃BTC solution at room temperature for 2 min. **4**: PP@Cu-TCPP was synthesized by reacting PP@HDS(Zn,Cu) with H₂TCPP solution at 40°C for 12 h.

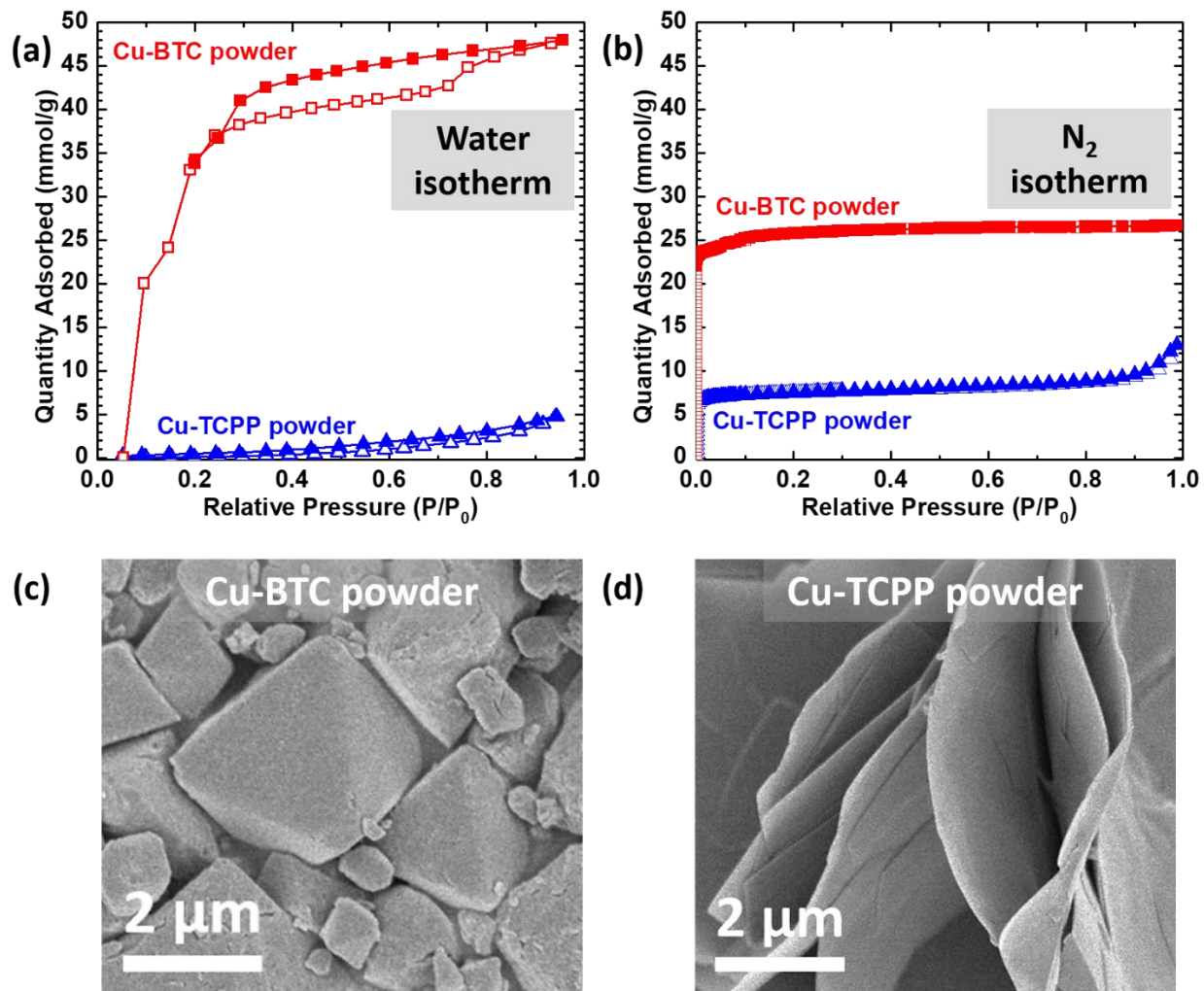


Figure S6.15. (a) Water vapor adsorption (open symbol) and desorption (closed symbol) isotherms at 298 K and (b) N_2 adsorption (open symbol) and desorption (closed symbol) isotherms at 77 K for Cu-BTC (red, square) and Cu-TCPP MOF powder (blue, triangle). SEM images of (c) Cu-BTC and (d) Cu-TCPP MOF powder.

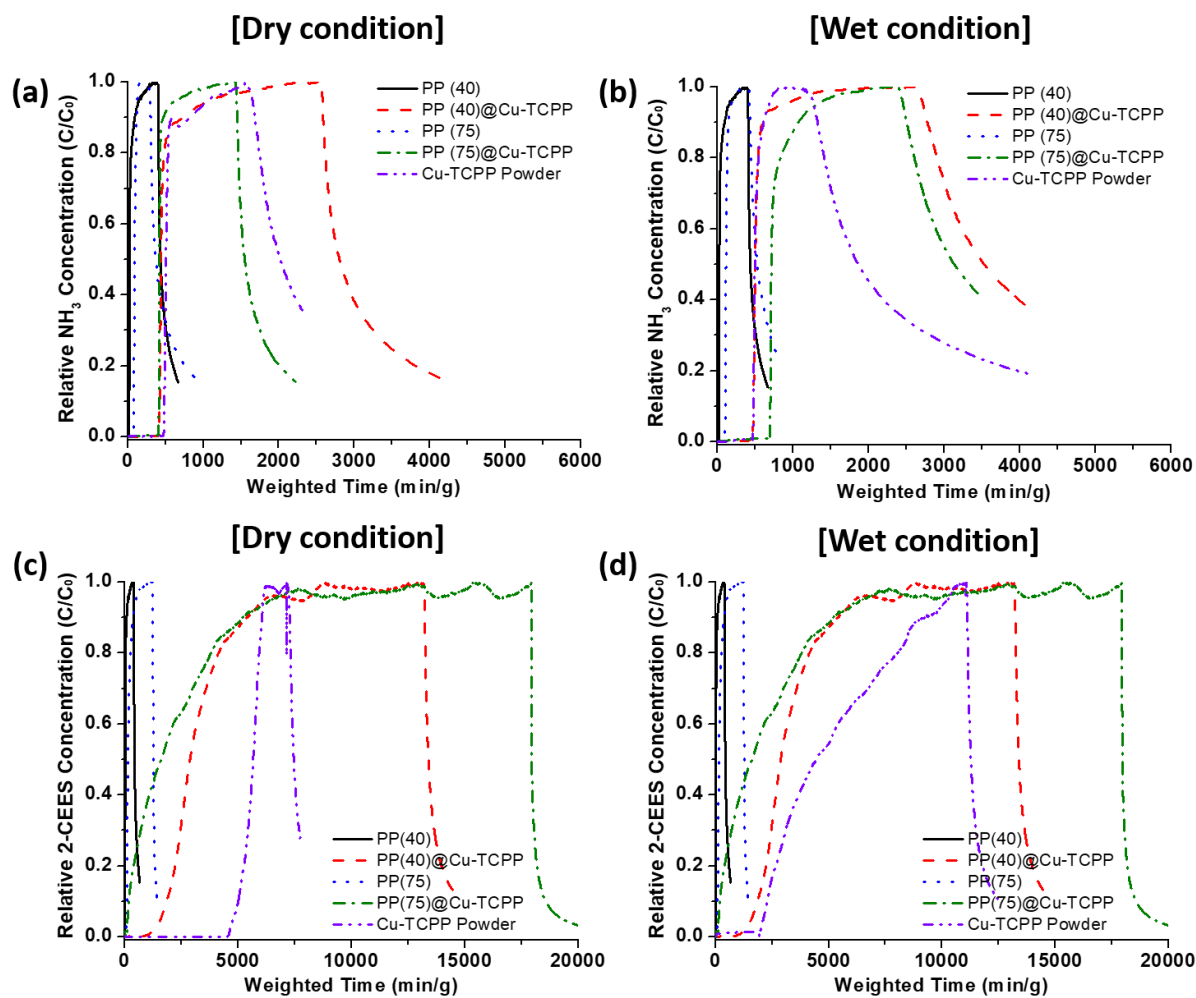


Figure S6.16. Ammonia microbreakthrough tested under (a) dry condition (0% RH) and (b) wet condition (80% RH) and 2-CEES microbreakthrough tested under (c) dry condition (0% RH) and (d) wet condition (80% RH) for PP(40), **4**: PP(40)@Cu-TCPP, PP(75), **4**: PP(75)@Cu-TCPP, and Cu-TCPP powder. Weighted time (min/g) is defined as time divided by adsorbent mass employed in the test. C/C_0 is a normalized concentration, with the feed concentration to the composite (C_0), and the concentration exiting the composite at time t (C). **4**: PP(75)@Cu-TCPP was synthesized by reacting PP@HDS(Zn,Cu) with H_2TCPP solution at 40°C for 12 h. Cu-TCPP MOF powder used was prepared by a conventional solvothermal method conducted at 80°C for 24 h.

Table S6.1. Material properties of PP fiber substrates, MOF-coated textiles, and Cu-TCPP powder.

	BET Surface area (m ² /g)	Total pore volume (cm ³ /g)	Dry (0% RH)		Humid (80% RH)		Ref
			NH ₃ loading (mol/kg)	2-CEES loading (mol/kg)	NH ₃ loading (mol/kg)	2-CEES loading (mol/kg)	
Polypropylene (PP)	1-2	0.001	0.1	0.1	0.2	0.1	This work
PP(40)@Cu-BTC ^[a]	201	-	-	-	2.0	-	4
PP(40)@Cu-TCPP	200	0.10	1.3	2.1	1.3	1.7	This work
PP(75)@Cu-TCPP	199	0.08	1.1	1.6	1.8	1.3	This work
Cu-TCPP powder	520 ± 84	0.30 ± 0.05	1.3	3.6	1.2	3.3	This work

[a]PP(40)@Cu-BTC was prepared by submerging PP(40)@ZnO in Cu(NO₃)₂·3H₂O and H₃BTC solution of water, ethanol, and DMF mixtures at ambient temperature for 3 min.⁴ *Parenthesis next to PP is indicative of density (grams per square meter) of fiber mats. BET surface area (m²/g_{MOF+fiber}) was measured by N₂ isotherms at 77 K. Total pore volume (cm³/g_{MOF+fiber}) was calculated at P/P₀=0.9 from N₂ adsorption isotherm at 77 K. PP(75)@Cu-TCPP was prepared by reacting PP(75)@HDS(Zn,Cu) and H₂TCPP in DMF solvent at 40°C for 12 h. PP@HDS(Zn,Cu)+TCPP is equal to 4: PP@Cu-TCPP. Cu-TCPP MOF powder was synthesized via conventional solvothermal method using Cu(NO₃)₂ and H₂TCPP at 80°C for 24 h.

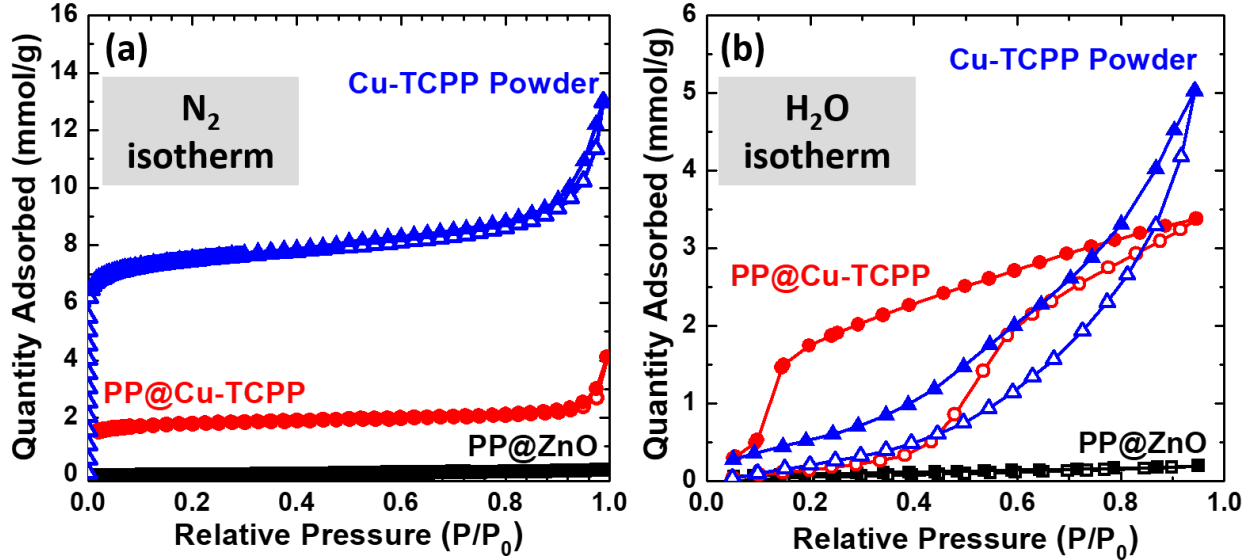


Figure S6.17. (a) N₂ isotherms at 77 K and (b) H₂O isotherms at 298 K for PP@ZnO, 4: PP@Cu-TCPP, and Cu-TCPP MOF powder. (c) BET surface area based on N₂ isotherms (m²/g_{MOF+fiber}) and total pore volume (cm³/g_{MOF+fiber}) based on H₂O isotherms for the samples measured.

[Calculation for water uptake of Cu-TCPP grown on polypropylene (PP) fibrous mats]

$$V_{t,(MOF)} \approx \frac{V_{t,(MOF+fiber)} \times m_{(MOF+fiber)} - V_{t,(fiber)} \times m_{(fiber)}}{m_{(MOF+fiber)} - m_{(fiber)}} \quad (1)$$

$V_{t,(MOF)}$: total pore volume of MOF grown on PP

$V_{t,(MOF+fiber)}$: total pore volume of PP@Cu – TCPP cloths

$V_{t,(fiber)}$: total pore volume of PP cloths

$m_{(MOF+fiber)}$: mass of PP@Cu – TCPP cloths

$m_{(fiber)}$: mass of PP cloths

*Total pore volumes of PP@Cu-TCPP ($V_{t,(MOF+fiber)}$), PP ($V_{t,(fiber)}$), and Cu-TCPP powder were calculated at $P/P_0=0.9$ based on the water vapor isotherm at 298 K.

[Example]

$$V_{t,(MOF)} \approx \frac{0.060 \frac{cm^3}{g} \times 0.1215 g - 0.001 \frac{cm^3}{g} \times 0.0813 g}{0.1215 g - 0.0813 g} = 0.18 cm^3/g_{MOF}$$

Water uptake of Cu-TCPP grown on PP cloths ($V_{t,(MOF)}$) is **0.18 cm³/g_{MOF}** as shown in the above calculation. This value is 2.4× larger than that of **Cu-TCPP powder (0.075 cm³/g_{MOF})**. This calculation result indicates that Cu-TCPP grown on PP fibrous mats by means of HDS intermediates causes substantial interaction at high $P/P_0 = (\sim 0.9)$ with water molecules due to the exotic vertical orientation of Cu-TCPP compared to Cu-TCPP powder.

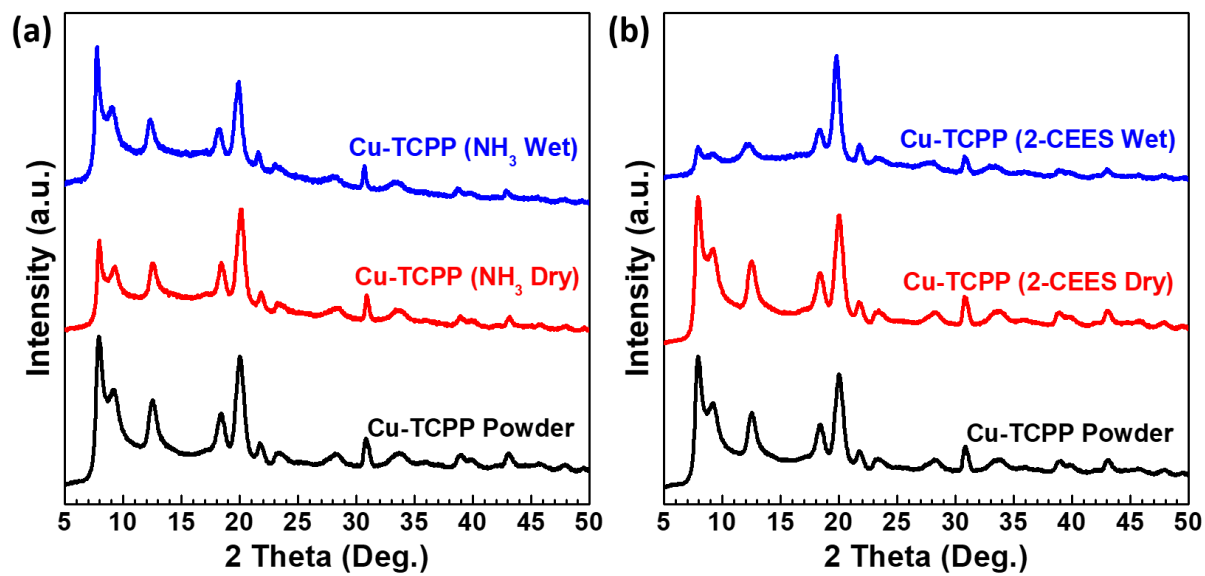


Figure S6.18. XRD patterns of Cu-TCPP powder before and after the microbreakthrough tests under dry (0% RH) and wet condition (80% RH) with ammonia or with 2-CEES. Cu-TCPP MOF powder used was prepared by a conventional solvothermal method conducted at 80°C for 24 h.

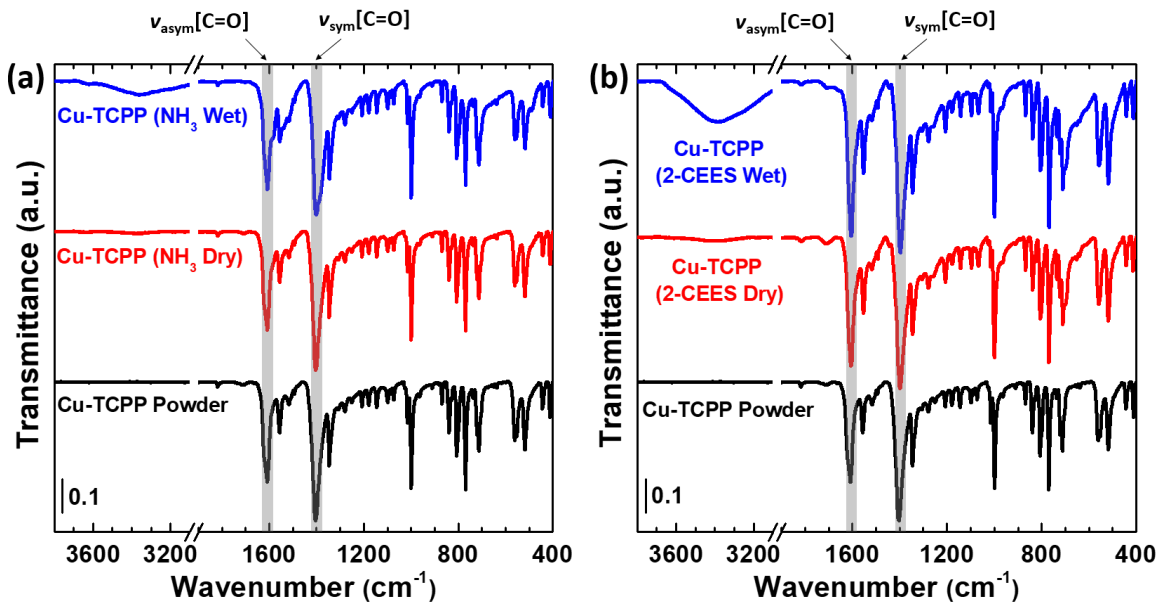


Figure S6.19. ATR-FTIR spectra for Cu-TCPP powder before and after the microbreakthrough tests under dry (0% RH) and wet condition (80% RH) with ammonia or with 2-CEES. Cu-TCPP MOF powder used was prepared by a conventional solvothermal method conducted at 80°C for 24 h.

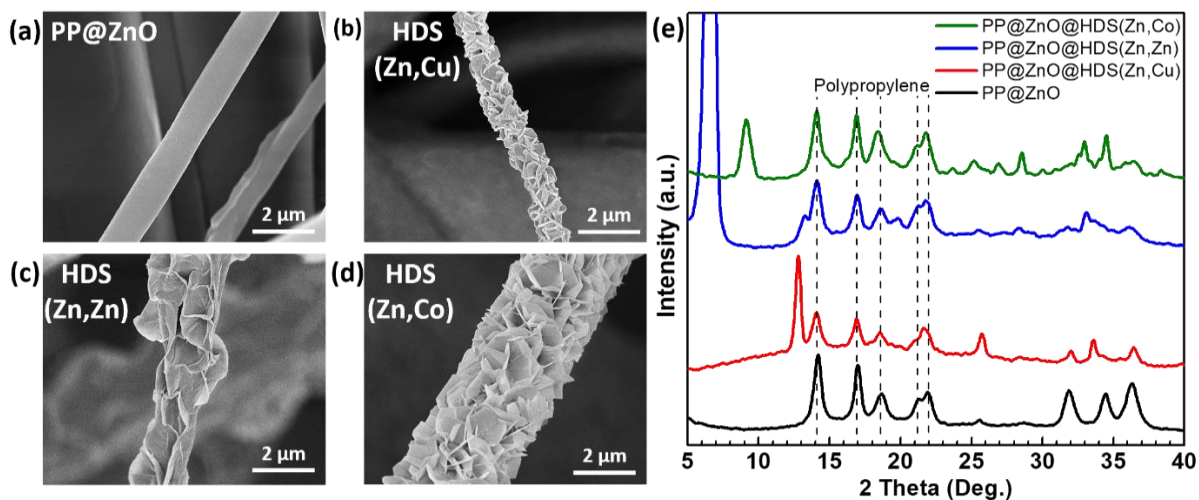


Figure S6.20. SEM images of (a) PP@ZnO, (b) PP@HDS(Zn,Cu), (c) PP@HDS(Zn,Zn), and (d) PP@(HDS) and (e) their XRD patterns.

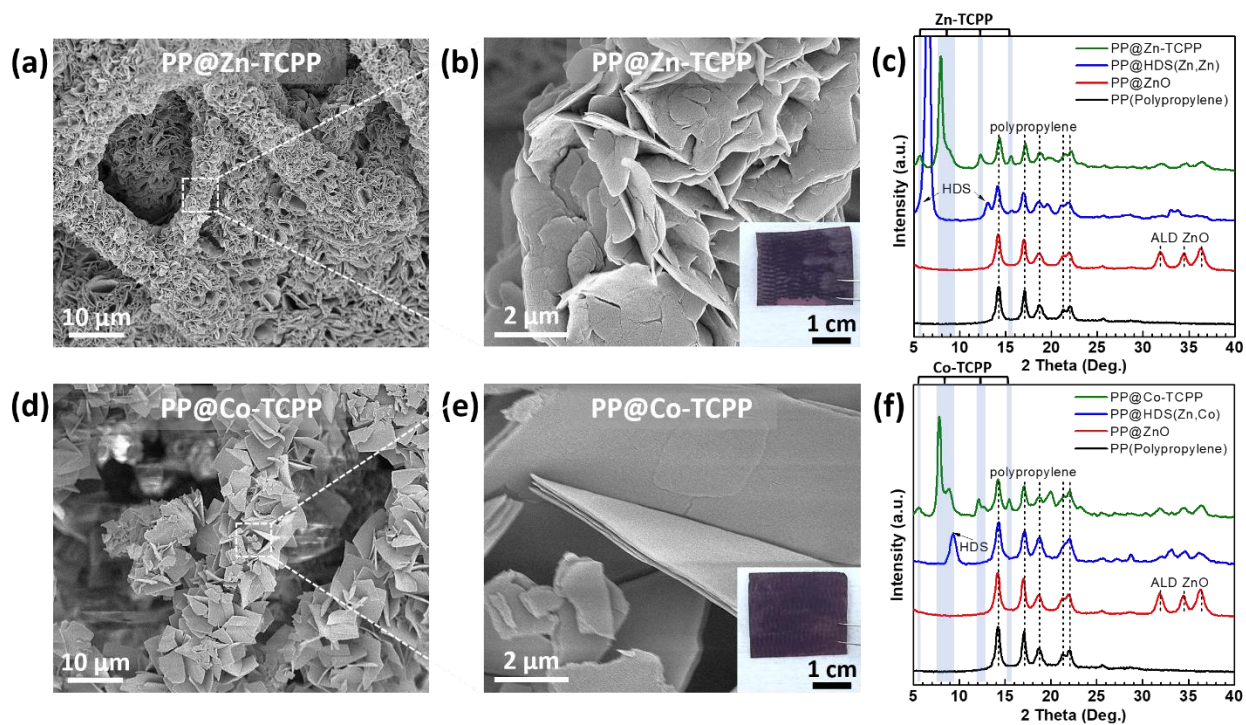


Figure S6.21. (a-b) SEM images for PP@Zn-TCPP composites synthesized via PP@HDS(Zn,Zn) + TCPP at 60°C for 12 h and XRD patterns (c) for PP, PP@ZnO, PP@HDS(Zn,Zn), and PP@Zn-TCPP. (d-e) SEM images for PP@Co-TCPP composites synthesized via PP@HDS(Zn,Co) + TCPP at 80°C for 20 h. XRD patterns for (e) PP, PP@ZnO, PP@HDS(Zn,Co), and PP@Co-TCPP. The insets in (a-b) and (d-e) are digital photographs of corresponding actual samples.

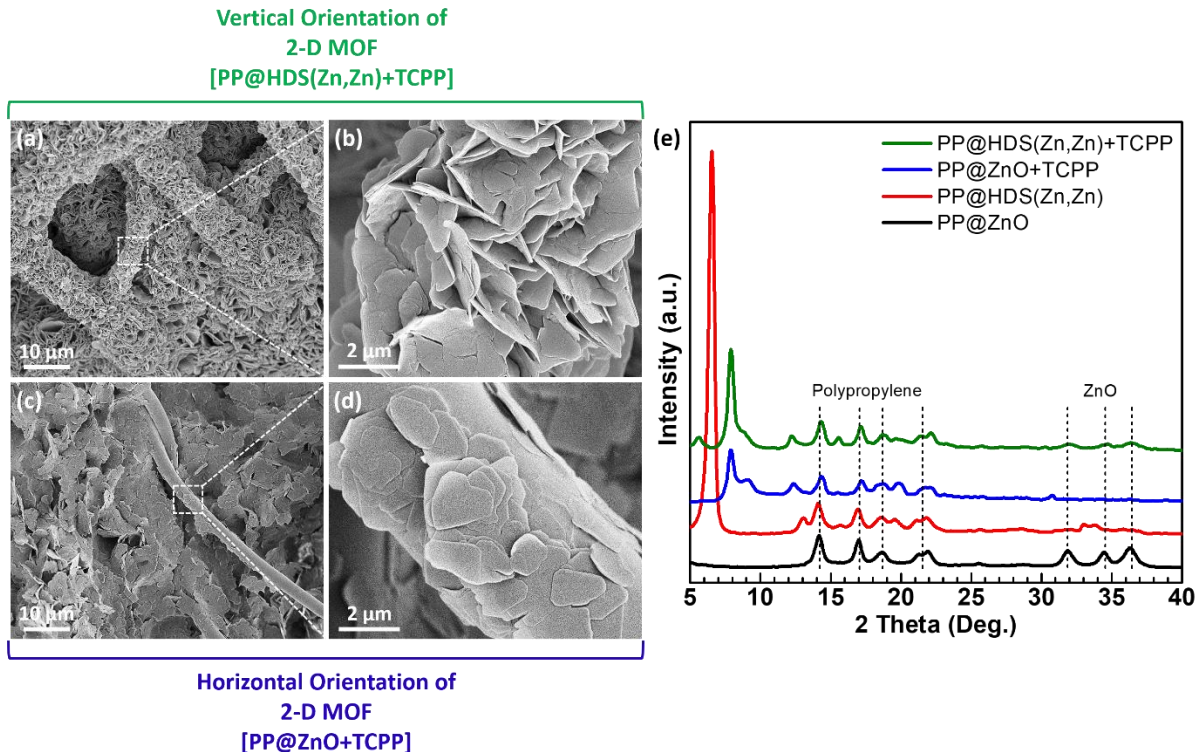


Figure S6.22. SEM images of Zn-TCPP MOFs grown on PP micro-fibers (a-b) (PP@HDS(Zn,Zn)+TCPP) in a vertical and (c-d) (PP@ZnO+TCPP) in a horizontal manner. (e) XRD patterns for PP@ZnO, PP@HDS(Zn,Zn), PP@HDS(Zn,Cu)+TCPP, and PP@ZnO+Cu(NO₃)₂+TCPP composite materials. Synthetic condition for both samples was performed at 40°C for 12 h.

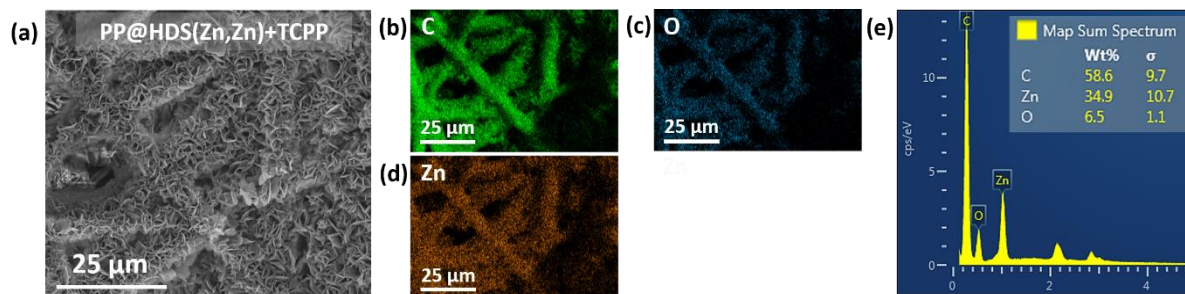


Figure S6.23. (a) SEM, (b-d) EDS mapping images, and (e) EDS spectra of PP@HDS(Zn,Zn)+TCPP prepared at 40°C for 12 h.

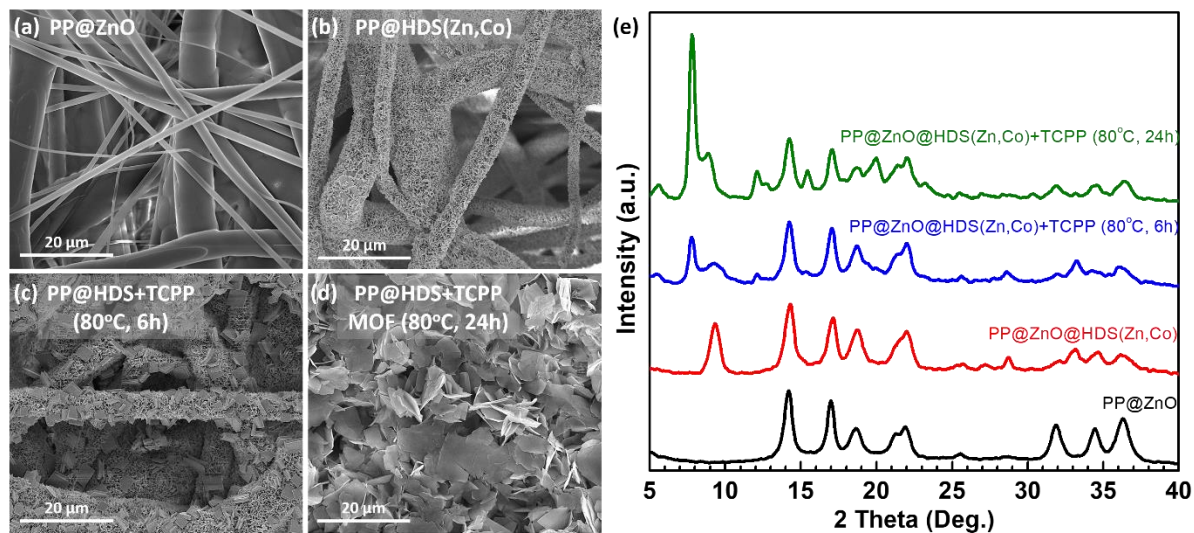


Figure S6.24. SEM images of (a) PP@ZnO, (b) PP@HDS(Zn,Co), (c) PP@HDS(Zn,Co) reacted with TCPP solution at 80°C for 6 h (PP@HDS(Zn,Co)+TCPP (80°C, 6 h)), and (d) PP@HDS(Zn,Co) reacted with TCPP solution at 80 °C for 24 h (PP@HDS(Zn,Co)+TCPP (80°C, 24 h)) (e) their XRD patterns.

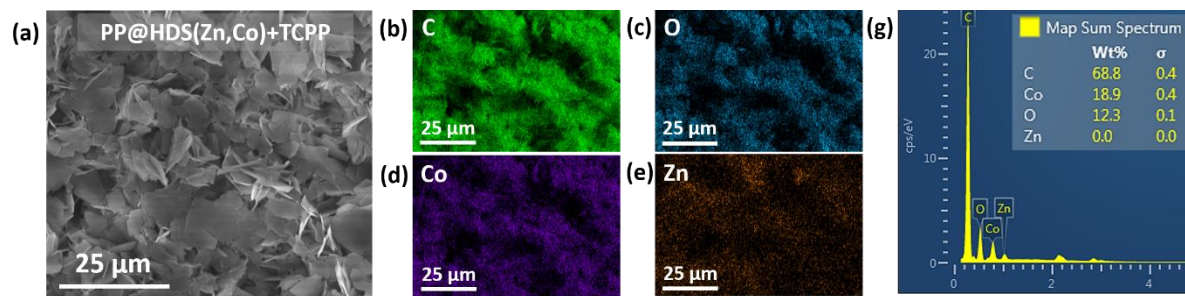


Figure S6.25. (a) SEM, (b-e) EDS mapping images, and (g) EDS spectra of PP@HDS(Zn,Co)+TCPP prepared at 80°C for 24 h.

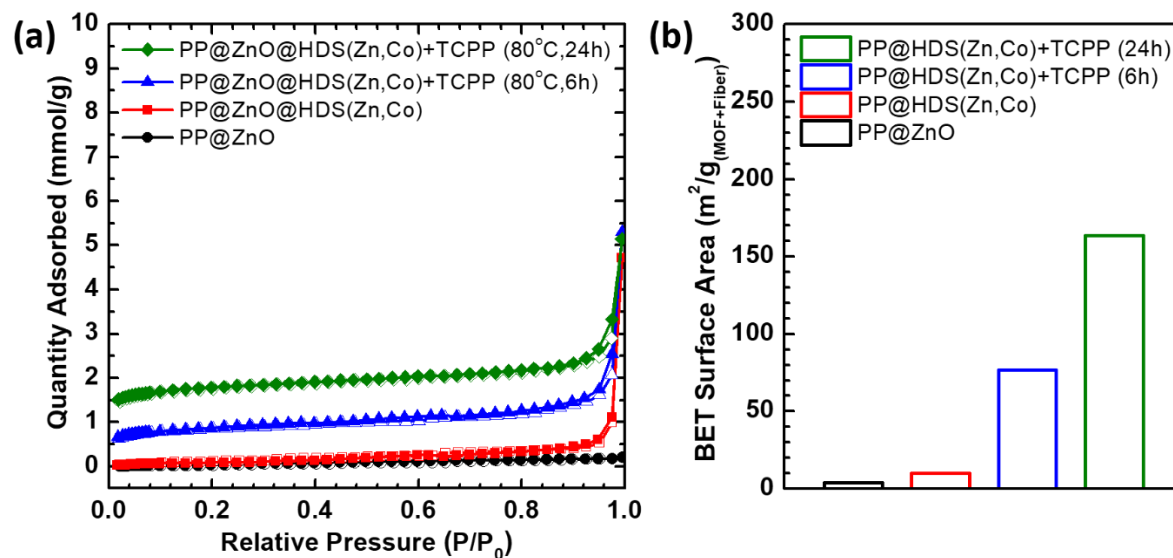


Figure S6.26. (a) N_2 isotherms at 77 K and (b) BET surface area ($m^2/g_{(MOF+Fiber)}$) for PP, PP@ZnO, PP@HDS(Zn,Co) reacted with TCPP solution at 80 °C for 6 h (PP@HDS(Zn,Co)+TCPP (80°C, 6 h)), and (d) PP@HDS(Zn,Co) reacted with TCPP solution at 80°C for 24 h (PP@HDS(Zn,Co)+TCPP (80°C, 24 h)).

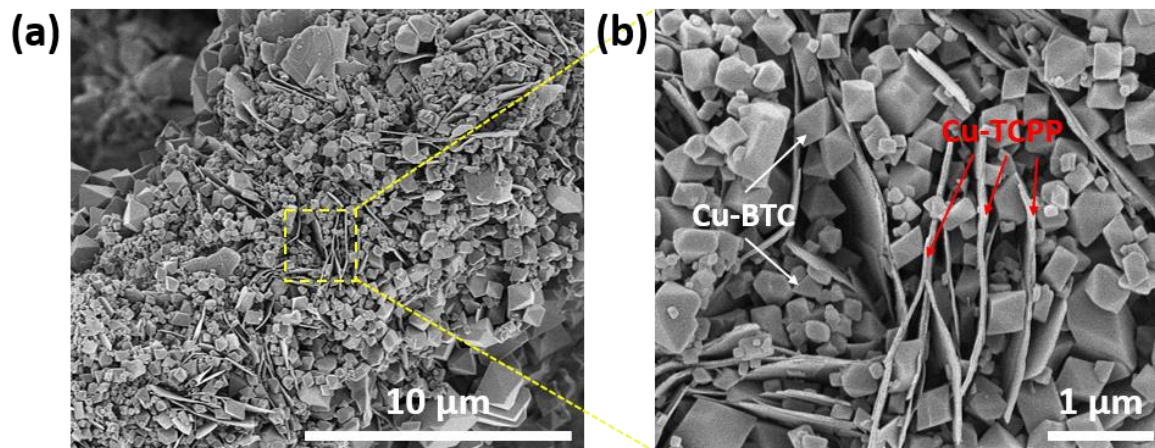


Figure S6.27. (a-b) SEM images of double MOF/fabric composites where Cu-BTC MOFs are overgrown on the 2D Cu-TCPP MOFs of PP@Cu-TCPP fibers prepared by reacting PP@HDS(Zn,Cu) with H₂TCPP solution at 40°C for 12 h. The Cu-BTC overgrowth was done by conducting 100 cycles of ALD ZnO to PP@Cu-TCPP composites, followed with reacting with a mixture of Cu(NO₃)₂ and H₃BTC at room temperature for 2 min to make PP@Cu-TCPP@Cu-BTC composites.

References

- (1) G. K. Hyde, K. J. Park, S. M. Stewart, J. P. Hinstroza, G. N. Parsons, *Langmuir* **2007**, *23*, 9844.
- (2) J. Zhao, B. Gong, W. T. Nunn, P. C. Lemaire, E. C. Stevens, F. I. Sidi, P. S. Williams, C. J. Oldham, H. J. Walls, S. D. Shepherd, M. A. Browe, G. W. Peterson, M. D. Losego, G. N. Parsons, *J. Mater. Chem. A* **2015**, *3*, 1458.
- (3) G. Xu, T. Yamada, K. Otsubo, S. Sakaida, H. Kitagawa, *J. Am. Chem. Soc.* **2012**, *134*, 16524.
- (4) J. Zhao, W. T. Nunn, P. C. Lemaire, Y. Lin, M. D. Dickey, C. J. Oldham, H. J. Walls, G. W. Peterson, M. D. Losego, G. N. Parsons, *J. Am. Chem. Soc.* **2015**, *137*, 13756.
- (5) J. Zhao, M. D. Losego, P. C. Lemaire, P. S. Williams, B. Gong, S. E. Atanasov, T. M. Blevins, C. J. Oldham, H. J. Walls, S. D. Shepherd, M. A. Browe, G. W. Peterson, G. N. Parsons, *Adv. Mater. Interfaces* **2014**, *1*, 1400040.
- (6) A. G. Wong-Foy, A. J. Matzger, O. M. Yaghi, *J. Am. Chem. Soc.* **2006**, *128*, 3494.
- (7) K. S. Walton, R. Q. Snurr, *J. Am. Chem. Soc.* **2007**, *129*, 8552.